

NASA TECHNICAL MEMORANDUM

NASA TM-75232

INVESTIGATION OF THE JET-WAKE FLOW OF A HIGHLY-LOADED  
CENTRIFUGAL COMPRESSOR IMPELLER

Dietrich Eckardt

Translation of "Untersuchung der Strahl/Totwasserströmung  
hinter einem Hochbelasteten Radialverdichterlaufgrad,"  
Doctoral Dissertation, Rhein Westfael Technical School,  
Aachen, West Germany, (1977), pp. 1-227.

(NASA-TM-75232) INVESTIGATION OF THE  
JET-WAKE FLOW OF A HIGHLY LOADED CENTRIFUGAL  
COMPRESSOR IMPELLER Doctoral Dissertation  
(National Aeronautics and Space  
Administration) 194 p HC AC9/MF A01

N78-16051

Unclas

G3/07 01899



NATIONAL AERONAUTICS AND SPACE ADMINISTRATION  
WASHINGTON, D.C. 20546 JANUARY 1978

## STANDARD TITLE PAGE

1. Report No. NASA TM-75232	2. Government Accession No.	3. Recipient's Catalog No.	
4. Title and Subtitle INVESTIGATION OF THE JET-WAKE FLOW OF A HIGHLY-LOADED CENTRIFUGAL COMPRESSOR IMPELLER.		5. Report Date January 1978	
		6. Performing Organization Code	
7. Author(s) Dietrich Eckardt Rheinisch-Westfälische Technische Hochschule, Aachen		8. Performing Organization Report No.	
		10. Work Unit No.	
9. Performing Organization Name and Address Leo Kanner Associates Redwood City, California 94063		11. Contract or Grant No. NASW-2790	
		13. Type of Report and Period Covered Translation	
12. Sponsoring Agency Name and Address National Aeronautics and Space Adminis- tration, Washington, D.C. 20546		14. Sponsoring Agency Code	
15. Supplementary Notes Translation of "Untersuchung der Strahl/Totwasserströmung hinter einem Hochbelasteten Radialverdichterlauf- rad," Doctoral Dissertation, Rhein Westfael Technical School, Aachen, West German, (1977), pp. 1-227.			
16. Abstract These investigations aimed at a better understanding of the complex flow field in high performance centrifugal compressors. Newly developed measuring techniques for unsteady static and total pressures (based on semiconductor transducers) as well as flow directions (special hot-wire probe), and a digital data analysis system for fluctuating signals (sampling technique) have been thoroughly tested. The loss-affected mixing process of the distorted impeller discharge flow has been investigated in detail, in the absolute and relative system, at impeller tip speeds up to 380 m/s. A theoretical analysis proved good coincidence of the test results with the DEAN-SENOO theory, which was extended to compressible flows.			
17. Key Words (Selected by Author(s))		18. Distribution Statement Unclassified-Unlimited	
19. Security Classif. (of this report) Unclassified	20. Security Classif. (of this page) Unclassified	21. No. of Pages	22. Price

## Foreword

The present study originated during my work at the Jet Propulsion Institute of the Deutsche Forschungs- und Versuchsanstalt für Luft- und Raumfahrt e.V. (DFVLR) [German Research and Test Center for Aeronautics and Space Travel] in Cologne-Porz. The directors of the Institute, G. Winterfeld, Ph.D Engineering and -- until 1973 -- Prof. H. Kühl, Ph.D Engineering, continually encouraged this study with their very kind and generous support. /9

Support in the form of valuable advice and encouragement was received from Prof. W. Traupel, Eidgenössische Technische Hochschule Zürich, within the framework of the centrifugal compressor research program of the Forschungsvereinigung Verbrennungskraftmaschinen e.V. (FVV) [Research Association for Internal Combustion Engines]. I would like to give my special thanks to Prof. Traupel and Prof. H. Gallus (Rheinisch-Westfälische Technische Hochschule, Aachen) for carefully reviewing this study and for agreeing to act as the referees.

In carrying out this study I received freindly support from many individuals. Here I would like to emphasize the helpful exchange of ideas with H. Weyer, Ph.D. Engineering, Prof. Y. Prof. Y. Senoo and Dr. R.C. Dean jr. I received much help from many of my colleagues at the Institute, especially K.-J. Trültzsch and W. Weimann. Their personal efforts assisted me in setting up the extensive experimental systems and in evaluating the experiments or numerical computations.

Finally, the FVV and its member companies furnished considerable financial and material support for this research project.

I am very grateful to all of those involved.

## Table of Contents

	Page
Foreword .....	ii
1. Notation .....	vii
2. Introduction .....	1
3. Development of Measurement and Evaluation Methods for Studying Nonsteady Flow Processes in Turbomachines .....	4
3.1 Special Technical Requirements for Flow Studies in Highly-Loaded Centrifugal Compressor Stages .....	4
3.1.1 High Time Resolution .....	6
3.1.2 Separation of the Factors Affecting the Signal .....	7
3.1.3 Small Probe Dimensions .....	8
3.2 Review of Possible Measuring Methods .....	8
3.3 Method of Instantaneous Pressure Measurement .....	9
3.3.1 Operational Behavior of Miniature Semiconductor Pressure Transducers .....	10
3.3.1.1 Frequency Resolution .....	10
3.3.1.2 Influence of the Installation Conditions .....	11
3.3.1.3 Thermal Effects .....	12
3.3.1.4 Results of the Studies on Operational Behavior ..	16
3.3.2 Development of Measuring Systems for Determining Changes in the Dynamic Wall Pressure and Total Pressure .....	17
3.3.3 Measurement Systems for Determining Exact Pressure Mean Values over Time .....	20
3.3.3.1 Special Pneumatic System for Wall Pressure Measurements .....	21
3.3.3.2 Hydraulic System for Total Pressure Measurements	22
3.4 Development of a Method for Measuring Direction in a Periodically Unsteady Flow .....	23
3.4.1 Problems in the Use of Hot-wire Anemometry .....	23

	Page
3.4.2 Construction and Measuring Principle of the Hot-wire Direction Probe .....	24
3.4.3 Probe Calibration and Frequency Characteristics ....	27
3.4.4 Discussion of the Measuring Technique for Nonsteady Direction Measurement .....	29
3.5 The Synchronized Sampling Technique -- an Electronic Evaluation Method for Test Signals from a Periodic, Strongly Fluctuating Flow .....	31
3.6 Basic Procedure for Determining, Processing and Evaluating Nonsteady Measured Variables .....	33
4. Design of the Test System, Operational Measuring Technique and Preliminary Experiments .....	36
4.1 Description of the Test Compressor .....	36
4.2 Total Layout of the Centrifugal Compressor Test Stand	40
4.3 Conventional Operational Measuring Technique and Data Determination .....	43
4.4 Preliminary Experiments (Performance Characteristics Measurements) .....	46
5. Experimental Procedure and Evaluation to Determine the Nonsteady Flow Behind the Impeller .....	51
5.1 Arrangement of Measuring Points and Test Program .....	51
5.2 Determination of Constant Variables over Time .....	55
5.3 Determination of Nonsteady Variables .....	56
5.4 System of Equations for Calculating further Nonsteady Flow Variables .....	60
5.5 System of Equations for Calculating the Characteristic Mean Value .....	64
5.6 Accuracy of the Selected Measuring Technique and Evaluation Technique .....	70
6. The Flow at the Outlet of the Centrifugal Compressor Impeller .....	74
6.1 Results of the Nonsteady Flow Measurement .....	75

	Page
6.1.1 Wall Pressure, Total Pressure and Distribution of Total Pressure Fluctuation .....	75
6.1.2 Direction Distribution of the Absolute Flow .....	83
6.2 Examples for Calculated Distributions .....	83
6.2.1 Conversion of Work and Total Temperature .....	83
6.2.2 The Velocity Field in the Absolute and Relative System .....	86
6.3 Analysis of Test Findings at the Impeller Outlet with Respect to the Jet-Wake Distribution .....	90
6.4 Discussion of Various Flow Mechanisms in the Centri- fugal Impeller which Contribute to the Formation of the Jet-Wake Distribution .....	94
6.4.1 Optical Flow Measurements in a Centrifugal Compres- sor Impeller .....	95
6.4.2 Qualitative Analysis of the Impeller Flow .....	102
7. Theoretical Treatment of the Jet-Wake Flow behind the Impeller Outlet .....	107
7.1 Expanded Dean-Senoó Theory .....	108
7.1.1 Analytical Flow Model .....	108
7.1.2 Fundamental Flow Equations .....	112
7.1.3 Structure of the Computation Program .....	116
7.1.4 Determination of the Wall Friction and Interface Friction Coefficients and the Boundary Layer Dis- placement Thickness .....	118
7.2 Expanded Model for Estimating the Influence of the Variable Relative Flow Direction in the Jet Region and Wake Region .....	122
8. The Behavior of the Jet-Wake Flow in the Unbladed Cen- trifugal Diffuser .....	124
8.1 The Three-Dimensional Development of the Real Flow in the Inlet Region of the Diffuser .....	124
8.1.1 Static Pressure and Total Pressure .....	125

	Page
8.1.2 Total Pressure Fluctuation and the Effect of Flow Line Bending on the Degree of Mixing .....	130
8.1.3 The Velocity Field in the Absolute and Relative System .....	135
8.2 Comparison between Theoretical and Experimental Results Using as a Basis the Jet-Wake Flow Model ....	140
8.3 Theoretical Parameter Study on the Jet-Wake Mixing Process .....	154
9. Summary .....	157
10. References .....	161
11. Appendix .....	168
I. Investigation of Temperature Effects on Miniature Semiconductor Pressure Transducers .....	168
II. The Synchronized Sampling Technique .....	170
III. Total Temperature Measurement in the Disturbed Flow behind the Impeller Outler .....	175
IV. Definition of the Relative Total Pressure Pt, rel .	179

## 1. Notation

The meaning of the most important symbols is given below. /10  
Where deviations occur in individual cases, these will be explained in the text.

a	Sonic speed
$a_t$	Quiescent speed of sound
A	Area
$A/A_0$	Amplitude ratio
b	Diffuser width
$b'$	Diffuser with ratio $b/b_e$
c	Absolute velocity
$c_d$	Dissipation coefficient
$c_f$	Skin friction coefficient
$c_p$	Specific heat at constant pressure
C	Relative absolute velocity $c/u_2$
d	Diameter
D	Diameter
DS	Pressure side
e	Base of the natural logarithm
E	Kinetic energy flow of the absolute velocity
f	Relative total pressure fluctuation factor, Eq. (6.2)
f	Excitation frequency
$f'$	Absolute total pressure fluctuation intensity, Eq. (6.2)
$f_m$	Mass flow correction value, Eq. (5.21)
$f_r$	Inherent frequency
$F_S$	Skin friction force in the jet, Eq. (7.1a)
$F_T$	Skin friction force in the wake, Eq. (7.1b)
h	Enthalpy
$h_t$	Total enthalpy
$h_{t,rel}$	Relative total enthalpy, Eq. (IV.1)
IDA	Program for instantaneous data evaluation
INTIDA	Program for integral, instantaneous data evaluation
$K_t$	Loss relation, Eq. (6.5)
KSO	Cathode ray oscillograph
l	Coordinate along the middle of the impeller blade channel



L	Length	
$\frac{L}{L_F}$	Specific work (on the fluid)	
$L_G$	Form changing work	<u>/11</u>
$L_R$	Drag work	
$L_{2F}$	Two-focus laser, velocity measuring method	
$\dot{m}$	Mass flow	
M	Sonic mach number	
$M_t$	Quiescent mach number	
$M_T$	Torque required to overcome the forces of friction	
MR	Mach number diffusion ratio, Eq. (5.55)	
n	Speed of rotation	
n	Number of measurements	
N	Power	
p	Static pressure	
$p_{ref}$	Reference pressure	
$p_t$	Total pressure	
$p_{t,rel}$	Relative total pressure, Eq. (6.6)	
q	Amount of heat added per unit mass	
q	Jet-wake pressure fluctuation, Fig. 7.1b	
r	Radial coordinate	
r	Interface radius of curvature	
R	Radius	
R	van Le mixing radius, Eq. (7.22)	
R	Gas constant for air	
R'	Simplified notation for $R/R_2$	
R*	Jet-wake mixing radius	
$R_K$	Channel radius of curvature	
Rf	Temperature recovery factor	
Re	Reynolds number	
RE	Unit of scanning	
$s_m$	Length of the outer contour of the impeller through the vertical center section	
S	Jet-wake interface frictional force, Eq. (7.2)	
S	Summary interface stability criterion, Eq. (8.4)	
$S_C$	Interface stability criterion under the effect of Coriolis accleration, Eq. (8.2)	

$S_N$	Interface stability criterion under the effect of normal acceleration due to streamline curvature, Eq. (8.3)	
SRS	Rear of jet (in direction of rotation)	
SS	Suction side	
SST	Synchronized sampling technique	
S/T	Jet-wake	
SVS	Front of jet (in direction of rotation)	<u>/12</u>
t	Blade pitch	
t	Time	
$t_g$	Gate opening time	
$t_i$	Integration time	
$t_m$	Measurement time	
$t_r$	Signal repetition rate	
$t_s$	Channel division in the probe measuring radius	
$T_s$	Cathode ray transit time	
T	Static temperature	
T	Signal period	
$T_t$	Total temperature	
TR	Total temperature ratio, Eq. (6.4)	
u	Circumferential speed	
u	Electric a.c. component	
U	Relative circumferential speed $u/u_2$	
U	Signal voltage	
$\bar{U}$	Electric d.c. component	
V	Volume	
w	Relative velocity	
W	Referred relative velocity $w/u_2$	
$x/s_m$	Relative external contour of the impeller in the vertical center section	
y	Coordinate in the direction of the circumferential speed	
y/t	Relative blade spacing	
$y'/t'$	Relative blade spacing between the blade surfaces	
z	Impeller blade number	
z	Coordinate along the axis	
z/b	Relative diffuser width	

$\alpha$	Absolute flow angle, relative to the positive circumferential direction	
$\alpha$	Expansion factor for the synchronized sampling technique	
$\beta$	Relative flow angle, related to the negative circumference direction	
$\beta_s$	Blade angle	
$\gamma$	Relative velocity ratio, Eq. (5.63)	
$\delta$	Boundary layer thickness	
$\delta$	Interference parameter, Eq. (5.64)	
$\delta_0$	Pressure norm correction factor, page	(74)
$\delta^*$	Boundary layer displacement thickness	
$\Delta$	Difference, e.g. $\Delta T$ = temperature difference	<u>/13</u>
$\Delta p_t$	Relative total pressure change, Eq. (8.1)	
$\epsilon$	Wake surface component, Eq. (5.61)	
$\epsilon_k$	Continuity form factor, Eq. (5.57)	
$\epsilon_e$	Energetic form factor, Eqs. (5.58) and (5.59)	
$\epsilon_p$	Relative pressure fluctuation, Eq. (4.2)	
$\zeta$	Interface coefficient of friction	
$\eta_i$	Internal efficiency, Eq. (4.3)	
$\eta_s^*$	Isentropic impeller efficiency, Eq. (5.67)	
$\eta_p^*$	Polytropic impeller efficiency, Eq. (5.68)	
$\eta_{t,s}^*$	Isentropic impeller total efficiency, Eq. (5.69)	
$\theta$	Cylinder coordinate	
$\theta_0$	Temperature norm correction factor, page	(74)
$\kappa$	Isentropic exponent	
$\lambda$	Twist parameter	
$\mu$	Reduced output factor, Eq. (6.3)	
$\mu_T$	Wake - mass flow component, Eq. (5.62)	
$\pi$	Circular constant	
$\Pi$	Pressure ratio	
$\Pi_t$	Total pressure ratio	
$\rho$	Density	
$\rho'$	Density ratio $\rho/\rho_e$	
$\tau$	Phase relationship of the samples to the signal period	
$\phi$	Flow factor, Eq. (5.54)	
$\phi$	Probe angle	

$\phi$  Phase shift  
 $\omega$  Angular velocity

Subscripts

a Indicated value  
a Exterior  
A Initial value  
e Diffuser input region  
e Relative to the energy equation  
E End value  
HD Hot wire  
i Internal  
IDA From the program for instantaneous data evaluation  
INTIDA From the program for integral, instantaneous data evaluation  
k Relative to the continuity equation  
m Meridional  
max Maximal  
min Minimal  
N Standard atmosphere condition  
N Blade wake  
O Design parameter  
r Radial  
red Parameter reduced to standard conditions  
ref Reference parameter  
rel Relative  
s Isentropic  
s Probe  
s Blade  
S Jet  
SST Synchronized sampling technique  
t Total condition  
T Wake  
u Circumferential component  
VENT Measured width Venturi tube  
O Compressor intake

/14

- 1 Impeller intake
- 2 Impeller exhaust
- 3 Diffuser intake region
- 4 Diffuser,  $R/R_2 = 1.687$
- 5 Compressor exhaust
- 7 Two-focus laser measuring surface in the Impeller,  
 $x/s_m = 0.08$
- 10 Two-focus laser measuring surface in the Impeller,  
 $x/s_m = 0.43$
- 11 Two-focus laser measuring surface in the Impeller,  
 $x/s_m = 0.59$
- 13 Two-focus laser measuring surface in the Impeller,  
 $x/s_m = 0.87$
- 14 Two-focus laser measuring surface in the Impeller,  
 $x/s_m = 1.01$
- I Measuring surface in the diffuser intake,  
 $R/R_2 = 1.017$
- II Measuring surface in the diffuser intake,  
 $R/R_2 = 1.039$
- III Measuring surface in the diffuser intake,  
 $R/R_2 = 1.089$
- IV Measuring surface in the diffuser intake,  
 $R/R_2 = 1.151$
- ' Turbulent or fluctuating component
- " Impeller
- Mean value, especially mean surface area, temporal or statistical mean value 15
- = Center of mass; value calculated by means of h-s equations from representative mean values
- \* Related to the mixing radius
- \* Calculated by using Eq. (5.66)

The equations are all homogeneous with regard to dimensional analysis, hence they are valid in any coherent system of units. Dimensions are given in the SI system.

INVESTIGATION OF THE JET-WAKE FLOW OF A HIGHLY-LOADED  
CENTRIFUGAL COMPRESSOR IMPELLER

Dietrich Eckardt  
Rheinisch-Westfälische Technische Hochschule, Aachen

2. Introduction

/17\*

High performance centrifugal compressors are today used primarily in mobile and stationary gas turbines -- with units of power of about 50-1,000 kW -- in turbo-superchargers and as process compressors in the chemical industry. The primary aim of aerodynamic developments is, in general, to increase the efficiency scale. Thus, for small gas turbines, for example, with a 1% improvement in compressor efficiency, one counts on about a 3% reduction in specific fuel consumption. Along with this, one tries to obtain high scale pressure ratios with a relatively large absorption capacity and a range of performance characteristics as large and as stable as possible.

The flow in the relatively long, narrow and three-dimensionally twisted channels of a centrifugal compressor stage is considerably influenced by friction effects. Potential theoretical computer methods are not capable of predicting the actual flow with sufficient accuracy. Given the present state of the art, it seems that further, desired improvements will only be possible if one is successful in obtaining basic, more profound knowledge of the actual flow conditions in heavily loaded centrifugal compressors. This will require a transition from the routine method used up to now -- by necessity -- of empirical correlation and extrapolation of existing stage designs. This would open up the possibility of modifying existing design procedures with simple but relevant model ideas -- relevant in terms of the physical flow -- in such a way that fairly optimal configurations would result. The precondition for fulfilling this aim is that it must be possible to accurately measure and analyze the complex centrifugal compressor flow under operating conditions. This study attempts to accomplish this in an important partial region of the flow.

In the flow field of heavily loaded centrifugal impellers a number of flow events occur which are subject to friction. The significance of these individual events and their interaction with each other is still largely unexplained (see section 6.4.2). As a result -- mostly in the radial portion of the blade channel -- three-dimensional flow separation occurs in the region of the suction side of the blades and the housing

/18

---

\* Numbers in the margin indicate pagination in the foreign text.

wall. Because of its almost insignificant, relative kinetic energy, this region of separation is called the "dead water" region or wake and it increases up to the impeller exhaust. Thus, for heavily loaded radial impellers, it leads to the characteristic shift of the main flow -- the "jet" -- in the region of the pressure side of the blades and the rear wall of the channel.

This relative speed distribution of the jet-wake has considerable influence on the conversion of energy in the centrifugal compressor stage:

- inside the impeller the theoretically desired flow slowdown is decreased,
- immediately after the impeller exhaust, equalization of the disturbed flow is completed with dissipation and
- finally, the instantaneous absolute flow resulting from the disturbed relative flow influences the pressure recovery in the following diffuser.

This also outlines the central role which studies on jet-wake flow behind a highly loaded radial impeller have for detailed flow analysis of the entire stage. With exact measurements in this region it is possible to draw important conclusions on the impeller flow. With these measurements -- in conjunction with measurements of the stage efficiency -- it is possible to make a separate loss analysis for the impeller and diffuser, and in so doing the mixing losses and equalization losses for the disturbed flow in the diffuser intake region can reasonably be charged to the impeller. Finally, exact knowledge of the development of jet-wake equalization after the impeller exhaust is important for the design of the subsequent diffusers and for the evaluation of this design in connection with standing questions on noise generation and on the stability of the range of performance characteristics for the compressor. The phenomenon of disturbed jet-wake impeller flow was recognized early on in the construction of radial engines. However, because of the well known difficulty in making measurements in a rotating system, this phenomenon was only rarely investigated quantitatively. As early as 1902 Smith [2.1]<sup>1</sup>, under certain operating conditions, observed the appearance of a "partial filling" in the impeller of a radial pump. The earliest,

/19

---

1. This information comes from an interesting bibliography on the topic of jet-wake flow which Moore included in his English translation of [2.2]. This was published as Technical Report CUED/A-Turbo/TR 73 (1975), University of Cambridge, England.

detailed measurements in a centrifugal compressor impeller include findings from the Brown-Boveri flow laboratory which were published by Carrard [2.2]<sup>1</sup> in 1923. These results give clear references to jet-wake distributions. Evidently Carrard was the first to try to consider theoretically the influence of the disturbed flow on the conversion of energy in the impeller using a simple jet-wake flow model. In his terminology he referred to this as the "le jet et la zone neutre" [the jet and the neutral zone]. After a number of further impeller studies at lower circumferential velocities (cf. section 6.4), it wasn't until 1960, after all, before the first quantitative studies were published on jet-wake mixing behind a centrifugal compressor impeller. Presumably, this delay was due to technical difficulties in making the necessary, exact measurements of the instantaneous absolute flow, both in magnitude and direction. Dean and Senoo [7.1], based on a few quantitative hot-wire measurements, developed their two-dimensional theory for calculating the jet-wake mixing under incompressible flow conditions. In 1974 Senoo and Ishida [7.5] first published a jet-wake flow analysis which was based on nonsteady measurements in several radii of the diffuser intake region. Two experimental studies [7.1, 7.5] were carried out behind centrifugal impellers with backward bent blades in the incompressible flow region at rotation speeds of  $n < 5000$  rpm. No results were given on the distribution of the disturbed flow over the diffuser width.

Until the time that the present study was begun, all quantitative investigations of the relative flow in centrifugal compressor impellers and of the absolute flow behind the impeller exhaust were limited to low rotation speeds and the region of incompressible flow because of the technical difficulties mentioned above. At higher rotation speeds, measurements were only possible in the absolute system with conventional averaging probes. Their readings in the region of the non-steady flow straining the probes can be affected with considerable errors. /20

In the first place, the aim of the studies presented here was to precisely measure and theoretically analyze the development of the disturbed, compressible flow behind a centrifugal compressor impeller with radial-ending blades under operating conditions approximating real conditions, i.e. with rotation speeds of up to  $n = 18,000$  rpm (circumferential velocity at the impeller exhaust  $u_2 = 377$  m/s). This would then provide sure data for improved methods for computing and designing high-performance centrifugal compressors. In order to achieve this program it was necessary to solve the following individual tasks:

---

1. See footnote, p. 2



1. Develop and test new, high-resolution (with respect to time) measuring and evaluation methods which are suitable for an exact study of a high level of nonsteady, absolute and relative flow.
2. Experimental analysis and interpretation of the physical flow characteristics of the disturbed flow lines in the diffuser intake region:
  - in several points in the characteristic field of the compressor,
  - in several radially staggered measuring surfaces behind the impeller exhaust,
  - with exact resolution in the circumferential direction over the flow region of a blade channel and over the diffuser width in the axial direction.
3. Expansion of the Dean and Senoo theory [7.1] for the region of compressible flows and testing the theoretical predictions on the basis of the two-dimensional jet-wake flow model by comparison with experimental results on the actual formation of the disturbed flow.

### 3. Development of Measurement and Evaluation Methods for Studying /21 Nonsteady Flow Processes in Turbomachines

We have already seen in the introduction that the development of suitable measuring methods is an important prerequisite for the analysis of the complicated flow conditions which exist at the exhaust of a highly loaded centrifugal compressor impeller. The experimental conditions in this region are distinguished by a number of technical difficulties involving measurements -- difficulties which, to a similar extent, are seldom met with in the experimental techniques of flow mechanics. From the outset, this considerably limits the number of fundamentally suitable measuring methods and evaluation methods.

After extensive laboratory studies which were used to create or further develop individual methods, a total measuring system was set up. With this system it is possible to solve the present problem -- and also a number of other problems -- in the study of nonsteady flow processes in turbomachines.

#### 3.1 Special Technical Requirements for Flow Studies in Highly-Loaded Centrifugal Compressor Stages

Consideration of the flow conditions after the impeller exhaust reveals the highly nonsteady nature of the flow in this region. This presents a considerable difficulty in making a precise and detailed determination of the flow condition.

Essentially, the variations in the flow field over time -- as observed in the absolute system -- can be divided into three

groups which are explained by means of Fig. 3.1. The figure shows a graphical representation of changes in pressure over time, as might be plotted, for example, with a wall pressure sensor placed in the compressor housing immediately behind the impeller exhaust.

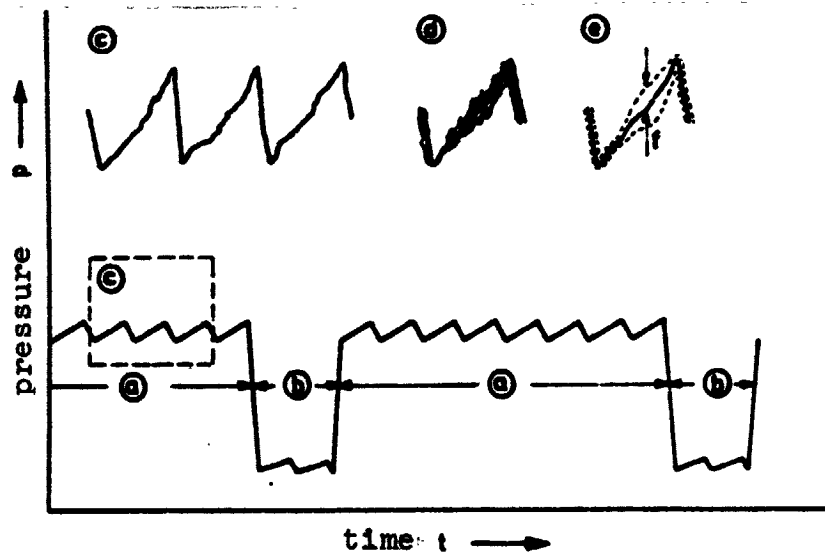


Fig. 3.1 Changes in wall pressure over time to explain various forms of instantaneous flow in centrifugal compressors.

The periodic variations observed in the stable operational region of the compressor -- (a) -- have a basic frequency corresponding to the product of the blade number and the rotation frequency of the impeller. The reason for these variations is the change in the condition of flow in the circumferential direction within an impeller-blade channel. This instantaneous flow pattern, in the case of a finite number of blades and frictionless flow, represents the necessary condition for any form of energy transfer (cf., for example, [3.1], p. 209). Real flow effects -- such as turbulence, boundary layers, secondary flow or flow separation and the manufacturing accuracy of the impeller -- can also affect the variation in the condition of flow from blade to blade. These periodic variations also apply to the flow field behind the impeller exhaust. Here they are balanced out by mixing and the exchange of energy after a certain radial distance.

/22

An additional instantaneous phenomenon in the operating behavior of the compressor stage occurs when the mass flow is reduced below certain limit values. Rotating stalls or pumps -- (b) -- are terms used to describe the partial or complete separation of the orderly compressor flow. The disturbances

caused by this in the absolute flow field can appear periodically, but their appearance can also be completely irregular.

The third type of instantaneous flow shows up if we consider the changes in pressure for several successive blade passages. For example, the enlarged portion of the graph for the changes in pressure labelled ©, which repeat themselves periodically with the blade frequency, have a generally similar curve which is superimposed by irregularly distributed interferences. These deviations from a statistically average pressure graph are especially clear if the individual signal characteristics are superimposed on the screen of an oscillograph by triggering with the blade frequency (d). /23

Irregularly occurring fluctuation magnitudes -- referred to below as flow fluctuation or rough turbulence -- are due to the overlapping of the general flow turbulence with nonsteady effects of the relative flow which, for example can sometimes be triggered by unstable regions of separation in the impeller-blade channels.

For the studies made within the scope of this work in the stable range of characteristics, the statistical average instantaneous flow pattern was determined in each case, as suggested by (e). In addition, a parameter referred to as a "fluctuation factor f" was determined. This describes the intensity of the rough turbulent fluctuations in the region of one blade spacing.

A quantitative impression of the measuring techniques required for analyzing these nonsteady flow forms is given by the figures listed in the following table, Table 3.1. These refer to measurements made 3.4 mm behind the exhaust of the centrifugal impeller studied with a diameter of 400 mm.

A few fundamental requirements can be deduced from this concise presentation of the extreme test conditions at the exhaust of a highly-loaded centrifugal compressor impeller. The sensors and measuring methods must satisfy these requirements for detailed flow studied in this region.

### 3.1.1 High Time Resolution

For the example given in Table 3.1, the blade and thus the frequency of the periodically recurring flow pattern turns out to be 6 kHz. Suitable measuring systems must be capable of exactly plotting the change in flow parameters in the region of one blade spacing. In so doing, as shown in Fig. 3.1e for the transition from the blade pressure side to the blade suction side, signal rise times can occur which exceed the blade frequency by a factor of 5-10. The inherent frequency of suitable measuring systems must then be at least 3 times greater than the test frequency, as, for example, shown in Fig. 3.3 for /24

TABLE 3.1 RANGE OF VARIATION FOR THE PERIODIC CONDITIONS OF FLOW  
BEHIND THE IMPELLER EXHAUST UNDER NORMAL CONDITIONS IN THE  
COMPRESSOR INTAKE (CF. FIG. 3.1e)

Example:

Rotation speed	18 000	U/min
Mass flow	7.40	kg/s
Blade number	20	-
Signal frequency	6	kHz
Total pressure	2.9 - 4.3	bar
Static pressure	1.7 - 1.9	bar
Total temperature	391 - 448	K
Static temperature	338 - 359	K
Static density	1.7 - 1.9	kg/m <sup>3</sup>
Absolute velocity	337 - 445	m/s
Absolute flow direction	9 - 31	°
Total pressure fluctuation with respect to the local average	10 - 25	%

the example of the miniature pressure sensor. This is to prevent impermissibly high errors in the signal amplitude and signal phase relationships. For measurements in the centrifugal compressor design point considered above, this yield necessary inherent system frequencies on the order of 100-150 kHz.

/25

3.1.2 Separation of the Factors Affecting the Signal

Table 3.1 shows that all of the possible parameters for describing the disturbed flow field at the impeller exhaust vary considerably in the region of 1 blade spacing. Of the basically suitable measuring methods -- suitable because of their high time resolution -- most of them, because of their physical relationships -- address themselves simultaneously to several of the variable flow parameters.

For example, the semiconductor strain gauge bridges of the pressure sensor can be put out of tune not only mechanically by compressive stress, but they also react to changes in ambient

temperature. Likewise, the heat transfer equations for hot-wire anemometry involve a large number of rapidly varying flow condition parameters in the exhaust region of a centrifugal impeller. Therefore, a measuring method for the case under consideration can basically only be used if either:

- the test signal depends only on the variable under study, or
- the influence of other variables can be eliminated by special measures or
- the signal variables can be separated by making supplementary measurements and by means of precisely known physical relationships.

### 3.1.3 Small Probe Dimensions

The requirement for high time resolution already partially contains the necessity of using miniaturized probes in order to reduce the slowness of the system. Extremely small probe dimensions are also necessary, however, so as not to falsify all too much the diffuser flow field which tends to separate. On the other hand, only probes with high mechanical resistance and corresponding dimensions possess the required service life for extensive measurements in the highly disturbed, roughly turbulent flow in the diffuser intake region.

126

Therefore, studies on larger compressor stages represent a certain compromise on this point. In these larger stages the larger probe dimensions required for mechanical reasons stand in a favorable relationship to the stage dimensions.

### 3.2 Review of Possible Measuring Methods

With respect to the special requirements of the measuring technique discussed above, only a few measuring methods are suitable for detailed, quantitative flow studies behind a highly loaded centrifugal impeller.

The following three measuring systems first of all possess the high time resolution mentioned above as a basic prerequisite:

- miniature pressure transducer with high inherent frequency
- hot-wire and hot-film anemometer and
- optical velocity measuring methods.

The use of these measuring systems in various procedures also permits the building of sufficiently small probes -- the optical methods operate completely free of contact -- so that, in principle, it is possible to record changes over time of the following flow parameters:

- wall pressures,
- total pressures,
- velocities, magnitude and direction, and
- flow fluctuations.

In the last analysis, the most critical criterion for the usability of a measuring technique is the test as to whether the initial test signal is affected by only one condition-of-flow variable or whether possibilities exist for separating the signal variables. In the case of the pressure transducer and hot-wire measuring technique, extensive laboratory tests were required to answer this question. These will be discussed in the appendix.

/27

The optical velocity measuring methods will not be included in the further discussion, since these methods were not yet available at the time of the experimental investigations behind the centrifugal impeller, which is the object of this study.

In the meantime, using a "dual-focus laser method" developed by Schodl [3.2] especially for measurements in turbomachines, it has been possible to record velocity distributions inside the blade channels of this impeller (cf. section 6.4.1). Besides the possibility of non-contact measuring, the essential advantage of this method consists in the fact that, in principle, the measured variable is not falsified by other flow variables.

### 3.3 Method of Instantaneous Pressure Measurement

The measurement of rapidly varying pressure changes observed in the absolute system within the sphere of influence of a turbomachine impeller requires measuring systems whose inherent frequencies are four times greater than the blade frequencies. Miniature pressure transducers on a piezoquartz or semiconductor base fulfill this condition.

In the first case, by means of the underlying Pezo effect -- release of an electric charge during deformation of a quartz crystal due to compressive forces -- it is only possible to measure the dynamic pressure components. Pressure transducers which operate on this principle have inherent frequencies of up to 400 kHz. To be sure, there are limits to how far they can be miniaturized because of increasing difficulties in the processing of small electric charges. The currently available piezoquartz pressure transducers have a pressure-sensitive front surface of about 5 mm in diameter. Thus they are unsuitable for insertion into Pitot tubes. In addition, in measuring instantaneous changes in wall pressure, the large membrane diameter is a drawback for the desired measurements which, as much as possible, should be point measurements.

By contrast, with the advances made in the miniaturization of electric components in recent years, it has been possible to develop strain gauge bridge pressure transducers based on semiconductors which present themselves for use in turbomachines. This is because of their small dimensions -- in general, they have a diameter between 1.2 and 3 mm.

/28

After detailed laboratory studies had produced information on the operational behavior of these transducers, measuring systems were developed from them to make instantaneous wall pressure measurements and total pressure measurements. These systems take into account the special requirements for use in highly-loaded centrifugal compressors.

### 3.3.1 Operational Behavior of Miniature Semiconductor Pressure Transducers

The extremely small dimensions of these pressure transducers are achieved by means of a special semiconductor photomasking technique by which a complete, 4-arm Wheatstone bridge is vapor deposited on the pressure-sensitive silicone membrane. The "blocking" p-n transfer (between positively and negatively doped semiconductor material) resulting in this way obviates separate insulation of the individual resistor elements. Fig. 3.2 shows, in principle, that when the membrane is put under compressive stress, the parallel arrangement of the resistor elements leads to variable deformation (elongation or compression) of the individual resistors and thus puts the bridge out of tune.

The following points are especially important in the use of these pressure transducers for flow studies on turbocompressors:

- the frequency resolution and the acceleration sensitivity of the transducer,
- the installation conditions and
- the influence of thermal effects on the pressure transducer output signal.

#### 3.3.1.1 Frequency Resolution

Miniature pressure transducers are a nearly undamped oscillating system, comparable to a simple spring-mass coupling, which is excited to forced oscillations by external pressure forces. In this process it is aimed at to keep the mass of the membrane and the bending of the membrane under stress as small as possible.

/29

In the case of the pressure transducers (made by Kulite, basic type CQL-080-25, outside diameter 2 mm) for these centrifugal compressor studies, the actual pressure-sensitive part of the membrane with a diameter of 1.2 mm is about 0.02 mm thick and at the maximum allowable pressure load it is deflected about 0.007 mm. At the same time, the density of the silicon membrane is less by a factor of 4 than that of the usual steel membranes (cf. [3.3, 3.4]).

This combination of a small membrane mass and a high spring constant determines the very small mechanical acceleration sen-

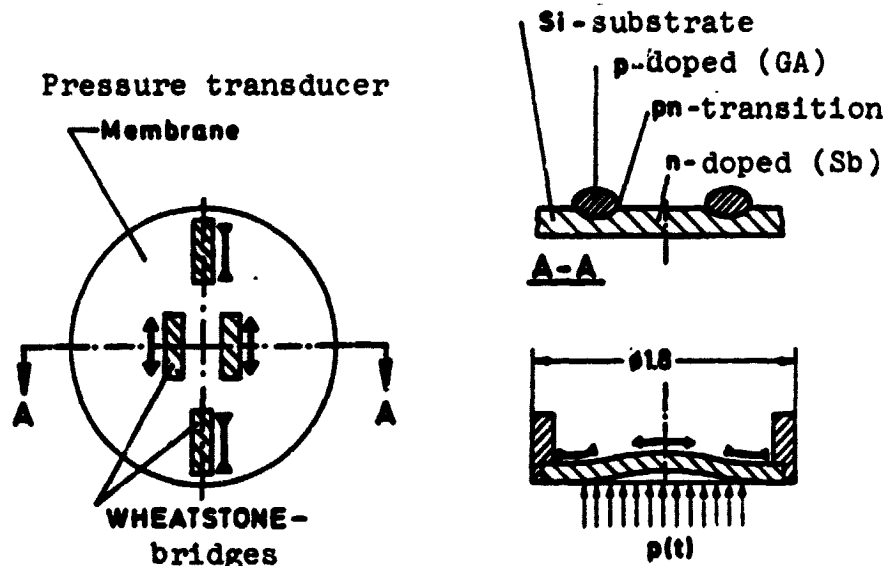


Fig. 3.2 Design and principle of operation of the pressure-sensitive membrane of a miniature semiconductor pressure transducer.

sitivity and the high mechanical inherent frequency of these pressure transducers --  $f_r = 150 \text{ kHz}$  -- as can be seen from the principle frequency curve shown in Fig. 3.3. From this curve of the amplitude ratio  $A/A_0$ , i.e. the phase shift  $\phi$  over the excitation frequency  $f$ , it can be deduced that with this measuring system even rise times corresponding to an upper test frequency of  $f_{\max} = 0.33 f_r$  can be measured without impermissibly high falsifications.

/30

In this connection it seems important to point out a few results of dynamic pressure calibrations. Weyer [3.5] checked the frequency behavior of these semiconductor transducers with a specially developed pressure generator which produced trapezoidal pressure curves up to a frequency of about 4 kHz and a doubled pressure amplitude of 0.8 bar. Kurtz and Kicks [3.3] reported on similar experiments in which small sinusoidal pressure variations up to 20 kHz were produced with a loud speaker. In both studies, deviations in the dynamic pressure transducer sensitivity of less than  $\pm 1\%$  with respect to the static value were found.

/31

### 3.3.1.2 Influence of the Installation Conditions

With respect to the requirements already mentioned in section 3.1.3 for small probe dimensions and measurements as close to "point" measurements as possible, it was tested to what



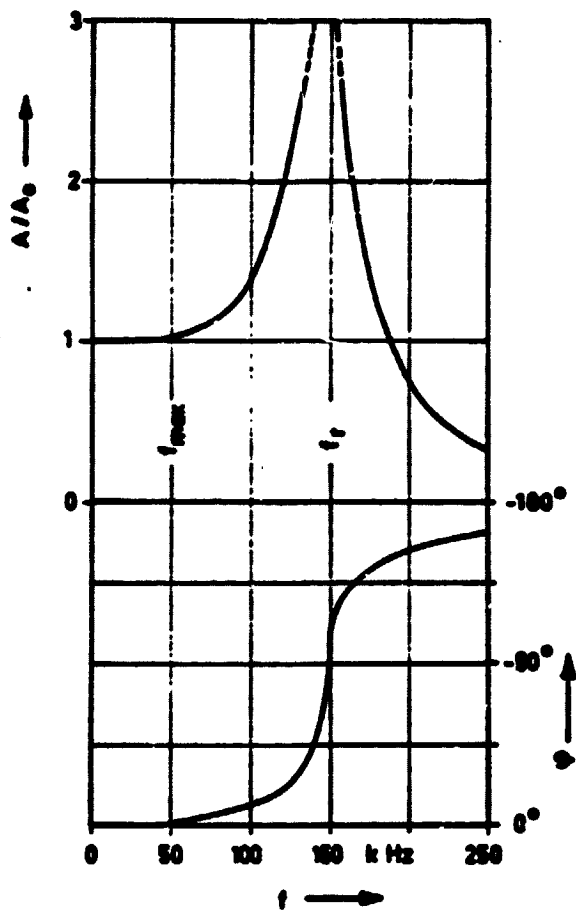


Fig. 3.3 Principle frequency characteristics of a miniature semiconductor pressure transducer,  $f$  = excitation frequency,  $A/A_0$  = amplitude ratio,  $\phi$  = phase shift.

point becomes especially important in measuring the nonsteady total pressure directly behind the centrifugal impeller exhaust because of the large fluctuations in direction which occur there (see Table 3.1).

### 3.3.1.3 Thermal Effects

In the layout point of the centrifugal compressor stage in question mean total temperatures up to about 430 K occur behind the impeller exhaust (see Table 3.1). Because of the necessary type of construction for the probes described in the preceding section, the semiconductor elements in the pressure transducer membrane are also exposed to temperatures

extent it is possible to set the transducer separate from the actual measuring site.

The results of simple estimates for the "organ pipe arrangements" shown in Fig. 3.4 (upper right), i.e. the Helmholtz resonator, show, however, that inherent system frequencies are to be expected with this arrangement on an order which is considerably less than those of miniature transducers. Conversely, it follows from this that the dynamic characteristics of these transducers can be taken advantage of for determining rapid changes in pressure only when the pulsating pressure acts directly on the membrane. In accordance with this, Fig. 3.5 shows favorable installation arrangements for the pressure transducers:

32

- for wall pressure measurements the pressure transducer membrane should be in as close contact as possible with the housing wall;

- for total pressure measurements it is advisable to set the membrane about 0.5 - 1  $d$  ( $d$  = probe head diameter) behind the input opening for the probe in order to achieve sufficiently high direction sensitivity for the probe. This

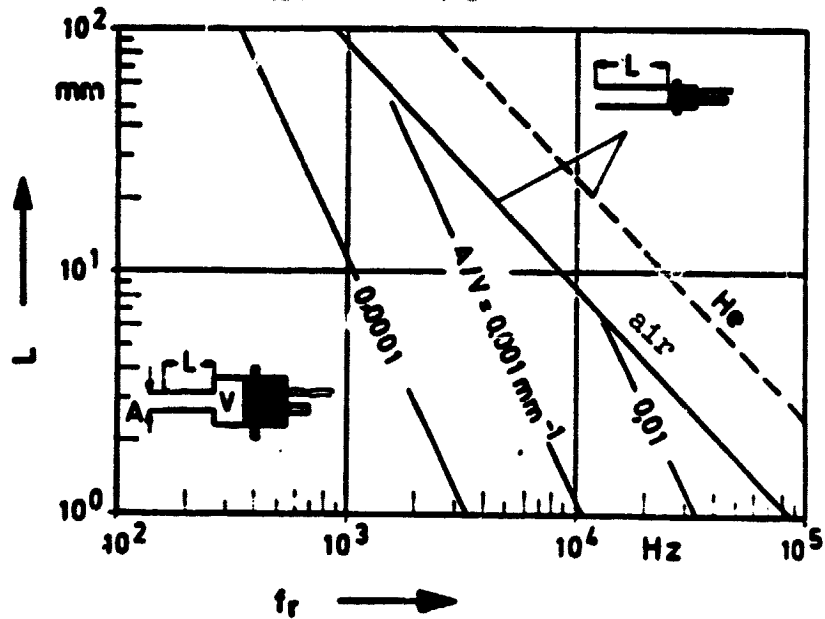


Fig. 3.4 Inherent system frequencies  $f_r$  of various measuring arrangements with a clearance volume in front of the pressure transducer membrane for air or helium (He) in the standard state,  $L$  = tube length,  $A$  = tube surface area,  $V$  = volume

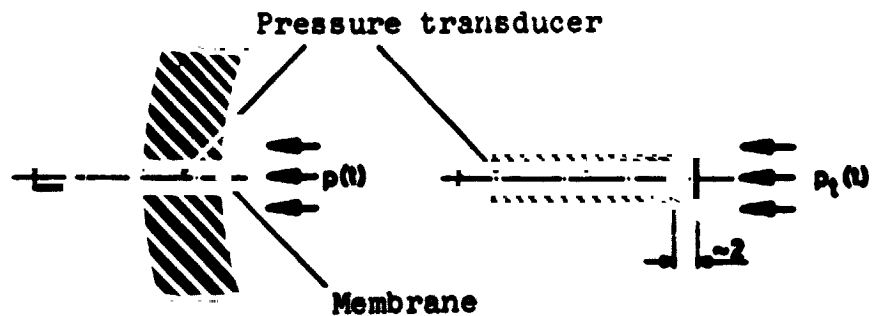


Fig. 3.5 Principle installation arrangements of Kulite pressure transducers for wall pressure measurements and total pressure measurements.

on this order. Therefore it is particularly important to check the effects of temperature on the pressure transducer reading.

With the various temperature effects on the output signal of semiconductor pressure transducers, one distinguished between

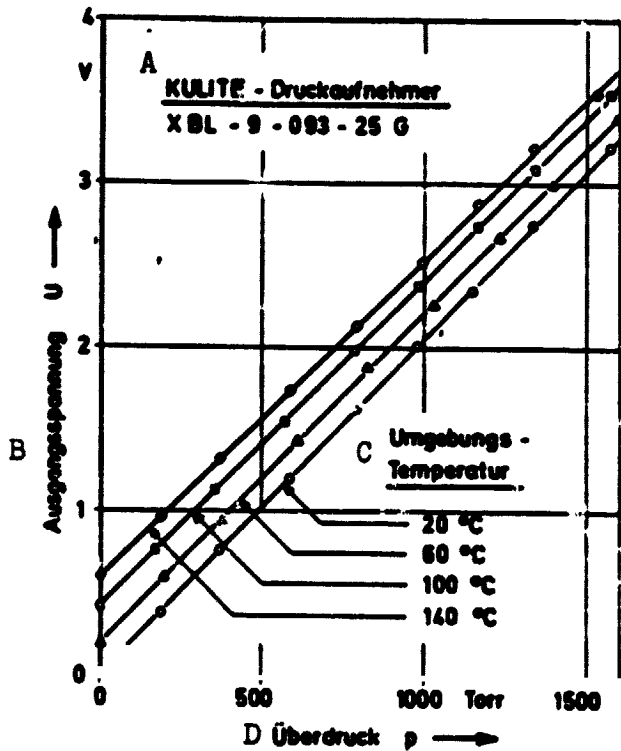


Fig. 3.6 Original calibration curves for a miniature semiconductor pressure transducer (total pressure probe) at various ambient temperatures. Feed voltage: 5 volts, electrical amplification factor: 40. Key: A) Pressure transducer B) Initial voltage C) Ambient temperature D) Excess pressure

studied, the temperature-related changes in sensitivity were less than  $-0.7\%/10\text{ K}$ . These findings were quite reproducible.

The temperature-related zero point drift is expressed in the shift in pressure calibration curves to higher voltage values observed with increasing temperature. In the example shown, the zero point drift between  $20^{\circ}\text{C}$  and  $140^{\circ}\text{C}$  is on average about  $+1.8\% \text{ f.s./}10\text{ K}$ . To be sure, large differences occurred from experiment to experiment and from one pressure transducer to another, so that in spite of considerable efforts we did not succeed satisfactorily in setting up mathematical relationships

the following according to existing U.S. test conditions (cf. [3.6, 3.7]):

- changes in pressure transducer sensitivity (rise in the calibration curve) due to temperature effects,
- temperature-related zero point drift and
- effects of temperature gradients.

In extensive laboratory tests, whose arrangement and procedure are described in appendix I, the operational behavior of the miniature pressure transducer was precisely investigated under conditions of variable ambient temperature. The following figures will elucidate the most important findings of these experiments and the conclusions deduced from them with respect to the method finally chosen to make non-steady pressure measurements.

Fig. 3.6 shows pressure calibration curves for a Kulite pressure transducer at 4 ambient temperatures. These were determined by using a U-tube manometer filled with mercury. With increasing temperature the sensitivity of the pressure transducer steadily decreases. In this example, at  $140^{\circ}\text{C}$  it is smaller by about 3% than at  $20^{\circ}\text{C}$ . In general, with all of the Kulite pressure transducers

134

for the changes in zero point drift with respect to temperature.

This can certainly be explained in part due to the very large sensitivity of response of the semiconductor elements with respect to temperature gradients. As a characteristic result of laboratory tests (also see appendix 1) which serves to clarify this question, Fig. 3.7 shows the changes in output signal over time for an unloaded pressure transducer. It was exposed to sudden jumps in ambient temperature. In so doing, the detuning of the semiconductor bridge reached a maximum value after about 1 minute. At  $\Delta T = 19$  K this is about 14% of the nominal pressure reading (25 psi, 20°C).

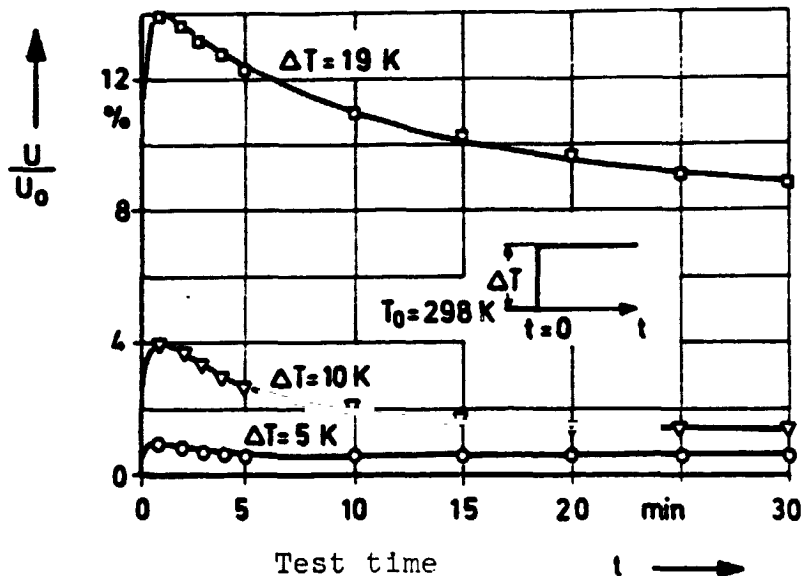


Fig. 3.7 Changes in zero point drift over time for an unloaded Kulite KQL-093-25 pressure transducer under the influence of temperature gradients,  $U_0$  = initial voltage at normal load (25 psi) and  $T_0 = 298$  K.

Tests with a water-cooled pressure transducer adapter (cf. Fig. 3.9), as was developed for wall pressure measurements, on the other hand produced extensive damping of the temperature gradient effects. Fig. 3.8 compares the detuning of cooled and uncooled pressure transducers 1 minute after a rise in temperature  $\Delta T$ .

The effectiveness of water cooling in suppressing temperature effects was also found in long-term tests and was tested in practice in the compressor. While blowing in a jet of hot air at a temperature of 150°C, the temperature on the pressure transducer membrane rose only about 6 K with respect to the temperature of the cooling water, as in nonsteady wall pressure

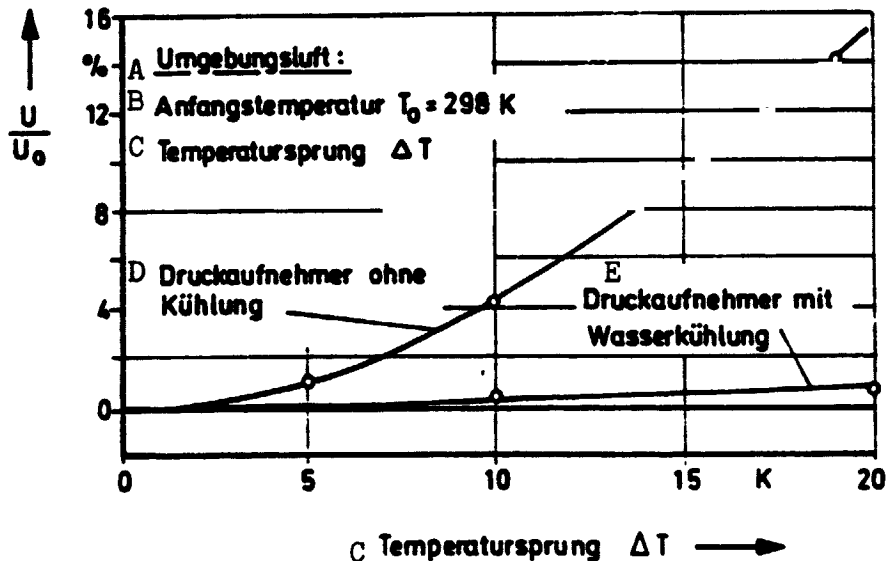


Fig. 3.8 The zero point drift of cooled and uncooled semiconductor pressure transducer under the influence of temperature gradients, test time  $t = 1$  minute,  $U_0 =$  initial voltage at normal load (25 psi) and  $T_0 = 298$  K.

- Key: A) Ambient air                      D) Uncooled pressure transducer  
 B) Initial temperature                E) Water-cooled pressure transducer  
 C) Rise in temperature

measurements in the exhaust region of the centrifugal impeller (up to 18,000 rpm) the deviation from the exact value of the mean pressure transducer reading (measured against atmosphere) was in the region of  $\pm 4\%$ .

#### 3.3.1.4 Results of the Studies on Operational Behavior

In summary, the following was found after the laboratory testing of the miniature semiconductor pressure transducers:

- very frequent pressure variations can be measured with sufficient accuracy up to 1/3 of the pressure transducer inherent frequency if the installation conditions are chosen in such a way that the pressure pulsation acts directly on the membrane;
- the pressure transducers permit exact measurement of the dynamic wall pressure or total pressure component (pulsating pressure changes) if the change in the transducer

- sensitivity with ambient temperature is taken into account in the evaluation;
- regularities in the zero point drift behavior of the transducers cannot be detected with any reliability. With water cooling the falsifying temperature effects can be considerably damped, however even with this measurements of the absolute pressure level with the desired accuracy are not possible.

On the basis of these conclusions a measurement and evaluation method was developed with which the nonsteady absolute pressure curve is reconstructed by superimposing separate measurements of the corrected pressure mean value over time and of the dynamic pressure component. This method is discussed in detail in section 5.3.1, while the individual measuring systems for nonsteady or average wall pressure and total pressure measurement over time are discussed in the following two sections.

### 3.3.2 Development of Measuring Systems for Determining Changes in the Dynamic Wall Pressure and Total Pressure /37

The basis of the nonsteady pressure measurement systems is formed by various types of miniature semiconductor pressure transducers made by Kulite. The most important operational data for these transducers is summarized in Table 3.2. In addition to the manufacturers' specifications, our own results obtained from the laboratory tests on the pressure transducers used on the centrifugal compressor are also listed. /38

The initial voltages of the pressure transducers were amplified by means of a differential d.c. amplifier with a linear frequency curve up to about 100 kHz. This was to facilitate the further processing of test signals by means of oscillographs or the synchronized sampling technique (see section 3.5).

The findings from the tests on the operational behavior of the semiconductor pressure transducers were taken into consideration in designing the nonsteady pressure measurement systems.

As shown in Fig. 3.9, for the wall pressure measurement a cylindrical pressure transducer, Kulite XQL-093-25, was installed flush with the housing wall in a cooling adapter. Thus the frequency resolution of the transducers is fully taken advantage of and at the same time temperature effects on the output signal of the transducers are largely suppressed. As a result of the water cooling, the transducer, whose nominal operational range extends up to 120°C, can be used up to substantially higher temperatures. /39

The preliminary tests also showed that with cooling, the temperature on the membrane increases only slightly even at a maximum temperature load in the centrifugal compressor (18,000 rpm). Thus it was possible to regularly use only the 20°C calibration curves for evaluating the dynamic wall pressure curves.

TABLE 3.2 OPERATIONAL DATA ON KULITE XQL-093-25 AND XBL-9-093-25 G SEMICONDUCTOR PRESSURE TRANSDUCERS

Pressure differential measurement range (against atmospheric pressure)	nom. 25 psi = 1.724 bar + 20 %
Sensitivity at feed voltage	nom. 36.25 mV/bar  5 V -
Temperature operating range	XQL: -20 °C to 120 °C XBL: -20 °C to 175 °C
Nonlinearity and hysteresis error	max. + 1 % f.s. *)
Change in sensitivity with Temperature	Kulite: 0 to -1%/10 K DFVLR: -0.25 to -0.7%/10K
Zero point drift with Temp. (Shift test bed, see App. I)	Kulite: +3%f.s.+0.36%f.s./10K DFVLR : max. + 2%f.s./10K
Zero point drift due to temperature gradients	DFLRV: see Fig. 3.7
Inherent frequency	approx. 150 kHz
Acceleration sensitivity	Perpendicular : 0.345 Pa/g**) horizontal : 0.034 Pa/g
*) % f.s.: in percent of the nominal test range (full scale) **) g: acceleration due to gravity	

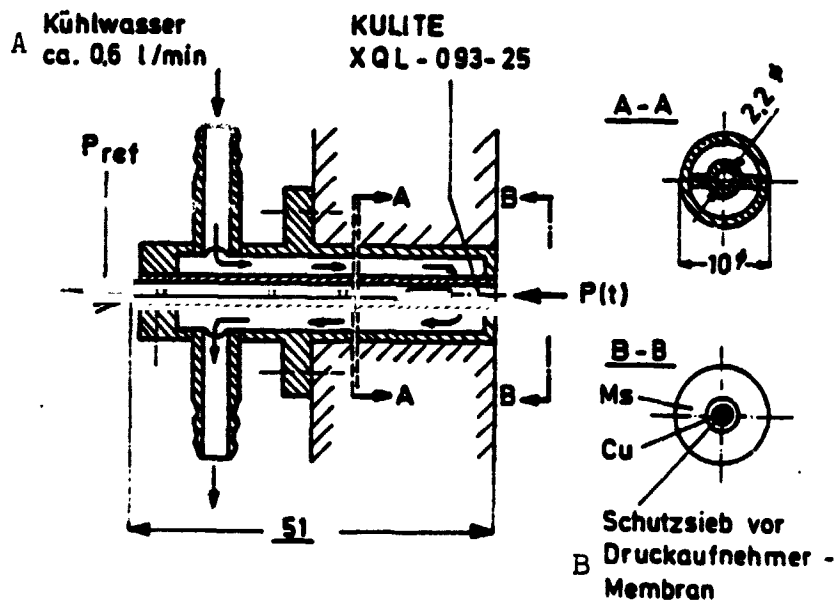


Fig. 3.9 Cooling adapter for measuring changes in dynamic wall pressure with a miniature semiconductor pressure transducer, measurement in mm.  
 Key: A) Cooling water about 0.6 liters per minute  
 B) Protecting screen in front of the transducer membrane

This considerably restricted the calibration costs for the 16 wall pressure transducers in simultaneous use. Moreover, even after longer operation times, no aging effects were detected in the calibration characteristics.

For measuring the dynamic changes in total pressure the hook-shaped probe, shown in Fig. 3.10, was designed and the head of the probe was completed with a built-in semiconductor pressure transducer according to DFVLR specifications by Kulite. The transducer was designated as XBL-9-093-25 G. By directly integrating the transducer in the manufactured product, a favorable probe intake diameter of 2.2 mm resulted in relation to the exhaust width of the centrifugal impeller (26 mm).

Effects of the probe shaft on the flow field to be studied are avoided by the probe head length of 14.5 mm. The design of the probe intake part (see Fig. 3.10, upper right) enables exact, direction-independent total pressure measurements in an angular range of  $30^\circ$  (cf. [3.8], pp. 10, 11). Our own tests with steady and nonsteady oncoming flow -- in a wind tunnel up to a mach number  $M = 0.5$  and with the probes mounted behind the centrifugal impeller -- confirms this data given in the literature.

/40



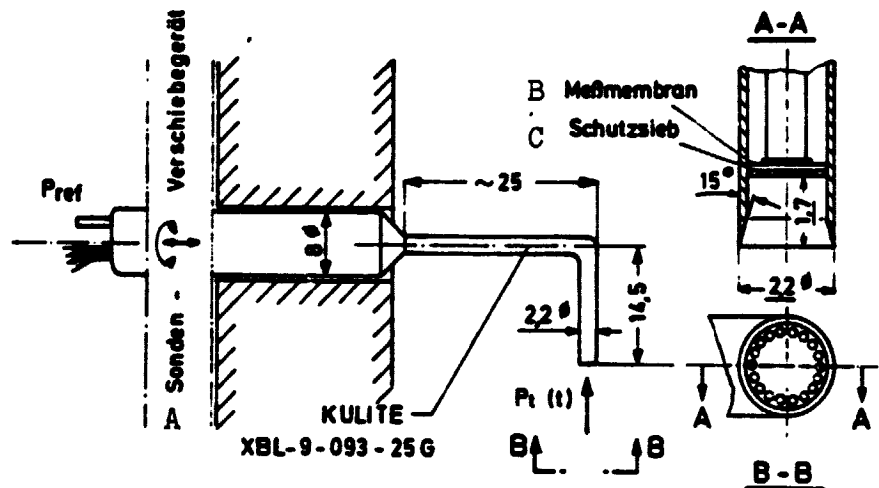


Fig. 3.10 Pitot tube with built-in miniature semiconductor for measuring changes in dynamic total pressure, measurements in mm.

Key: A) Device for adjusting the probe  
 B) Membrane  
 C) Protecting screen

To protect the silicone membrane of the pressure transducer from dust erosion a perforated screen was installed in the head of the probe on the tip. In studies by Kurtz and Kicks [3.3] it was found that this protective screen (also shown in Fig. 3.9, perforated form covering the entire area) only insignificantly affects the frequency characteristics up to 30 kHz of the transducer with variations in pressure.

The pressure transducer built into these probes can be operated without cooling up to a temperature of 175°C. In order to correct the temperature effect on the sensitivity of the transducer pressure calibration curves were plotted between 20°C and 140°C -- after artificial thermal aging of the transducers (see Appendix I). These calibration curves were used as the basis in evaluating the dynamic total pressure curve in accordance with the mean temperature load in each case. Subsequent calibrations of the probes after being in operation for 25 hours at temperatures in excess of 100°C showed no measureable changes in the probe characteristics.

### 3.3.3 Measurement Systems for Determining Exact Pressure Mean Values over Time

Simple pneumatic measurement systems for determining pressure mean values over time -- e.g. the following arrangement: Pitot tube or static wall pressure hole -- test line -- slow

manometer -- can produce substantial erroneous readings when used in regions with quickly changing pressures and high pressure amplitude (e.g. within the sphere of influence of a turbo-machine impeller). In studies on transonic axial compressor stages variations up to 10% of the correct pressure mean value over time were found (cf. [3.5]).

/41

This measurement uncertainty is influenced by a large number of parameters, the most important of which are the following:

- the ratio of pressure amplitude to the mean pressure value,
- the shape of the pressure curve over time and
- the shape of the probe intake or hole intake.

The problem of determining mean pressure values over time in turbomachine has been extensively discussed by Weyer [3.5]. In the scope of these studies 3 different measuring methods were developed. Two of these methods are described below which were used in the centrifugal compressor for measuring correct mean wall pressure or total pressure values over time.

#### 3.3.3.1 Special Pneumatic System for Wall Pressure Measurements

The difference between the indicated and correct mean pressure value over time in the case of the usual pneumatic systems can be attributed to inflow and outflow phenomena of the gas in the measuring system during a period of variation in pressure.

Starting with the laws of mass conservation and energy conservation (cf. [3.5]), it is possible to calculate this difference for a special measuring system in which the conditions present can be readily grasped in physical terms because of the shape of the measuring hole and the choice of the cross-section ratio of the measuring hole to the connecting line. However, the dynamic pressure curve (without reference level) must of course be known in order to make the correction.

Fig. 3.11 shows the principle construction of this special pneumatic system. The measurement hole is in the shape of a semicircular nozzle. In this way, nearly constant and uniform flow coefficients are obtained for the inflow and outflow phenomena in the interesting Reynolds number range. The cross-section of the measurement nozzle is very small in relation to the connecting measurement line, so that pressure and temperature fluctuations within the system can be ignored.

Moreover, the axial extent of the nozzle is very small in relation to the wavelength of the pressure fluctuation, so that the flow phenomena in the region of the measurement hole may be regarded as quasi-steady.

/42

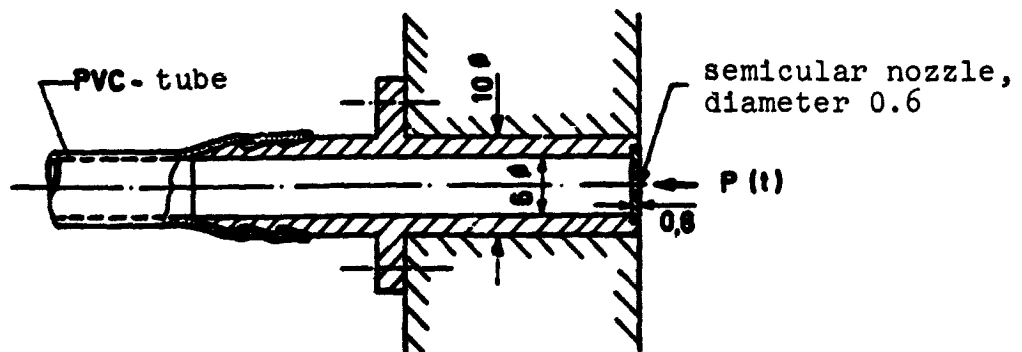


Fig. 3.11 Special pneumatic measuring system for determining exact mean wall pressure values over time, measurements in mm.

For recording the mean pressure value determined with this system (which is still corrected mathematically) a common, slow pressure measuring instrument can be used (U-tube manometer, pressure transducer with a low inherent frequency). Because of the necessarily large cross-section of the connection line connected to the measurement nozzle, this system is suitable only for wall pressure measurements, but not for total pressure measurements in the narrow flow channels of the centrifugal compressor stage.

### 3.3.3.2 Hydraulic System for Total Pressure Measurements

The principle construction of this measuring system is shown in Fig. 3.12. A capillary tube ① 0.35 mm in diameter and 50 mm long is rigidly attached to the pressure transducer adapter ②. A pressure transducer with a low inherent frequency ④ serves as a signal modulator. The total pressure varying over time acts on the open end of the capillary tube at the head of the probe ⑤. The pressure pulsation is damped by the viscosity forces acting in the capillary tube so that nearly constant pressure is adjacent to the pressure transducer ④. /43

The entire system is filled with silicon oil whose kinematic viscosity at room temperatures is about  $1.5 \text{ cm}^2/\text{s}$ . During the pressure measurement, a small amount of oil (about  $100 \text{ mm}^3/\text{hour}$ ) is put in at point ③ in order to make sure that the capillary tube is always filled up to the input point.

The measurement principle is based on the impulse equilibrium between the almost constant pressure over time on the pressure

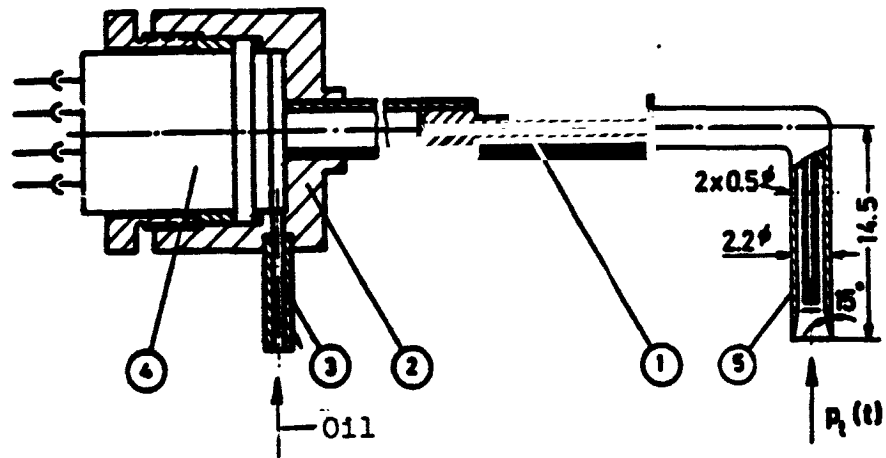


Fig. 3.12 Hydraulic measuring system for determining exact mean total pressure values over time, measurements in mm.

1 = capillary tube, 2 = pressure transducer adapter, 3 = oil input, 4 = pressure transducer with low inherent frequency, 5 = probe head with lateral holes for oil outflow, measurement in mm.

transducer membrane and the integral value over time of the variation in pressure at the probe intake. To determine the exact value two corrections are generally necessary: the first concerns a possible difference in height between the test point and the pressure transducer membrane, while the second concerns the slight drop in pressure of about 5 mb which is caused by the necessary flow of oil in the capillary tube.

Because of the small dimensions of the probe head (5), whose sensitivity is nondirectional up to  $\pm 30\%$ , the hydraulic method is especially well suited for determining the correct mean total pressure value over time of the strongly fluctuating flow at the exhaust of the centrifugal impeller. The accuracy of the total system depends basically on the pressure transducer used. With this system, even when used at high temperatures on the centrifugal compressor with appropriate water cooling of the pressure transducer, reliable results were obtained.

/44

### 3.4 Development of a Method for Measuring Direction in a Periodically Unsteady Flow

#### 3.4.1 Problems in the Use of Hot-wire Anemometry

For detailed studies of the strongly disturbed flow field at the exhaust of highly-loaded centrifugal compressor

impellers, precise information is necessary on the distribution of the absolute flow direction. Following the successful testing of the miniature pressure transducers in measuring rapidly changing wall pressures and total pressures over time, it was obvious to use the high frequency resolution of hot-wire anemometry to measure other fluctuating flow variables, such as the magnitude and direction of flow velocities and total temperatures.

A glance at the mathematical relationships of heat transfer on thin, freely stretched hot wires (cf. for example, [3.9], p. 75) shows, however, that direct measurement of the flow parameters mentioned above is only possible in a few experimentally idealized cases without being falsified by other influences.

The following are the important variables which affect a hot-wire test signal:

- Reynolds number,
- mach number,
- Prandtl number,
- flow direction,
- degree of turbulence,
- over heating rate,
- dust deposit and aging, and
- isentropic exponent of the flow medium.

145

Of these variables at least 3 occur in the impeller exhaust flow of a highly loaded centrifugal compressor, sometimes with large, rapidly changing fluctuations. Since each probe must be calibrated individually in the total range of variation for the different variables, it very quickly becomes clear that the required cost of calibrations is out of proportion with the relatively short life span of hot-wire probes.

From this list of fundamental problems involved in the use of hot-wire anemometry, it follows that for centrifugal compressor studies only those hot-wire techniques can be used with any prospects for success in which the number of variables affecting the test signal is reduced by special measures. A measuring technique for measuring nonsteady directions developed on the basis of this requirement is discussed below. This uses only the high time resolution of hot-wire anemometry, but with which the difficult interpretation of signal amplitudes is not applicable. A measuring technique of similar design for quickly changing total temperatures is discussed in [3.10, 9.1]. This has not yet been tested on the centrifugal compressor, however.

#### 3.4.2 Construction and Measuring Principle of the Hot-wire Direction Probe

The design of the probe is elucidated by referring to Fig. 3.13. A tungsten wire 0.6 mm long and 5  $\mu$ m in diameter is

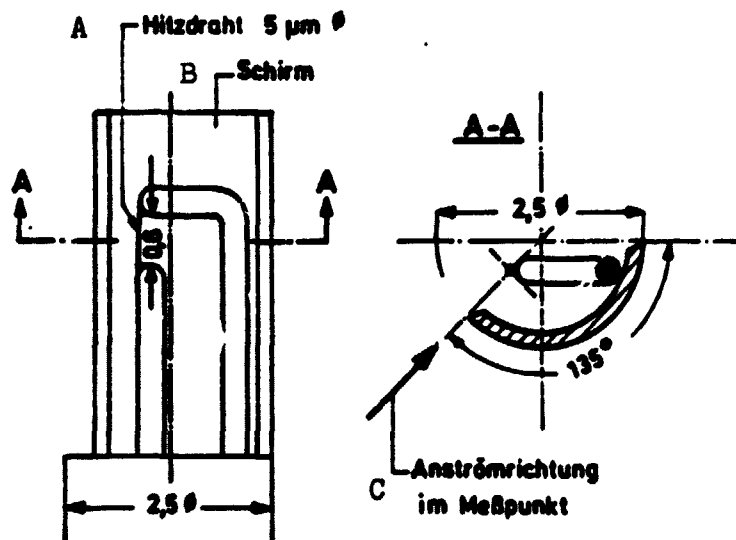
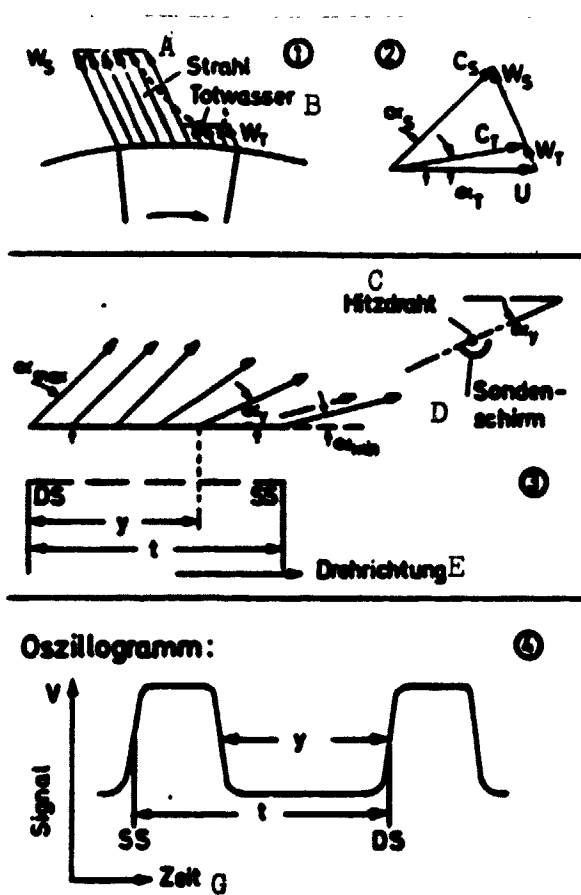


Fig. 3.13 Head of the hot-wire shielded probe for measuring the nonsteady flow direction, measurement in mm.

- Key: A) Hot-wire diameter 5 μm  
 B) Shield  
 C) Direction of oncoming flow at the test point

stretched parallel to the axis of the probe. The shaft of the probe with a diameter of 2.5 mm is formed into an umbrella-shaped screen in the vicinity of the probe head (135° cylinder segment). The sharpened leading edge also lies parallel to the axis of the hot wire and the probe. The probe is connected to a Disa 55 D 01 constant temperature anemometer by means of a 30-meter high frequency cable and is operated in a modified 1:1 bridge circuit. The overheating rate of the wire is selected such that the temperature of the wire is close to the upper load limit of 300°C, thus ensuring the greatest band width and sensitivity of the measuring system. /46

Fig. 3.14 helps clarify the principle on which the measuring technique is based. At position ① it showed schematically the characteristic, disturbed relative flow at the blade channel exhaust of a highly-loaded centrifugal impeller. An idea of the real velocity curve is given by the broken line which is approximated by the jet-wake velocity block profiles. Position ② shows the corresponding velocity triangle for this jet-wake distribution. One can clearly see that the irregular changes in relative velocity in the circumferential direction in the absolute system are expressed in a change in the flow direction α



F) Oszillogramm:

- A) Jet
- B) Wake
- C) Hot-wire
- D) Probe shield
- E) Direction of rotation
- F) Oscillogram
- G) Time

between the extreme values  $\alpha_s$  (for the jet) and  $\alpha_T$  (for the wake).

This variation in direction of the absolute velocity vector over a blade spacing  $t$  between the pressure side DS and the suction side SS) is diagrammed at (3). As shown here, the hot-wire shielded probe is mounted in such a way immediately behind the impeller output so that the axis of the probe lies parallel to the rotor axis and the alignment line between the leading edge of the shield and the straight line between leading edge of the shield and the hot wire forms a "probe adjustment angle"  $\alpha_y$  with the circumferential direction.

If the wake region in the vicinity of the suction side SS passes the probe with  $\alpha < \alpha_y$  during the rotation of the impeller, the oncoming flow strikes the hot wire directly and a high signal voltage is observed on the oscillogram during the time  $t-y$ , position (4). In passing the jet region with  $\alpha > \alpha_y$  the hot-wire is shielded from the direct oncoming flow. It lies in the wake region of the shield and for this period  $y$  a small hot-wire signal voltage is recorded. Precisely in the transition region from a high to low signal voltage, the absolute flow direction has the preselected probe adjustment angle of  $\alpha_y$ .

With appropriate triggering the test signals of several sequential blade passages -- as shown in Fig. 3.15, can be superimposed on the oscillograph screen or plotted on an x-y recorder as a statistical mean value (based on 1,500 blade passages) by means of the synchronized sampling technique.

In these signal curves the position of  $\alpha_y$  relative to the limit of the signal period  $t$  on the pressure side is determined

/47

/48

by  $y$ , i.e. by means of the tip clearance signal recorded at the same time -- and the position relative to the position of the blade pressure side at the impeller exhaust is determined by  $Y$ .

By gradually changing the probe adjustment angle and by moving the probe over the diffuser width in several radial test positions towards the impeller output, the total direction field of the absolute flow in the region of the diffuser intake can thus be determined.



Fig. 3.15. Test signal curve of the hot-wire shielded probe. About 50 individual signals superimposed. Above - internal reference signal. (Clearance transducer installed at a point shifted by  $t/2$  against the direction of the probe.)  $\gamma=40^\circ$ ,  $n=12,000$  rpm,  $R/R_2=1.075$   
Oscillograms: horiz.  $40 \mu\text{s/cm}$ , vert.  $1 \text{ V/cm}$ .

### 3.4.3 Probe Calibration and Frequency Characteristics /49

For developing and testing the hot-wire probes a small calibration wind tunnel was setup with a nozzle outlet diameter of 20 mm. At the test point within the free jet of the nozzle the mach numbers can be set independently of one another between  $M = 0.2$  and  $M = 0.9$ , the densities can be independently set at values between  $\rho = 0.8$  and  $\rho = 2.0 \text{ kg/m}^3$  and the total temperature between room temperature and  $250^\circ\text{C}$ .



For direction calibration the hot-wire shielded probe -- as indicated schematically on the left in Fig. 3.16 -- is rotated in the parallel stream of the jet flow and the probe output signal is recorded on an x-y recorder. In so doing, during the transition from direct to shielded flow onto the hot-wire, this gives the change in d.c. voltage shown from which the zero setting for the probe  $\phi = 0^\circ$  is determined.

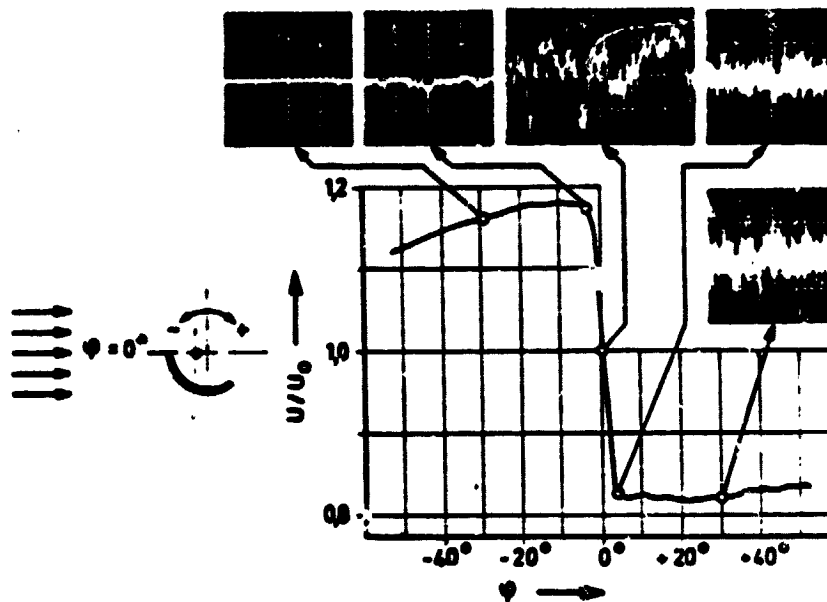


Fig. 3.16 Calibration of the hot-wire shielded probe in a parallel jet: change in d.c. signal voltage  $U/U_0$  as a function of the angle  $\phi$  at  $M = 0.7$ ,  $T_t^0 = 288$  K,  $\rho = 1.5$  kg/m<sup>3</sup>. Oscillograms: a.c. component of the hot-wire signal, horizontal 20 ms/cm, vertical 0.1 V/cm.

The angular range in which the signal transition is accomplished is  $\Delta\phi = \pm 4^\circ$  in the example shown. A subsequent test showed no measurable change in the position of the probe zero setting and in the width of the transition region in the Mach number range studied.

The oscillograms shown in Fig. 3.16 show the a.c. component of the hot-wire signal in each case in the angular position indicated. While at an angle of  $\phi = -30^\circ$  the oncoming flow strikes the hot-wire directly, at  $\phi = -4^\circ$  initial smaller signal variations occur which reach a maximum in the probe zero setting. In the angular positions  $\phi = +4^\circ$  and  $\phi = +30^\circ$  the hot wire then lies completely in the highly turbulent wake region of the probe shield.

For an exact evaluation of the hot-wire measurements, especially for correlating the test signal with a blade spacing data is also required on the frequency curve of the measuring system. In obtaining this information in the case of the direction measuring technique described, in which only time components are determined, only the phase shift of the test signals is to be considered. The frequency curve of the anemometer is dependent on a large number of parameters, such as the geometry of the transmitter, the arrangement of the bridge and the band width of the anemometer as well as the flow condition and the velocity of the medium in which the measurements are made. Under these circumstances, direct dynamic calibrations are very costly and time consuming. Because of the relatively small influence of the phase shift on the accuracy of the measurement, results, even in the present case, obtained with indirect methods are sufficient for making an estimate. Simple, indirect test methods, in which the transmitter current is modulated sinusoidally or in a square-wave by means of a frequency generator to simulate a fluctuation in flow, have been described by Nielsen and Rasmussen in [3.11].

Fig. 3.17 shows results determined according to this procedure for the hot-wire shielded probe. It is conspicuous in the graph that the phase shift decreases very sharply with increasing flow velocity. If after a Fourier estimate for the steep signal transmission of the shielded probe one applies about a 4-fold blade frequency, then it can be estimated that in the centrifugal compressor operating range in question (10,000-18,000 rpm) excitation frequencies of about 10-25 kHz are to be expected at oncoming flow velocities between 100 m/s and 400 m/s. Thus in the evaluation, phase shifts of less than  $30^\circ$  are to be taken into account. Under the assumption made above, this corresponds to about 3% of the signal period. /51

#### 3.4.4 Discussion of the Measuring Technique for Nonsteady Direction Measurement

The probe design shown in Fig. 3.13 was selected from a number of possible solutions as the most suitable for the studies on the centrifugal compressor test stand. First of all, it was attempted, by means of continuous recording methods, to avoid the main drawback of this technique, namely that about 50 time consuming individual measurements are required to determine the direction field in the region of 1 blade spacing. Probes with freely stretched individual or crossed wire arrangements, which use the well-known  $\cos \phi$  direction effect of hot wires (cf. [3.9]), were not considered here because of the complex heat transfer conditions (cf. section 3.4.1) and the small amount of protection with respect to dust damage. Also eliminated was a probe principle which at first seemed promising, /52 in which hot film transmitters were operated in separation from

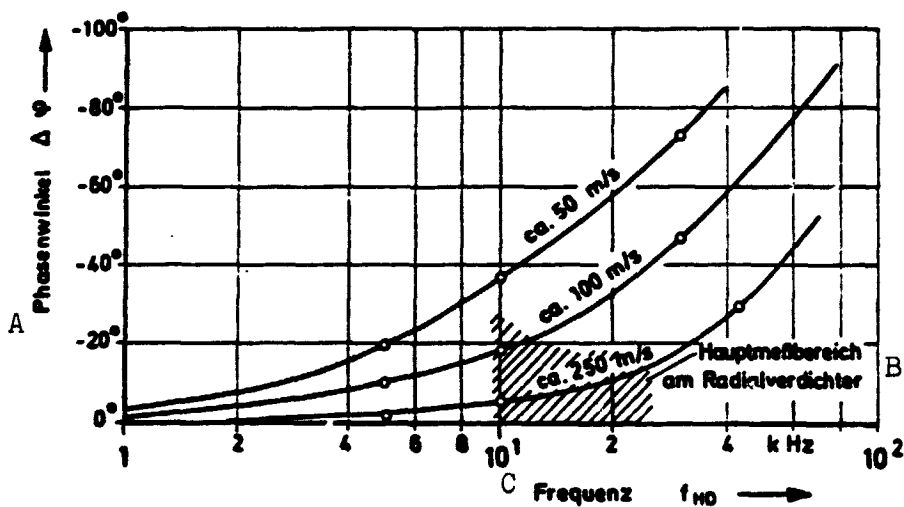


Fig. 3.17. Result of an indirect frequency curve study for estimating the signal phase shift using measurements made with the hot-wire shielded probe.

Key: A) Phase angle  
 B) Main test range on the centrifugal compressor  
 C) Frequency

one another on the sides of a 50° quartz glass wedge. This method was not used since the risk of different changes in drift over time of the two transmitters on the glass substrate could not be eliminated.

Finally, another measuring technique, which likewise operated on an intermittent principle and was developed by Giese and Schreck [3.12], was tried out in a practical test on the centrifugal compressor. In this probe the hot-wire was stretched over a distance of 0.1 mm parallel to the flow direction in front of a galss cylinder with a diameter of 0.6 mm. The directional characteristic of the probe shows up when the hot-wire lies in the sphere of influence of the stagnation point flow line of the cylinder, i.e. in a region of low flow velocity. In the strongly fluctuating flow at the centrifugal impeller exhaust it was very difficult, however, to determine a distinct recording medium in the signal curve. Moreover, with this probe design, hot-wire service lives of only about 15 minutes could be achieved.

In the extensive flow studies on the centrifugal compressor test stand -- in spite of built-in air filters which separated out dust particles over 1 μm in diameter -- the last-named point

took on increasing importance. With respect to the hot-wire life spans, the shielded probe possesses decisive advantages.

Because of the principle of the measuring technique the hot-wire is in the direct line of flow basically only during about 50% of the test time, and during test pauses the hot-wire can simply be protected in the wind shadow of the probe shield. Moreover, the use of tungsten wire is more advantageous because of its tensile strength which is 5 to 10 times greater than that of platinum wire or platinum-rhodium wire (cf. [3.13], Table II).<sup>1</sup>

Finally, shortening the length of the wire to 0.6 mm contributed significantly to an increase in the service life of the wire, so that test series lasting several days at an extremely high load are possible with these probes. Another side effect of this measure is that the aim of obtaining measurements which are as close to point measurements as possible is closely approximated and that the transition range of the test signal is reduced by about  $\pm 4^\circ$  to the value shown in Fig. 3.16. /53

This signal transition range is set by the fact that, in spite of using a stereo microscope and micromanipulator in making the probes, it is not possible to setup the hot-wire exactly parallel at a distance of about 0.7 mm from the leading edge of the shield. If, however, one assumes an approximately constant degree of uncertainty in the making of the probes (angle of inclination of the hot-wire to the edge of the shield), then it turns out that the  $\pm 4^\circ$  signal transition range of a 0.6 mm long hot-wire at a length of 2 mm would correspond to an aperture range of about  $\pm 13^\circ$  and thus the accuracy of the evaluation would be considerably limited.

### 3.5 The Synchronized Sampling Technique -- an Electronic Evaluation Method for Test Signals from a Periodic, Strongly Fluctuating Flow

The rapidly fluctuating, periodic flow events within the sphere of influence of the impeller flow -- as are observed, for example with fixed semiconductor pressure transducers or hot-wire probes with high time resolution -- can usually be recorded photographically and evaluated only by means of cathode ray oscillographs.

The image impression resulting from multiple overlapping

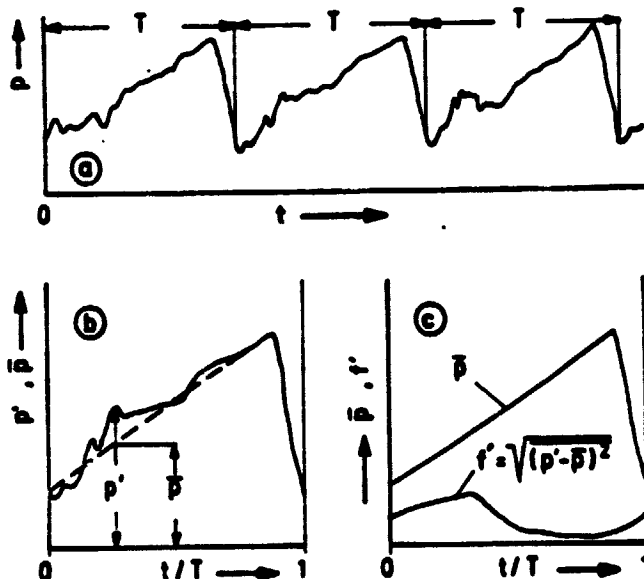
---

1. A certain disadvantage, to be sure, is the fact that tungsten cannot be soldered. For making the hot-wire shielded probe it was necessary to use an electric spot welding technique.

of the resulting periodic signal curves is strongly disturbed by fluctuations over time in the sequential events, caused, for example, by fluctuations in the relative flow of the impeller. The second crucial disadvantage of this evaluation method consists in the fact that the analysis of test results recorded photographically is very painstaking, time consuming and inexact.

Instead of this, especially with respect to the wealth of measurement data in 3-dimensional flow studies, it would be desirable to have a method which averaged the stochastically distributed signal fluctuations and at the same time slowed

154



possible to convert the information directly into digital form and store the measured values for separate data processing. By using the relatively simple electronic principle of the synchronized sampling technique (SST) it becomes possible to fulfill these requirements. A detailed discussion of this technique and a description of the SST instrument used is found in Appendix II.

The accuracy of the signal averaging process basically depends on the constancy of the test condition, in particular the rotational speed of the compressor, during the test period of about 2 minutes. The small deviations of  $\pm 0.03\%$  in the desired adjusted value of the rotation speed creates extremely favorable conditions for this on the centrifugal compressor test stand.

Fig. 3.18. Application, in principle, of the synchronized sampling technique:  
 a - periodic pressure curve,  
 b - definition of the local instantaneous pressure value  $p'$  and the average pressure value  $\bar{p}$  in the region of a blade spacing  $T$ , c - statistically averaged pressure curve  $\bar{p}(t/T)$  and fluctuation factor  $f'(t/T)$  after SST separation of periodically recurring and stochastically occurring signal components.

As an example, in principle, 155 for possible SST applications, Fig. 3.18 shows schematically the changes in wall pressure over 3 successive blade spacings - (a) - whereby the real pressure curve  $p'(t)$  is composed of a periodically recurring average pressure pulsation  $\bar{p}(t)$  and stochastically distributed pressure fluctuations

(b). After passing through the sampling process the average non-

steady pressure  $\bar{p}(t)$  and the effective value of the fluctuation intensity  $f'(t)$  are available as separate signals ©. Strictly periodic test signals can thus be separated from stochastically distributed fluctuations and at the same time they can be slowed down to the extent that recording them on x-y recorders or -- after appropriate analog-digital conversion by means of a digital voltmeter -- on perforated tapes or magnetic tapes presents no difficulties.

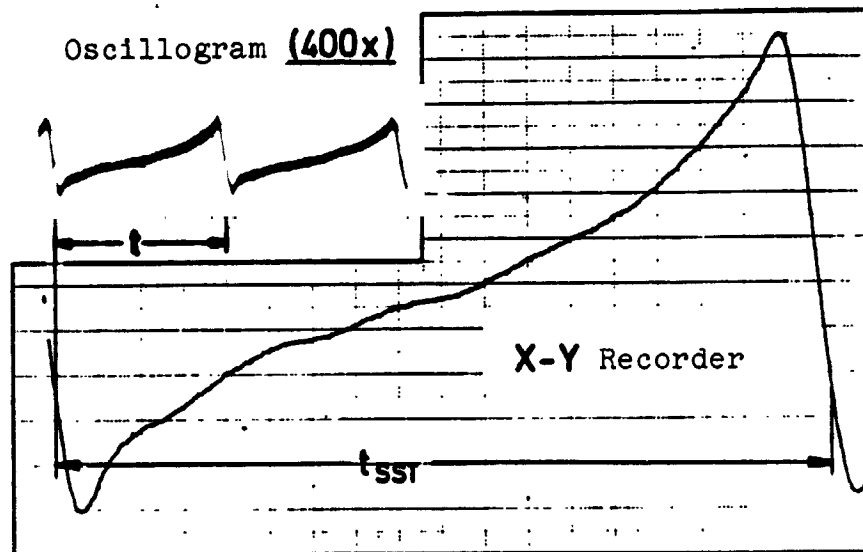


Fig. 3.19. Slowed down and statistically averaged transfer of a rapidly changing wall pressure curve (oscillogram: 0.25 ms/blade spacing  $t$ ) to an x-y recorder (2 minutes/blade spacing  $t_{SST}$ ) using the synchronized sampling technique.

For example, Fig. 3.19 shows the transfer of a wall pressure curve shown on the oscillogram used to an x-y recorder. In parallel with this, the slowed down, statistically averaged pressure curve was stored in about 250 digital values. The special importance of this is in the sampling signal analysis in regions with highly turbulent, strongly fluctuating flow, e.g. /56 in the wake region at the impeller output where quantitatively exact data can be obtained only in this way.

### 3.6 Basic Procedure for Determining, Processing and Evaluating Nonsteady Measured Variables

After discussing various test methods which have been used for investigating nonsteady flow events in centrifugal compressors and after describing the technique for averaging periodic, strongly fluctuating test signals by means of the synchronized sampling technique, the entire chain of measurement will now be briefly outlined extending from the electronic

determination of the flow variables via the processing of the test signal to the final evaluation. Detailed information on the measurement technique and evaluation technique in the analysis of the total flow field behind the impeller output are given below in Section 5.

Fig. 3.20 gives an overview of the various possibilities for processing the measurement data in the form of a signal flow diagram.

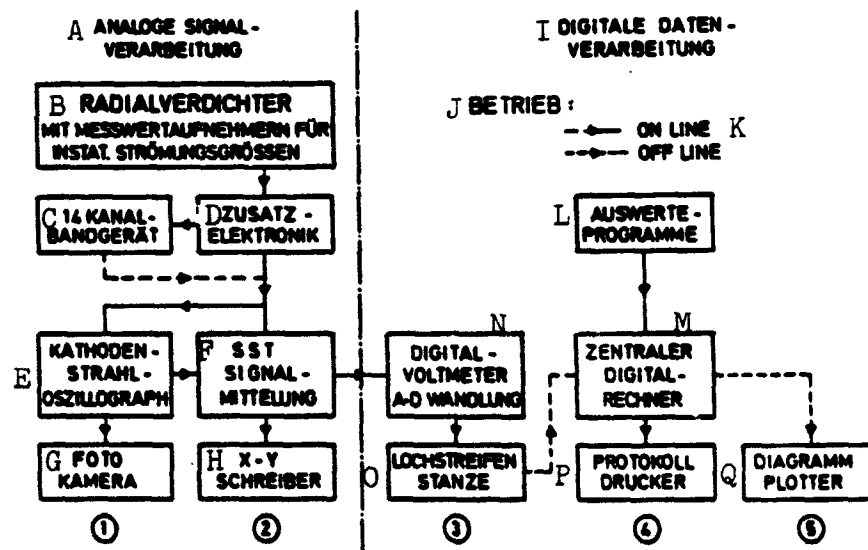


Fig. 3.20. Test signal flow diagram for the determination, processing and evaluation of nonsteady flow events occurring at the centrifugal compressor.

Key:

- |   |                                     |
|---|-------------------------------------|
| A) Analog signal processing   | I) Digital data processing          |
| B) Centrifugal compressor with transducers for nonsteady flow variables | J) Operation                        |
| C) 14-channel tape recorder   | K) On line, Off line                |
| D) Additional Electronics   | L) Evaluation programs              |
| E) Cathode ray oscillograph   | M) Central digital computer         |
| F) SST signal averaging   | N) Digital voltmeter A-D conversion |
| G) Camera   | O) Tape puncher                     |
| H) x-y recorder   | P) Protocol printer                 |
|   | Q) Diagram plotter                  |

Directly at the test point in the centrifugal compressor the flow variables are converted via the transducer -- total pressure and wall pressure sensor and hot-wire shielded probes -- into electric analog signals. In addition, synchronously running trigger impulses are also measured. The necessary additional electronics basically consist of a voltage supply, d.c. amplifiers and the hot-wire anemometer. After passing through this first stage, by interposing a 14-channel tape recorder (upper limit frequency 80 kHz), the possibility exists of storing the analog signals and separating them from the actual compressor experiment for further processing. /57

Depending on the case, 5 different possibilities present themselves for recording and evaluating the signal (cf. Fig. 3.20):

① Direct photographic recording of several superimposed signal curves from the screen of a cathode ray oscillograph with an instant-picture camera. This method is used to get a quick idea of the data. It is unsuitable for precise evaluation of a large number of quickly fading measurements.

② With the aid of the synchronized sampling technique (SST), periodic, strongly fluctuating test signals are separated by averaging their fluctuating components and slowed down to the extent that the curve of the average test signal and the fluctuation intensity can be recorded directly on x-y recorders. Operation of the SST instrument requires the saw tooth output of the oscillograph triggered synchronously with the test signal.

From these displays are obtained results of the non-steady direction measurement, the curve of the pressure fluctuation factor and information with respect to the temporal correlation of all of the test results behind the impeller output.

③ Occurring in parallel with the SST scanning is the analog-digital conversion of the test signals by means of a digital voltmeter and the output of the some 250 values per period on a perforated tape puncher. In this way, all of the alternating pressure curves are stored on a central computer for further exact, automatic processing. /58

④ Input data to be processed by the extensive evaluation programs on the central digital computer TR440 include, besides the pressure curve perforated tapes, the following: the results of the nonsteady direction measurement, the correct mean pressure values and temperature values over time, the operational data for the compressor and the necessary geometric data.



- The following were calculated:
- the exact nonsteady absolute pressure distributions, by superimposing the alternating pressure curves with the correct mean pressure values over time;
  - the complete flow fields (absolute system and relative system) in 4 coaxial test areas immediately behind the impeller output and
  - characteristic integral mean values for describing both the total flow field and the individual jet or wake components of the flow.

The results of the flow field calculation are stored in magnetic tape files and printed out when needed.

⑤ In an easy-to-read form, the data for describing the complex flow field at the output of the centrifugal impeller can be given in three-dimensional representations on a diagram plotter. In so doing, the accuracy of the digital evaluation is coupled with the clarity of the analog signal presentation.

#### 4. Design of the Test System, Operational Measuring Technique and Preliminary Experiments

##### 4.1 Description of the Test Compressor

The compressor is designed for a rotation speed of 18,000 rpm and a mass flow of 7.16 kg/s.<sup>1</sup> Important data in the design point is listed in Table 4.1.

In the design of the compressor stage, besides the demand for greater unit output -- large absorption capacity with a high stage pressure ratio -- points of measuring technique were also considered which, in keeping with the aim of the project, facilitate exact studies of the impeller flow. To be included here are, above all, the diffuser, which is unbladed and connected to the outlet side of the impeller -- this permits unfalsified analysis of the impeller outlet flow -- and the large stage dimensions, which stand in a favorable relationship to the size of the probes. /60

Fig. 4.1 shows the centrifugal compressor impeller studied with 20 radially ending blades which extend far into the axial inlet region. The impeller was milled from an aluminum maleable

---

1. The compressor was designed during the planning of the "centrifugal compressor" research project by the member companies of the Forschungsvereinigung Verbrennungskraftmaschinen e.V. [Research Association for Internal Combustion Engines].

TABLE 4.1 DESIGN DATA FOR THE CENTRIFUGAL COMPRESSOR STAGE IN QUESTION ( $z=20$ ) ACCORDING TO [4.1], RELATED TO THE STANDARD STATE IN THE COMPRESSOR INTAKE ( $p_{t0,N}=1.0133$  bar,  $T_{t0,N}=288.1$  K). FOR INDICATION OF THE MEASURING POINTS SEE FIG. 4.2

Rotation speed	$n$	rpm	18 000
Reduced output factor	$\mu$		0,83
Total pressure ratio	$\Pi_{t,05}$		2,683
	$\Pi_{t,02}$		3,014
Total efficiency	$\eta_{i,05}$		0,80
	$\eta_{i,02}$		0,91
Total temperature ratio	$T_{t2}/T_{t0}$		1,406
Mass flow	$\dot{m}$	kg/s	7,16
Power required	$N$	kW	844
Velocity vector diagram			
At impeller intake	$u_{1a}$	m/s	263,9
(a - external)	$c_{m1a}$	m/s	112,0
	$w_{1a}$	m/s	287,0
	$M_{w1a}$		0,852
	$\alpha_1$	°	90,0
	$\beta_{1a}$	°	23,0
Velocity vector diagram			
impeller exhaust	$u_2$	m/s	377,0
	$c_2$	m/s	335,1
	$M_{c2}$		0,894
	$c_{u2}$	m/s	312,9
	$c_{r2}$	m/s	120,0
	$w_2$	m/s	136,0
	$\alpha_2$	°	21,0
	$\beta_2$	°	61,9

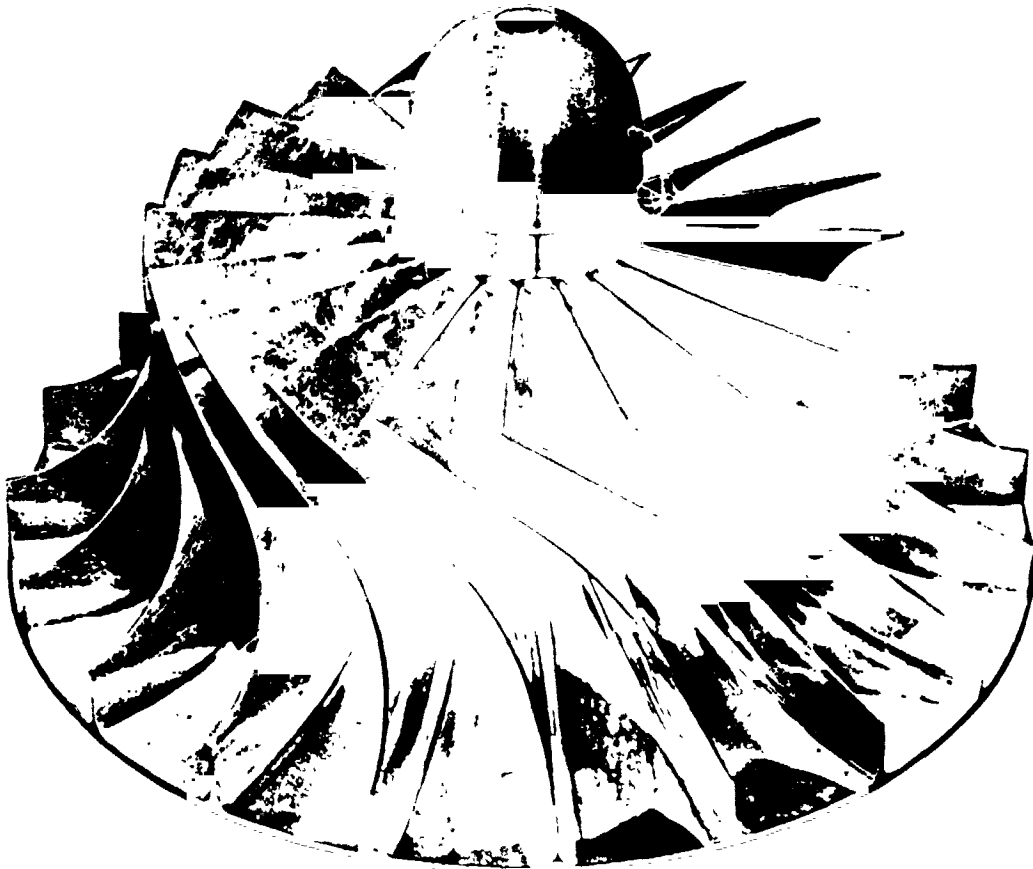


Fig. 4.1. Centrifugal compressor impeller, blade number  $z = 20$ , blade outlet angle  $\beta_{s2} = 90^\circ$ , material AlCuMg2F45.

alloy. Thus, in terms of the hardness of the metal, circumferential velocities at the tip of approximately 525 m/s are permissible.

The main dimensions of the flow channel are given in Fig. 4.2. The centrifugal impeller is taper bore mounted, so that the flow is sucked undisturbed through an axial intake pipe with a diameter of 281 mm. Because of the high stress of centrifugal force, all of the blade units of the impeller stand radially. The mean camber line (in cylinder section A-A) has an elliptical shape. The approximate curve of the flow cross-section A/A<sub>intake</sub> of an impeller blade channel over the average flow path length  $l/l_{\max}$  is shown in the lower right corner of Fig. 4.2. Behind the impeller outlet extends an unbladed centrifugal diffuser with a constant orifice area over the radius.

/61

In order to even out the diffuser flow field in the circum-

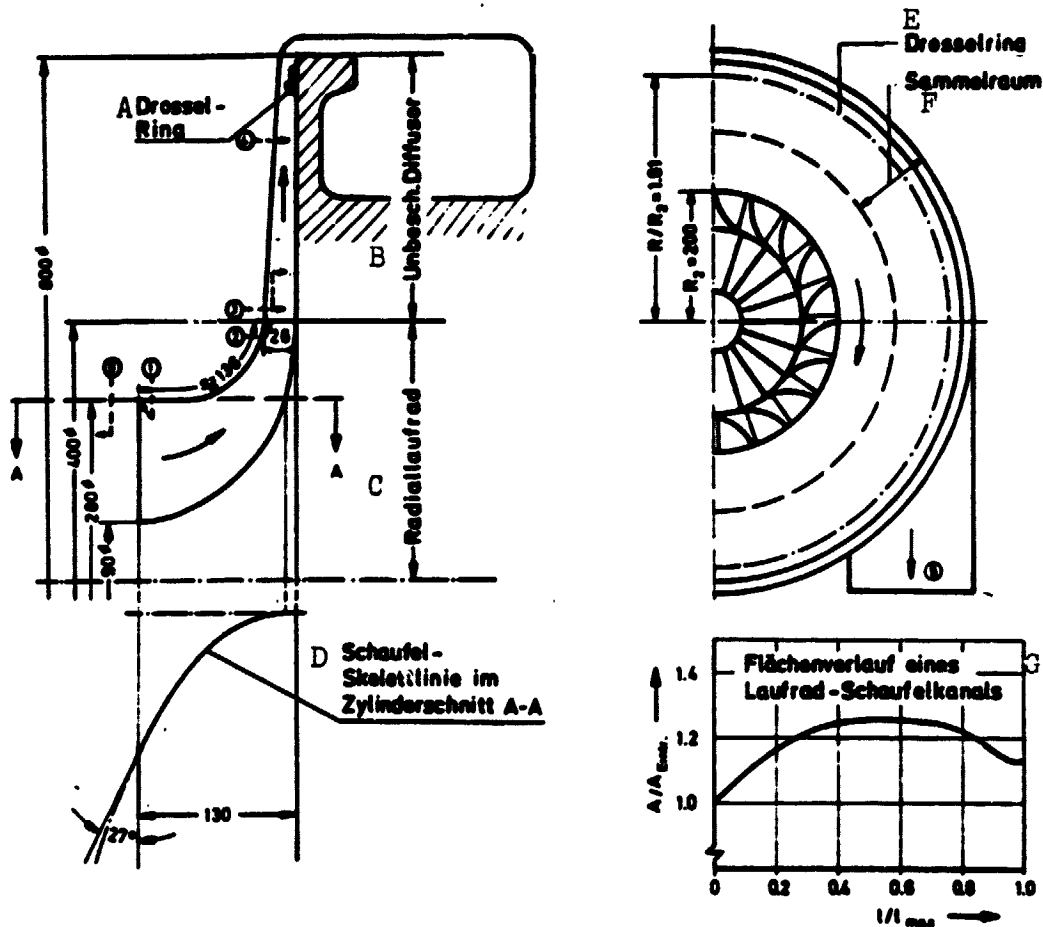


Fig. 4.2. Centrifugal compressor flow channel. Main dimensions and measuring point positions ① ... ⑤, measurements in mm, (Intake width of the diffuser which is equal in area,  $b_2 = 26.7$  mm).

- |  |  |
|--|--|
| Key: A) Throttle ring                                    | E) Throttle ring                           |
| B) Unbladed diffuser                                     | F) Correcting chamber                      |
| C) Centrifugal impeller                                  | G) Area curve of an impeller blade channel |
| D) Mean camber line of the blade in cylinder section A-A |  |

ferential direction a throttle ring was installed at the diffuser outlet with a radii ratio of  $R/R_2 = 1.91$ . The manner of operation of this ring is explained in detail in section 4.4. /62

After a deflection in the axial direction, the air then flows into annular collecting chamber of equal area. The compressor outlet pipes branch off from this tangentially.

Fig. 4.2 also shows the positions of the different test

points or reference points within the compressor stage:

- ① - compressor intake (also see Fig. 4.3, no. 7),
- ② - impeller inlet edge,
- ③ - impeller outlet edge,
- ④ - diffuser inlet region ( $1.0 R/R_2$  1.2)
- ⑤ - diffuser outlet ( $R/R_2=1.687$  in performance characteristics measurements)
- ⑥ - compressor outlet.

#### 4.2 Total Layout of the Centrifugal Compressor Test Stand

Fig. 4.3 shows an overall view of the complete centrifugal compressor test stand.

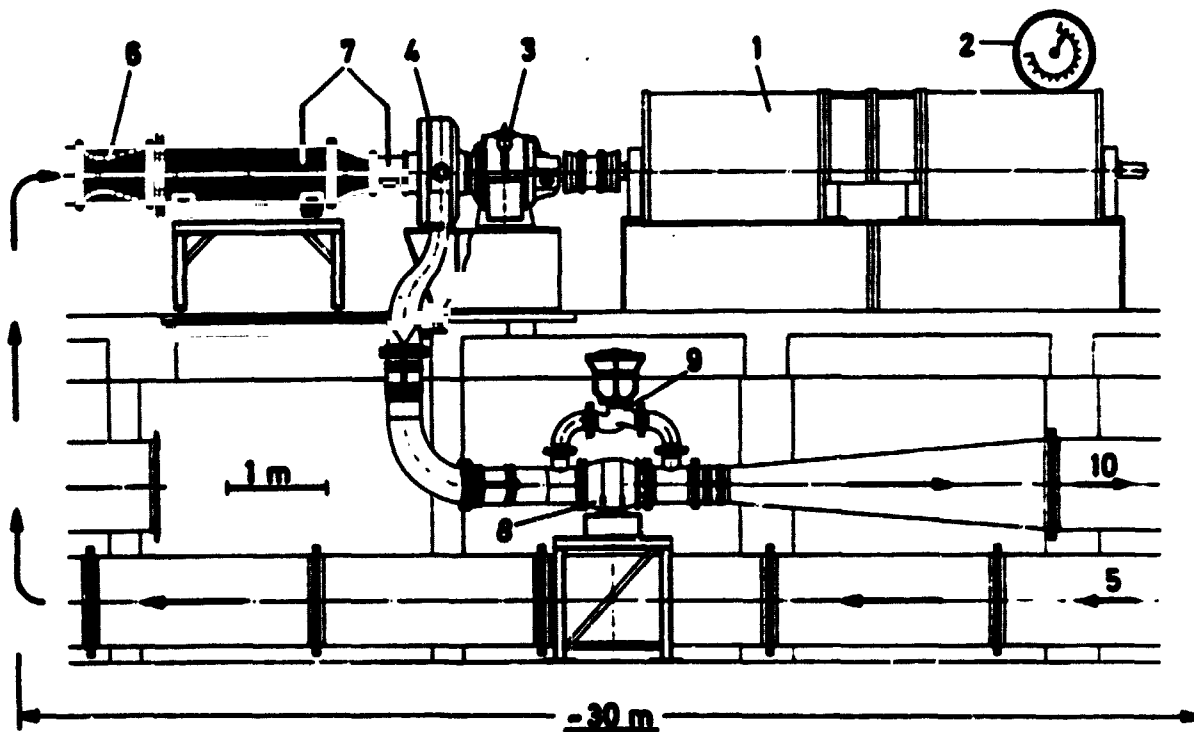


Fig. 4.3. Overall view of the Centrifugal ompressor test stand.

- 1 - D.C. swivel bearing motors (2 x max. 750 kW)
- 2 - Torque scale
- 3 - Planetary gearing
- 4 - Centrifugal compressor
- 5 - Air intake line NW 800 with dust filter
- 6 - Venturi tube NW 500
- 7 - Compressor intake working planes NW 500 and Nw 281
- 8 - Annular throttle slide NW 300
- 9 - Pneumatic membrane valve with pump by-pass line
- 10 - Hot air line NW 800 with cooler and noise damper at the outlet

The test compressor is driven by two coupled, separately excited D.C. electric motors - ① - which together have a maximum output of 1,500 kW. These can be continuously adjusted over a range of 0-3,000 rpm. The motors are mounted in pendulum bearings, so that with the air of the calibrated scale - ② - the power take-off torque can be determined. The planetary gearing - ③ - in a compact arrangement (gear ratio, 1:9) and the centrifugal compressor - ④ - are mounted on a separate base. This suppresses the propagation of motor oscillations and reduces the noise of the rapidly turning part of the system. In principle, it is possible to run the test stand with an open or closed air circuit. With open operation, the air is taken in from the atmosphere and again blown out into the atmosphere. In this mode of operation the performance limit of the drive motors is reached at a compressor rotation speed of about 22,000 rpm. If one wants to increase the rotation speed up to the maximum value of 27,000 rpm, then the switch must be made to close operation, with which the compressor intake pressure drops below atmospheric pressure and the air is recooled behind the compressor.

/63

All of the experiments described within the scope of this study at rotation speeds up to 18,000 rpm were performed with an open air circuit:

- The air flows through the intake line - ⑤ - (Fig. 4.3) to the compressor after dust particles  $> 1 \mu\text{m}$  in diameter have been separated out by a filter (precondition for hot-wire measurements). The air mass flow is determined with the air of a standard built-in short Venturi tube NW 500 - ⑥. In the straight part of the line in front of the Venturi tube inlet a series of straightening blades and turbulence screens was built in. These were spaced about 6 meters apart. Their purpose is to eliminate the effects of the upstream pipe bend.

/64

In the hot-air line on the pressure side an annular motorized slide is built in as a throttle - ⑧. On the pressure side, the compressor can be quickly relieved by means of a pneumatically activated membrane valve - ⑨ - in case the pump limit is unintentionally exceeded. The air circuit terminates with an air cooler and noise damper - ⑩.

The entire test stand was equipped with extensive control and monitoring systems which are briefly discussed below. A detailed description is found in [4.2].

The purpose of an axial thrust control is to keep the load on the axial journal bearing of the compressor caused by the axial thrust of the impeller (max. about 20 kN) under approximately 1.5 kN. The static pressure increase in the centrifugal impeller is used as a reference quantity to control the pressure of the compressed air which acts upon the axial thrust compen-

/65

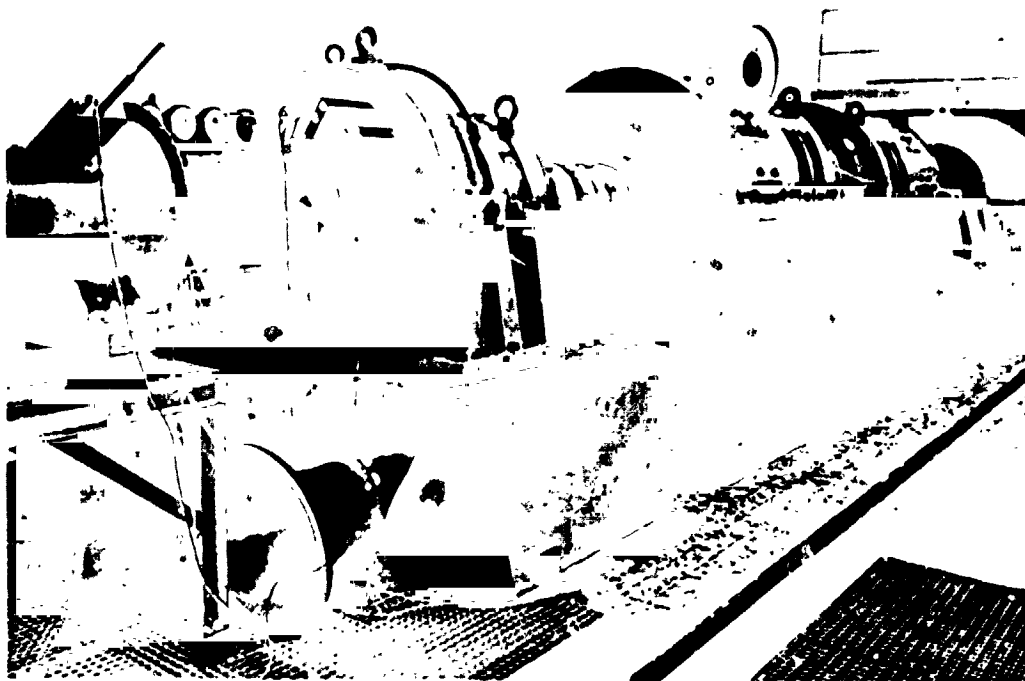


Fig. 4.4. Centrifugal compressor test stand with 1,500-kW drive motors.

sating piston co-rotating on the compressor shaft.

For an alternative possibility of automatic pump limit monitoring, when a dynamic pressure limit value is exceeded in the compressor intake, the by-pass line mentioned above around the throttle unit (Fig. 4.3, position 8) is opened and the compressor is relieved on the pressure side. This assumes, of course, that the location of the pump limit is already known. According to our experience, operational instabilities, such as incipient rotating stall, can be most accurately determined by installing a wall pressure sensor in the impeller intake region.

In the case of close circuit operation, two additional fixed-point control loops are used to keep the intake pressure and intake temperature constant.

With the operation monitoring systems we should, in the first place, mention the non-contact control of the clearance between the individual impeller blades and the compressor housing. This is accomplished by means of a capacitive measuring method which was adapted to the special operating conditions encountered during use on highly-loaded compressor stages (cf. [4.3]). Thus on the centrifugal compressor -- after appropriate calibration -- the changes in clearances at the impeller inlet and outlet -- which are about 0.5 and 0.7 mm respectively when

the impeller is not running -- where monitored with an accuracy of better than 0.05 mm. At the same time, the output signal of the clearance transducer serves the purpose of exact coordination and evaluation of the nonsteady test signals which are picked up within the impeller or behind the impeller outlet.

To monitor the vibration of the centrifugal compressor a commercial measuring system was used which operates on the induction principle with seismic transducers. These are mounted on the compressor housing in an axial, tangential and radial direction. With appropriately careful balancing of the rotor, the vibration velocities in all of the transducer directions were less than the very good value of 3 mm/s. /66

Other monitoring included the continuous recording of compressor bearing temperatures, separate for cylinder roller bearings and axial journal bearings, the recording of to and from oil temperatures for the compressor and gears, as well as continuous, digital measurement of the flow of oil for the circulation of oil for the gears and separate for the supply of oil for the ball bearings and journal bearings. All together, some 30 different variables are monitored automatically, plotted on a recorder and when preselected limit values are exceeded this activates both aural and visual alarms.

#### 4.3 Conventional Operational Measuring Technique and Data Determination

In order to evaluate the overall operational behavior of the centrifugal compressor stage, characteristic performance studies and a number of detailed measurements with conventional time-averaging measuring techniques were carried out prior to the nonsteady flow measurements in the diffuser inlet region. These measuring techniques, which are necessary for measuring performance characteristics and, in part, for setting the operating levels, determine the rotation speed, mass flow, static pressure, total pressure and total temperature. These techniques and the corresponding parts of the data acquisition system are discussed in the appendix.

A trigger disc -- attached on the gear side of the compressor shaft -- with 60 radial notches uniformly distributed on the circumference of the disc is used to measure the speed of rotation. The disturbances in the magnetic field caused by these notches are converted into electric impulses by magnet-resistor transducers. These impulses are summed by a counter with a 1-second integration time and shown in digital form as a direct speed of rotation reading in rpm.

As already mentioned above, the air mass flow is determined with the aid of a standard short Venturi tube installed in the compressor intake line. The DIN 1952 specification for flow



measurement were observed in the layout for a mass flow range of 2-10 kg/s. These specifications were also observed in the installation of the Venturi tube and during the evaluation of the measured values.

The following, time-averaging measuring techniques were used 67 outside the direct sphere of influence of the nonsteady impeller flow.

The usual wall pressure holes with a sharp-edged inlet (diameter 0.8 mm) were used for static pressure measurements. The axis of these holes is perpendicular to the housing contour of the flow channel.

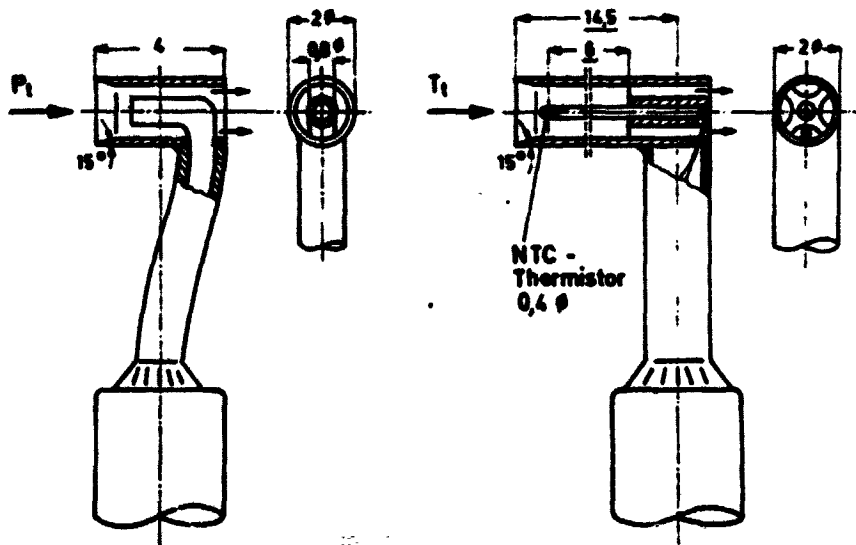


Fig. 4.5. Conventional, time-averaging probes. Left: total pressure probes; right: NTC total temperature probe, measurement in mm.

The probe shown on the left in Fig. 4.5 is used for the total pressure measurements. The probe shown on the right was developed to measure total temperature. The temperature sensor is a NTC thermistor. The reading given by both of these types of probes is independent of direction with subsonic flow and in an angular range of  $\pm 30^\circ$ . The use of glass-encapsulated NTC temperature sensors in place of thermoelements in the centrifugal compressor studies is based on a number of advantages:

- these transducers have long service lives in the strongly fluctuating flow. They are insensitive to dust erosion and dust deposits;

- the high internal resistance (1,000  $\Omega$ ) makes possible higher signal voltages by a factor of  $10^3$  during operation in a bridge circuit. With less expense (without an amplifier) these signal voltages can be accurately transferred and further processed.

On the other hand, a possible disadvantage may appear that, with NTC thermistors, the calibration curve is more temperature-dependent in comparison with thermoelements. However, since with precise thermoelement measurements a calibration curve for the sensors must also be taken, this point does not have much bearing.

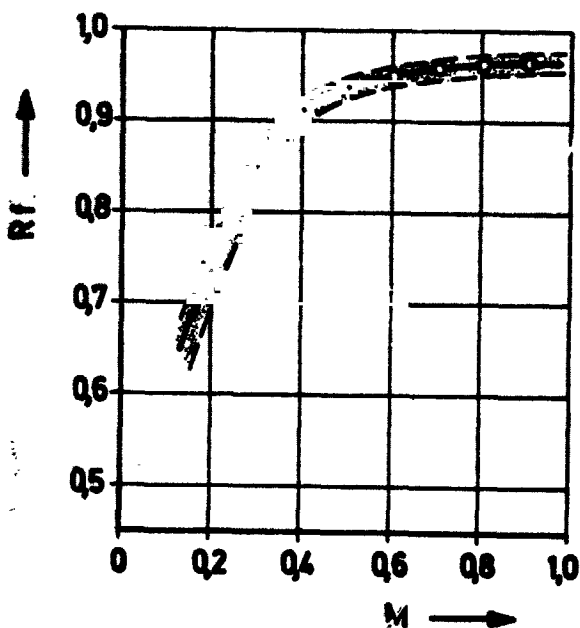


Fig. 4.6. Curve of the temperature recovery factor  $R_f$  plotted over the mach number  $M$  of the oncoming flow for NTC total temperature probes (see Fig. 4.5).

of heat between the thermistor bead and the shaft of the probe. This considerably increases the  $R_f$  value and at the same time ensures that the temperature reading remains unaffected by the installation location of the probe. For this type of probe, fairly optimal conditions lie at an area ratio (ventilation opening/probe inlet opening) of 0.4.

Fig. 4.6 shows the corresponding curve of the recovery

In developing the temperature probe special attention was placed on the fact that the temperature recovery factors  $R_f$  should be easily reproducible in operation, i.e. effects due to the positioning of the probes (e.g. due to increase carrying-off of heat in the vicinity of the wall) should be largely eliminated. The following equation applies:

$$R_f = (T_{t,a} - T) / (T_t - T) \quad (4.1)$$

with  $T$  = static temperature,  
 $T_t$  = true total temperature and  
 $T_{t,a}$  = indicated total temperature.

Because of the necessary sensitivity of response, the probe has ventilation holes through which the test gas flow out axially along the shaft of the sensor. At the same time, the front portion of the NTC sensor (about 6 mm long) is free-standing. Both of these measures reduce the carrying-off

769

factor  $R_f$  as a function of the mach number  $M$  of the oncoming flow. The half-tone curve path corresponds to the variation width of the  $R_f$  curve which depends on the accuracy of manufacture and the effect of contamination after longer periods of operation.

For fast determination of the mean compressor inlet temperature at operational level settings, a platinum resistance thermometer with an active sensor length of 0.35 m is also mounted in the intake line NW 500 (see Fig. 4.3, position 7) obliquely to the direction of flow. The probe possesses a cylindrical dust shield. An  $R_f$  correction of the indicated value is unnecessary, however, because of the low mach number of the oncoming flow ( $M < 0.15$ ).

With the aid of a data acquisition system, the flow variables measured with the conventional measuring systems are converted into electric potential signals. They are scanned in a measuring cycle of about 1 minute and stored on perforated tapes. The system possesses 20 NTC temperature terminals, 10 pressure measurement points with -- in the adapted test range -- individual pressure transducers (e.g. for the small differential pressures encountered during mass flow determinations) and 2 pressure measuring point switches (scanivalves) each with 48 wall pressure and total pressure terminals. The pressure transducers measure differential pressures with respect to atmospheric pressure. The exact atmospheric pressure is determined by means of a Hg bulb barometer.

In addition, by means of the data acquisition system, it is also possible to record the exact position of up to 20 probes simultaneously by scanning the path potentiometer and angle potentiometer on the probe adjustment devices.

170

#### 4.4 Preliminary Experiments (Performance Characteristics Measurements)

Before the start of the actual test program designed to analyze the flow field behind the impeller outlet, the general test conditions were studied for the use of the nonsteady measuring techniques and at the same time the operational characteristics of the entire centrifugal compressor stage were obtained in the form of a performance graph. This was done with the aid of various conventional measuring techniques.

The measured pressure and temperature values revealed that the nonsteady measuring techniques described in Section 3 would be loaded within their operating limits up to 18,000 rpm.

In the blade  $\rightarrow$  diffuser, the circumferential distributions of total pressures, total temperatures and wall pressures showed large dysymmetries. It was found that, starting from the com-

pressor outlet (see Fig. 4.2, position 5) and working back through the collection chamber and the unbladed diffuser, disturbances of the axially symmetric flow field could be detected clear into the compressor inlet. Thus, for all that, nonsteady measurements in a certain radii ratio at any desired position on the circumference would no longer have been representative for this radii ratio and anyhow the already large expenditure for measuring the 3-dimensional development of the flow after leaving the impeller would have assumed impractical dimensions.

To even out the flow a throttle ring was installed a short distance in front of the diffuser outlet (see Fig. 4.2). This was designed in such a way that in its narrowest cross-section a critical state appears and thus downstream disturbances cannot react on the bladeless diffuser. The effects of these measures are explained with the aid of the following figures:

First of all, using as an example the wall pressure distribution in the bladeless diffuser at an operating level of 16,000 rpm, Fig. 4.7 shows the disturbed flow field before

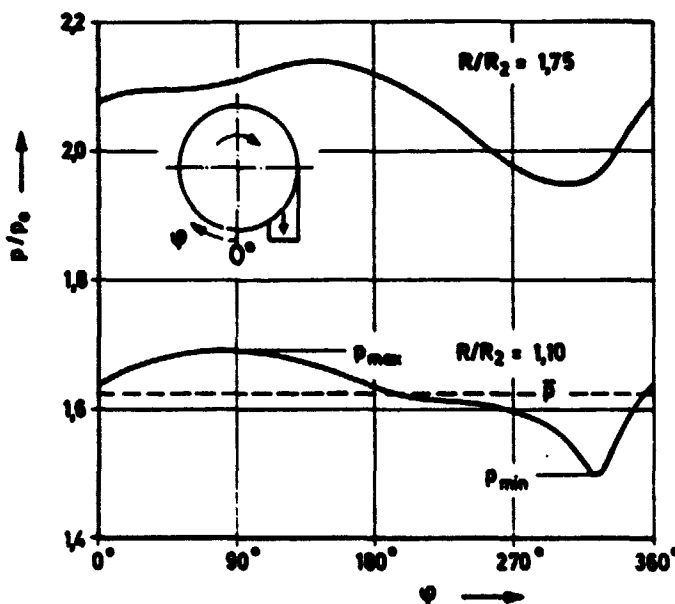


Fig. 4.7. Distribution of the static pressure ratio over the circumference of the unbladed centrifugal diffuser,  $n = 16,000$  rpm,  $\dot{m} = 5.7$  kg/s.

installation of the throttle ring. The drop in pressure in the region of the outlet pipe can clearly be seen ( $270^\circ < \phi < 360^\circ$ ).

With the variables shown in Fig. 4.7, a relative pressure variation  $\epsilon_p$  can be defined as follows to characterize the intensity of the disturbance:

$$\epsilon_p = (p_{\max} - p_{\min}) / (2\bar{p}). \quad (4.2)$$

Fig. 4.8 compares the measured  $\epsilon_p$  distributions with and without the built-in throttle ring within the range of performance characteristics of the compressor. While without the throttle ring relative pressure variations up to a maximum of 15% were observed, the distribution on the circumference is evened out under the influence of the throttle ring to such an

extent ( $\epsilon_p < 2.5\%$ ) that satisfactory conditions exist for making the nonsteady measurements.

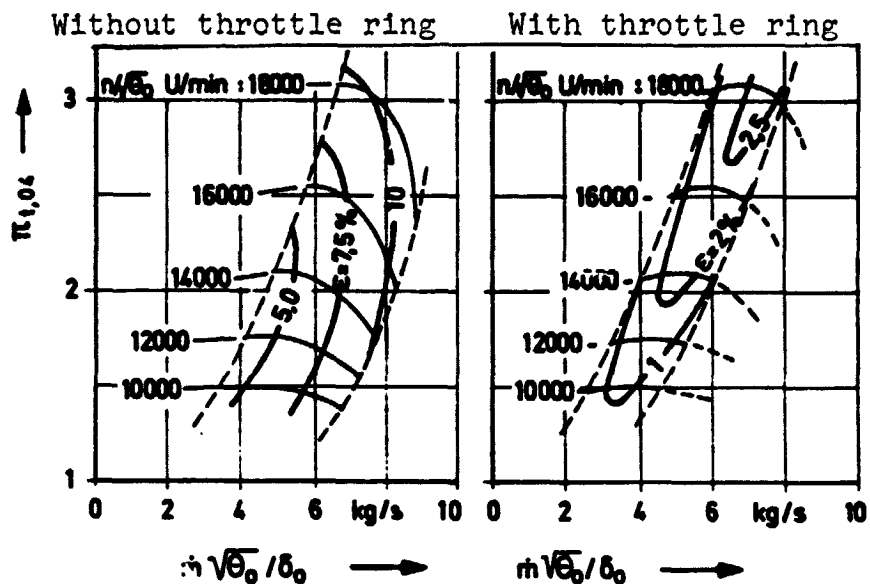


Fig. 4.8. Distribution of the relative variation in wall pressure  $\epsilon_p$  in the compressor performance graph, relative to  $R/R_2 = 1.1$ .

To be sure, as shown in Fig. 4.8, the throttle ring reduces the width of the performance graph available for measurements by 10% (18,000 rpm) up to 40% (10,000 rpm) of the original mass flow difference between the stopper limit and the pump limit. While the system stop limit is shifted to a new "throttle ring curve" (cf. also Fig. 4.9), the pump limit also shifts for the throttle ring configuration by about 25-35% of the original width of the performance graph towards smaller mass flows.<sup>1</sup>

/72

For the practical situation, it follows from this that by

1. Extensive studies on the development of operational instabilities (cf. [3.10], p. 71 f.) have shown that the disturbances in the pressure distribution along the circumference trigger premature pumping even with mass flows which still lie in the stable range of operation with an axially symmetrical flow field. As a further difference, it was found that, without the throttle ring, continuously increasing, low-frequency pumping developed ( $f_{\text{pump}} < 100$  Hz), whereas with the throttle ring a rotating stall suddenly developed (rotational frequency about 60% of the blade frequency). In both cases the operations' instability in the region of the diffuser inlet are initiated before the total flow upstream and downstream is measured from this.

homogenizing the flow field in the circumferential direction -- in the present case, for example, by means of an adjustable ring throttle at the diffuser outlet -- the operational range of the compressor is substantially increased.

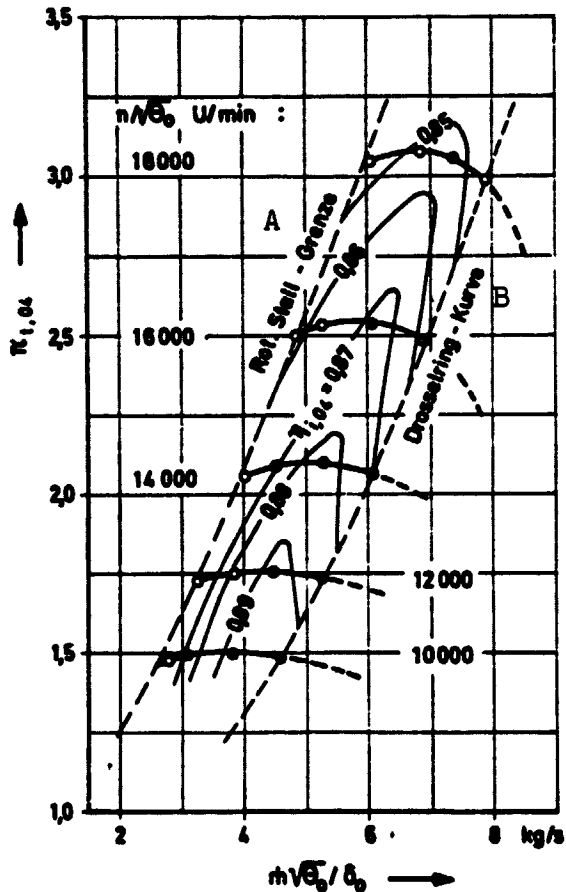


Fig. 4.9. Performance graph of the centrifugal compressor stage studied, with built-in throttle ring.

Test points at which additional nonsteady detail measurements were made in the region of the diffuser inlet. Key: A) Rotating stall limit B) Throttle ring curve

For determining the performance graph for the compressor, Fig. 4.9, the following variables were measured:

- corrected rpm

$$n/\sqrt{\theta_0} \text{ [rpm]},$$

- corrected mass flow

$$\dot{m} \sqrt{\theta_0}/\delta_0 \text{ [kg/s]},$$

- total pressure ratio

$$\Pi_{t,04} = p_{t4}/p_{t0},$$

- internal total efficiency

$$\eta_{i,04}$$

with

$$\eta_{i,04} =$$

$$(4.3)$$

$$T_{t0} [(p_{t4}/p_{t0})^{(\kappa-1)/\kappa} - 1] / (T_{t4} - T_{t0}),$$

Each of these variables was determined at 4 operation levels for a total of 5 rotation speeds between  $n/\sqrt{\theta_0} = 10,000$  rpm and 18,000 rpm. All of the variables were related to the standard state in the compressor inlet:

- total pressure

$$p_{t0,N} = 1,0133 \text{ bar},$$

- total temperature

$$T_{t0,N} = 288,1 \text{ K}$$

From this we get the correction factors for

- pressure:

$$\delta_0 = p_{t0}/p_{t0,N}$$

and

- temperature

$$\theta_0 = T_{t0}/T_{t0,N}$$

/73

/74

In addition to the wall pressure distribution along the entire flow channel, we also measured total pressure profiles and total temperature profiles in each of the 9 equidistant points of the intake line radius in the compressor inlet (test point ①, cf. Fig. 4.2 and Fig. 4.3, position 7) or over the diffuser width in the radii ratio  $R/R_2 = 1.687$  (Fig. 4.2, test point ④).

In the profile measurements in the diffuser, first of all the distributions of total pressure were measured at 6 uniformly distributed positions on the circumference. In so doing, along with the probes shown in Fig. 4.5, three 3-hole probes were also used. Besides the total pressure, these also show the flow direction. This direction measurement is necessary for exact averaging. At the same time, it is used for aligning the largely angle-insensitive total pressure and total temperature probes with which measurements were made with them in the same positions in a separate experiment. By this means, it was ensured that the adverse effect on the flow field due to obstruction by the probes remains within limits, and such measurements of total pressure, direction and total temperature which were taken at the same test point were expressed in relation to one another. This requires that the experimental conditions with respect to the corrected rpm and corrected mass flow can be adjusted so as to be exactly reproducible. A control program for a table top computer was worked out with which the speed of rotation and the mass flow are continuously adjusted to the altered intake conditions.

In evaluating the performance graphs, the suggestions of Traupel (see [3.1], p. 174 i. and [4.4]) were taken into consideration for the correct averaging.

By integrating the flow field, measured in detail, in the compressor intake pipe, the mass flow measurements were checked in a few points with the aid of a Venturi tube and very good agreement was found (deviation  $< 1.5\%$ ).

75

To check the measuring and averaging method for total temperatures -- which is especially important for the evaluation of the nonsteady measurements and for exact determination of the internal efficiency -- the total increase in enthalpy (i.e. total temperature increase), corresponding to the input of energy into the flow medium, was also determined indirectly. We measured the torque and rpm of the motors, as well as the exact flow of oil and increase in oil temperature in the compressor and gears. From this we determined the output of the motors and the oil dissipation losses. Mathematically, the external disc friction loss was taken into consideration on the basis of data from Daily and Nece [4.5]. Ignoring the losses by radiation on the compressor and gears, the corresponding increase in the total temperature in the test compressor was determined

in a performance rating of these variables. The deviations in the measured temperature increases were less than 1% in comparison with the values determined from the performance rating -- less than 1.5% in the case where the speed of rotation was 18,000 rpm.

A detailed discussion of the results for this complex set of factors is found in [4.2].

## 5. Experimental Procedure and Evaluation to Determine the Non-steady Flow Behind the Impeller

176

### 5.1 Arrangement of Measuring Points and Test Program

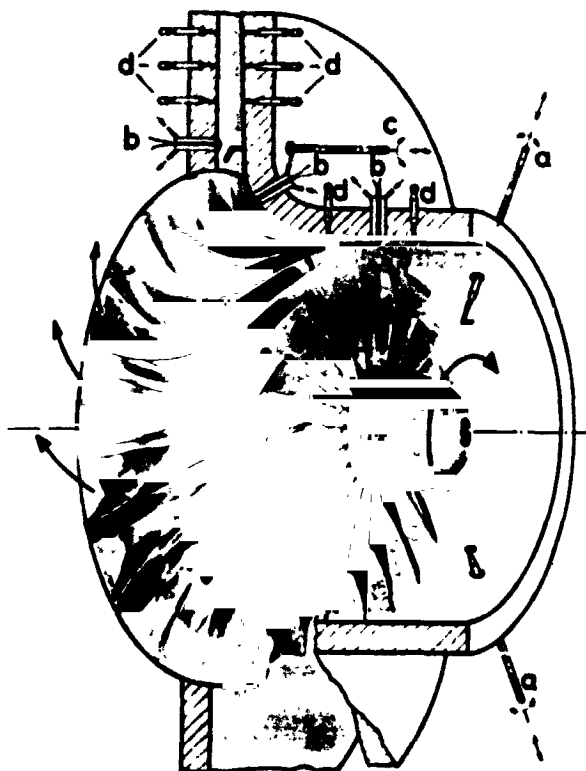


Fig. 5.1. Sectional view of the centrifugal compressor with the principle built-in locations of the various measuring systems: (a) conventional total pressure and total temperature probes; (b) cooled wall pressure sensor and window positions for optimal velocity measurement; (c) probes for time-averaging and nonsteady total pressure

Fig. 5.1 shows an overall view of the principle arrangement of test points within the centrifugal compressor stage. In keeping with the aim of the project, the main focus of the experimental studies is directed on the diffuser inlet region, where, for example, probe - (c) - stands for a large number of probes for time-averaging and nonsteady total pressure measurement and for nonsteady direction measurement. In each case here, the shaft of the probe lies parallel to the axis of the rotor. The probes are handled from the front wall of the diffuser over the width of the diffuser with the aid of a device to slide them into position and they are rotated into the desired angular position. The measuring systems - (b) - and - (d) - for the nonsteady and time-average wall pressure measurement are also installed in the impeller region, each of them perpendicular to the housing contour. In a few places in the impeller region, glass windows were installed for making optical velocity measurements in place of

measurement and nonsteady direction measurement; (d) time-averaging wall pressure measurement.

177



the cooled wall pressure adapters. The measurements of the velocity curve in the impeller-blade channels and of the blade load along the outer contour represent a considerable amount of added information for interpreting the flow field, measured in detail, behind the impeller outlet.

To explain the exact measuring points in the diffuser inlet region, we introduce the rectangular coordinate system shown in Fig. 5.2.

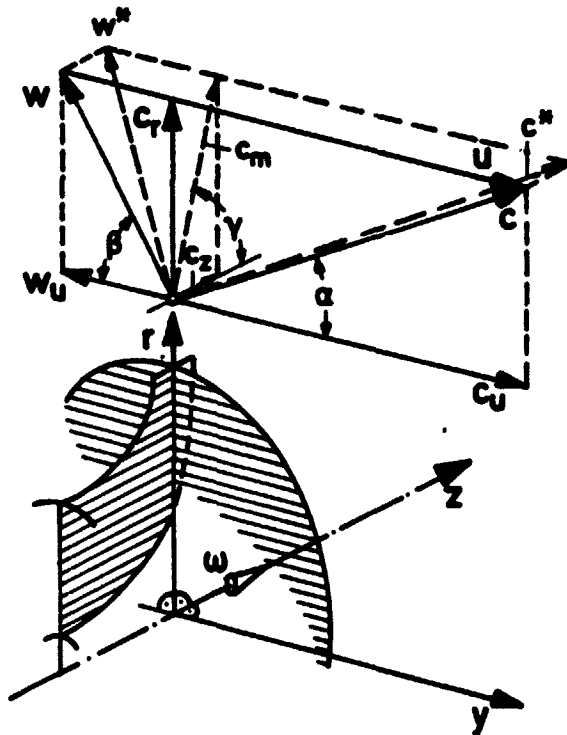


Fig. 5.2. Centrifugal compressor coordinate system and position of the  $r, y$  working plane and reference plane with velocity vector diagram behind the impeller outlet.

The positive  $z$  direction lies parallel to the rotor axis, i.e. in the direction of the angular velocity vector  $\omega$ . Perpendicular to this extends the  $r, y$  measuring plane and reference plane in which the flow angle  $\alpha$  of the absolute velocity vector  $c$  is measured. It is not possible to determine exactly the flow angle  $\gamma$  in the  $z, r$  plane with existing measuring techniques, including the dual-focus laser method for optical velocity measurement. Thus, in evaluating the velocity field at the impeller outlet, the  $z$  components are not taken into consideration. /78

The existing relationship of the diffuser width  $b$  to the channel spacing  $t$  (between the radii ratios  $R/R_2 = 1.017$  and  $1.151$ ,  $b/t$  varies between  $0.41$  and  $0.32$ ) proves to be especially favorable here. It prevents the development of pronounced cross-current components in the  $z$  direction, so that it appears permissible to ignore these components (cf. section 5.6).

Fig. 5.3 shows the exact location of the coaxial measuring planes and reference planes in which the flow field behind the impeller outlet was measured and evaluated.

The measuring surfaces designated I-IV lie in the following radii ratios:  $R/R_2 = 1.017, 1.039, 1.089$  and  $1.151$ . /79

For purposes of clarity, in Fig. 5.3 only the measuring surfaces closest to (I) and most remote from (IV) the impeller are shown.

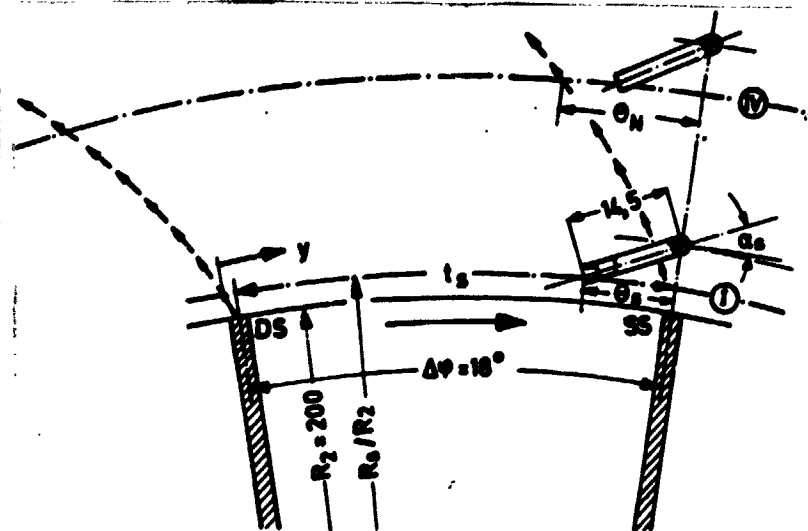


Fig. 5.3. Definition of coaxial measurement and references at the outlet of an impeller blade channel.

I:  $R_s/R_2 = 1,017$ ,  $\alpha_s = 25^\circ$   
 IV:  $R_s/R_2 = 1,151$ ,  $\alpha_s = 30^\circ$

By definition, the measuring surfaces in the radii ratios  $R_s/R_2$  lie through the middle of the inlet opening of the total pressure probes. The total pressure probes (see Fig. 3.10 and 3.12) were all installed with  $\alpha_s = 25^\circ$  (measuring surface I), or  $30^\circ$  (measuring surfaces II-IV) and were handled over the diffuser width in this angular setting.

By means of the gradations in the measuring surface radii ratios, it is possible to exactly measure the development of mixing processes and equalization processes in the disturbed flow behind the impeller outlet. In preliminary experiments it was found that

up to measuring surface IV the periodic character of the flow -- which is required for the use of the total measuring technique described -- still exists, however, as soon as a radii ratio of  $R/R_2 = 1.2$  is reached, for example, it was not longer possible to detect any clear variation in the variables in the circumferential direction because of the extensive equalization of the flow in conjunction with a greater amount of fluctuation.

Fig. 5.4 shows an overall view of the various measuring points in the diffuser inlet region. In each case, the measuring point -- probe inlet for total pressure probes, shield edge for hot-wire direction probes and pressure transducer membrane for wall hole for wall pressure measurements -- is indicated by a circle.

As described above, the coaxial reference planes for the nonsteady flow analyses I-IV are determined by the position of the total pressure probes ① ②. For the nonsteady direction measurement - ⑦ - the hot-wire shielded probes are installed in the circumferential position  $\phi = 270^\circ$  in a wall stop with finely graduated measuring positions in the radial direction. Hence the flow direction can be detected in nearly identical radii ratios. Because of the tight conditions of installation, it was sometimes necessary to make compromises in arranging the wall pressure measuring systems - ③ ④ ⑤ ⑥ - so that the valid value in each respective reference plane is found by interpolating measured values which are determined in the immediately adjacent measuring points. /80

The test program for determining the nonsteady flow field behind the impeller outlet altogether include 11 operational levels at rotation speeds between 10,000 and 18,000 rpm. These are marked separately in the compressor performance graph, Fig. 4.9. The corresponding quiescent mach numbers of the absolute velocity at the outlet lie between approximately  $M_{t,c3} = 0.4-1.0$ . For the 10,000 and /81

14,000 rpm rotation speed characteristic curves the mass flow is varied in the 3 operating points from the stop limit up to the vicinity of the pump limit. By this, it is possible to study, within wide limits, influences if the Mach number and the blade channel load on the flow fields in the diffuser inlet.

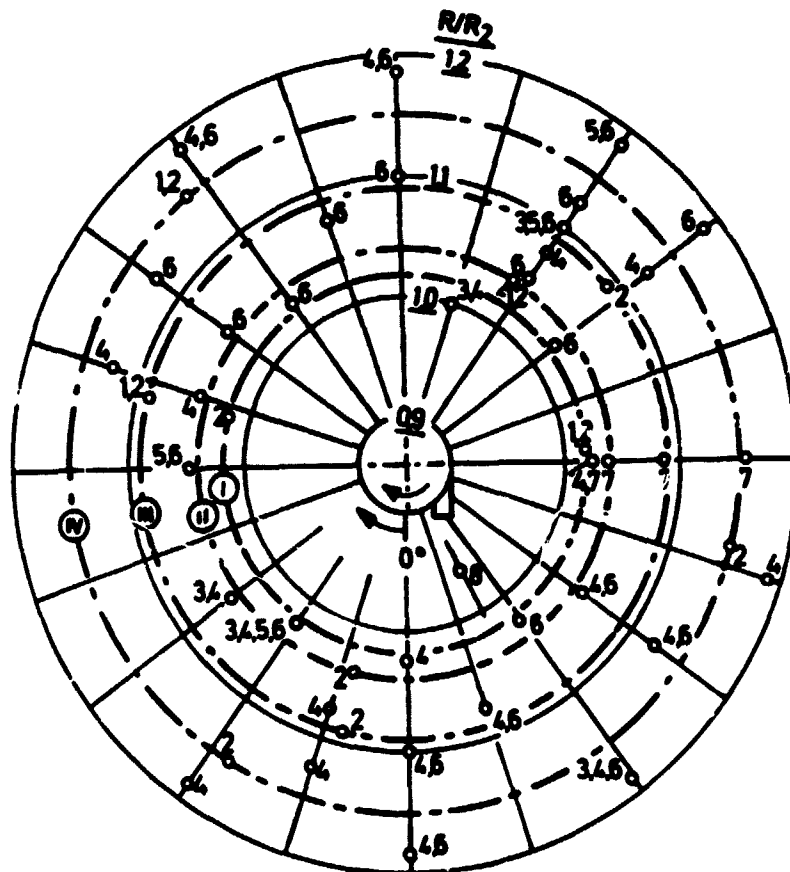


Fig. 5.4. Overall view of the measuring points in the diffuser inlet region with the measuring surfaces and reference surfaces for the non-steady flow analysis in the following  $R/R_2$  radii ratios: I = 1.017, II = 1.039, III = 1.089, IV = 1.151. Circumferential spacing:  $360^\circ/z = 18^\circ$ .  
 Measuring systems: 1 = dynamic total pressure; 2 = time-averaged total pressure; 3 = dynamic pressure, front wall; 4 = time-averaged pressure, front wall; 5 = dynamic pressure, rear wall; 6 = time-averaged pressure, rear wall; 7 = non-steady flow direction; 8 = impeller blade clearance.

In order to determine the flow immediately after the impeller outlet with as much detail as possible, the probes in measuring surface I are moved in 8 steps (step width  $z/b = 0.1$ ) between test point  $z/b = 0.1$  on the front wall of the diffuser and  $z/b = 0.9$  on the rear wall of the diffuser. In the remaining test surfaces II-IV the flow process is determined in the wide positions

$z/b = 0.1, 0.3, 0.5, 0.5, 0.7$  and  $0.9$ .

The entire test program consists of 4 individual measurement series which were performed one after the other:

- a) performance graph measurement, to determine the stage characteristics and the mean total temperatures behind the impeller outlet;
- b) determination of the correct, mean pressure value over time in the diffuser inlet region with the aid of special pneumatic or hydraulic pressure measuring systems;
- c) measurement of the dynamic wall pressure and total pressure curves with miniature semiconductor transducers: and
- d) determination of the direction distribution of the absolute velocity vector in the region of the outlet flow of a blade channel.

This procedure presupposes the setting of operating points which can be accurately reproduced. In so doing, besides the reduced rotation speed and reduced mass flow, which are continuously checked during the experiments and adjusted to the desired values, in addition all the other variables are uniformly related to the standard state in the compressor inlet (total intake pressure  $p_{t0,N} = 1.0133$  bar, total intake temperature  $T_{t0,N} = 288.1$  K).

In order to obtain information on the flow field behind the impeller outlet with as much general validity as possible, the nonsteady measuring systems are triggered with the blade frequency. By including the sampling signal processing, one thus practically obtains one nonsteady flow curve, statistically averaged over all of the impeller blade channels. This characterizes the outlet flow behind any desired blade channel of the centrifugal impeller. /82

#### 5.2 Determination of Constant Variables over Time

Mean values for total temperature, as well as total pressure and wall pressure, are necessary for the exact mathematical determination of the nonsteady flow field behind the impeller outlet.

The mass averaged total temperature is determined from the measurements to define the compressor performance graph in the radii ratio  $R/R_2 = 1.687$ , because -- as explained in Appendix III -- total temperature probes which are installed immediately behind the impeller outlet in the region of very strongly disturbed flow show considerable deviations from the

mass average total temperature.

The mean total pressure values, correct with respect to time and measured with the oil-filled capillary probes, are given by the summation of the excess pressure reading of the individual pressure transducers connected to each probe and calibrated with the barometric reading.

To compensate for the remaining, small circumferential dysymmetries -- in spite of the throttle ring -- a total pressure isobar distribution in the range  $1.0 < R/R_2 < 1.2$  is plotted for each measuring width position  $z/b$ , and from this a total pressure profile over the diffuser width is determined by arithmetical circumferential averaging for the measuring surface radii ratios I-IV.

In a similar way, the wall pressures measured with the pneumatic systems are averaged over the circumference and the reference values on the front wall and rear wall in the measuring surfaces I-IV are interpolated from the curve of the increase in wall pressure in the radial direction.

In each case the correction of the pressure reading for the pneumatic system with respect to nonsteady effects was carried out according to the method described in [3.5, p. 67 f]. It turns out, however, that because of the relatively small wall pressure fluctuations behind the impeller outlet, the reading for the pneumatic systems deviates less than 0.15% from the correct mean wall pressure value with respect to time.

### 5.3 Determination of Nonsteady Variables

For accurate reconstruction of the disturbed flow field in the diffuser inlet region the various nonsteady data on wall pressures and total pressures and on the distribution of pressure fluctuations and flow direction must first of all be classified with respect to one another and to the impeller over time. Furthermore, restricting the evaluation of the data and flow analysis to the characteristic outlet flow of a blade channel requires that the location and shape of the blade wake be determined relative to the impeller. This implies, as indicated, in principle, in Fig. 5.3, the determination of the wake shift  $\theta_N$  in the individual measuring surfaces I-IV and over the diffuser width.

The mutual coordination of the test signals with respect to time is assured by uniform triggering with the blade frequency.

The determination of the blade wakes over the diffuser width is explained, in principle, by Fig. 5.5. The data used here are the sampling signal plots of the nonsteady wall pressure curves and total pressure curves, and the corresponding fluctuation factors.

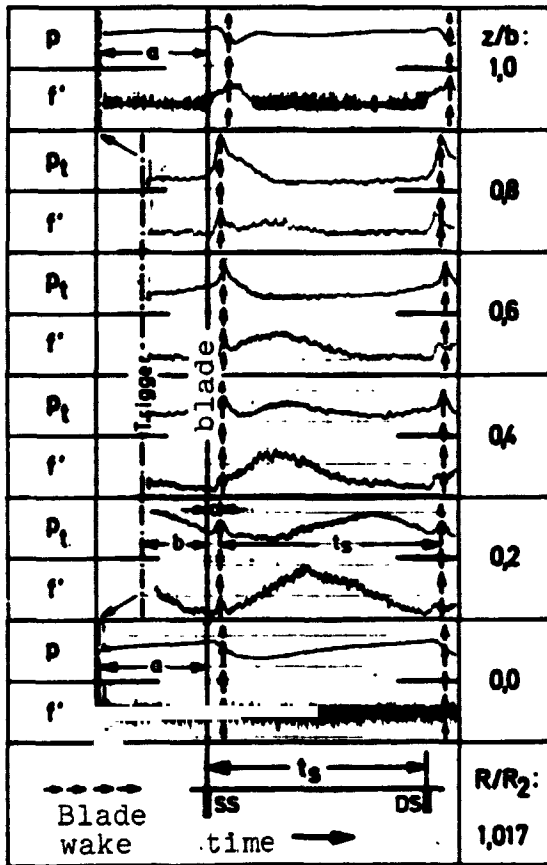


Fig. 5.5 Sampling signal recordings of the curves for wall pressure  $p$ , total pressure  $p_t$  and the corresponding fluctuation intensity  $f'$  for determining the blade wakes over the diffuser width, operating point  $n/\sqrt{\theta_0} = 10,000$  rpm,  $\dot{m}\sqrt{\theta_0}/\delta_0 = 3.81$  kg/s (different ordinate scale for wall pressures and total pressures).

increase in absolute velocity  $c$  on the order of  $c \geq u$ , and thus with a comparatively small variation in static pressure there is an increase in total pressure. This interpretation is supported by the curve for total pressure fluctuation  $f'$  which, after the relative calm curve in the region of the pressure side of the

Starting from the known trigger position (start of the sampling process), first of all the position with respect to time of the outlet edge of the blade is determined by simple geometric coordination of trigger points and test points. For example, in the wall pressure curves ( $z/b = 0$  and  $z/b = 1$ ) the quantity  $a$  corresponds exactly to  $t_s/2$ , because in this case the blade clearance transducer used as the trigger installed at the impeller outlet is shifted exactly 1/2 of a blade spacing with respect to the spacing network for the measuring points (see Fig. 5.4, position 8). With the total pressure curves, it logically holds that  $b = t_s/2 - \theta_s$  because -- as Fig. 5.3 shows -- the blade passes the probe inlet opening earlier by a time component of  $\theta_s$ .<sup>1</sup>

/84

In the immediate vicinity of the impeller -- Fig. 5.5 shows the ratios in the radii relationship  $R/R_2 = 1.017$  -- the blade wakes are visible as pronounced total pressure peaks. Assuming a dip in relative velocity and taking as a basis the secondary flow curve in this region which is explained later on, it follows from the velocity vector diagram -- Fig. 5.2 -- that there is an

/85

1. In addition, deviating from the simplified graph shown here, the small twist of the blade over the diffuser width and with respect to the trigger position is taken into consideration in the evaluation.

blade, in each case here, clearly shows an initial increase in the fluctuation intensity.

In the wall pressure curves the sharp drop in pressure seen in the impeller region during the transition from the pressure side to the suction side is also still visible at a certain distance behind the impeller, so that here the blade wake is set in the middle of the pressure side. The time component  $c$  thus determined corresponds to the blade wake shift  $\theta_N$  in the measuring surface in question. This is shown in Fig. 5.3.

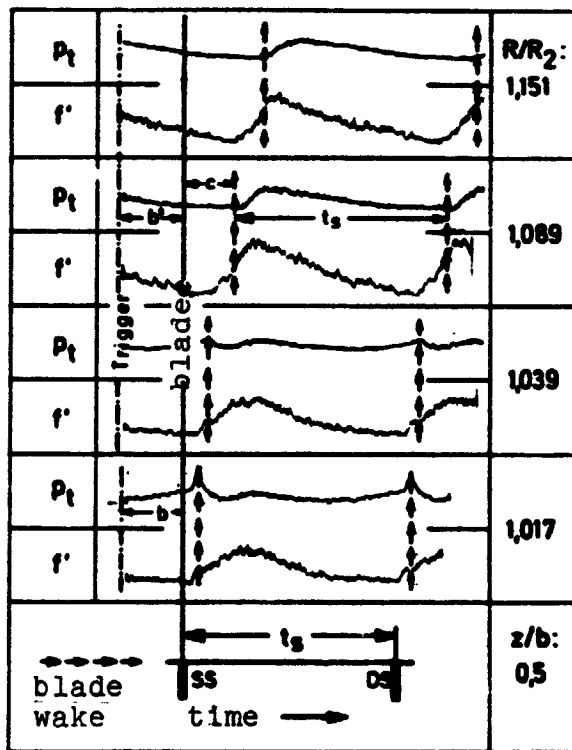


Fig. 5.6. Example for determining the blade wakes in the diffuser inlet region, same operational data as in Fig. 5.5,  $b' \neq b$  since  $\alpha_{s,I} \neq \alpha_{s,II-IV}$  (cf. Fig. 5.6).

Up to a radii ratio of  $R/R_2 = 1.039$  the dips in the blade wakes can be detected in the form of local total pressure peaks. For larger radii ratios, in which the wake dips are obviously largely mixed, it is more difficult to exactly determine the wake shift. A certain approximation is first of all obtained by extrapolating the blade wake in the form of a logarithmic spiral over the known reference points in  $R/R_2 = 1.0, 1.017$  and  $1.039$ . From the qualitative fluctuation curves in  $R/R_2 = 1.017$  and  $1.039$  one sees that directly behind the impeller outlet the pressure fluctuation intensity in the region of the suction side clearly exceeds the values on the pressure side. Starting from the notion that the flow is mixed with increasing distance from the impeller outlet and that by means of turbulent exchange the increased flow fluctuation also extends to the flow region on the pressure side, the blade wake separating line is placed in the region of increasing pressure fluctuation

intensity. By the simultaneous evaluation of several measurements over the diffuser width in a measuring surface, the data on the shape and path of the blade wake in the diffuser inlet region take on additional certainty. As an example of an evaluation performed in this way, Fig. 8.1 shows the three-dimensional path of the interface between the outlet flow of two adjacent blade channels.

After the position of the blade length in the sampling analog recording of the wall pressure and total pressure curves is determined, these points are also determined in the digitalized signal curves. The intermediate curve path, which corresponds to a channel spacing of  $c_s$ , is described by approximately 250 values of the pressure transducer output voltage.

In an "IDA" computer program for nonsteady data evaluation (cf. [4.2]) the integral mean voltage value is determined over  $t_s$ , set equal to the correct mean pressure value over time in the corresponding measurement point. Based on this, with the aid of the known pressure transducer calibration factors, the exact nonsteady absolute pressure flow is reconstructed. Then the pressure curves are standardized by means of a SPLINE interpolation program to exactly 101 values per channel division (interval in the circumferential direction  $\Delta y/t = 0.01$ ) and these are made dimensionless with the corresponding mean pressure value directly in front of the impeller inlet. Assuming a linear static pressure curve over the diffuser width, finally the static pressure curve is determined from the wall pressures for all  $z/b$  positions, in which directly measured total pressure curves exist, by interpolating between corresponding  $y/t$  positions on the front and rear wall of the diffuser. /87

In the same positions over the width of the diffuser measurements are also made to determine the absolute flow direction. The measuring technique and the evaluation of the data have already been discussed in detail in Section 3.4.2 with reference to Figure 3.15. For each probe position  $z/b$ , the exact position of 5-8 pre-selected probe setting angles within a wake channel spacing is determined. These measurements are evaluated in the form of an isocline graph (cf., for example, Fig. 6.5). From this then is obtained the direction input data for the IDA program by interpolation for each  $z/b$  position at 11 equidistant reference points ( $\Delta y/t = 0.1$ ).

With the aid of the SPLINE interpolation program already mentioned, intermediate values in an interval of  $\Delta y/t = 0.1$  are calculated, so that in each of the 9 (or 5) x 100 points of the  $z,y$  screen (in measuring surfaces I, or II-IV) data is available on the local total pressure  $p_t(y,z)$ , the static pressure  $p(y,z)$  and the absolute flow direction  $\alpha(y,z)$  to describe the flow field behind the outlet of an impeller blade channel.

In addition, as another nonsteady variable, the distribution of the relative fluctuation factor

$$f = \sqrt{(p_t' - \bar{p}_t)^2 / \bar{p}_t} \quad /88$$

in the region of a blade spacing can be calculated from the



sampling analog recordings of the total pressure fluctuation intensity  $f'$  (cf. Fig. 3.18) and from the average nonsteady total pressure curve.

#### 5.4 System of Equations for Calculating further Nonsteady Flow Variables

In the "IDA" evaluation program a number of further flow variables was calculated from the distributions of the directly measured nonsteady flow variables  $p_t(y,z)$ ,  $p(y,z)$  and  $\alpha(y,z)$ . The exact determination of these variables for the outlet flow region of a blade channel was described in the preceding section. By calculating these further variables, it is possible to give a detailed description and make a detailed study of the disturbed flow field behind the impeller outlet in the absolute system and in the relative system.

Additional input data include the following:  
with respect to the standard state in the compressor:

- total intake pressure  $p_{t0,N} = 1.0133$  bar,
- total intake temperature  $T_{t0,N} = 288.1$  K,

relative operational data:

- corrected rotation speed  $n_{red}$ ,
- corrected mass flow from Venturi tube measurements  $\dot{m}_{VENT}$ ,
- mass averaged total temperature at the diffuser outlet  $T_{t4}$ ,

geometric data, such as

- impeller outside diameter  $D_2$
- diffuser width at the impeller outlet  $b_2$ ,
- the measuring surface radii ratio  $R/R_2$ .

The following variables are also included for calculating the thermodynamic state in which -- as usual -- the test air is regarded as an ideal gas:

- the gas constant  $R$ ,

---

1. The position subscript is based on the data in Fig. 4.2; the subscript t means "total state."

- the specific heat at constant pressure  $c_p$ , which is used as a mean value for the range of temperature increase under consideration and
- the isentropic exponent  $\kappa$ , which in each case fulfills the following condition:

$$\kappa = c_p / (c_p - R). \quad (5.1)$$

The following calculations were made: the circumferential velocity at the impeller outlet:

$$u_2 = D_2 \cdot \pi \cdot n_{red}, \quad (5.2)$$

with which all velocities were made dimensionless in the presentation of the results; and the circumferential velocity at the measuring point in question in the diffuser inlet region:

$$u_3 = u_2 \cdot R/R_2. \quad (5.3)$$

The following equations are valid in each measuring surface behind the impeller outlet for any scanning element within the spacing of one flow channel. From the distributions of the static pressure and of the total pressure the local quiescent mach number of the absolute velocity is determined:

$$M_{t,c_3}^2(y,z) = \frac{2}{\kappa - 1} \{1 - [p_3(y,z)/p_{t3}(y,z)]^{(\kappa-1)/\kappa}\}. \quad (5.4)$$

In the following iteration loop, which is run through 5 times in the evaluation program, the quiescent velocity of sound is first of all determined from the mass average total temperature  $T_{t4}$  -- in the following passes determined from the local value  $T_{t3}$ . The connection equations serve to determine the absolute velocity  $c_3$ , its circumferential component  $u_3$  and -- at the end of the iterative calculation -- the total temperature  $T_{t3}$

$$a_{t3}(y,z) = [\kappa \cdot R \cdot T_{t3}(y,z)]^{1/2}; \bar{a}_{t3} = (\kappa \cdot R \cdot \bar{T}_{t4})^{1/2}; \quad (5.5)$$

$$c_3(y,z) = a_{t3}(y,z) \cdot M_{t,c_3}(y,z); \quad (5.6)$$

$$c_{u3}(y,z) = c_3(y,z) \cdot \cos \alpha_3(y,z); \quad (5.7)$$

$$T_{t3}(y,z) = T_{t0,N} + u_3 \cdot c_{u3}(y,z)/c_p. \quad (5.8)$$

In this process, Eq. (5.8) corresponds to the well known Euler moment equation for non-twisting flow to the impeller, in which the component of the rise in total pressure caused by internal disc friction and turbulent exchange movements (back flow) at the impeller inlet and outlet are ignored. This problem is discussed in detail in section 5.6 within the context of error estimation.

The following equations for calculating the radial component of the absolute velocity  $c_{r3}$ , the relative velocity  $w_3$ , its circumferential component  $w_{u3}$  and the relative flow angle  $\beta_3$  result from the velocity vector diagram (cf. Fig. 5.2):

$$c_{r3}(y,z) = c_3(y,z) \cdot \sin \alpha_3(y,z), \quad (5.9)$$

$$w_{u3}(y,z) = u_3 - c_{u3}(y,z), \quad (5.10)$$

$$w_3(y,z) = [c_{r3}^2(y,z) + w_{u3}^2(y,z)]^{1/2}, \quad (5.11)$$

$$\beta_3(y,z) = \arccos[w_{u3}(y,z)/w_3(y,z)]. \quad (5.12)$$

Finally, the static temperature  $T_3$ , speed of sound  $a_3$ , relative mach number  $M_{w3}$ , density  $\rho_3$ , static enthalpy  $h_3$  and entropy  $s_3$  follow from the equations given below:

$$T_3(y,z) = T_{t3}(y,z) - c_3^2(y,z)/(2c_p), \quad (5.13)$$

$$a_3(y,z) = [\kappa \cdot R \cdot T_3(y,z)]^{1/2}, \quad (5.14)$$

$$M_{w3}(y,z) = w_3(y,z)/a_3(y,z), \quad (5.15)$$

$$\rho_3(y,z) = p_3(y,z)/[R \cdot T_3(y,z)], \quad (5.16)$$

$$h_3(y,z) = c_p \cdot T_3(y,z), \quad (5.17)$$

$$s_3(y,z) = c_p \cdot \ln[T_3(y,z)/T_{t0,N}] - R \cdot \ln[p_3(y,z)/p_{t0,N}], \quad (5.18)$$

whereby in the last equation  $s$  is arbitrarily set equal to zero for the inlet standard state:  $p_{t0,N}$ ,  $T_{t0,N}$ .

In part using indirect methods, thus we have developed all of the variables for a detailed analysis of impeller outlet flow in the absolute and relative system. For an integral check of the accuracy of the measurements and of the evaluation a mass balance  $\dot{m}_{IDA}$  is setup over the impeller outlet cross-section  $A_3$ :

$$\dot{m}_{IDA} = A_3 \int_{y/t=0}^1 \left[ \int_{z/b=0}^1 \rho_3(y,z) \cdot c_{r3}(y,z) \cdot d(z/b) \right] d(y/t), \quad (5.19)$$

whereby because of the diffuser, which is equal in area, the following equation applies:

$$A_3 = A_2 = D_2 \cdot \pi \cdot b_2 \int_{y/t=0}^1 \left[ \int_{z/b=0}^1 d(z/b) \right] d(y/t). \quad (5.20) \quad \underline{/92}$$

As the error in this mass flow determination, the relative deviation with respect to the Venturi tube measurement is determined. (cf. Section 5.6):

$$f_m = (\dot{m}_{IDA} - \dot{m}_{VENT})/\dot{m}_{VENT} \quad (5.21)$$

In order to ensure the coherence of the experimental data the measured flow angle corresponding to the mass flow difference are corrected and the evaluation is once again repeated between equation (5.5) and (5.19) with the flow angle  $\alpha_{3,korr}$ :

$$\alpha_{3,korr}(y,z) = \arcsin[\sin \alpha_3(y,z)/(1 + f_m)] . \quad (5.22)$$

With this correction, all of the measurement errors are unilaterally charged to the nonsteady direction measurement. Since this is in fact the most uncertain, and since  $f_m$  is generally smaller than 0.05, this simplified procedure seems allowable here.

### 5.5 System of Equations for Calculating the Characteristic Mean Value

The variables already defined above and the distribution calculated in the program for instantaneous data evaluation (IDA) form the input data for an extensive integration sub-program (INTIDA) (cf. [4.2]). In the context of this study, the calculation equations for important, characteristic mean values to determine the condition of flow at the impeller input and output are listed here.

When using the following geometric data

- $D_0$  - intake line diameter directly in front of the impeller input and
- $D_{1a}, D_{1i}$  - outside and inside impeller inlet diameters respectively

the following equations are valid at the impeller input for -static temperature

/93

$$\bar{T}_0 = T_{t0,N} (\bar{p}_0/p_{t0,N})^{(\kappa-1)/\kappa} , \quad (5.23)$$

- speed of sound

$$\bar{a}_0 = (\kappa R \bar{T}_0)^{1/2} , \quad (5.24)$$

- density

$$\bar{\rho}_0 = \bar{p}_0/(R \bar{T}_0) , \quad (5.25)$$

- inlet cross-section

$$A_0 = \pi (D_0^2 - D_{1i}^2)/4 , \quad (5.26)$$

- average absolute velocity (with non-twisting oncoming flow)

$$\bar{c}_0 = \dot{m}_{VENT}/(\bar{\rho}_0 A_0) , \quad (5.27)$$

and especially at the outer section for

- the circumferential velocity

$$u_{1a} = D_{1a} \pi n_{red} \quad , \quad (5.28)$$

- or the relative velocity

$$\bar{w}_{1a} = (\bar{c}_0^2 + u_{1a}^2)^{1/2} \quad . \quad (5.29)$$

If, in Eq. (5.28) one substitutes the following diameter, which halves the intake cross-section, in place of  $D_{1a}$ :

$$\bar{D}_1 = [(D_0^2 + D_{1i}^2)/2]^{1/2} \quad , \quad (5.30)$$

then from this follows  $\bar{u}_1$ , thus from Eq. (5.29)  $\bar{w}_1$ , and for the average, relative angle of the oncoming flow (measured against the circumferential direction): /94

$$\bar{\beta}_1 = \text{arc tg}(\bar{c}_0/\bar{u}_1) \quad . \quad (5.31)$$

As mean values for characterizing the impeller inlet state, the following values are determined:

- the relative mach number in the outer section

$$M_{w1,a} = \bar{w}_{1a}/\bar{a}_0 \quad , \quad (5.32)$$

and in the diameter  $\bar{D}_1$

- the average relative mach number

$$M_{w1} = \bar{w}_1/\bar{a}_0 \quad , \quad (5.33)$$

- or the incidence of the oncoming flow

$$\Delta\beta_1 = \bar{\beta}_{1, \text{MEAN CAMBER}} - \bar{\beta}_1 \quad . \quad (5.34)$$

In the various measurement radii ratios of the diffuser inlet region the relevant thermodynamic mean values of state for the nonsteady flow are again -- as with the performance graph evaluation -- derived from the mean values of the extensive variables of state -- static enthalpy  $h$  and entropy  $s$  -- (cf. [4.4]).

The following equations apply

$$\bar{h}_3 = \left( \int_{A_3} \rho_3 c_{r3} h_3 dA_3 \right) / \dot{m}_{IDA} \quad , \quad (5.35)$$

$$\bar{s}_3 = \left( \int_{A_3} \rho_3 c_{r3} s_3 dA_3 \right) / \dot{m}_{IDA} \quad , \quad (5.36)$$

$$\bar{T}_3 = \bar{h}_3 / c_p \quad , \quad (5.37)$$

$$\bar{p}_{30} = \bar{p}_3 / p_{t0,N} = (\bar{T}_3 / T_{t0,N})^{\kappa / (\kappa - 1)} \cdot e^{-\bar{s}_3 / R} \quad , \quad (5.38) \quad /95$$

$$\bar{p}_3 = \bar{p}_{30} \cdot p_{t0,N} / (R \cdot \bar{T}_3) \quad , \quad (5.39)$$

$$\bar{T}_{t3} = \left( \int_{A_3} \rho_3 \cdot c_{r3} \cdot T_{t3} \cdot dA_3 \right) / \dot{m}_{IDA} \quad ; \quad (5.40)$$

Thus for the mean total temperature ratio we finally obtain the following:

$$\bar{T}_{t,30} = \bar{p}_{30} (\bar{T}_{t3} / \bar{T}_3)^{\kappa / (\kappa - 1)} \quad (5.41)$$

Furthermore, mean velocity values can be determined from the experimental data. The mean values to be inserted into the continuity equation carry the subscript k and those to be inserted in the energy equation carry the subscript e. Mean values which derive from the impulse flow are of special importance for the formation of the mean velocity vector diagram (cf. Fig. 5.2). They do not carry any special subscript.

The following equations hold:

$$\bar{v}_{r3k} = \left( \int_{A_3} \rho_3 \cdot c_{r3} \cdot dA_3 \right) / (A_3 \cdot \bar{p}_3) \quad , \quad (5.42)$$

$$\bar{v}_{r3} = \left( \int_{A_3} \rho_3 \cdot c_{r3}^2 \cdot dA_3 \right) / \dot{m}_{IDA} \quad , \quad (5.43)$$

$$\bar{c}_{u3} = \left( \int_{A_3} \rho_3 \cdot c_{r3} \cdot c_{u3} \cdot dA_3 \right) / \dot{m}_{IDA} \quad (5.44)$$

$$\bar{w}_{u3} = \left( \int_{A_3} \rho_3 \cdot c_{r3} \cdot w_{u3} \cdot dA_3 \right) / \dot{m}_{IDA} \quad (5.45)$$

and for the mach numbers in the absolute system and relative system the following equations hold using Eqs. (5.4), (5.5), (5.14) and (5.15):

$$\bar{M}_{t,c3} = \left( \int_{A_3} \rho_3 \cdot c_{r3} \cdot M_{t,c3} \cdot dA_3 \right) / \dot{m}_{IDA} \quad (5.46) \quad \underline{/96}$$

$$\bar{M}_{w3} = \left( \int_{A_3} \rho_3 \cdot c_{r3} \cdot M_{w3} \cdot dA_3 \right) / \dot{m}_{IDA} \quad (5.47)$$

$$\bar{c}_3^2 = \bar{c}_{r3}^2 + \bar{c}_{u3}^2 \quad (5.48)$$

$$\bar{w}_3^2 = \bar{c}_{r3}^2 + \bar{w}_{u3}^2 \quad (5.49)$$

$$\bar{c}_{3e}^2 = \left( \int_{A_3} \rho_3 \cdot c_{r3} \cdot c_3^2 \cdot dA_3 \right) / \dot{m}_{IDA} \quad (5.50)$$

$$\bar{w}_{3e}^2 = \left( \int_{A_3} \rho_3 \cdot c_{r3} \cdot w_3^2 \cdot dA_3 \right) / \dot{m}_{IDA} \quad (5.51)$$

and for the mean flow direction in the absolute system and relative system the following equations follow:

$$\bar{\alpha}_3 = \arcsin(\bar{c}_{r3} / \bar{c}_3) \quad (5.52)$$

$$\bar{\beta}_3 = \arcsin(\bar{c}_{r3} / \bar{w}_3) \quad (5.53)$$

In particular, from the mean velocity values the following equations are formed:

---

1. Since the individual measuring surfaces lie on constant radii ratios, the averaging over the angular momentum  $R \cdot c_u$  is simplified in accordance with Eq. (5.44).



- the flow through coefficient for indicating the operational point

$$\bar{\phi}_3 = \bar{c}_{r3k} / u_2 \quad , \quad (5.54)$$

- the mach number diffusion ratio for characterizing the retardation of flow in the impeller

$$MR = \bar{M}_{w1} / \bar{M}_{w3} \quad , \quad (5.55)$$

- or the mach number diffusion ratio for the jet region in the flow pipe along the outer contour of the impeller, which is especially threatened by flow separation

$$MR_S = \bar{M}_{w1,a} / \bar{M}_{w3,S} \quad , \quad (5.56)$$

- the most important form factors for describing the flow distribution at the impeller outlet (cf. [4.4])

$$e_{k3}(c) = e_{k3}(w) = 1 - \bar{c}_{r3k} / \bar{c}_{r3} \quad , \quad (5.57)$$

$$e_{e3}(c) = \bar{c}_{3e} / \bar{c}_3 - 1 \quad , \quad (5.58) \quad /97$$

$$e_{e3}(w) = \bar{w}_{3e} / \bar{w}_3 - 1 \quad . \quad (5.59)$$

Finally, in order to set off the healthy region of the jet (subscript S) from the wake region (subscript T) within the disturbed flow distribution the following relationships were determined:

$$e_{r3,T}(y,z) < \bar{c}_{r3k} < e_{r3,S}(y,z) \quad (5.60)$$

and Eqs. (5.19), (5.20) and (5.35)-(5.54) -- maintaining this relationship -- were recalculated separately for the jet region and the wake region.

To characterize the typical jet/wake velocity distribution at the outlet of the centrifugal compressor impeller and the maxing of the disturbance in the diffuser inlet region, the following equations were derived:

- the relative area component of the wake from Eq. (5.20)

$$\epsilon = \dot{A}_{3,T} / A_3 \quad , \quad (5.61)$$

- the relative mass flow component of the wake from Eq. (5.19)

$$v_T = \dot{m}_{IDA,T} / \dot{m}_{IDA} \quad , \quad (5.62)$$

- the relative velocity ratio from Eq. (5.49)

$$\gamma = \bar{w}_{3,T} / \bar{w}_{3,S} \quad (5.63)$$

- and the interference parameter

$$\delta = \epsilon (1 - \gamma) \quad . \quad (5.64)$$

In the efficiency definitions listed at the end it should /98  
be noted that for the total temperature, or the static temperature, the following equations were used, for reasons of coherence, in place of Eqs. (5.40) and (5.37) which were uniformly used in the system of equations setup so far:

$$\bar{T}_{t3}^* = \bar{T}_{t4}^* \quad , \quad (5.65)$$

$$\bar{T}_3^* = \bar{T}_{t3}^* - \bar{c}_{3e}^2 / (2c_p) \quad . \quad (5.66)$$

Thus -- as also shown by an estimate in Section 5.6 -- the effect of the internal disc friction and the turbulent exchange movements is largely taken into consideration in determining the efficiency. This effect was ignored in the basic equation (5.8) used to calculate the rise in total temperature.

The following equations apply for:

- the isentropic impeller efficiency

$$\eta_s^* = \Delta h_s^* / \Delta h^* = \quad (5.67)$$

$$= T_0 \left[ \left( \bar{M}_{30} \cdot P_{t0,N} / P_0 \right)^{(\kappa-1)/\kappa} - 1 \right] / (\bar{T}_3^* - T_0) \quad .$$

- the polytropic impeller efficiency

$$\eta_p^{**} = \left( \int_{P_0}^{P_3} v dp \right) / \Delta h^{**} = \quad (5.68)$$

$$= (1 - 1/\kappa) \cdot \ln(\bar{\Pi}_{30} \cdot P_{t0,N} / P_r) / \ln(\bar{T}_3 / \bar{T}_0) \quad .$$

- and the isentropic total efficiency

$$\eta_{t,s}^{**} = \Delta h_{t,s}^{**} / \Delta h_t^{**} = \quad (5.69)$$

$$= T_{t0,N} (\bar{\Pi}_{t,30}^{(\kappa-1)/\kappa} - 1) / (\bar{T}_{t4} - T_{t0,N}) \quad .$$

#### 5.6 Accuracy of the Selected Measuring Technique and Evaluation Technique

/99

In estimating the error, one basically distinguishes the separate errors in the following areas:

- a) channel geometry, arrangement of measuring points and probe adjustment;
- b) calibration of the measuring system;
- c) experimental procedure and
- d) data reduction and test evaluation.

The adjustment accuracy of the probe adjusting devices is around  $\pm 0.2$  mm for the adjustment along the long axis and  $\pm 0.2^\circ$  for the angular adjustment. Thus possible errors in the adjustment of the probes, just like variation in the geometry of the flow channels due to manufacturing and mounting inaccuracies, are on an order of magnitude which can be ignored in comparison with other measurement uncertainties.

From the discussion of the measuring program (cf. Section 5.1) it becomes clear that the ability to exactly reproduce the operating level takes on special importance with respect to the detailed reconstruction of the flow based on various individual measurements. The uncertainty in determining the rotation speed is less than  $\pm 0.03\%$ , in determining the mass flow with a Venturi tube installed in the standard manner it is less than approximately  $\pm 1\%$ . In this latter case, only the components due to accidental errors have any effect with respect to the reproducibility of the adjustment.

In estimating the error in the flow measurements behind the impeller outlet, the usual statistical error analysis for multiple measurements at one test point cannot be used directly because of the unsteady measurement signal curves and the signal processing with the aid of the synchronized sampling technique.

Therefore, an integral measurement error is estimated for the individual measuring methods. This is based on the results of repeated calibrations and laboratory tests, as well as the reproducibility of the experimental results.

With this integral error information it is also attempted to take into consideration the uncertainties discussed in connection with Figs. 5.5 and 5.6 in the exact arrangement of the various nonsteady individual measurements uniformly distributed over the variables. In so doing, the measurement uncertainty increases for larger measurement radii ratios.

/100

In addition to this effect and the test errors caused by the temperature sensitivity of the semiconductor pressure transducers, the total pressure reading contains a certain error reading which arises from the secondary flow at the impeller outlet. The flow components in the axial z direction are measured over the total pressure probes, and in the evaluation they are added to the components in the r,y reference plane. For the error estimate it is assumed that the  $c_z$  velocity component (cf. Fig. 5.2) equals at most 20% of the absolute velocity c.

Finally, we must still discuss Eq. (5.8) based on the Euler equation of moments for calculating the distribution of total temperature behind the impeller outlet.

The general integral energy equation for the impeller runs as follows:

$$\bar{h}_{t3} - \bar{h}_{t0} = (\bar{h}_3 + \bar{c}_3^2/2) - (\bar{h}_0 + \bar{c}_0^2/2) = \bar{L}_F + \bar{q}, \quad (5.70)$$

wherein  $\bar{L}_F$  stands for the specific work done on the fluid and  $\bar{q}$  stands for the heat added.

This equation is valid only for appropriately formed integral mean values, but not along an individual flow line. In general, for the individual flow particle, the condition for Eq. (5.70):  $dL_R + dL_G = 0$ , with  $L_R$  = the drag work due to friction and  $L_G$  = the work of deformation, is not fulfilled. However, even for the mean value, the validity of this equation is not guaranteed under all circumstances, for the character of the flow can be so complex that no cross-sectional areas can be found within which no work is transferred due to frictional stresses (cf. [3.1], p. 75 f).

This restriction applies to a special extent to a boundary surface which is placed around the impeller circumference at the outlet of a highly loaded centrifugal impeller and which is mixed with flow fluctuations and back currents.

/101

These exchange processes, and also the usual friction of the impeller, produce in their totality a torque  $M_T$  with respect to the axis of rotation turning at an angular velocity of  $\omega$ . The energy equation for nontwisting flow striking the impeller runs as follows:

$$\bar{h}_{t3} - \bar{h}_{t0} = c_p (\bar{T}_{t3} - \bar{T}_{t0}) = u_3 c_{u3} + M_T \omega / \dot{m}. \quad (5.71)$$

With respect to what has been said above, Eq. (5.8), which is developed for an individual unit area at the impeller outlet, violates several of the limiting conditions mentioned. In using total temperatures, which have been calculated according to Eq. (5.8), static temperatures derived from them according to Eq. (5.13) and their integral mean values (Eq. (5.37) and Eq. (5.40)) care must be taken that in calculating these values the effects of impeller friction or, behind the impeller outlet, the effects of friction on the diffuser walls are not ignored.

The mean order of magnitude of this error is determined from the difference between the total temperature  $\bar{T}_{t4}$  measured far downstream in the diffuser and the total temperature  $\bar{T}_{t3}$  calculated from Eq. (5.40). In so doing, the maximum value for the range of error, again for the outer measuring radii ratio  $R/R_2$ , equals 1.151.

Table 5.1 lists the estimated, mean relative measurement errors for the individual variables. In addition, for a few of the flow parameters derived from these, a mean range of error was calculated using the Gaussian Law of Error Propagation (cf., for example, [5.1]).

Consideration of the errors shows that inaccuracies in the total temperature determination due to the use of the Euler equation of moments, Eq. (5.8) have only a relative small effect on the velocity evaluation. At the same time, this equation certainly produces the best possible approximation of the real total temperature distribution, as long as no possibility exists for direct measurement. Therefore, it seems justified to use Eq. (5.8) to determine the exact jet/wake velocity distribution at the impeller outlet. /102

In comparison with the pressure measurement, the relatively large uncertainty in the direction measurement was taken into account in estimating the relative range of error for this measuring method. As a result, we obtain the large upper error limits for the  $c_{r3}$  and  $w_3$  velocity components. However, it remains to be considered that, in measuring direction, random errors prevail due to the form of the individual measurement and evaluation (in contrast to the continuous recording of

TABLE 5.1 LIST OF RELATIVE ERRORS FOR A FEW NONSTEADY FLOW VARIABLES AT THE IMPELLER OUTLET

EXAMPLE:  $n = 14,000$  rpm,  $\dot{m} = 5.31$  kg/s,  $R/R_2 = 1.017$ .

	Relative error	Example
$p_3(y,z)$	$\pm 0,5 \dots 1$	1,48 bar
$p_{t3}(y,z)$	$\pm 0,5 \dots 1,5$	2,25 bar
$\alpha_3(y,z)$	$\pm 2 \dots 8$	25,3°
$T_{t3}(y,z)$	$\pm 0,5 \dots 1,5$	365 K Eq.(5.8)
	Sequential error	According to Eq.
$c_3(y,z)$	$\pm 1 \dots 3,5$	(5.6)
$c_{r3}(y,z)$	$\pm 3 \dots 11$	(5.9)
$w_3(y,z)$	$\pm 4 \dots 13$	(5.11)

pressure measurements). In forming integral mean values of the total flow, or of the jet-wake flow regions, these errors largely cancel each other out. /103

This also explains the good agreement of the mass balances from nonsteady measurements behind the impeller outlet and from Venturi tube measurements. For the relative variations in mass flows  $\dot{m}$  determined according to Eq. (5.21) we obtain values of 2% immediately behind the impeller outlet. In the extreme case, for  $R/R_2 = 1.151$ , these rose to about -7%. In this connection, the essential uncertainty consists in the consideration of the boundary layer portion on the difusser walls.

A qualitative impression of the accuracy of the selected measuring method and evaluation method is also given by a comparison with velocity measurements performed in the meantime with a dual-focus laser velocimeter (L2F method) after the

experimental portion of these investigations. For the same operating level, Fig. 6.13b (14), shows the velocity distribution  $c_m/u_2$  for an impeller blade channel as it was recorded with the L2F method directly at the outlet edge of the impeller. Fig. 6.8b shows the comparable velocity distribution  $c_{r3}/u_2$  in the radii ratio  $R/R_2 = 1.017$ . This was determined using the nonsteady probe measuring technique.

If one considers the small differences in the measuring position in the formation of the jet-wake distribution and the considerable difficulties involved in the measuring techniques -- above all in the region of the strongly fluctuating wake flow -- then the agreement of these results, which were obtained with basically different measuring systems, seems very satisfactory.

## 6. The Flow at the Outlet of the Centrifugal Compressor Impeller

The measuring and evaluation techniques discussed in the previous chapter setup for the first time the possibility of analyzing more exactly the complicated flow field at the outlet of highly-loaded centrifugal compressor impellers. In the following discussion of the results of these studies, we will first of all restrict ourselves to measuring plane and reference plane I in the radii ratio  $R/R_2 = 1.017$ , immediately behind the impeller outlet. In so doing, the results of direct measurements -- nonsteady wall pressure distributions, total pressure distributions and flow direction distributions -- and calculated flow distributions, which were determined on the basis of certain simplified assumptions, will be discussed separately from one another.

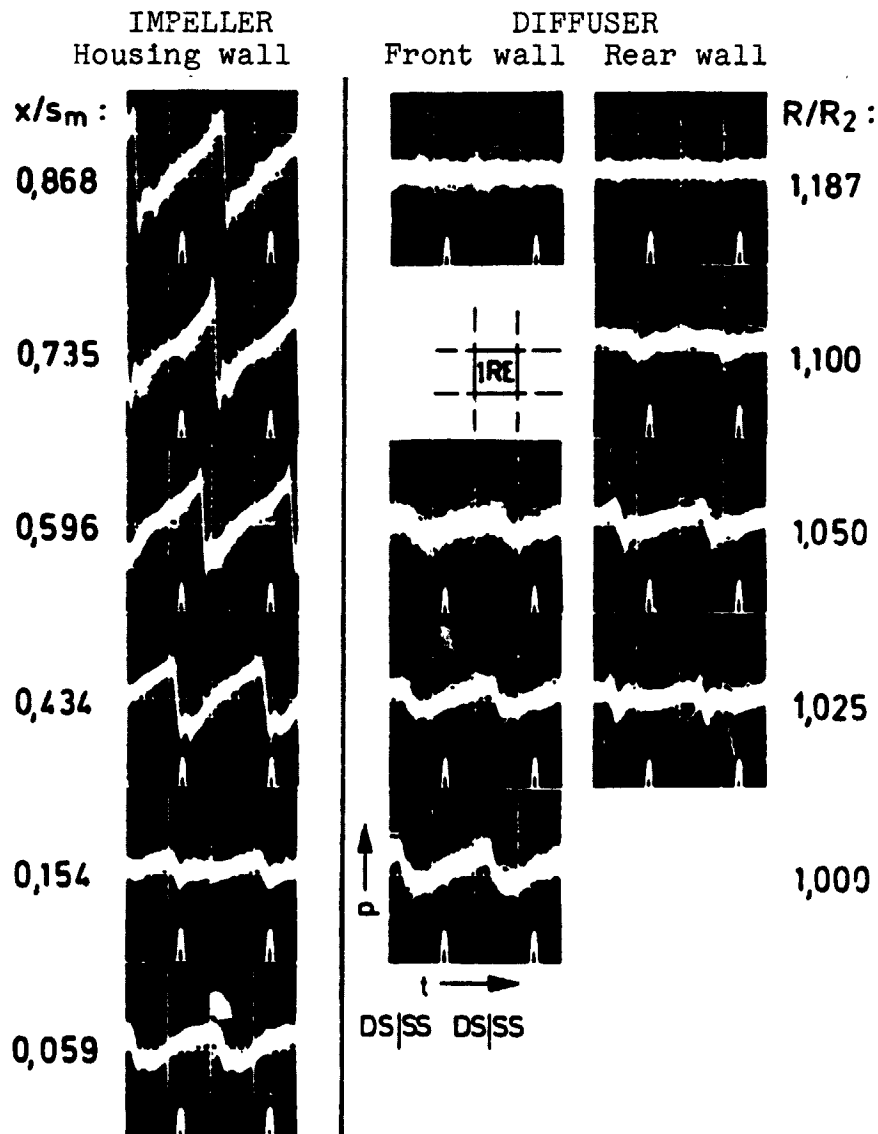
This flow analysis is interesting in two respects:

1. On the one hand, the disturbed flow condition being studied determines the initial conditions for the mixing and equalization processes occurring in the bladeless diffuser behind the impeller. These will be discussed in detail -- theoretically and experimentally -- in section 7 and 8 below.
2. On the other hand, these studies of nonsteady events in the transition region between the impeller and the diffuser permit important conclusions to be drawn as to the flow mechanisms in the impeller and -- in the context of a consideration of the losses involved -- to the aerodynamic-thermodynamic efficiency of the individual stage components.

## 6.1 Results of the Nonsteady Flow Measurements

### 6.1.1 Wall Pressure, Total Pressure and Distribution of Total Pressure Fluctuation

As a qualitative example of nonsteady pressure measurement with miniature semiconductor pressure transducer, Fig. 6.1 shows wall pressure curves along the housing wall in the impeller region and on the front wall and rear wall of the



/105

Fig. 6.1 Nonsteady wall pressure curve over approximately two blade divisions, measured on the housing wall in the impeller region and on the front and rear wall of the diffuser. Operating level:  $n/\sqrt{\theta_0} = 14,000$  rpm,  $m \sqrt{\theta_0}/\delta_0 = 5.31$  kg/s; Oscillograms: horizontal, 0.1 ms/RE (RE = scanning unit); vertical, 0.09-0.14 bar/RE.



bladeless diffuser behind the impeller. The measuring points in the impeller region are specified by the relative outer contour of the impeller in the meridian section  $x/s_m$  (cf. Fig. 4.2, impeller inlet:  $x/s_m = 0$ ), whereas in the diffuser, the radii ratio  $R/R_2$  is given. All of the oscillograms were recorded with the same sensitivity and in so doing the exposure time was so chosen that 30 signal uns were photographically superimposed. A blade clearance transducer at the impeller outlet was used to trigger and at the same time order the test signal exactly with respect to time (cf. section 5.3, (see Figs. 5.4 and 6.2). The signal peaks for this transducer are visible on the lower edge of the image for the individual oscillograms.

/106

For interpreting these experimental results it seems appropriate to introduce the nonsteady energy equation for the absolute flow which reads as follows for compressible, frictionless flow:

$$Dh_t/dt = 1/\rho \partial p/\partial t \quad (6.1)$$

i.e. the total change in total enthalpy  $h_t$  with respect to time is, under the conditions mentioned, directly proportional to the change with respect to time of the static pressure at a determined point in space.

In considering the results shown in Fig. 6.1, the following phenomena are conspicuous:

Not only is the absolute flow periodically nonsteady with the blade frequency -- as is to be expected with the transfer of energy to the flow medium on the basis of the nonsteady energy equation -- but also the relative velocity is subjected to irregular fluctuations which correspond to the width of the superimposed "pressure band."

The following possible reasons for this phenomenon may be mentioned:

- pulsations in the oncoming flow to the compressor;
- inspite of the throttle ring, residual circumferential asymmetries in the diffuser pressure field and
- disturbances which can be superimposed in the flow, for example by fluctuations of separation regions in the impeller.

A striking fact here is the increase in this signal fluctuation intensity behind the impeller outlet, above all in the region of the front wall of the diffuser where -- as will clearly be shown by the results discussed below -- the disturbed flow discharged from the impeller is especially pronounced.

This phenomenon in the static pressure curve illustrated the mixing losses coupled with the equalization processes of the disturbed jet-wake flow.

/107

The periodic wall pressure measurements observed in the impeller extend with increasing amplitude into the diffuser inlet region and are almost totally evened out only at  $R/R_2 \approx 1.2$ . For this region behind the impeller outlet it can be deduced from Eq. (6.1) that the zone of energy fluctuation extends as far as the region of nonsteady flow. Comparable to this, a reversible exchange of energy between the two partial flows is introduced into the two-dimensional theory of jet-wake mixing processes described in section 7. This flow mechanism is jointly responsible for the rapid -- in comparison with steady conditions -- mixing of the disturbed flow behind centrifugal impellers.

The nonsteady wall pressure curves shown in Fig. 6.1 were evaluated numerically in Fig. 6.2 for the flow region of an impeller blade channel. The isobar distribution of the static pressure ratio  $p/p_0$  shown in Fig. 6.2 is determined by interpolating between the individual measuring positions  $x/s_m$  on the housing wall in the impeller region and on the front wall of the diffuser which connects to it. In so doing, the static intake pressure  $p_0$  immediately in front of the impeller inlet was measured. In this graph,  $y$  corresponds to the circumferential radian measurement on the housing wall,  $x$  is the coordinate along the outer contour of the impeller in the meridian section, pressure side and suction side of the blades are, as usual, labelled DS and SS respectively, and also the positions of the blade clearance trigger and of measuring planes and reference planes I-IV in the diffuser inlet are given (see Fig. 5.3). The position of the boundary lines of the flow region for a blade channel on the front wall of the diffuser (relative to the impeller) were determined according to the method described in section 5.3.

From the isobar curve it can be deduced that the axial inlet region of the impeller up to  $x/s_m \approx 0.5$  is, depending on the layout, relatively less loaded, and the region of greatest addition of energy to the flow medium is concentrated in the final third of the blade channel. This fact, described by Eq. (6.1), is readily illustrated in Fig. 6.1 by the magnitude of the pressure gradient  $dp/dt$  at  $x/s_m = 0.735$  and  $0.868$ . Immediately behind the impeller outlet the sharp pressure gradient in the radial direction between  $R/R_2 = 1.0-1.05$  is especially noticeable. This expresses another effect of the jet-wake mixing processes in the diffuser inlet region which will be discussed in detail in Section 8.

/108

From studies of the impeller flow field with the laser velocimeter it is known that the flow in the preceding operating level at  $x/s_m = 0.55$  separates from the housing wall and a

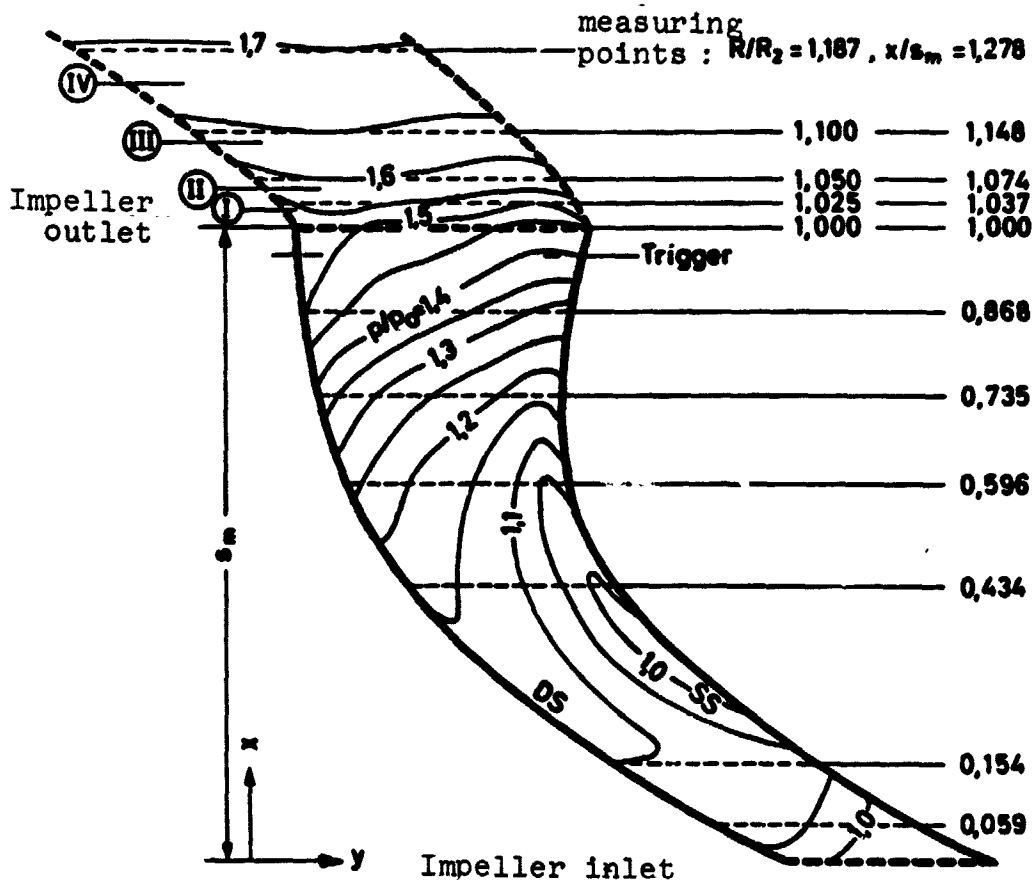


Fig. 6.2. Isobar distribution of the static pressure ratio  $p/p_0$  for the flow region of a blade channel, measured at the front wall of the housing. Operating level:  $n/\sqrt{\theta_0} = 14,000$  rpm,  $\dot{m} \sqrt{\theta_0}/\delta_0 = 5.31$  kg/s.

pronounced wake area is developed in the region of the housing wall and the suction side of the blades up to the impeller outlet (cf. Figs. 6.13a and 6.13b). This wake area is indicated in the wall pressure curves of Figs. 6.1 and 6.2 only by the tendency towards a smaller circumferential pressure gradient on suction side, however a clear separation of separated and non-separated flow -- based simply on the nonsteady wall pressure measurements -- is not possible. Other experimental wall pressure measurements at other operational levels, which provide information on blade channel load and the supply of energy to the flow medium, have been presented, for example, in reports [4.2] and [6.1].

/109

Typical examples of the nonsteady total pressure distribution immediately behind the impeller outlet are shown in Fig. 6.3 such as they turn out after passing through the sampling process

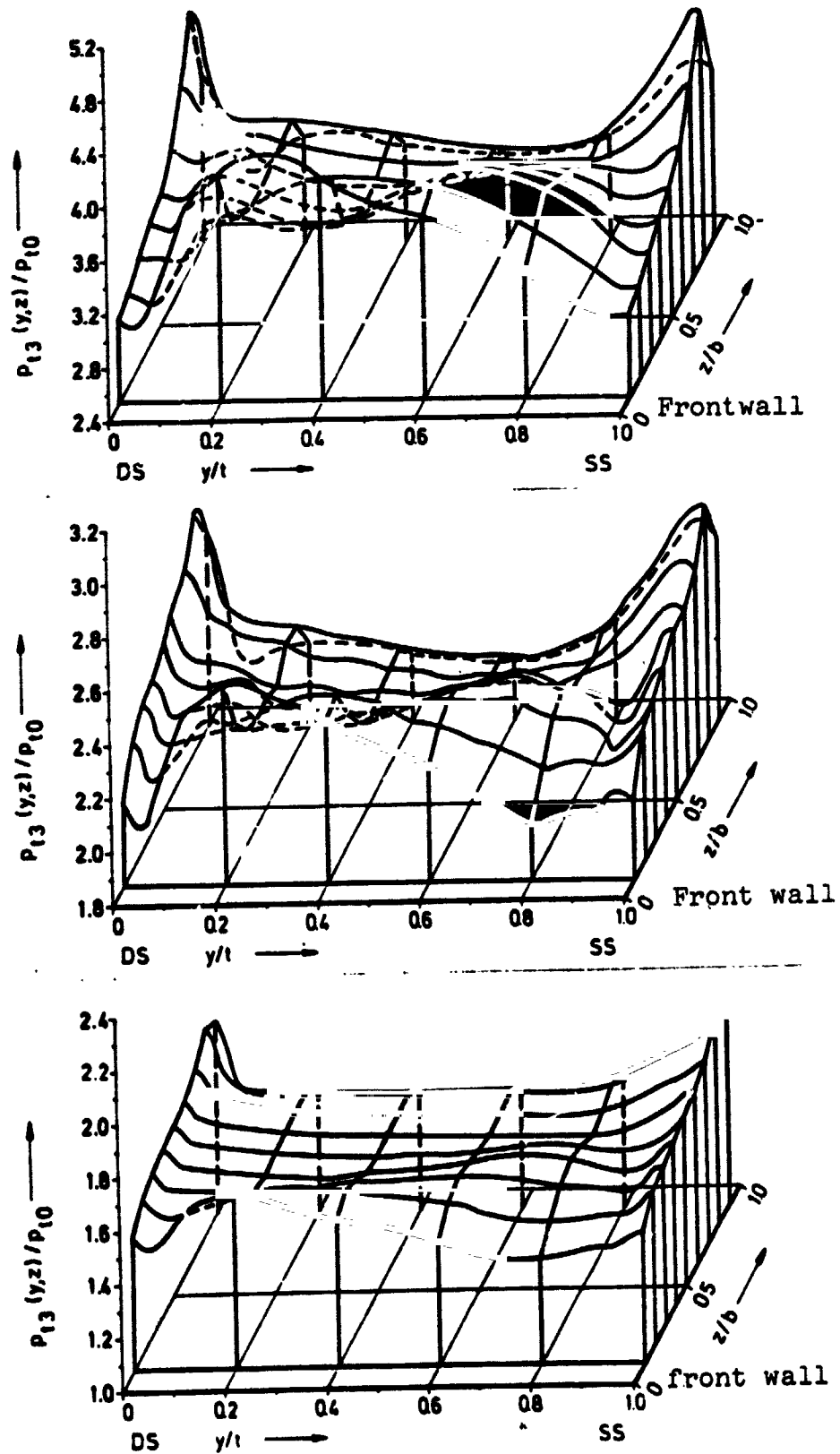


Fig. 6.3, caption on following page.

Fig. 6.3. Total pressure distribution  $p_{t3}(y,z)/p_{t0}$  at the outlet of an impeller blade channel, measured in the radii ratio  $R/R_2 = 1.017$ .

Operating levels:

- |   |   |  |
|---|---|--|
| a | $n/\sqrt{\theta_0} = 18\ 000\ \text{rpm}$ , | $\dot{m} \sqrt{\theta_0}/\delta_0 = 7,40\ \text{kg/s}$ , |
| b | $n/\sqrt{\theta_0} = 14\ 000\ \text{rpm}$ , | $\dot{m} \sqrt{\theta_0}/\delta_0 = 5,31\ \text{kg/s}$ , |
| c | $n/\sqrt{\theta_0} = 10\ 000\ \text{rpm}$ , | $\dot{m} \sqrt{\theta_0}/\delta_0 = 3,81\ \text{kg/s}$ . |

and the three D plotter program. The perspective graph of these results is restricted to the region of the outlet flow of a blade channel in the radii ratio  $R/R_2 = 1.017$ . In this representation, the lateral separating lines ( $y/t = 0$  and  $1$ ) which in the actual flow -- corresponding to the dips in the blade wake -- are twisted (see Fig. 8.1) were straightened out in order to simplify the drawing. What was plotted were the nonsteady total pressure curves  $p_{t3}(y,z)$ , related to the total intake pressure in the compressor inlet  $p_{t0}$ , which was measured between the measuring points  $z/b = 0.1$  on the front wall and  $z/b = 0.9$  near the rear wall at 9 equidistant axial settings.

A striking feature is, first of all, the basically similar curve -- down to the smallest details -- for all three operating levels shown. This fact reinforces the assumption that the flow mechanisms occurring in the impeller are active in the entire range of performance characteristics studies, and as a result their relative importance with respect to the development of the flow field is largely maintained. To be sure, with increasing rpm the amplitudes in the pressure curve over channel division and channel width increase considerably, and at 18,000 rpm the range of fluctuation in the circumferential direction on the front wall of the diffuser ( $z/b = 0.1$ ) already equals 40% (1.3 bar!) of the mean total pressure (note the change in the ordinate scale in Fig. 6.3 a with respect to Figs. 6.3 b and c).

As a result, the total pressure curve measured in the absolute system gives hardly any indication of the strongly disturbed jet-wake velocity distribution observed in the relative system. The corresponding velocity vector diagram -- Fig. 7.2 -- /111 explains this phenomenon which is characteristic for impellers with radially ending blades:

In spite of considerable fluctuations in relative velocity, the absolute velocities and thus -- because of the small fluctuation in static pressure (cf. Fig. 6.2) -- also the total pressures in the two areas are on the same order of magnitude. To be sure, a considerable increase in entropy occurs in the region of the separated wake flow, but at the same time the transfer of energy in this region of lower mass flow density is considerable greater than in the flow-through region. Conversely, the greater efficiency of the compressor process in the jet region is contrasted with a smaller reduced output factor

and thus a smaller addition of energy (cf. Fig. 6.6).

Especially pronounced in these total pressure graphs of the area immediately behind the impeller outlet are the pressure peaks on the pressure side and suction side. They are caused by the wake dips of the impeller blades and they increase steadily over the channel width -- corresponding to the increasing blade thickness. If one assumes that in this region of the blade wake flow only a small or, in the case of back flow, even a negative relative velocity prevails, then the total pressure levels can easily be derived from the velocity vector diagram.

The signal processing of the nonsteady total pressure curves by means of the synchronized sampling technique offers -- in addition to the determination of the statistically averaged pressure curve -- the possibility of measuring the fluctuation intensity of the measurement signal  $f'$  in an analog fashion on a second output of the sampling instrument (cf. Figs. 3.18 and 5.5).

As the result of such measurements made directly behind the impeller outlet, Fig. 6.4 shows the distributions of total pressure fluctuation coefficient  $f$  for the flow region of an impeller blade channel in 5 operating points of the compressor performance graph. In the equation which defines the local total pressure fluctuation coefficients:

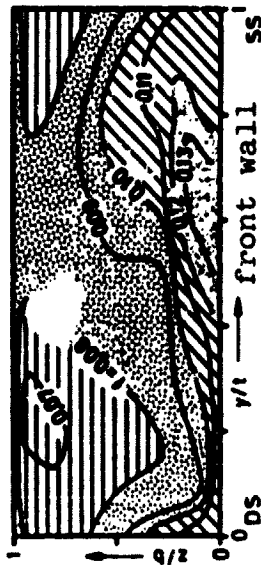
$$f(y, z) = \sqrt{(p_t^i - \bar{p}_t)^2} / \bar{p}_t = f' / \bar{p}_t \quad (6.2) \quad \underline{/113}$$

$p_t^i$  stands for the instantaneous value, while  $\bar{p}_t$  indicates the statistically averaged total pressure.

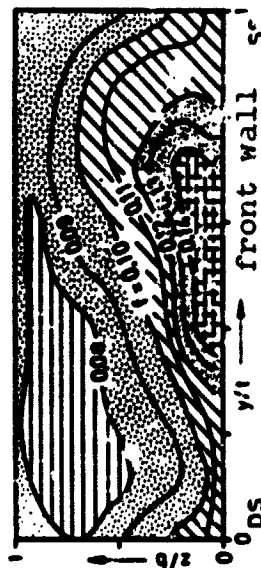
In considering the individual distributions, the first striking fact is that the fluctuation intensity -- to be sure, on average -- increases with increasing rpm (Figs. 6.4 e, c, a) and -- at constant rpm -- with increasing mass flow, however the basic shape of the distribution remains approximately the same in all cases. Characteristically, a more or less (steep) diagonally running surface separates a region of higher fluctuation intensity, the core of which is shifted on the front wall of the channel of towards the pressure side, from a region of relative calm along the pressure side of the blades and the rear wall of the channel. Here there is already a hint of the basic jet-wake distribution of the disturbed flow. This can be seen in the total pressure fluctuation, in which the greatest flow fluctuations occur in the region of the wake.



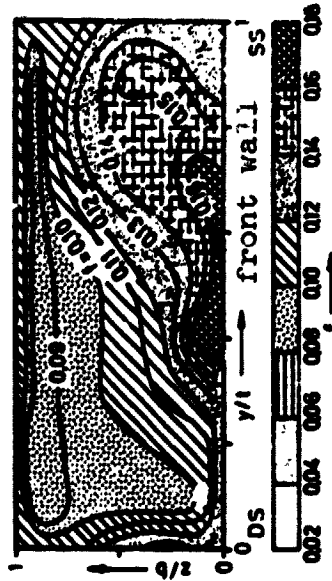
a)  $n=18\ 000$  rpm,  $\dot{m}=7,40$  kg/s



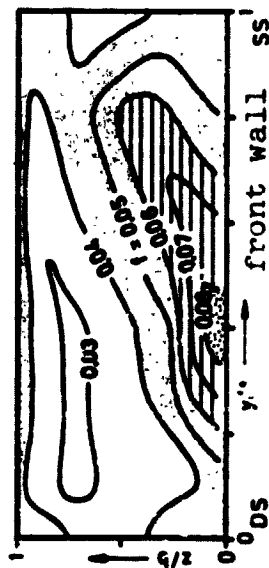
b)  $n=14\ 000$  rpm,  $\dot{m}=4,53$  kg/s



c)  $n=14\ 000$  rpm,  $\dot{m}=5,31$  kg/s



d)  $n=14\ 000$  rpm,  $\dot{m}=6,07$  kg/s



e)  $n=10\ 000$  rpm,  $\dot{m}=3,81$  kg/s

Fig. 6.4. Distribution of total pressure fluctuation coefficients  $f$  at the outlet of an impeller blade channel, measured in 5 operating points (a-e) of the compressor performance graph,  $R/R_2 = 1.017$

### 6.1.2 Direction Distribution of the Absolute Flow

An exact separation and clearer delineation of the jet region and wake region in the area of the outlet flow of an impeller blade channel is possible by determining the absolute flow direction with the aid of the measuring technique described in Section 3.4 using shielded hot-wire probes. Fig. 6.5 shows a selection of direction distributions of the absolute velocity vector measured immediately behind the impeller outlet for the region of one impeller blade channel. In these graphs the flow direction  $\alpha$  is defined according to the graph shown in Fig. 5.2.

As with the total pressure fluctuation graphs of Fig. 6.4, the characteristic basic form of the isocline curve is maintained with small variations in the total performance range studied. Separated by a steep direction gradient, the jet region with large angles of flow  $\alpha$  and the region of the separated wake flow with small angles of flow and a correspondingly small mass flow component clearly stand out. The wake region -- nearly unchanged for all operating points -- lies at  $y/t = 0.6-0.8$ , with its core on the front wall of the channel. As a function of the speed of rotation, one observes in Figs. 6.5 e, c, a an increase in the width ( $z/b = 0.4-0.7$ ), while the variation in mass flow in question at 14,000 rpm (Fig. 6.5 b, c, d) reveals itself only slightly by comparison. /115

Taken together, the results of the nonsteady measurements made directly after the impeller outlet already permit a very extensive reconstruction of the disturbed flow discharged from the impeller. In this connection, the nonsteady direction measurement deserves special attention. This makes possible the important transition into the relative system for the theoretical treatment of the jet-wake mixing processes. The signal processing by means of the synchronized sampling technique also deserves attention. By means of the statistical averaging, this technique sets up the necessary requirement for a quantitative treatment of the strongly fluctuating flow.

### 6.2 Examples for Calculated Distributions

With the aid of the system of equations listed in Section 5.4, the required flow variables, for a complete evaluation of the flow field at the impeller outlet, are calculated from the measured nonsteady values.

#### 6.2.1 Conversion of Work and Total Temperature

Using the Euler equation of moments, the angular momentum component of the absolute velocity  $c_{u3}$  and the total temperature at the impeller outlet  $T_{t3}$  follows from the iteration loop of Eqs. (5.5)-(5.8).



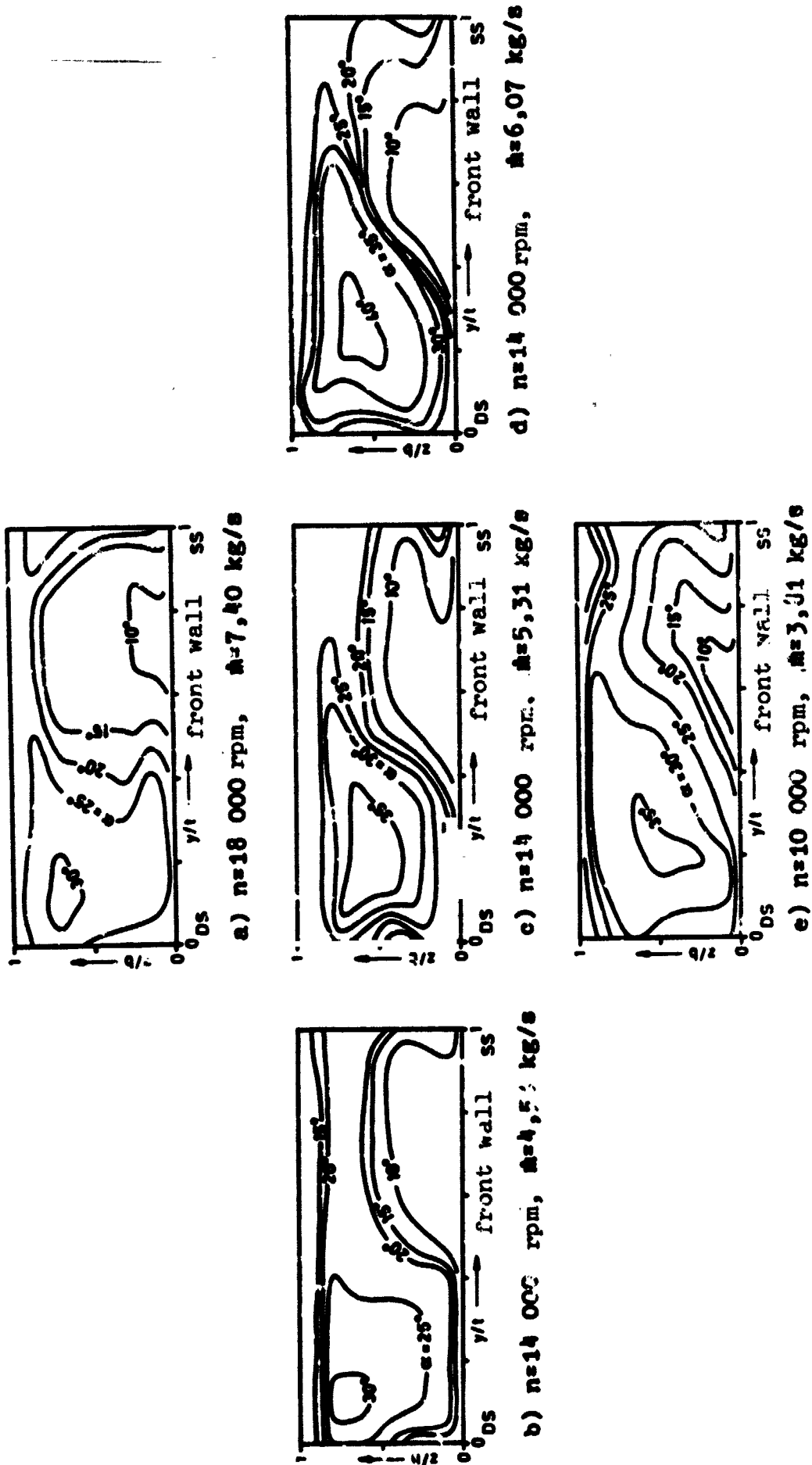
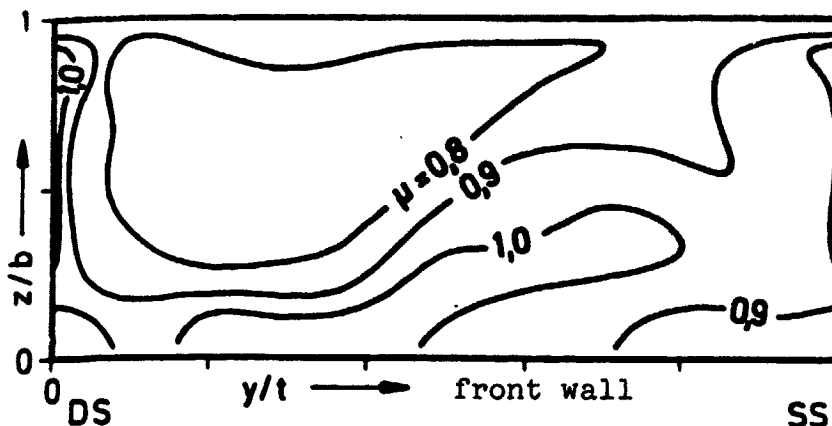


Fig. 6.5. Isocline graphs of the absolute flow direction at the outlet of an impeller blade channel, measured in 5 operating points (a-e) of the compressor performance graph,  $R/R_2 = 1.017$ .

As an example of this evaluation, Fig. 6.6 shows the distribution of the reduced output factor  $\mu$ ,

$$\mu = c_{u3}/u_3, \quad (6.3)$$

for the flow region of an impeller blade channel, with respect to measuring surface I in the radii ratio  $R/R_2 = 1.017$ .



/116

Fig. 6.6. Distribution of the reduced output factor  $\mu$  at the outlet of an impeller blade channel,  $R/R_2 = 1.017$ .  
Operating point:  $n/\sqrt{\theta_0} = 14,000$  rpm,  
 $\dot{m} \sqrt{\theta_0}/\delta_0 = 5.31$  kg/s

It can clearly be seen that the conversion of work in the centrifugal impeller -- which is expressed in the curve of the reduced output factor -- is quite considerably affected by the jet-wake distribution of the impeller flow. In the jet region, the addition of jet energy is clearly less than the mean momentum value for the total flow  $\mu = 0.801$ , while in the wake region, with its small mass flow component, it even exceeds in places the values expected with an infinite blade number ( $\mu > 1$ ). This phenomenon can be explained by the secondary flow field at the impeller outlet, where a strong joint angular momentum component occurs in the region of the front wall of the channel (cf. Fig. 6.9 and 6.6).

For the same operating point, Fig. 6.7 shows the corresponding total temperature distribution at the impeller outlet. In the isotherm graph for the region of a blade channel a total temperature ratio TR was plotted:

$$TR(y,z) = [T_{t3}(y,z) - T_{t0,N}] / (\bar{T}_{t4} - T_{t0,N}) ; \quad (6.4)$$

C-2

TR is thus defined as the ratio of the local increase in total temperature to the mass averaged increase in total temperature, whereby measuring point "4" (cf. Fig. 4.2) is at  $R/R_2 = 1.687$ , outside the region of nonsteady flow striking the probes. /117

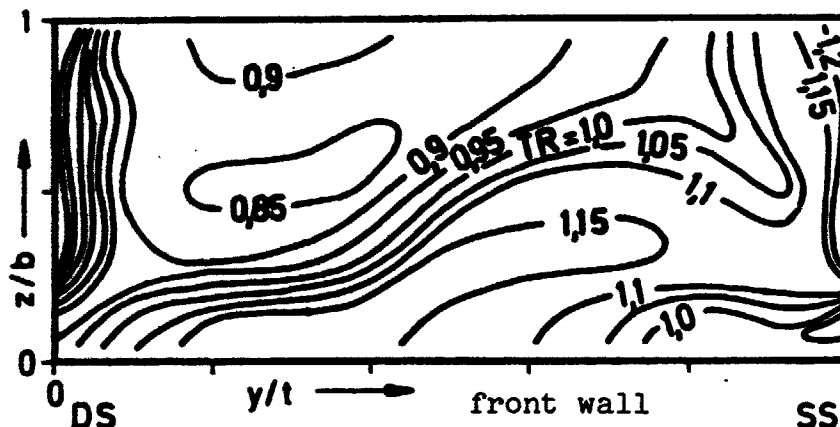


Fig. 6.7. Isotherm graph of the total temperature ratio TR at the outlet of an impeller blade channel,  $R/R_2 = 1.017$ .  
 Operating point:  $n/\sqrt{\theta_0} = 14,000$  rpm,  
 $\dot{m} \sqrt{\theta_0}/\delta_0 = 5.31$  kg/s.

For the case shown in Fig. 6.7, the mass average  $\overline{TR}$  equals 0.987 instead of the exact value 1.0. In the section where errors were considered (Section 5.6) we discussed in detail the restricted validity of the Euler equation of moments, Eq. (5.8), for determining the local pressure distribution behind the impeller outlet. In view of the still unsolvable difficulties involved in making a direct, exact measurement of this quantity under the given flow conditions, the results shown in Fig. 6.7 take on even greater importance.

As this typical total temperature distribution shows -- for this disturbed flow at the impeller outlet -- the variable addition of energy to the jet region and wake region leads to total temperature fluctuations in the area of a blade division which are on the order of  $\pm 15-20\%$  of the mass averaged temperature increase.

### 6.2.2 The Velocity Field in the Absolute and Relative System

With the measured distribution of total pressure, wall pressure and direction and the calculated total temperature curve, all of the variables are fixed which are required to calculate

the complete velocity field with the aid of Eqs. (5.9)-(5.12).

/118

For three operating points at 14,000 rpm in the radii ratio  $R/R_2 = 1.017$ , Fig. 6.8 and 6.9 show the thus determined velocity distribution in the absolute and relative system, in each case for the flow region of an impeller blade channel.

In the plotter graph of Fig. 6.8 the radial component of the absolute velocity  $c_{r3}(y,z)$ , with respect to the circumferential velocity of the impeller  $u_2$ , was plotted for the entire flow channel, whereas Fig. 6.9 shows the curve of the related relative velocity vector  $w_3/u_2$  in magnitude and direction in 5 circumferential positions  $y/t$  over the channel width  $z/b$  (cf. Fig. 5.2).

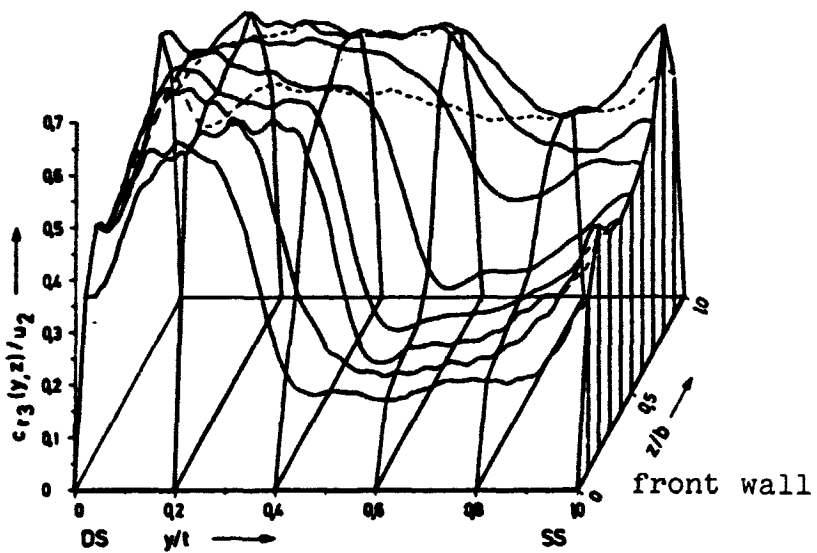
In the graph of the radial velocity curve  $c_{r3}/u_2$  the steep velocity gradient clearly localizes the region of separated wake flow. On the front wall of the diffuser -- starting from the suction side SS -- this extends over approximately  $2/3$  of the blade spacing and in so doing takes up about 60% of the channel width  $b$ . The main portion of the mass flow leaves the impeller through the jet region along the pressure side of the blade DS and along the rear wall of the channel. In considering Figs. 6.8 and 6.9, the following points stand out:

- the large degree of similarity of the disturbed flow at the impeller outlet for various operating points. As already mentioned in connection with the total pressure results shown in Fig. 6.3, this implies that the relative importance of the individual flow mechanisms, which contribute to the shape and development of the region of separated flow in the impeller, is largely maintained in the operating region in question;
- the relatively small difference in velocity, both in magnitude and direction, within the jet region and wake region -- this suggests a "block-shaped" model simplification of the flow field for the theoretical treatment of the jet-wake mixing processes in Section 7;
- the small -- in spite of the high fluctuation intensity -- clearly detectable mass flow through the wake region, which plays an important role in the theoretical analysis of the intensity of jet-wake mixing.

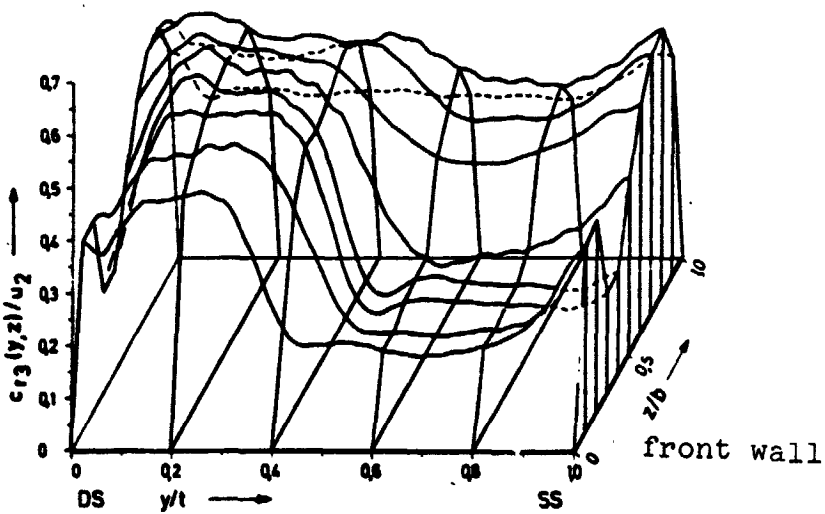
As a further important result of the flow studies at the impeller outlet, the distribution of the relative total pressure will be presented and discussed in detail in connection with the laser measurements in Fig. 6.14 and on page 101.

/121

a



b



c

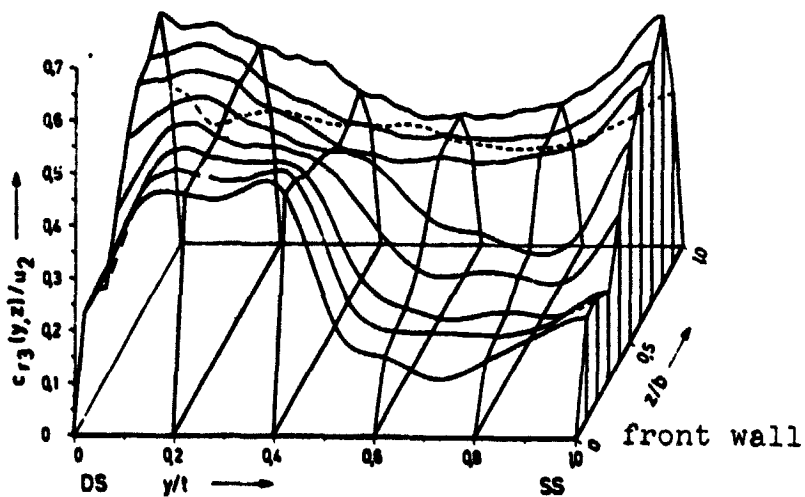


Fig. 6.8. Caption on p. 90.

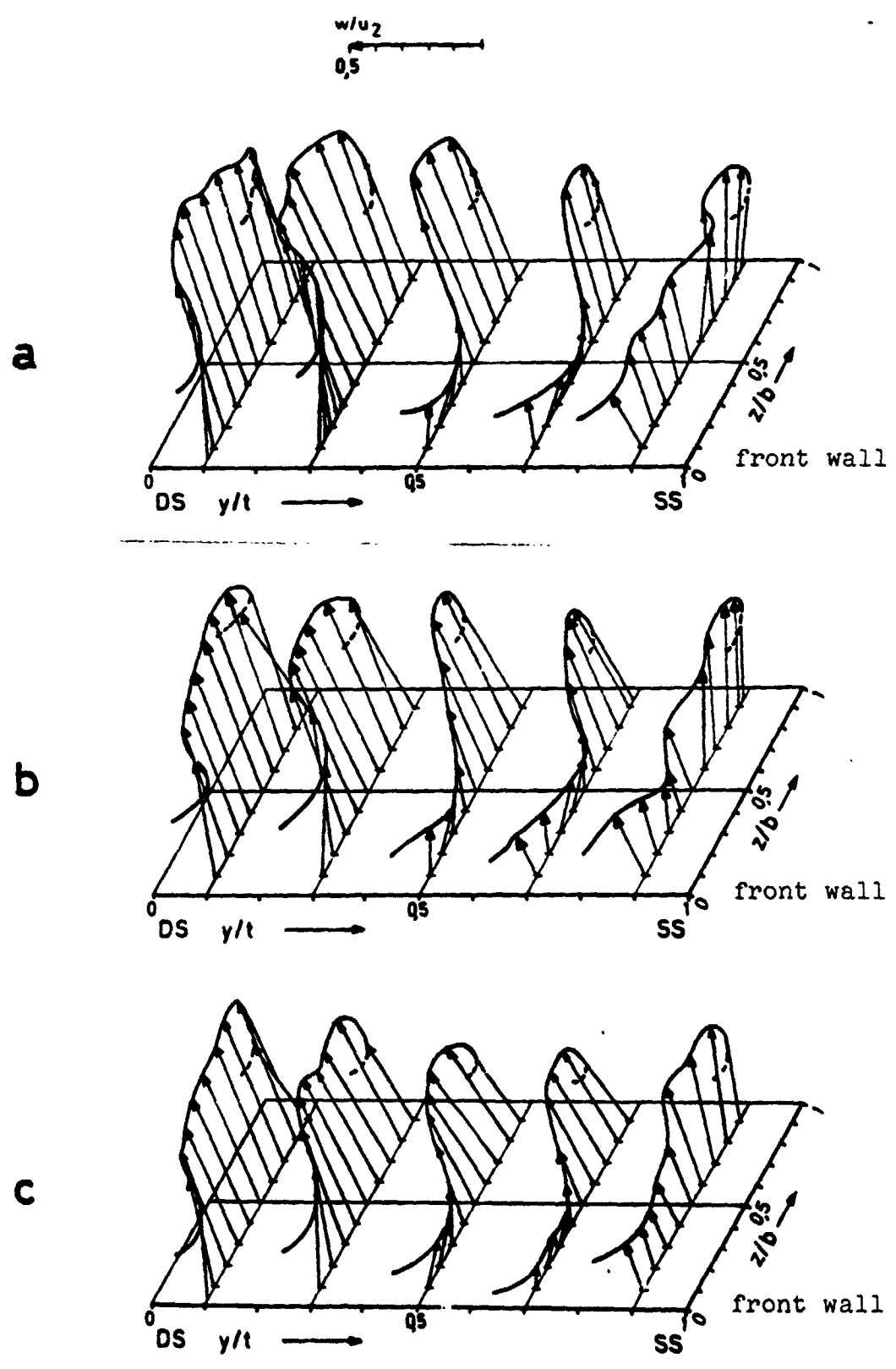


Fig. 6.9. Caption on p. 90.

Fig. 6.8. Plotter evaluation of the absolute velocity distribution  $c_{r3}(y,z)/u_2$  behind an impeller blade channel,  $R/R_2 = 1.017$ .  
 Operating points at  $n/\sqrt{\theta_0} = 14,000$  rpm,  
 $\dot{m} \sqrt{\theta_0}/\delta_0$ : (a) 6.07 kg/s; (b) 5.31 kg/s; (c) 4.53 kg/s.

Fig. 6.9. Vector graph of the relative velocity distribution  $w_3/u_2$  at the outlet of an impeller blade channel,  $R/R_2 = 1.017$ .  
 Operating points at  $n/\sqrt{\theta_0} = 14,000$  rpm,  
 $\dot{m} \sqrt{\theta_0}/\delta_0$ : (a) 6.07 kg/s; (b) 5.31 kg/s; (c) 4.35 kg/s.

### 6.3 Analysis of Test Findings at the Impeller Outlet with Respect to the Jet-Wake Distribution

Since it turned out that the qualitative study of the flow at the impeller outlet showed a large degree of similarity in the velocity distributions and pressure distributions for various operating points, in what follows, the detailed, quantitative analysis of the jet-wake flow will be limited to 5 operating points of the compressor stage between 10,000 and 18,000 rpm. For overall evaluation of the flow condition in these performance graph points, the most important mean flow values at the impeller inlet and outlet ( $R/R_2 = 1.017$ ) were listed in Table 6.1. In this table, the equation numbers refer to the corresponding definition equations in Section 5.5.

Figs. 6.10 and 6.11 below illustrate two particularly remarkable partial aspects of the test data listed in Table 6.1. Starting with the isentropic total efficiencies  $\eta_{1,03} = \eta_{1,03}^{t,s}$  (pos. 3 -  $R/R_2 = 1.017$ ) and  $\eta_{1,04}$  (pos. 4 -  $R/R_2 = 1.687$ ), which were formed identically according to Eqs. (4.3) and (5.69), a loss ratio between the impeller and diffuser is setup:

$$K_t = (1 - \eta_{1,03}) / (\eta_{1,03} - \eta_{1,04}) \quad (6.5)$$

Fig. 6.10 shows the  $K_t$  curve as a function of the discharge coefficient  $\Phi_3$ . In this graph, the experimental points listed in Table 6.1 are indicated by the all-black symbols. A striking feature is the general decrease in  $K_t$  values, i.e. the relative increase in diffuser losses with respect to total losses, as the discharge coefficient increases. Above all, as a function of rpm, at the transition from 10,000 to 14,000 rpm we first of all see a sharp decline, then at  $n \geq 14,000$  rpm the  $K_t$  values vary within relative narrow limits between  $K_t = 0.3-0.7$ .

In a first approximation, this curve suggests the conclusion /123

TABLE 6.1 CHARACTERISTIC MEAN FLOW VALUES AT THE IMPELLER INLET AND IMPELLER OUTLET FOR 5, NONSTEADY OPERATING POINTS MEASURED /122

$n/\sqrt{\theta_0}$	rpm	10 000	14 000			18 000
$\dot{m}\sqrt{\theta_0}/\delta_0$	kg/s	3,81	6,07	5,31	4,53	7,40
	G1.	Impeller inlet				
$\bar{M}_{w1,a}$	(5.32)	0,464	0,669	0,653	0,639	0,861
$\bar{M}_{w1}$	(5.33)	0,363	0,532	0,512	0,495	0,682
$\Delta B_1$ °	(5.34)	+ 6,9	+ 2,9	+ 6,6	+10,3	+ 3,6
		Impeller outlet (R/R <sub>2</sub> = 1,017)				
$\bar{\Phi}_3$	(5.54)	0,383	0,395	0,338	0,284	0,327
$\bar{M}_{t,c3}$	(5.46)	0,552	0,776	0,750	0,729	0,926
$\bar{a}_3$ °	(5.52)	27,6	29,3	25,3	21,5	22,9
$\bar{M}_{w3}$	(5.47)	0,283	0,417	0,356	0,303	0,405
$\bar{B}_3$ °	(5.53)	67,8	73,2	71,2	67,7	76,6
MR	(5.55)	1,283	1,276	1,438	1,634	1,684
MR <sub>S</sub>	(5.56)	1,497	1,408	1,641	1,863	1,844
$\epsilon_{k3}(c)$	(5.57)	0,126	0,191	0,183	0,179	0,164
$\epsilon_{e3}(c)$	(5.58)	0,009	0,016	0,013	0,009	0,009
$\epsilon_{e3}(w)$	(5.59)	0,036	0,060	0,061	0,058	0,057
$\Pi_{30}$	(5.38)	1,226	1,413	1,462	1,488	1,779
$\Pi_{t,30}$	(5.41)	1,529	2,218	2,219	2,209	3,449
$\eta_s^*$	(5.67)	0,904	0,926	0,920	0,881	0,925
$\eta_p^*$	(5.68)	0,907	0,931	0,925	0,888	0,932
$\eta_{t,s}^*$	(5.69)	0,944	0,962	0,954	0,936	0,949



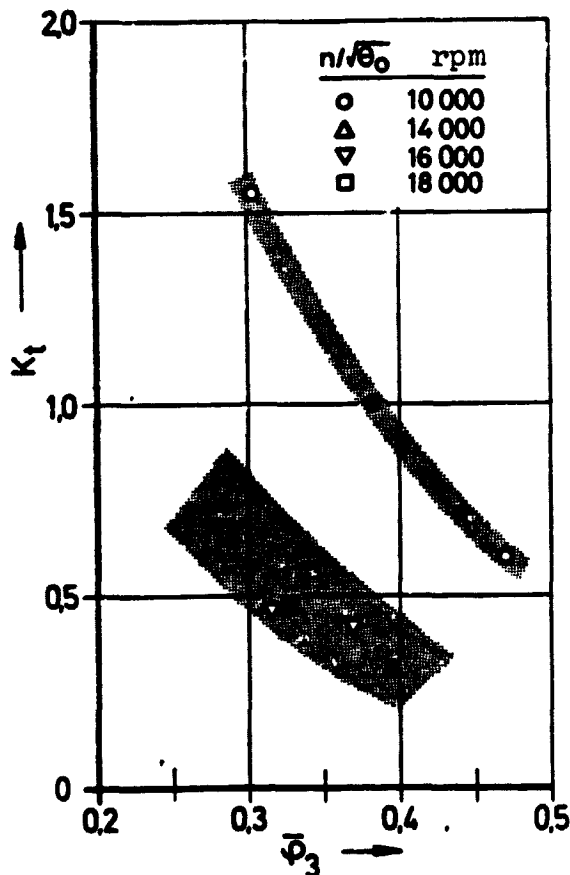


Fig. 6.10. Curve of the loss ratio  $K_t$  between the impeller and diffuser as a function of the discharge coefficient  $\bar{\phi}_3$ , (●▲■, see Table 6.1).

the impeller outlet. The detailed loss analysis in Section 8 will show, to be sure, that a portion of this is due to mixing and equalization processes of the disturbed impeller flow (and thus can reasonably be attributed to impeller losses).

Since the losses in unbladed diffusers with steady flow can be determined with satisfactory accuracy (cf., for example, [6.2], [6.3] and [6.4]), the loss distribution shown in Fig. 6.10 underlines the necessity of studying flow mechanisms and loss mechanisms in the diffuser input region in greater detail.

Fig. 6.11 shows the curve of the relative mach number diffusion ratio determined according to Eq. (5.56) in the jet region  $MR_S$  as a function of the discharge coefficient  $\bar{\phi}_3$ . Besides the almost linear relationship of  $MR_S + f(\bar{\phi}_3)$  for the

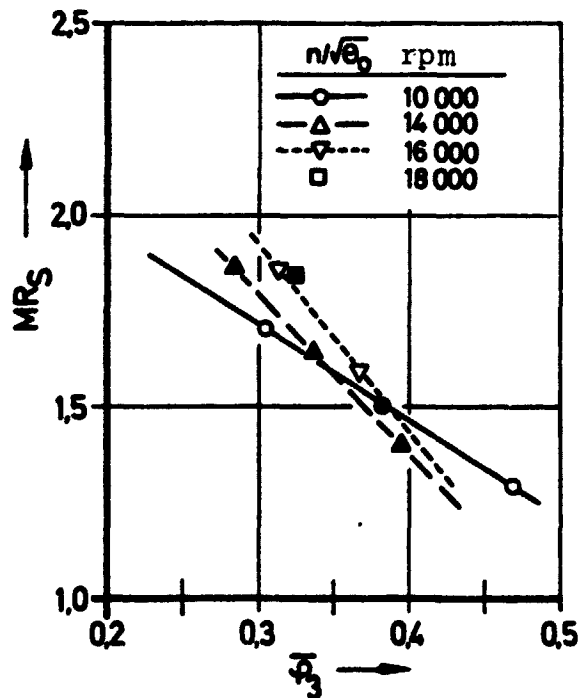


Fig. 6.11. Relative mach number diffusion ratio for the jet region  $MR_S$  as a function of the discharge coefficient  $\bar{\phi}_3$ , reference surface at impeller outlet  $R/R_2 = 1.017$  (●▲■, see Table 6.1).

that -- with the exception of operating points with an extremely small load on the stage -- approximately 2.3 of the stage losses up to the diffuser outlet first occur after

individual rotation speeds, the relatively small effect of the rotation speed is, on the whole, striking:

For operations points with a constant  $\bar{\phi}_3$ , the jet-wake configuration obviously establishes itself in just such a way that approximately the same retardation of flow is produced for the "healthy" jet flow. A limiting curve of the possible flow retardation stands out which is not exceeded for the impeller design in question.

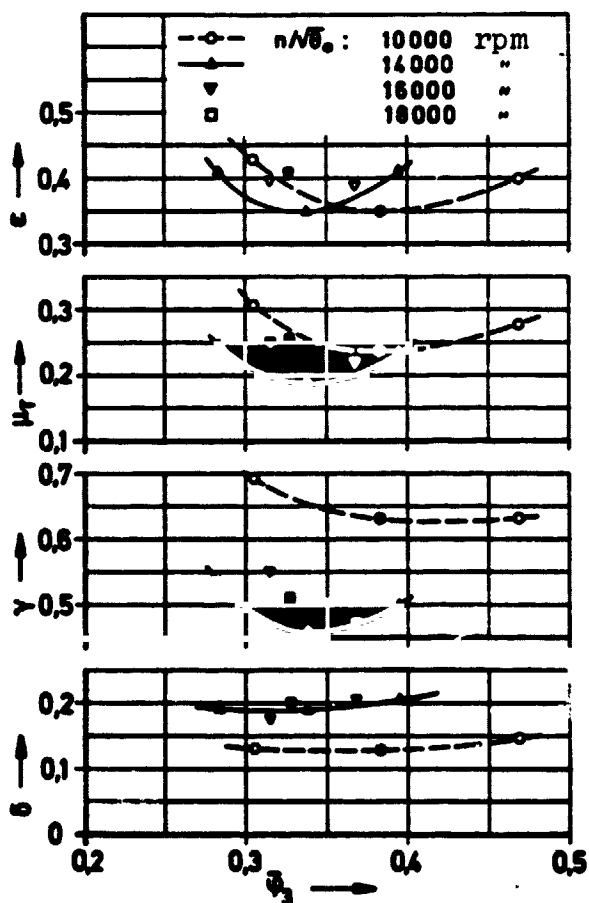


Fig. 6.12. Area component of the wake, wake mass flow component  $\mu_T$ , wake-jet relative velocity ratio and interference parameter  $\gamma$ , plotted over the discharge coefficient  $\bar{\phi}_3$ . Reference surfaces at the impeller outlet  $R/R_2 = 1.017$  ( $\bullet\blacktriangle\blacksquare$  - , see Table 6.1).

Detailed studies of the impeller flow which have been carried out in the meantime with the optical dual-focus laser velocimeter (also see Section 6.4), have well confirmed this data, just like the data shown in Fig. 6.12 to characterize the jet-wake distribution at the impeller outlet ( $R/R_2 = 1.017$ ). In these graphs the following distributions were plotted, going from top to bottom:

- the area component  $\epsilon$  of the wake, Eq. (5.61);

- the wake mass flow component  $\mu_T$ , Eq. (5.62);

- the relative velocity ratio (wake-jet)  $\gamma$ , Eq. (5.63) and

- the interference parameter  $\delta$ , Eq. (5.64)

as a function of the discharge coefficient  $\bar{\phi}_3$ , Eq. (5.54), for three rotation speeds between 10,000 and 18,000 rpm. Again in these graphs, the test point treated in detail in this study are indicated by the blacked-in symbols (cf. Table 6.1).

With the exception of the test points for the rotation speed of 10,000 rpm, where the velocity distribution at the impeller outlet is clearly less

/125

/126

severely disturbed (cf.  $\gamma$  and  $\delta$  curves), the characteristic mean values of the jet-wake flow lie within these band widths:

$$\begin{aligned}0,35 < \epsilon < 0,41, \\0,19 < \mu_T < 0,26, \\0,46 < \gamma < 0,55, \\0,17 < \delta < 0,21.\end{aligned}$$

Thus these interference variables are sometimes considerably smaller than the extreme values found in the literature, and one can assume that in the impeller outlet flow studied here -- which by comparison is only slightly disturbed -- correspondingly small losses will arise in the course of the mixing and equalization processes. For example, the flow analysis of the well known Boeing-Avlab centrifugal compressor stage, at a total pressure ratio of  $\Pi_t = 10$ , gave a wake area component of  $\epsilon = 0.7$ , an interference parameter of  $\delta = 0.5$ , and 9 points of the stage efficiency were taken into account only for the mixing losses behind the impeller outlet (cf. [6.5]).

#### 6.4 Discussion of Various Flow Mechanisms in the Centrifugal Impeller Which Contribute to the Formation of the Jet-Wake Distribution

In the past, the study of complicated flow processes within centrifugal impellers was restricted to the range of low circumferential velocities for the impeller, primarily because of the quite considerable difficulties in making measurements in a rotating system. Previous investigators, e.g. Fischer and Thoma [6.6], Hamrick and co-workers [6.7], Fujie [6.8], Senoo and co-workers [6.9] and Fowler [6.10] have managed to give a qualitatively comprehensive description of fundamental flow forms. Only in recent times has the development of new, non-contact velocity measuring methods made it possible to make a quantitatively exact analysis of internal impeller flow processes, even at circumferential velocities and blade channel loads which are on the order of magnitude of modern industrial compressors. Thus, the impeller flow of the centrifugal compressor stage studied within the scope of this work was exactly measured and analyzed with the dual-focus laser velocimeter developed by Schodl [3.2, 6.11]. The comprehensive investigation covered circumferential velocities of up to 400 m/s [6.12, 6.13, 6.14].

/127

The discussion of the flow mechanisms in the centrifugal compressor impeller fundamental for the jet-wake distribution is based on a few findings from these investigations.

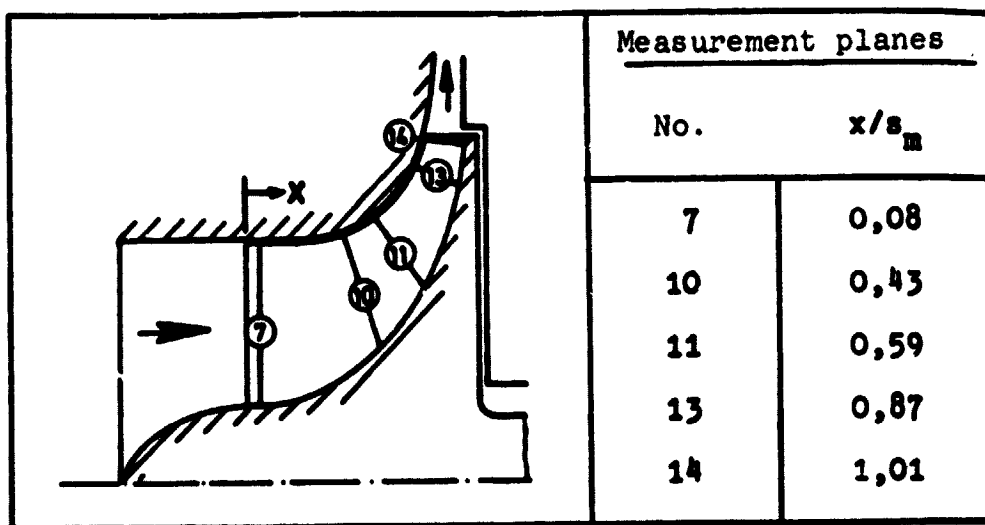
### 6.4.1 Optical Flow Measurements in a Centrifugal Compressor Impeller

The following selection of characteristic impeller velocity distribution refers to an operating point in the vicinity of the optimum line of the performance graph:

$$n/\sqrt{\theta_0} = 14\ 000\ \text{rpm}, \quad \dot{m} \sqrt{\theta_0}/\delta_0 = 5,31\ \text{kg/s}.$$

The velocity measuring method using the dual-focus laser which we employed makes it possible, at any optically accessible measuring points, to determine the absolute and relative velocity vectors in a measuring plane which lies perpendicular to the axis of the laser beam. For showing the change in flow from the inlet to the outlet of a centrifugal impeller, velocity measurements were made in 5 measuring planes. The numbers and locations of these planes are shown in Table 6.2. The laser measuring planes are perpendicular to the outer contour of the housing. The exact location of the measurement position is defined by the relative outer contour of the impeller in the meridian section  $x/s_m$  (impeller inlet, outside:  $x/s_m = 0$ , impeller outlet:  $x/s_m = 1$ ).

TABLE 6.2 LOCATION OF MEASURING PLANES FOR OPTICAL VELOCITY MEASUREMENTS IN THE CENTRIFUGAL COMPRESSOR IMPELLER  
 $s_m$ : LENGTH OF THE OUTER CONTOUR OF THE IMPELLER IN THE MERIDIAN SECTION



In Figs. 6.13 a and b are plotted the distributions of the meridian component of the absolute velocity  $c_m$  in each respective measuring plane. This meridian component is made dimensionless with the circumferential velocity at the impeller outlet  $u_2$ .

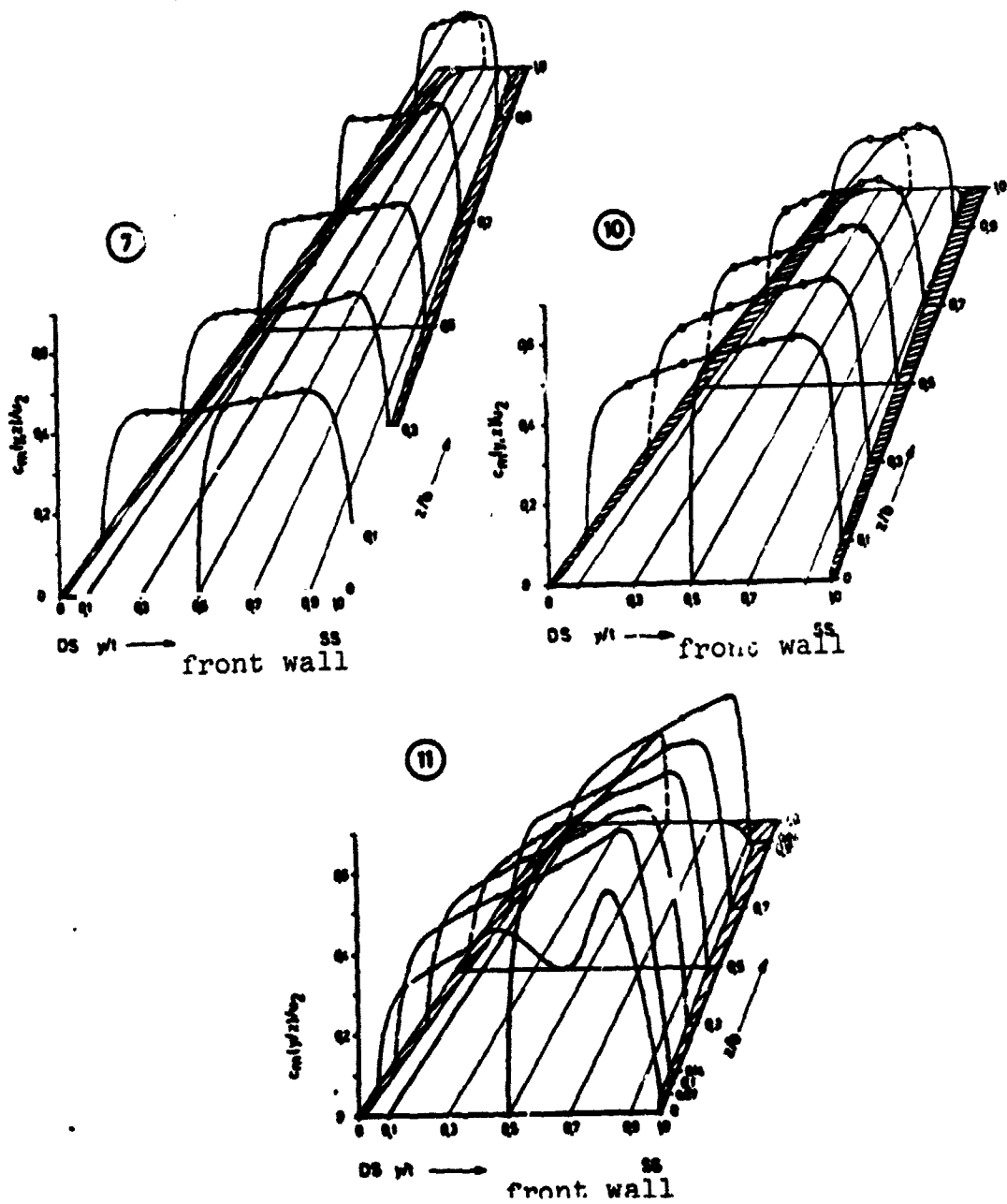


Fig. 6.13a. The velocity distribution  $c_m/u_2$  in the impeller blade channel, measured in the 3 optical measuring planes 7, 10 and 11 in the axial impeller region (o = measuring points).  
 Operating level:  $n/\sqrt{\theta_0} = 14,000$  rpm,  
 $\dot{m} \sqrt{\theta_0}/\delta_0 = 5.31$  kg/s.

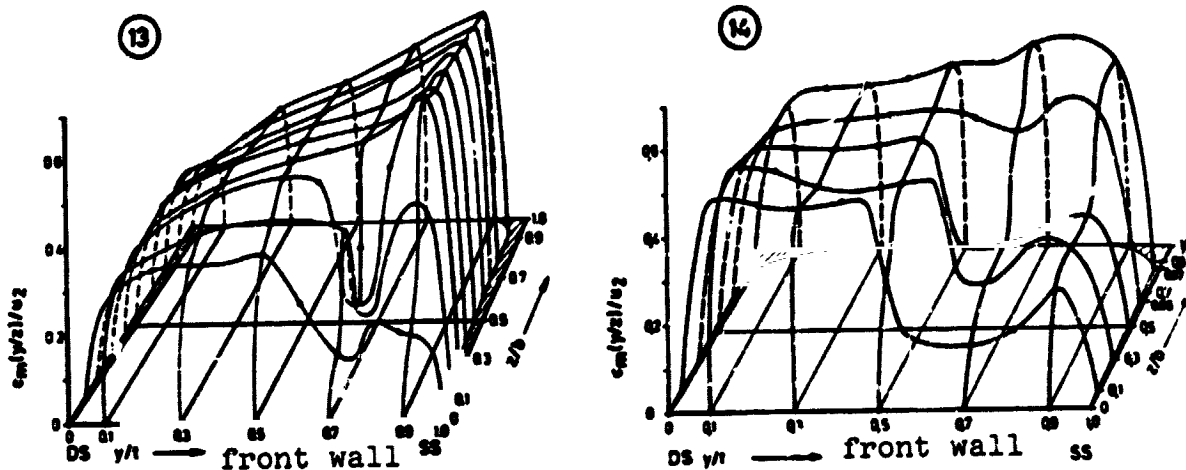


Fig. 6.13b. The velocity distribution  $c_m/u_2$  in the impeller blade channel, measured in the two optical measuring planes 13 and 14 in the centrifugal impeller region (o = measuring points).  
 Operating point:  $n/\sqrt{\theta_0} = 14,000$  rpm,  
 $\dot{m} \sqrt{\theta_0}/\delta_0 = 5.31$  kg/s.

In the prospective views, the measuring planes were represented in a simplified way as trapezoids, and the dimensions of the channel (spacing and height) were shown in the same scale. "Front wall" indicates the limit of the measuring plane ( $z/b = 0$ ) on the side of the housing which lies opposite the hub in the background of the figure ( $z/b = 1$ ). The shaded areas along the pressure side DS ( $y/t = 0$ ) and the suction side SS ( $y/t = 1$ ) correspond in each case to  $1/2$  a blade thickness. /128

The velocity distribution in measuring planes (7) -- immediately behind the impeller inlet -- and (10) -- at the end of the axial inlet region -- show that the flow largely exhibits the expected distribution based on potential theory up to the beginning of the meridional bend in the channel. With a comparatively small load on the channel, we observe a regular velocity curve with maximum values along the housing wall in the meridional section, i.e. in the circumferential direction on the suction side of the blades.

A first disturbance in the impeller velocity distribution is seen in measuring plane (11) in the region of the front wall of the channel. In this area, the load on the blade channel increases sharply at the same time, as is verified by Fig. 6.2. This disturbance indicates an incipient region of flow separation which -- as shown by the findings in measuring planes (13) and

(14) -- becomes still considerably larger in the region of the front wall of the channel and the suction side of the blades up to the impeller outlet.

Likewise for the outlet measuring plane (14), Fig. 6.14 /129 shows the loss distribution at the impeller outlet in the form of an isobar graph  $p_{t,rel}/p_{t0,N}$ . This was determined from:

$$p_{t,rel}(y,z)/p_{t0,N} = e^{-s(y,z)/R} \quad (6.6) \quad /130$$

with  $p_{t,rel}$  = relative total pressure in measuring plane (14) at the impeller outlet

and  $p_{t0,N}$  = standard total intake pressure directly in front of the impeller inlet.

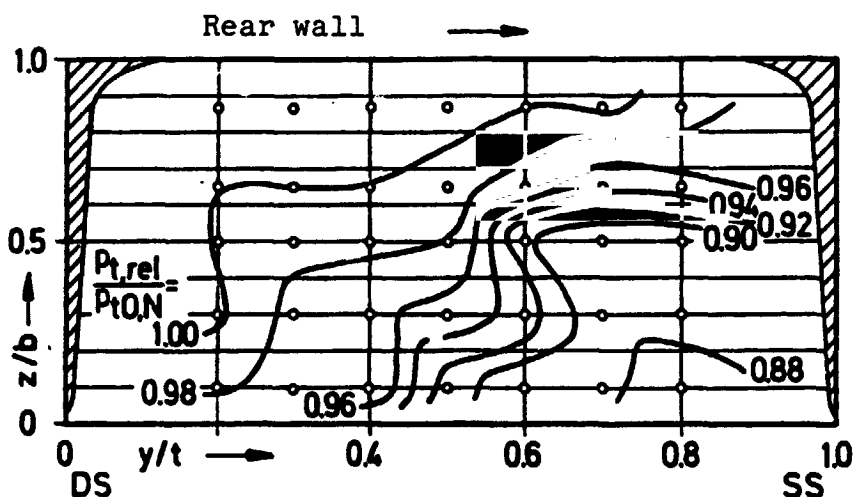


Fig. 6.14. Loss distribution at the outlet of the impeller blade channels: isobar graph of the relative total pressure  $p_{t,rel}(y,z)$  in measuring plane (14), relative to the "standard" total intake pressure  $p_{t0,N}$  directly in front of the impeller inlet. Operating point:  $n/\sqrt{\theta_0} = 14,000$  rpm,  $m\sqrt{\theta_0}/\delta_0 = 5.31$  kg/s.

The relative total pressure in this calculation is defined analogously to the relative total enthalpy so that for loss-free flow  $p_{t,rel} = p_{t0,N} = \text{constant}$ . A detailed discussion of the relative total pressure  $p_{t,rel}$  with a derivation of Eq. (6.6) is found in Appendix IV. The entropy distribution used  $s(y,z)$  was determined according to Eq. (5.18) under the following assumptions:

- that the curve of nonsteady pressure values measured on the housing wall is constant over the measuring surface;
- that the energy transferred to the relative flow due to friction on the housing wall can be ignored, so that the static temperature distribution can be determined from the energy equation for the relative flow with the aid of the optically measured velocities.

/131

Finally, as a basis for the discussion of flow mechanisms subject to friction in the centrifugal compressor impeller, the optically measured velocity curves in Fig. 6.15 are compared with the results of a calculation of the impeller flow based on potential theory. In the upper graph is plotted the relative velocity profiles  $w/u_2$  between the housing and the hub at one-half the blade spacing  $y/t = 0.5$ , and in the lower graph are plotted the corresponding curves between the pressure side and suction side at half the channel height  $z/b = 0.5$ .

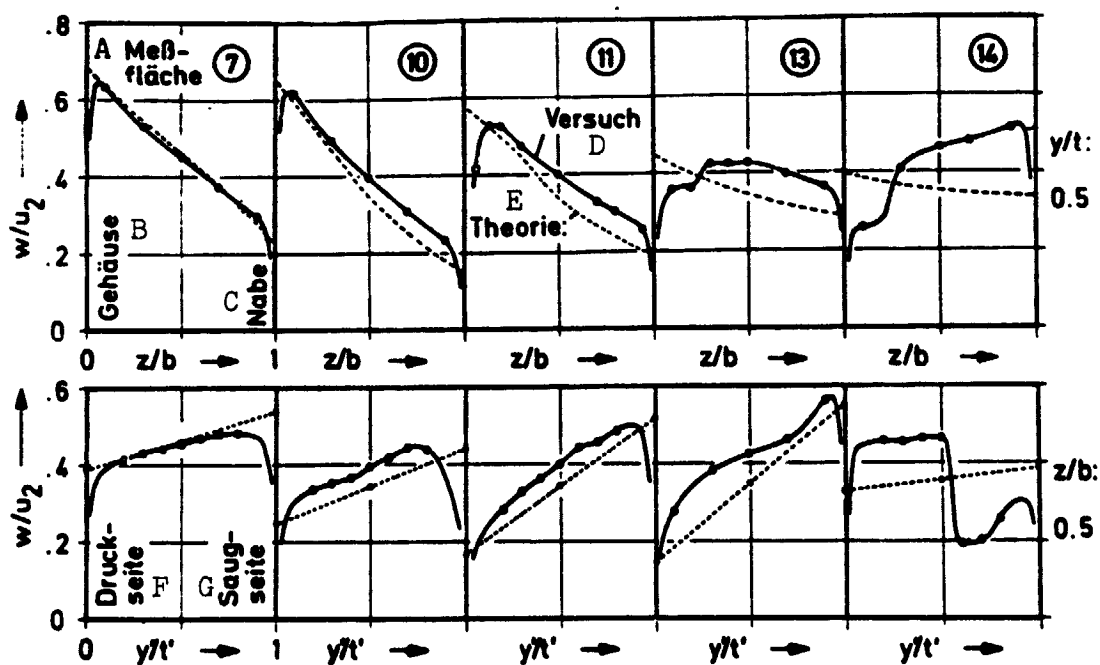


Fig. 6.15. Comparison of experimentally determined relative velocity profiles  $w/u_2$  with calculated curves of the impeller flow based on potential theory.

Operating point:  $n/\sqrt{\theta_0} = 14,000$  rpm,

$m\sqrt{\theta_0}/\theta_0 = 5.31$  kg/s;

$y'/t'$ : relative blade division between blade surfaces.

- Key:
- |                    |                  |
|--------------------|------------------|
| A) Measuring plane | E) Theory        |
| B) Housing         | F) Pressure side |
| C) Hub             | G) Suction side  |
| D) Experiment      |                  |



The calculations based on potential theory were made with a quasi three-dimensional method. The calculation of the meridian flow is based on the flow line bending method given by Stanitz [6.15]. In this method, blade-congruent flow is assumed to 75% of the meridional flow path in the impeller before a given flow-reducing deflection is taken into consideration continuously up to the impeller outlet. The solution found in this way is used to determine the flow areas in which the velocities on the blade surfaces are determined with the approximation methods suggested by Stanitz and Prian [6.16]. Other calculations which can be compared with these experimental data, among other things based on the "energy layering theorem," have been presented by Traupel [6.27].

/132

In summary, the following characteristic picture of the flow in the centrifugal compressor impeller studied follows from the experimental findings available so far:

1. The flow in the impeller blade channel possesses form -- into the radial portion -- which can largely be described in terms of potential theory. This is shown by the good agreement between the loss-free calculation and the experimental results (Fig. 6.15). Up to measuring plane (11), the observed deviations can be explained by the boundary layer displacement which is not considered theoretically. The same is true for the calculated velocity gradients in the circumferential direction. These are in good agreement with the experimental data up to the beginning of flow separation at  $x/s_m = 0.6$ .
2. In the region of the meridional bend in the channel observes on the housing wall a sharp retardation in flow. As a result of this and due to the rapidly increasing region of separation in the region of the front wall of the channel and the suction side, a displacement of the main flow occurs in the radial portion of the impeller in the direction of the pressure side of the blades and the rear wall of the channel. This effect appears in amplified form immediately in front of the impeller inlet, so that the disturbed velocity curve measured in the diffuser inlet deviates strongly from the curve calculated in advance using potential theory equations. This clearly illustrates the large influence of the region of separation on the energy conversion in the impeller and underlines the necessity for developing improved calculating methods for this flow region.
3. The position of the separation point in the meridian section changes only slightly, as shown by studies

/133

at rotation speeds between 10,000 and 18,000 rpm. In general, (cf. Fig. 6.13) the first sign of flow separation is observed in the form of a disturbance in the velocity profile on the housing wall in measuring plane 11. As this happens, the core of the interference region (at constant rpm) is shifted from  $y/t = 0.8$  in the vicinity of the suction side up to  $y/t = 0.4$  near the pressure side as the mass flow becomes increasingly smaller [6.28].

4. After the beginning of flow separation, the wake region increases very rapidly. Between measuring planes (13) ( $x/s_m = 0.87$ ) and (14) at the impeller outlet, its proportion of the available channel cross-section increase from 20 to 35%, while the wake mass flow at the impeller outlet in the test point in question is approximately 18%. The jet-wake relative velocity ratio in the impeller generally lies between  $\gamma = 0.45-0.7$  for the operating points studied. In none of the test points studied was it possible to detect a complete stagnation of the wake flow by means of the velocity measurement method using the dual-focus laser. A striking feature is the strongly pronounced and relatively stable velocity gradient between the main flow (jet) region and the wake region. While in the core of the area of separation a sharp rise in the absolute velocity fluctuation up to 1.5 to 3 times the values in the jet region are observed, the shape and position of the wake region are, by comparison, subjected to only small fluctuations [6.14].

/134

5. In the loss distribution  $p_{t,rel}/p_{t0,N}$ , Fig. 6.14, is found the same sharp delineation between the wake of lower energy and the main flow. This suggests a small amount of mixing of the two regions. Whereas in the wake region a pronounced loss concentration occurs in the corner formed by the front wall of the channel and the suction side of the blade, in the jet flow -- in addition to small total pressure losses -- is found an extensive isentropic core. For this core, in the area along the rear wall of the channel and along the pressure side of the blades, even slight "overisentropic" values were measured ( $1.0 < p_{t,rel}/p_{t0,N} < 1.02$ ). Independent of the more exact laser measurements (for Fig. 6.14 the error in local values was estimated at a maximum of  $\pm 2\%$ ), this result had already been found using the nonsteady probe measuring method [4.2, 6.1]. Comparable results are also

discussed by Prian and Michel in [6.17] (also see [6.4, p. 102]). Traupel [6.29] has explained this phenomenon as follows in terms of the "energy layering mechanism"<sup>1</sup>:

"Energy layering has its origin in the very sharp fluctuations in the flow velocity. If in a channel large pressure gradients prevail at the same time transverse to the flow direction, then it follows from the law of motion [sic] that particles with above average velocity drift primarily into the region of high static pressure, and those with below average velocity drift into the region of low pressure. From this it is clear that velocity distributions are found at the outlet of a centrifugal compressor impeller which contradict the predictions of classical theories, and that the total pressures of the relative flow can in places even exceed the value which is suggested by a theory of frictionless flow."

The characteristic loss distribution shown here for centrifugal impellers is essentially not new. Comparable results are discussed in the works of Hamrick and co-workers [6.7] and Domm and Hergt [6.18]. With the results shown in Fig. 6.14, however, it was possible -- possibly for the first time -- to clearly detect an isentropic flow core in the jet region for an angular velocity range such as is typical for modern, high performance centrifugal compressors. Thus, it was also possible to confirm an important aspect of the simplified flow model proposed by Dean [6.5, 6.19] for calculating the complex centrifugal compressor impeller flow.

/135

#### 6.4.2 Qualitative Analysis of the Impeller Flow

The flow separation revealed in the above test results at approximately 60% of the meridional channel length and the subsequent development of a pronounced wake area up to the impeller outlet adversely affect the efficiency of the centrifugal compressor stage (see Fig. 8.25). The separation of flow decreases the slow down of the flow in the impeller and thus the (also) desired conversion of kinetic energy into static pressure in the impeller layout. The strongly disturbed jet-wake velocity distribution at the impeller outlet also reduces the stage efficiency

---

1. A detailed description is found in [3.1, third ed.].

as a result of mixing and equalization losses, as well as due to loss-affected, nonsteady flow processes in the diffuser which comes after it. Accordingly, it is of prime importance, using the results available, to study the formation and development of areas of flow separation in order to derive from them possibilities for improved stage design.

From currently available experimental results, which were obtained both from rotating individual channels (diffusers) and from centrifugal impellers, it follows that boundary layer separations in rotating flow channels are particularly promoted by two flow mechanisms [6.12, 6.13]:

- secondary flow effects which lead to a correction of flow material of lower energy and
- turbulence damping effects, i.e. a local reduction in turbulent shearing stresses under the effect of flow line bending and system rotation (Coriolis forces).

By secondary flows is here meant all flows within the blade channels which possess a velocity component perpendicular to the blade-congruent main flow. Theoretically, we distinguish two causes of secondary flows (cf. Traupel [6.20]):

/136

- a primary vortex system which is induced solely by the deflection of a (frictionless) flow which at the blade channel inlet possesses velocity gradients or relative total enthalpy gradients,
- and a secondary vortex system which is limited to the (friction-affected) boundary layer region. The cause of this type of secondary flow is the existence of pressure gradients which are impressed on the boundary layers by the main flow and which, because of the small velocities within the boundary layers, cannot be counterbalanced by any dynamic forces. The result is then a secondary flow from higher to lower pressure.

For the case being studied here of an impeller blade channel with radial ending blades, what results, therefore, under the effect of Coriolis acceleration and standard acceleration (due to flow line bending) is a collection of low-energy boundary layer materials in the region of the front wall of the channel and suction side of the blades (cf. measured secondary flow curve in Fig. 6.16). The secondary flow effects occurring in centrifugal impellers have been theoretically treated in detail by Howard in [6.21].

Besides the development of the secondary flow field, the pressure gradients in a cross-sectional area of the relative flow in the impeller induced by ideal field forces also affect

the turbulence structure of the wall boundary layers. On a concave curved wall or on the pressure side of the rotating blade channel, with transverse movements in the turbulent wall boundary layer, the faster flow particles are forced towards the wall under the effect of centrifugal or Coriolis forces, and the slower particles are forced away from the wall. Conversely, on a convex curved wall or on the suction side of the blade channel the slow particles become stabilized in their path on the wall and thus reduce turbulent exchange movements with faster flow particles. This damping of the turbulent mixing also reduces the Reynolds shearing stresses and thus -- with positive pressure gradients in the flow direction -- the drag effect of the outer flow on the boundary layers close to the wall, so that, on the whole, the tendency of the flow to separate increases. In the case of flow separation, the turbulence damping effect also involves the free plane of shear between the jet region and the region of separated flow. As a result, the turbulent mixing of high-energy and low-energy material is suppressed.

/137

With the centrifugal impeller with radially ending blades in question here, what results in the transition region from the axial into the radial portion of the impeller is an intensified overlapping of the damping effects mentioned (due to rotation, or the bending of the channel in the meridian and circumferential direction) in the corner of the channel between the housing wall and the suction side of the blade channel [6.12, 6.13].

Studies by Bradshaw [6.22] on the effect of longitudinal channel bending have shown that already at a ratio of  $\delta/R_K = 1/80$  (boundary layer thickness / bending radius of the wall) the wall friction coefficient  $c_f$ , or the distance to the point of separation, decreases by 10% in comparison with the case without any bending.

As Johnston and co-workers [6.23] in both theoretical and experimental studies have shown, an increase in the angular velocity of the rotating system likewise causes an increase in the turbulence damping effects which, under certain circumstances, can lead to a complete relaminization of the blade boundary layer on the suction side.

In spite of this fundamental finding on the essential flow mechanisms in the centrifugal impeller, quantitative treatment of this phenomenon is still in its early stages. Even for the comparatively simple case of a rotating diffuser with radial, straight side walls, the solutions available at this time are still unsatisfactory. This is true both for the consideration of secondary flows (cf. Moore [6.24]) and for bending and rotation effects on the structure of the turbulence (cf. Eide and Johnston [6.25]).

In view of this situation, the detailed analysis of the flow measurements made in the centrifugal compressor impeller being studied here [6.12, 6.14] have up to now been limited to a qualitative discussion of the observed flow mechanisms. As an example, Fig. 6.16 shows the main secondary flow pattern in the centrifugal impeller region. This pattern was derived from relative velocity distributions in measuring surface (13) ( $x/s_m = 0.87$ ). In this case, for reasons of simplicity -- and

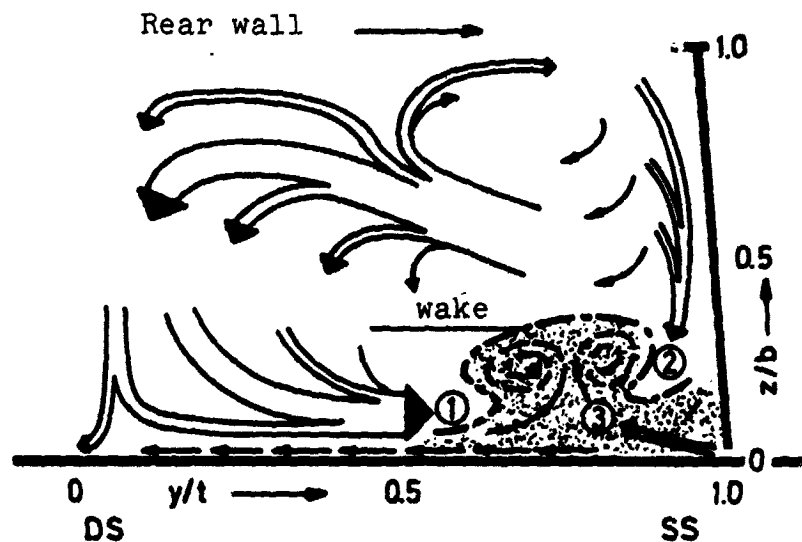


Fig. 6.16. Principle secondary flow pattern in the radial portion of the impeller blade channel (with respect to the blade-congruent main flow).

deviating from the usual definition -- all velocity components transverse to the blade-congruent flow are designated as secondary flow. The movement of the core flow in the direction towards the pressure side of the blade channel certainly in this channel cross-section already contains components which are determined by the flow reducing deflection in the region of the impeller outlet (relative channel vortex). This transverse movement ends up in the region of the front wall of the channel (arrow 1) as a dominating primary vortex. This removes low-energy flow material from the channel surfaces passed over and feeds it into the wake region. The same is true for a weaker secondary vortex in the region of the rear wall of the channel and blade suction side (arrow 2). Finally, due to the gap between the outer contour of the impeller and the housing, additional low-energy material is brought into the wake (arrow 3). By contrast, the effect of friction with the housing wall on the measured relative velocity curve remain remarkably small. /139

Studies on the development of secondary flow intensity [6.12]

have shown that in the axial inlet portion of the centrifugal compressor impeller (measuring surfaces ⑦ and ⑩) practically blade-congruent flow predominates (deviation between blade angles and relative flow direction  $\Delta\beta < \pm 1^\circ$ ); in measuring surface ⑪ -- at the beginning of the radial impeller region -- appear the first, clearly measurable signs of secondary movements ( $\Delta\beta < \pm 5^\circ$ ) which rapidly increase in intensity up to the impeller outlet ( $\Delta\beta \approx \pm 25^\circ$ ).

The principle pattern and the sharp increase in intensity in the secondary flows towards the impeller outlet are largely in keeping with theoretical expectations [6.12]. It is obvious to assume that the rapid increase in the wake region observed at the same time is closely connected with this. The following model describes this interaction:

The slowdown in flow in the axial region of the impeller leads to an increase in thickness in the housing boundary layer (cf. measuring surface ⑪ in Fig. 6.15, upper graph). The incipient loss-affected region of separation in measuring surface ⑪ also increases the total enthalpy gradient transverse to the direction of flow. As a result of this and as a result of the additional displacement effect of the wake, the intensity of the secondary flow increase in the region of the meridional bend in the channel. This in turn leads to an increased feeding of low-energy flow material into the wake (arrow 1 in Fig. 6.16). The turbulence damping effect present in the free plane of shear between the jet region and wake region suppress the turbulent mixing of the two regions. This finds its expression in the steep, relatively stable velocity gradients at the edge of the wake region (cf. Fig. 6.13, measuring surfaces ⑬ and ⑭) and in the loss concentration shown in Fig. 6.14. The process described explains the rapid increase in wake regions even in such cases where the flow separates relatively late in the impeller flow channel.

To be sure, the flow development described does not yet permit us to say anything about the exact causes of the separation of flow. The interpretation of the available findings here provides only clues on the relative importance of the flow mechanisms in question. The separation begins in measuring surface 11 in the region of the greatest channel bending. In actuality, measurements here show a clear drop in the fluctuation intensity of the absolute velocity vector in the region of the front wall of the channel and the blade suction side [6.12, 6.14]. This indicates the turbulence damping effects described. By contrast, in view of the small secondary flow intensity in this region, the collection of low-energy flow material appears still less important. /140

Taylor, in [6.26] has discussed in detail the shapes of two-dimensional and three-dimensional boundary layer separations.

In the first case, the flow separates at a singular point at which the wall friction coefficient  $c_f = 0$ . What develops downstream then are pulsating back currents and high flow losses in the region of separation. By contrast, three-dimensional separations have as the only criterion [sic] that the flow leaves the blade surface; the wake flow proceeds steadily and less loss-affected (also see discussion section in [6.14]).

In the present case, the three-dimensional character of the total flow, the absence of complete flow stagnation at the point of separation (Fig. 6.13, measuring surface (11)) and the relative stable form of the wake area can be interpreted as characteristics of three-dimensional flow separation.

Perhaps what happens -- as suggested in Fig. 6.6 in the region of the wake -- when secondary flows (1) and (2) + (3) collide, the boundary layers curly up. This forces the main flow away from the wall and thus initiates the separation. It is conceivable that a new state of equilibrium is then established in the flow, in the process of which the separation point migrates upstream into the region where turbulence damping effects and weak secondary flows already increase the tendency towards separation of the channel boundary layers.

## 7. Theoretical Treatment of the Jet-Wake Flow behind the Impeller Outlet /141

The experimental findings discussed in the previous section are characteristic of the disturbed flow behind highly-loaded centrifugal compressor impellers. The strongly pronounced jet-wake distributions of the relative velocity at the outlet of the individual blade channels rotate with the impeller and in so doing extend radially so far into the bladeless diffuser until the velocity differences in the circumferential direction disappear as a result of mixing and equalization processes. In this region the absolute flow in the diffuser is periodically non-steady. With the usual assumption of a steady, i.e. axially symmetric diffuser flow, it is therefore not possible to accurately determine the flow mechanisms occurring in the wake region of the centrifugal impeller.

Starting with a simplified, two-dimensional model of the disturbed flow at the impeller outlet, Dean and Senoo [7.1] developed a theoretical solution method with which it is possible to determine, at least approximately, the mixing processes in the sphere of influence of the wake region. From this can then be drawn important inferences as to the inter-relationship between the impeller and diffuser, which, for example, find their expression, in connection with stage design, in the selection of the inlet diameter of the bladed diffuser. Detailed knowledge of jet-wake mixing processes is also important for evaluating noise problems and answering questions concerning



mechanical strength in connection with diffuser-blade vibration.

Dean and Senoo set up their theory, which was published in 1960, for two-dimensional, incompressible flow. Subsequently, Johnston and Dean [7.2] simplified, in comparison with the original Dean-Senoo theory, the calculation of mixing losses. In their simplification the mixing process is treated theoretically like the Carnot transition. In [6.4, p. 109 f] Traupel discusses a comparable method for calculating mixing losses behind a centrifugal impeller. The sudden expansion analysis given by Johnston and Dean for two-dimensional, incompressible flow was expanded by Dean and co-workers [6.5, app. II] to two-dimensional flows, while Watson and Ingham [7.3] setup a solution for compressible flow.

/142

The measuring techniques developed within the scope of this study made it possible for the first time to exactly measure the disturbed flow in the diffuser inlet region up to circumferential velocities for the impeller of  $u_2 < 400$  m/s. Therefore, for the analysis of flow mechanisms in a complex flow the comparison of experimental results with theoretical calculations based on the theory given by Dean and Senoo presented itself. Of course, this required extending the theory to the region of compressible flow. In spite of the strongly idealized model, the thus modified theory had the advantage that the continuous development of jet-wake mixing can be determined with it. The comparison with measurements made at different distances behind the impeller outlet should then provide information on to what extent the theoretically considered flow mechanisms affect the actual flow, and from this to derive, if necessary, further refinements of the theory.

## 7.1 Expanded Dean-Senoo Theory

### 7.1.1 Analytical Flow Model

The mixing and equalization processes behind the impeller outlet were considered in the reference system rotating with the impeller. Within the relative system the flow can be considered steady and two-dimensional in a plane perpendicular to the compressor axis ( $\delta/\delta z = 0$ ). In the circumferential direction the disturbed real flow is schematically approximated by the periodic curve at the impeller outlet shown in Fig. 7.1 a. The flow region of a blade spacing is divided into two areas, each with a constant relative velocity vector.

Analogous to the designations "wake" and "jet" in the original work of Dean and Senoo, here, too, the region of separated flow is labelled "wake" and the region of undisturbed flow is called "jet." The wake component  $\epsilon_2$  extends along the blade suction side with low relative velocity  $w_{2T}$ , while the jet region with higher velocity  $w_{2S}$  fills up the rest of the cross-section up to the blade pressure side.

/143

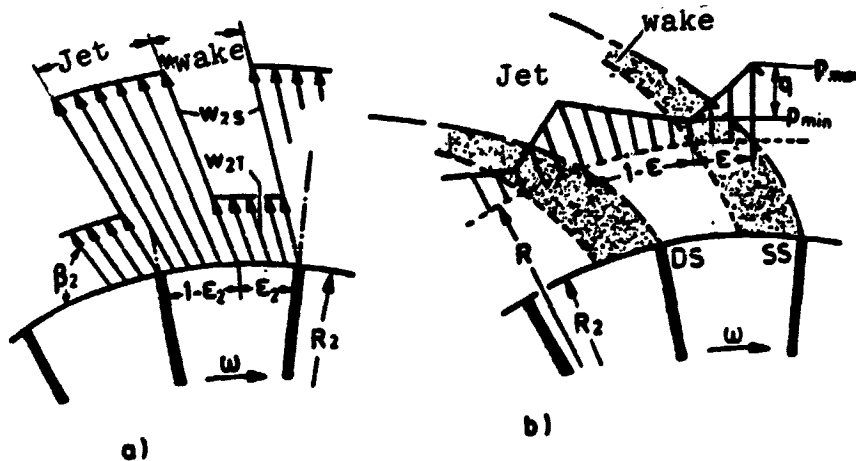


Fig. 7.1a. Analytical flow model at the impeller outlet; b. Schematic diagram of the development of jet-wake mixing in the bladeless diffuser.

The two partial flows are not supposed to mix on their way through the bladeless diffuser, but rather -- as shown schematically in Fig. 7.1b with a constant mass flow component in the rotating system, they are supposed to flow next to one another. As a compatibility condition for the steady relative flow it then holds that at the jet-wake interfaces the static pressure and the direction of the relative velocity are equal on both sides.

As Fig. 7.1b illustrates, the wake component  $\epsilon$  steadily decreases as the radii ratio increases. Strictly speaking, therefore, on the same radii the flow direction at the front side of the jet (in the direction of rotation) must be distinguished from that on the rear side. However, in this simplified, integral flow analysis a uniform flow direction  $\beta$  in each radius is assumed for the total flow. The nonsteady absolute velocity  $c$ , however, is not made unidirectional, as is obvious from the velocity vector diagram shown in Fig. 7.2.

The last-mentioned, limiting condition of the Dean-Seno /144 theory is not included in the expanded model discussed in Section 7.2 for estimating the influence of variable relative flow direction in the jet region and wake region.

The expanded theory proposed here takes into consideration changes in density in the radial direction, but in so doing ignores density differences between the two partial flows.

With respect to the equalization of the disturbed jet-wake

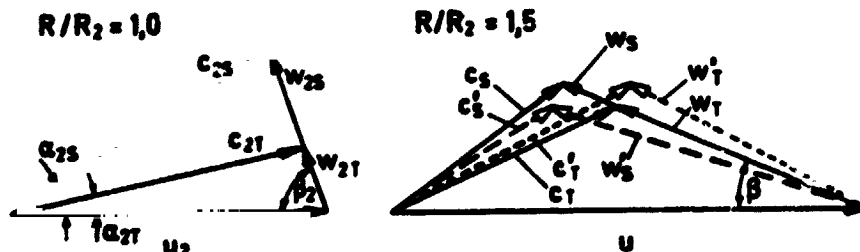


Fig. 7.2. Velocity vector diagrams in various radii ratios to illustrate, by way of example, the exchange of energy between jet regions and wake regions.

velocity distribution, the Dean-Senoo theory takes into account three flow mechanisms:

- 1) Friction on the diffuser side walls;
- 2) Interface friction and
- 3) Reversible exchange of energy between jet and wake regions.

The diffuser wall friction force per unit area in their theory is expressed in the usual manner by a constant friction coefficient  $c_f$  proportional to the square of the absolute velocities, whereby this force acts in both regions against the absolute velocity direction in each case:

/145

$$F_S = c_f \rho c_S^2 / 2 \quad (\text{jet}) \quad (7.1a)$$

$$F_T = c_f \rho c_T^2 / 2 \quad (\text{wake}) \quad (7.1b)$$

To take into account friction at the interface, equal and opposite turbulent shearing stresses tangential to the jet-wake boundaries are assumed. Over a plane of shear friction coefficient  $\zeta$  these stresses are set proportional to the square of the relative velocity difference:

$$S = \zeta \rho (w_S - w_T)^2 / 2 \quad (7.2)$$

Besides these two loss-affected flow mechanisms, the reversible energy exchange between jet and wake regions only influences the intensity of the mixing of the disturbed flow.

This type of energy exchange arises under the effect of standard stresses between two (nonsteady) partial flows in the absolute system which in the rotating reference system flow

steadily next to one another (as everyone knows, in so doing, the transfer of work due to normal stresses, in contrast to that due to shearing stresses, is reversible).

Foa [7.4] has studied a number of jet engines which operate according to this principle. In the present case of disturbed jet-wake flow, the velocity vector diagram shown in Fig. 7.2 illustrate, by way of example, this effect:

If the jet-wake partial flows shown in the diffuser inlet ( $R/R_2 = 1.0$ ) were continued with absolute velocities  $c_{2S}$  and  $c_{2T}$  as in the axially symmetrical case -- mutually unaffected -- then in the radii ratio  $R/R_2 = 1.5$  the absolute velocities  $c'_S$  and  $c'_T$  would occur. In the rotating system these would correspond /146 to the -- no longer unidirectional -- relative velocity vectors  $w'_S$  and  $w'_T$ . However, to fulfill the compatibility condition between the jet and wake, both regions must interact in such a way that the real relative velocity vectors  $w_S$  and  $w_T$  turn out to have a common relative flow direction  $\beta$ . As Fig. 7.2 clearly shows, this only becomes possible with a simultaneous change in angular momentum  $R \cdot \Delta c_u$  in the jet and wake. In so doing, the energy equilibrium for the example shown requires that the energy given off by the wake regions equals that picked up by the jet regions. The force which causes these changes in angular momentum and which provides for the fact that the real absolute velocities  $c_S$  and  $c_T$  occur instead of  $c'_S$  and  $c'_T$  is theoretically approximated by a sawtooth-shaped curve in the circumferential direction of the static pressure -- Fig. 7.1b -- with equal and opposite compressive forces on the jet and wake region. This compressive force rotates together with the disturbed velocity distribution in the absolute system where it is recorded at a determined place in the diffuser as a periodic alternating pressure with a fluctuation range  $q$ .

For a theoretical illustration of the reversible energy exchange between relative flow lines, the energy equation introduced above for nonsteady, compressible and frictionless absolute flow -- Eq. (6.1) -- is rewritten for the case in question. With the designations in Figs. 7.1 and 7.2 and with  $\theta$  as the circumferential coordinate (positive in the direction of rotation), it holds for the change in angular momentum along a differential path length  $ds$  of a relative flow line:

$$d(Rc_u)/ds = -1/(w_p) \cdot \partial p / \partial \theta \quad (7.3)$$

In regions with -- in the direction of rotation -- negative pressure gradients (e.g. in the jet region in Fig. 7.1b) the angular momentum along the relative flow line increases, while in regions with positive pressure gradients the opposite effect occurs and thus the loss-free, energy mixing of the disturbed

flow is encouraged.<sup>1</sup>

As the measurements made at the impeller outlet confirm, the 90°-centrifugal impeller studied here generally possesses the higher kinetic energy in the wake. Therefore, in general, with the same mean static pressure at the diffuser inlet, the wake must perform work on the jet region in order to mix the flow in an axially symmetric manner on its way through the diffuser. However, as is confirmed by sample calculations made in Section 8.2, cases are theoretically quite possible in which the jet region first performs work on the wake in the diffuser inlet region and thus the difference in energy level between the two regions is increased even more. With larger radii ratios, the wake then transfers more energy back to the jet than it originally received, and in turn the tendency to axially symmetric mixing arises. The conditions shown in Fig. 7.2 for  $R/R_2 = 1.5$  (with the corresponding pressure curve in Fig. 7.1b) are therefore to be understood only as a typical example which illustrates the necessity for the exchange of energy between the jet and wake as a result of the required geometric compatibility within the disturbed relative flow.

/147

### 7.1.2 Fundamental Flow Equations

Since according to our hypothesis the jet and wake regions do not mix, the fundamental equation for steady relative flow between a position in the diffuser inlet (subscript e) and anyplace downstream in the diffuser (without subscripts) can be setup separately for both regions. In so doing, all velocities are made dimensionless with the circumferential velocity at the impeller inlet  $u_2$ , e.g.  $W_S = w_S/u_2$  and  $U = u/u_2$ . Symbols are given corresponding to the definitions in Figs. 7.1 and 7.2. In addition,  $c_f$  stands for the wall friction coefficient,  $\zeta$  the shearing stress coefficient,  $b$  the axial diffuser width,  $z$  the number of blades,  $\rho$  the density. As for the subscripts, S stands for jet, T wake,  $u$  circumferential component, and by way of simplification  $R' = R/R_2$ ,  $b' = b/b_e$  and  $\rho' = \rho/\rho_e$ .

Continuity Equation:

/148

$$a) \text{ Jet region} \quad 2 \pi R' b (1-\epsilon) \rho W_S \sin\beta =$$

$$2 \pi R'_e b_e (1-\epsilon_e) \rho_e W_{eS} \sin\beta_e, \quad (7.4)$$

with  $A = R'_e (1-\epsilon_e) W_{eS} \sin\beta_e$  it follows that

---

1. Also see the discussion on the corresponding experimental results in the diffuser inlet region, Section 6.1.1, and the quantitative estimates on reversible energy exchange by Senoo and Ishida in [7.5].

$$1-\epsilon = A / (R' W_S \sin\beta b' \rho') \quad , \quad (7.4a)$$

$$\epsilon = 1 - A / (R' W_S \sin\beta b' \rho') \quad . \quad (7.4b)$$

b) Wake Region

$$2 \pi R' b \epsilon \rho W_T \sin\beta = 2 \pi R'_e b_e \epsilon_e \rho_e W_{eT} \sin\beta_e \quad , \quad (7.5)$$

with  $B = R'_e \epsilon_e W_{eT} \sin\beta_e$  it follows that

$$W_T = B / (R' \epsilon \sin\beta b' \rho') \quad (7.5a)$$

and with Eq. (7.4b) we obtain

$$\gamma = W_T / W_S = B / (R' W_S \sin\beta b' \rho' - A) \quad . \quad (7.6)$$

Angular Momentum Equation:

a) Jet Region

$$\begin{aligned} & 2 \pi R' b (1-\epsilon) \rho W_S \sin\beta [d(R' U - R' W_S \cos\beta) / dR'] = \\ & = - 2 \pi R'^2 R_2 c_f (1-\epsilon) \rho C_S (U - W_S \cos\beta) + \quad (7.7a) \\ & + \zeta z b R' \rho (W_S - W_T)^2 \operatorname{ctg}\beta - z b R' q / u_2^2 \end{aligned}$$

On the left side of Eq. (7.7a) stands the change in angular momentum flow through the annular volume with the width  $b$  and the radial distance  $dR'$ , while on the right hand side of the equation are arranged the moments of the external forces. The first expression stands for the moment due to friction on the front wall and rear wall of the diffuser, the second stands for the moment of plane of shear friction in the  $2z$  jet-wake boundary areas and the last expression stands for the torque which arises as a result of the pressure difference  $q$  between the front and rear boundary (in the direction of rotation) of the jet region (cf. Fig. 7.1b). By definition,  $q$  is positive if the static pressure on the front side of the jet is greater than on the rear side.

With  $Q = q / (\rho u_2^2)$  it finally follows that

/149

$$\begin{aligned} & (1-\epsilon) \{W_S \sin\beta [d(R' U - R' W_S \cos\beta) / dR'] + \\ & + c_f R' R_2 C_S (U - W_S \cos\beta) / b\} = \quad (7.7b) \\ & = [\zeta z (W_S - W_T)^2 \operatorname{ctg}\beta - z Q] / (2 \pi) \quad . \end{aligned}$$



If one replaces  $Q$  in Eq. (7.9a) with  $Q$  from Eq. (7.7b) then it follows that:

$$\begin{aligned} dP/dR' &= U^2 / R' - (dW_S^2/dR') / 2 - \\ &- c_f R_2 C_S (W_S - U \cos\beta) / (b \sin\beta) - \\ &- \zeta z [(W_S - W_T) / \sin\beta]^2 / [2 \pi R' (1-\epsilon)] \end{aligned} \quad (7.11)$$

and by combining Eq. (7.10) with Eq. (7.8) according to

$$\begin{aligned} dP/dR' &= U^2 / R' - (dW_T^2/dR') / 2 - \\ &- c_f R_2 C_T (W_T - U \cos\beta) / (b \sin\beta) + \\ &+ \zeta z [(W_S - W_T) / \sin\beta]^2 / (2 \pi R' \epsilon) ; \end{aligned} \quad (7.12)$$

in so doing, use is made of the following equations for the jet region and wake region:

$$\begin{aligned} W^2 &= (W \sin\beta)^2 + (W \cos\beta)^2 \quad \text{and} \\ dW^2/dR' &= 2 W \sin\beta [d(W \sin\beta)/dR'] + \\ &+ 2 W \cos\beta [d(W \cos\beta)/dR'] . \end{aligned}$$

If one eliminates  $dP/dR'$  from Eqs. (7.11) and (7.12), then this gives us:

$$\begin{aligned} d(W_S^2 - W_T^2)/dR' + \zeta z (W_S - W_T)^2 / [\pi R' \epsilon (1-\epsilon) \sin^2\beta] + \\ + 2 c_f R_2 [C_S (W_S - U \cos\beta) - C_T (W_T - U \cos\beta)] / (b \sin\beta) = 0. \end{aligned} \quad (7.13)$$

Setting the right side equal to Eqs. (7.7b) and (7.8) leads to:

$$\begin{aligned} W_S (1-\epsilon) [d(R' W_S \cos\beta)/dR'] + W_T \epsilon [d(R' W_T \cos\beta)/dR'] - \\ - 2 U [W_S (1-\epsilon) + W_T \epsilon] - \\ - c_f R' R_2 [C_S (1-\epsilon)(U - W_S \cos\beta) + C_T \epsilon (U - W_T \cos\beta)] / \\ / (b \sin\beta) = 0 . \end{aligned} \quad (7.14)$$



Since the absolute velocity  $C$  -- for the jet region and wake region -- can be expressed by means of the cosine equation by  $W$ ,  $U$  and  $\beta$ :

/151

$$C = (W^2 + U^2 - 2 U W \cos\beta)^{1/2}, \quad (7.15)$$

then Eqs. (7.13) and (7.14) still contain only the four unknowns  $W_S$ ,  $W_T$ ,  $\epsilon$  and  $\beta$ . Of these,  $\epsilon$  and  $W_T$ , for example, can be replaced by Eqs. (7.4b and (7.6). The equations derived above -- (7.13) and (7.14) -- thus represent a system of two coupled differential equations of the first order for the dependent variables  $W_S(R')$  and  $\beta(R')$ . This system of equations is solved according to the Runge-Kutta method (for differential equation systems) discussed in detail in [7.6].

### 7.1.3 Structure of the Computation Program

As starting conditions, the variables  $W_{eS}$ ,  $W_{eT}$ ,  $\beta_e$ ,  $\epsilon_e$  and  $R'_e$  are given. Additional information on the static pressure  $p_e/p_{t0}$  and the total temperature in the diffuser  $T_{t4}$  are given for the calculation for compressible flow. In addition, the friction coefficients  $c_f$  or  $c_f(R)$  and  $\zeta$ , the impeller blade number  $z$  and the effective width<sup>1</sup>  $b(R)$  are known.

The Runge-Kutta approximation method consists of two coupled calculations running in parallel in accordance with the specification given below for differential equations. Progressively, in each case, two function values are calculated at four equidistant reference points between the known initial values (subscript A) and the end values being sought (subscript E) (total interval  $\Delta R' = R'_E - R'_A = 0.01$ ). From the function values determined in this way two mean values are then formed for calculating the new final values.

With  $\epsilon = \text{Eq. (7.4b)}$ ,  $\gamma = \text{Eq. (7.6)}$ ,  $C_{S,T} = \text{Eq. (7.15)}$  and the following notation:

/152

$$\begin{aligned} C_1 &= (1-\epsilon) \epsilon \sin^2\beta (1-\gamma^2)^2 + \gamma^2, \\ C_2 &= (1-\epsilon) \sin^2\beta (1-\gamma^2) + \gamma^2, \\ C_3 &= C_S (W_S - R' \cos\beta) - C_T (W_T - R' \cos\beta), \end{aligned}$$

---

1. Section 7.1.4 contains data for taking into account the boundary layer displacement thickness.

$$\begin{aligned}
C_4 &= C_S (1-\epsilon) (R' - W_S \cos\beta) + C_T \epsilon (R' - W_T \cos\beta) , \\
C_5 &= \epsilon (1-\epsilon) (1-\gamma^2)^2 + \gamma^2 , \\
C_6 &= \epsilon (1-\gamma^2) + \gamma^2 , \\
C_7 &= 1 - \epsilon (1-\gamma^2) , \\
C_8 &= 1 - \epsilon (1-\gamma) \quad \text{and} \\
D &= (dp'/dR') / \rho'
\end{aligned}$$

it holds that:

$$\begin{aligned}
dW_S/dR' &= \\
&- \gamma^2 \cos\beta (W_S \cos\beta C_7 - 2 R' C_8) / (R' C_1) - \\
&- W_S z \zeta (1-\gamma)^2 C_2 / [2 \pi (1-\epsilon) R' \sin^2\beta C_1] - \\
&- c_f R_2 (\epsilon C_2 C_3 - \gamma^2 \cos\beta C_4) / (W_S b \sin\beta C_1) - \\
&- W_S \sin^2\beta \gamma^2 C_7 D / C_1 ;
\end{aligned}$$

(7.17)

$$\begin{aligned}
d\beta/dR' &= \\
&(W_S \sin\beta \cos\beta C_5 - 2 R' \sin\beta C_6 C_8) / (W_S R' C_1) - \\
&- \zeta z (1-\gamma)^2 (1-\gamma^2) \cos\beta / (2 \pi R' \sin\beta C_1) - \\
&- c_f R_2 [\epsilon (1-\epsilon) (1-\gamma^2) \cos\beta C_3 + C_4 C_6] / (W_S^2 b C_1) - \\
&- \gamma^2 \sin\beta \cos\beta D / C_1 .
\end{aligned}$$

If one of the limiting conditions  $\epsilon < 0.01$  or  $\delta = \epsilon (1-\gamma) < 0.001$  is fulfilled, then the disturbed flow can be regarded as "mixed" [equalized], and  $\epsilon$  is set equal to 0 and  $\gamma$  is set equal to 1 in Eqs. (7.16) and (7.17).

In Eqs. (7.16) and (7.17)  $D$  expresses the variation in density in the radial direction. The expanded Dean-Senoo theory presented here takes into consideration the compressibility effects in an iteration cycle after each step of the Runge-Kutta method. In so doing, two equations of the computing method given by Traupel ([6.4], Eqs. 4.5(16) and 4.5(21)) are introduced for the compressible, axially symmetric diffuser flow. As written here, these equations are expressed as follows:

/153

$$\int_{p_A}^{p_E} dp/\rho = \kappa/(\kappa-1) p_A/\rho_A [(p_E/p_A)^{(\kappa-1)/\kappa} - 1], \quad (7.18)$$

$$\rho_E = [p_A/(p_E \rho_A) + (\kappa-1)/(2\kappa) (\bar{C}_A^2 - \bar{C}_E^2) u_2^2/p_E]^{-1}. \quad (7.19)$$

During the first iteration loop, since  $D = 0$  in Eqs. (7.16) and (7.17) the change in density is ignored to begin with. With the aid of Eq. (7.11), the results found in this way permit the computation of the left side of Eq. (7.18). From this follows the static pressure at the end of the interval  $p_E$ . After determination of the momentum-averaged absolute velocity  $\bar{C}$  of the total flow, Eq. (7.19) makes possible a first approximation for the density at the end of the step  $\rho_E$ . For the following iteration loops  $D$  is then set equal to

$$D = (d\rho'/dR') / \rho' = 2 [(p_E - p_A)/\Delta R'] / (\rho_A + \rho_E) \quad (7.20)$$

and thus the radial change in density is approximately taken into account.

Finally, the total pressure in each of the step points is calculated from:

$$p_t = p [1 - (\kappa-1)/2 \bar{C}^2 u_2^2 / (\kappa R T_{t4})]^{1/(1-\kappa)}; \quad (7.21)$$

whereby  $R$  stands for the gas constant of the air which is regarded as an ideal gas.

Computer results regarding the course of the jet-wake mixing process are presented in section 8.2 and 8.3.

#### 7.1.4 Determination of the Wall Friction and Interface Friction Coefficients and the Boundary Layer Displacement Thickness

The Dean-Seno theory contains two unknown parameters -- the wall friction coefficient  $c_f$  and the jet-wake interface friction coefficient  $\zeta$ . All other parameters are given by the conditions in the inlet of the unbladed diffuser and by the geometry of the flow channels. In view of the complicated flow conditions in the diffuser inlet region, these coefficients cannot be determined theoretically with sufficient accuracy. There-

fore, one is directed to direct measurements or, as in the case of  $\zeta$ , to adopting values which have been determined for visible flows.

In Fig. 7.3 are plotted experimentally determined curves of  $c_f$  as a function of the diffuser radii ratio  $R/R_2$ . For the centrifugal compressor stage studied here, a typical  $c_f$  curve (DFVLR) was determined according to the method given by Traupel in ([6.4], p. 113f) for the test point at 14,000 rpm,  $\dot{m} = 5.31$  5.31 kg/s. In so doing, the basis of the  $c_f$  calculation is formed by "conventional," time-average measurements of the wall pressure  $\bar{p}$ , the total pressure  $\bar{p}_t$ , the total temperature  $\bar{T}_t$  and the flow direction  $\bar{a}$  as a function of  $R/R_2$ .

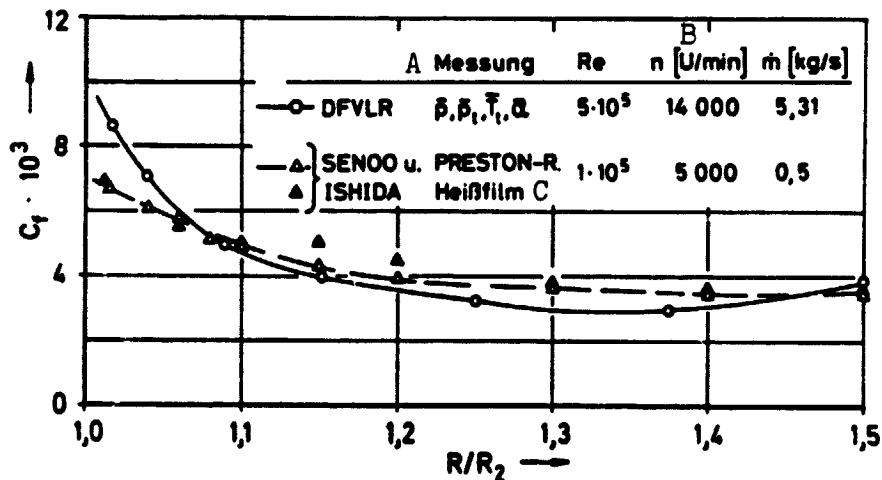


Fig. 7.3. Experimentally determined curve of the wall friction coefficient  $c_f$  as a function of the radii ratio  $R/R_2$  of an unbladed centrifugal diffuser. (Re number at the diffuser inlet established with diffuser width).

Key: A) Measurement      C) Hot film  
B) rpm

For purposes of comparison,  $c_f$  values were plotted which were measured by Senoo and Ishida [7.8] in a parallel-walled diffuser behind an impeller with backward bent blades. In the region of the approximately axially symmetric diffuser flow,  $R/R_2 > 1.15$ , the  $c_f$  values shown at the given Reynolds numbers largely agree with the values for technically rough tubing. /155

It should be noted that the  $c_f$  values of Senoo and Ishida were measured directly by means of a Preston tube, or nonsteadily by means of a hot-film probe which was inserted transversely into

the diffuser wall.<sup>1</sup> While for  $R/R_2 > 1.15$  the DFVLR curve, corresponding to the varying Reynolds numbers, clearly lies below the measurements made by Senoo and Ishida, the DFVLR results for  $R/R_2 = 1.15$  increase comparatively more sharply up to the impeller outlet. This difference is presumably a result only of measuring techniques, since the total pressure measurements in the diffuser inlet region used to determine the wall friction coefficient also involve the momentum loss which arises due to the mixing of the disturbed flow in the diffuser inlet region.

For calculating friction losses, Traupel ([6.4], p. 125) recommended  $c_f = 0.0045-0.006$ . Dean and Senoo [7.1] and later Senoo and Ishida [7.5] used  $c_f = 0.005$ , independent of the radii ratio  $R/R_2$ . The shaded curve for  $c_f(R)$  in Fig. 7.3 is based primarily on the calculations in sections 8.2 and 8.3. In one example,  $c_f$  is set equal to 0.0065.

For the interface friction coefficients  $\zeta$ , Dean and Senoo [7.1], in their parameter study, gave the values 0.094 and 0.037 without explaining how these numerical values were derived.

Shearing stress measurements for "free" turbulent shear flows are currently available only for a few simple sample cases. In ([3.9], Fig. 6-21) Hinze cites measurements by Corrsin made in a round free jet (2.5 cm in diameter) and in ([3.9] Fig. 6-6) he cites measurements by Townsend made in the wake region of a circular cylinder (1.59 mm in diameter). In these cases, maximum shearing stress coefficients  $\zeta$  of 0.03 (free jet) and 0.12 (cylinder wake) respectively were observed. These values coincide well with the theoretical computer results of Rotta ([7.9], Fig. 74) for the maximum values of the Reynolds shear stresses on a level free jet.

Thus the order of magnitude of the  $\zeta$  values originally used by Dean and Senoo are well confirmed by these results. Of course, it must still be taken into consideration that the simple cases cited above for purposes of comparison can certainly be applied only to a very limited extent to jet-wake shearing surface friction in the rotating system. Therefore, Dean also assumes in a qualitative consideration [7.10] -- which is essentially based on the variable effect of Coriolis forces in jet and wake regions -- that the friction coefficient on the rear side of the jet (in the direction of rotation) is strongly increased ( $\zeta < 0.5$ ), while on the front side of the jet the turbulent mixing is drastically reduced ( $\zeta = 0$ ). Therefore he proposes an average jet-wake friction coefficient of  $\zeta = 0.25$  in place of the value of  $\zeta = 0.094$  used in the original study.

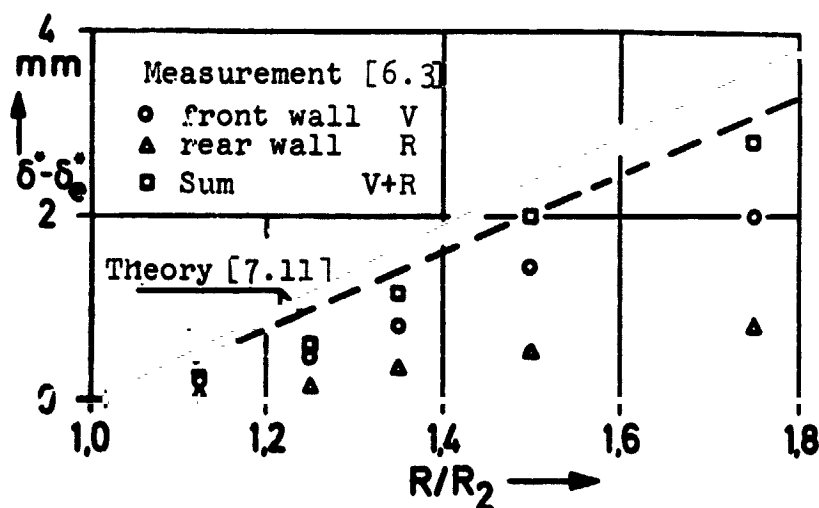
/156

---

1. Fig. 7.3 shows the mean values over time determined from this.

In the friction-affected diffuser flow, boundary layers occur on the front wall and rear wall of the diffuser which, due to their displacement effect which increase with downstream distance, cause a decrease in the flow cross-section with respect to the geometrical cross-sectional contour. This displacement effect is characterized by the boundary layer displacement thickness  $\delta^*$ . Since no boundary layer measurements are contained in the test program discussed here, we will refer to data given in the literature.

Fig. 7.4 shows experimental results obtained by V.D. Voorde and Bos [6.3] in a parallel-walled centrifugal diffuser with a superimposed, axial-radial deflection with purely radial flow. A striking feature here is the sharper increase in boundary layer thickness on the front wall of the diffuser. At the same time, Fig. 7.4 contains results of a theory<sup>1</sup> given by Scholz [7.11] on the increase in boundary layer displacement thickness in a plate diffuser with level source flow. The good agreement between theory (broken line) and experimental results from [6.3] shows that the simplifying theoretical assumption of a linear increase in the displacement thickness is justified.



/157

Fig. 7.4. Increase in boundary layer displacement thickness  $\delta^* - \delta^*_0$  in an unbladed, centrifugal diffuser, with respect to the radii ratio of the DFVLR stage ( $R_e/R_2 = 1.017$ ).

Theoretical prediction [7.11]:

- a) ----- for the test conditions in [6.3],
- b) ————— for DFVLR measurements at 14,000 rpm

1. This theory is based on the "Quadrature Method for Calculating Turbulent Friction Layers" by Truckenbrodt.

The solid line marks the theoretical prediction for operating conditions such as were present with the DFVLR measurements at 14,000 rpm. This curve of the boundary layer displacement thickness was used as a basis for all of the sample calculations with the effect of wall friction discussed in Sections 8.2 and 8.3.

### 7.2 Expanded Model for Estimating the Influence of the Variable Relative Flow Direction in the Jet Region and Wake Region

According to the Dean-Seno Theory it had been assumed up to now that jet and wake regions possessed a uniform relative flow direction  $\beta$ . However, in the actual flow the integral values  $\beta_S$  and  $\beta_T$  can differ distinctly. For example, evaluation of our experiments in the measuring plane directly behind the impeller outlet shows variations in direction on the order of  $10^\circ$  (cf. Fig. 8.22).

In order to estimate the influence of this effect which is not taken into account in the Dean-Seno theory, a simple, supplementary flow analysis -- following a proposal by Van Le [7.7] -- is carried out for the jet-wake flow model shown in Fig. 7.5.

/158

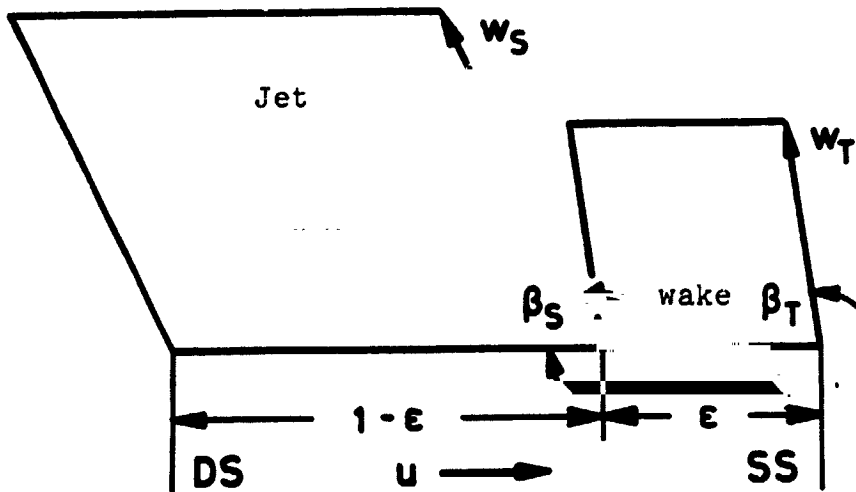


Fig. 7.5. Flow model with variable relative flow direction in the jet region and wake region.

Between a place with the jet-wake velocity distribution in the diffuser inlet region (subscript e, or S (jet) and T (wake)) and

the radius, where the disturbed flow has become completely mixed, equations for the mass flow, the angular momentum and the kinetic energy were setup. Effects of friction and compressibility are not taken into consideration.

On the basis of this purely integral approach to the mixing of the jet and wake -- between the disturbed initial state and the fully mixed final state -- the discontinuity at the jet-wake boundary surfaces in the model, Fig. 7.5, is also permissible. All of the variables used in this analysis are defined in accordance with the graph shown in Fig. 7.5, 7.2 and 5.2.

Continuity Equation:

$$2 \pi (R b)_e [(1-\epsilon) W_S \sin\beta_S + W_T \sin\beta_T] = 2 \pi R b C_r, \quad (7.22)$$

$$R b C_r / (R b C_{rS})_e = (1-\epsilon) \{1 + \epsilon \gamma \sin\beta_T / [(1-\epsilon) \sin\beta_S]\}, \quad (7.22a)$$

For the parallel-walled diffuser it is valid that  $b = b_e$ , and for  $Rb$  (equal in area) =  $(Rb)_e$ .

Angular Momentum Equation:

/159

$$(1-\epsilon) (R^2 b C_{rS} C_{uS})_e + \epsilon (R^2 b C_{rT} C_{uT})_e = R^2 b C_r C_u, \quad (7.23)$$

$$R^2 b C_r C_u / [(1-\epsilon) (R^2 b C_{rS} C_{uS})_e] = 1 + \epsilon C_{rT} C_{uT} / [(1-\epsilon) C_{rS} C_{uS}] \quad (7.23a)$$

with Eq. (7.22a) it follows that

(7.23b)

$$R C_u / (R C_{uS})_e = \{1 + \epsilon \gamma \sin\beta_T C_{uT} / [(1-\epsilon) \sin\beta_S C_{uS}]\} / \{1 + \epsilon \gamma \sin\beta_T / [(1-\epsilon) \sin\beta_S]\} .$$

Finally, using the velocity components  $C_r$  from Eq. (7.22a) and  $C_u$  from Eq. (7.23b), if we calculate the kinetic energy flow of the absolute velocity  $C$ :

$$\dot{E} = \int \text{Masse} \cdot C^2 / 2$$

then we obtain the following as an



Equation for the Kinetic Energy:

$$(1-\epsilon) (R b C_{RS} C_S^2 / 2)_e + \epsilon (R b C_{RT} C_T^2 / 2)_e = (7.24)$$

$$R b C_r C^2 / 2$$

$$R b C_r C^2 / [(1-\epsilon) (R b C_{RS} C_S^2)_e] = (7.24a)$$

$$1 + \epsilon \gamma \sin\beta_T C_T^2 / [(1-\epsilon) \sin\beta_S C_S^2]$$

and setting in Eq. (7.22a):

$$\dot{E}/\dot{E}_e = (C / C_S)^2 \{1 + \epsilon \gamma \sin\beta_T / [(1-\epsilon) \sin\beta_S]\} / (7.24b)$$

$$/ \{1 + \epsilon \gamma \sin\beta_T C_T^2 / [(1-\epsilon) \sin\beta_S C_S^2]\}$$

The ratio  $\dot{E}/\dot{E}_e$  given with Eq. (7.24b) thus defines the upper limit value of the mixing losses of the partial flows discharged from the impeller with various relative flow directions. Results of an numerical parameter study using the above equations are presented in Section 8.3.

## 8. The Behavior of the Jet-Wake Flow in the Unbladed Centrifugal Diffuser /160

### 8.1 The Three-Dimensional Development of the Real Flow in the Inlet Region of the Diffuser

In Section 6 we discussed in detail the disturbed velocity distributions measured immediately behind the impeller outlet and its origination from a flow separation in the impeller. There we also showed that the observed, fundamental flow processes in the entire range of the performance graph studied between 10,000 and 18,000 rpm are largely similar so that the following, comprehensive discussion of jet-wake flow development in the diffuser inlet region can be restricted to measurements obtained at 14,000 rpm. In general, in so doing the curve for the operating point in the region of the optimum line,  $\dot{m}/\sqrt{\theta_0}/60 = 5.31$  kg/s, is described in detail by results obtained in measuring planes I-IV (corresponding to  $R/R_2 = 1.017, 1.039, 1.089$  and  $1.151$ ; cf. Section 5.1). Supplementing this information, the flow condition in measuring planes I and IV in the operating point near the stopper border and pump border is compared.

As in Section 6, the results are plotted for the outlet flow region of an impeller blade channel. This flow region is graphically simplified as a rectangle. In the real flow the

interfaces (cf. Section 5.3) between two adjacent flow regions are twisted in three-dimensions, as clearly illustrated in Fig. 8.1. These interfaces are determined from the position of the blade wake shifts in measuring planes I-IV. For the three operating points analyzed -- a -- c -- the graphs of interface development are largely congruent so that it appears permissible to compare the flow curves with one another for the various operating points in the simplified rectangular graph.

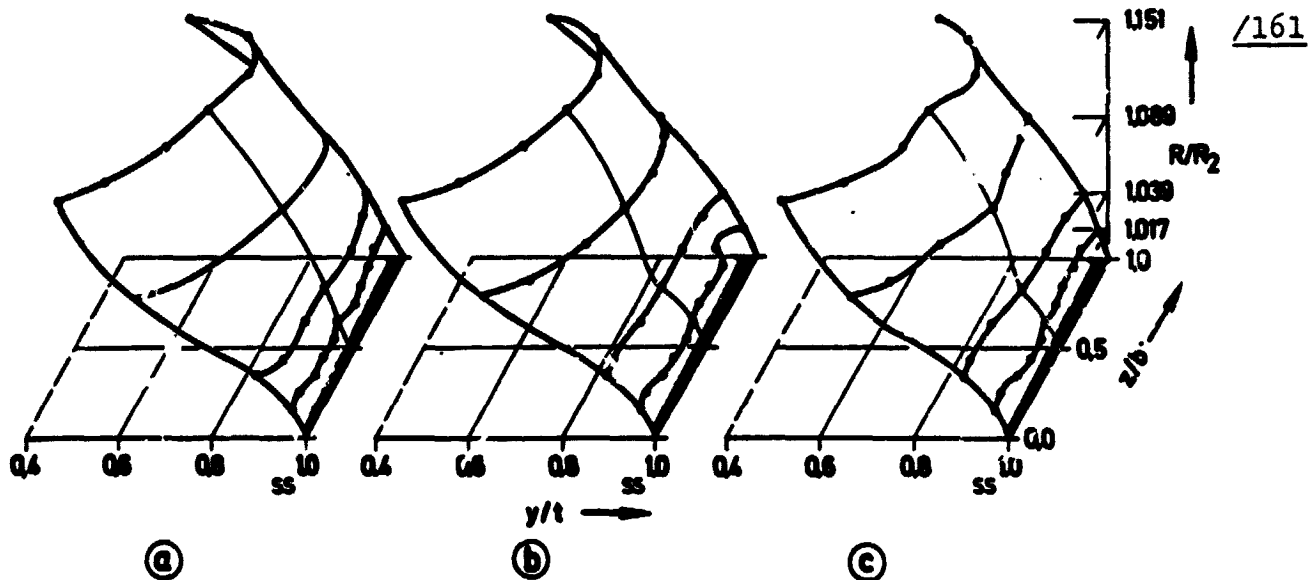


Fig. 8.1 Development of the interface between the flow regions of two adjacent blade channels in the diffuser input. Operating points at  $n/\sqrt{\theta_0} = 14,000$  rpm,  $\dot{m} \sqrt{\theta_0}/\delta_0$ : a 4.53 kg/s, b 5.31 kg/s, c 6.07 kg/s/

### 8.1.1 Static Pressure and Total Pressure

Fig. 8.2 shows the static pressure curve interpolated from the nonsteady pressure measurements made on the front and rear wall of the diffuser. In the circumferential direction, the flow region of an impeller blade channel is bounded by the interfaces mentioned.

First of all, a striking feature is the rapid reduction in the pressure gradient over the channel width  $z/b$  (front wall of the diffuser  $z/b = 0$ , rear wall  $z/b = 1$ ) between measuring planes I and II ( $R/R_2 = 1.017-1.039$ ). This is explained by the transition from the meridional channel deflection (in the impeller) into the straight centrifugal diffuser. In the circumferential direction, the variations in static pressure offset each other almost completely only up to measuring plane IV.

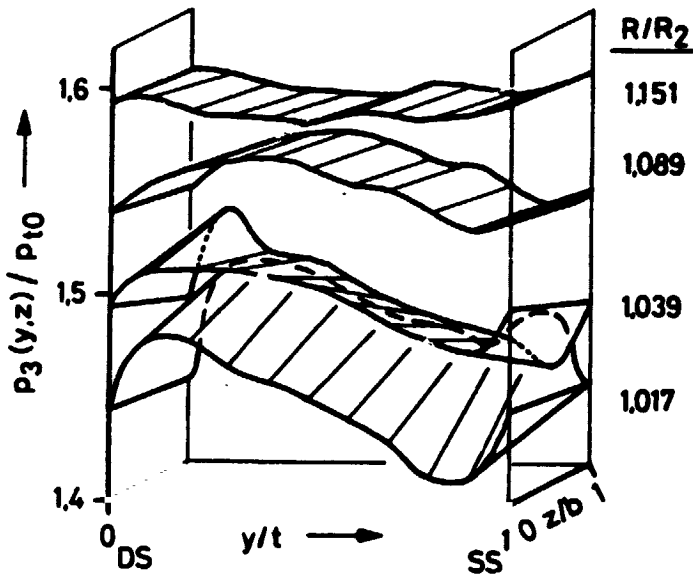


Fig. 8.2. Static pressure curve  $p_3(y,z)$  in the diffuser inlet region (measuring planes I-IV), with respect to the total intake pressure  $p_{t0}$ .

Operating point:  
 $n/\theta_0 = 14,000$  rpm,  
 $\dot{m}/\theta_0/\delta_0 = 5,31$  kg/s.

observed in comparison with the measured values determined at the same spot in plane I (while, of course, the total pressure mean value clearly decreases between the two planes, cf. 8.18).

As an example, the  $\Delta p_t$  curve in Fig. 8.5 -- which was determined from the local total pressures in planes I and III:

$$\Delta p_t(y,z) = [p_{t,IV}(y,z) - p_{t,I}(y,z)]/p_{t,I}(y,z), \quad (8.1)$$

shows a clear increase in pressure for the development of total pressure presented in detail in Fig. 8.3 in the suction half of the channel. By contrast, the total pressure losses are concentrated in the corner formed by the diffuser front wall and the pressure side and on both sides of the flow channel interface ( $y/t = 0$  or  $1$ ). This pronounced increase in total pressure in parts of the flow channel cannot be interpreted either as an effect of the turbulent mixing process or as an effect of a secondary movement within the disturbed jet-wake flow. To be sure, a flow line shift would be conceivable, in principle, so

The corresponding development of the total pressure ratio  $p_{t3}(y,z)/p_{t0}$  in measuring planes I-IV of the diffuser inlet region is shown by the plotter diagram in Fig. 8.3. Immediately behind the impeller outlet what is first of all striking in the transition from measuring plane I to II is the rapid mixing of the total pressure peaks in the blade wake region. Further downstream, in measuring planes III and IV at  $y/t \approx 0.7$  and  $z/b = 0.5-0.7$ , a distinct total pressure maximum is then formed in the flow channel. These observations are confirmed in Fig. 8.4 which compares measurements made in planes I and IV for operating points near the pump limit and absorption limit.

In particular, in this connection we should emphasize the at first surprising fact that in the region of this pressure maximum in plane IV, an increase in total pressure is clearly

/162

/163

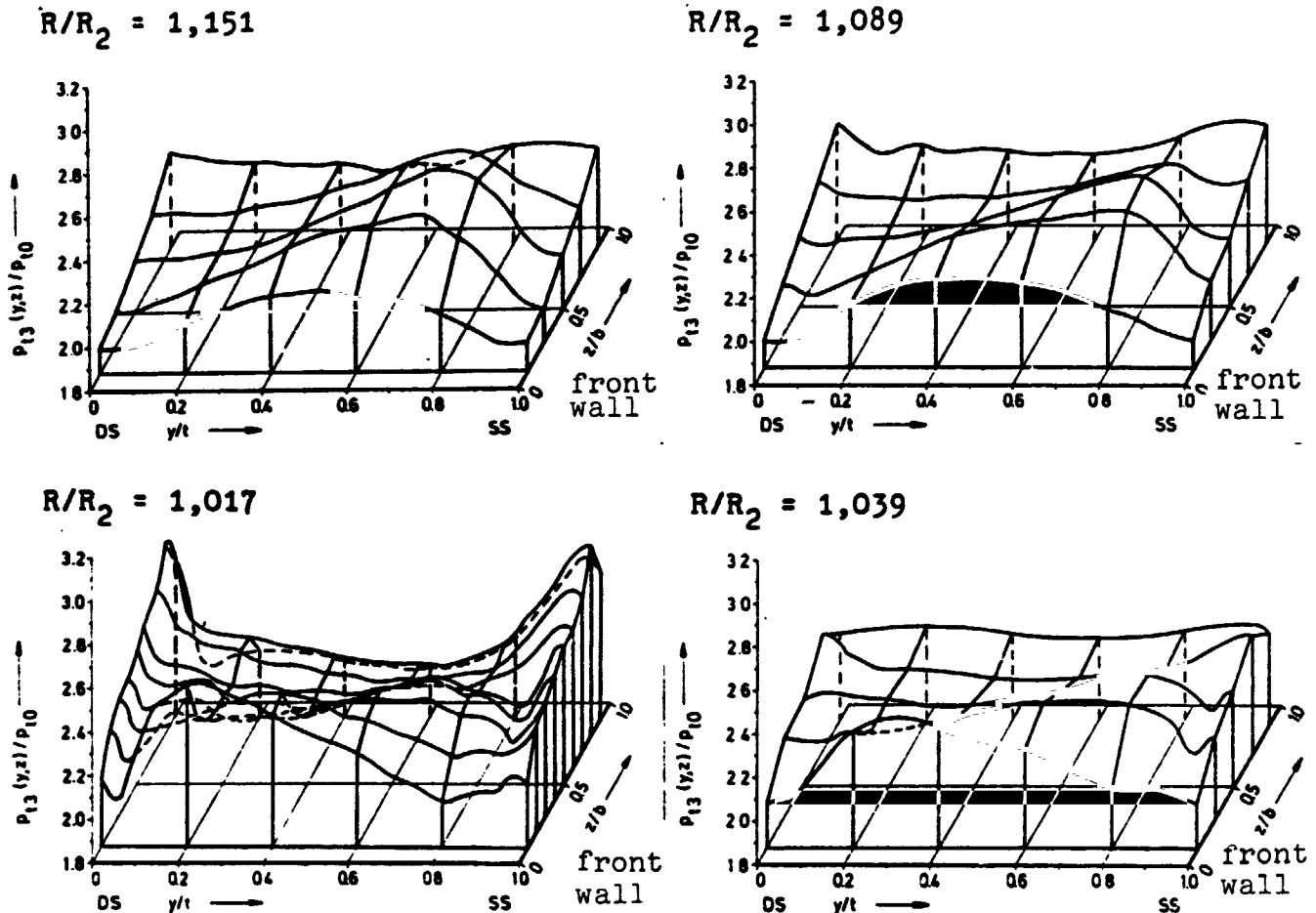


Fig. 8.3. Plotter diagrams of the total pressure distribution  $p_{t3}(y,z)/p_{t0}$  in measuring planes I-IV.

Operating point  $n/\sqrt{\theta_0} = 14,000$  rpm,

$$\dot{m} \sqrt{\theta_0}/\delta_0 = 5,31 \text{ kg/s.}$$

that the "pressure mountain" which appears in Fig. 8.3 at  $R/R_2 = 1.107$  in the region of the front wall of the diffuser ( $y/t = 0.2$ ) is shifted into the area of maximum total pressure at  $R/R_2 = 1.151$ . Arguing against this, however, is the almost unchanged outer contour of the wake region in both measuring planes (cf. Fig. 8.14) and the existing ratio of the circumferential component to the radial component of the relative velocity which, under favorable assumptions, allows a flow line shift of less than  $0.2 \cdot t$  on the flow path between planes I and IV (cf. Figs. 8.15 and 8.16).

/165

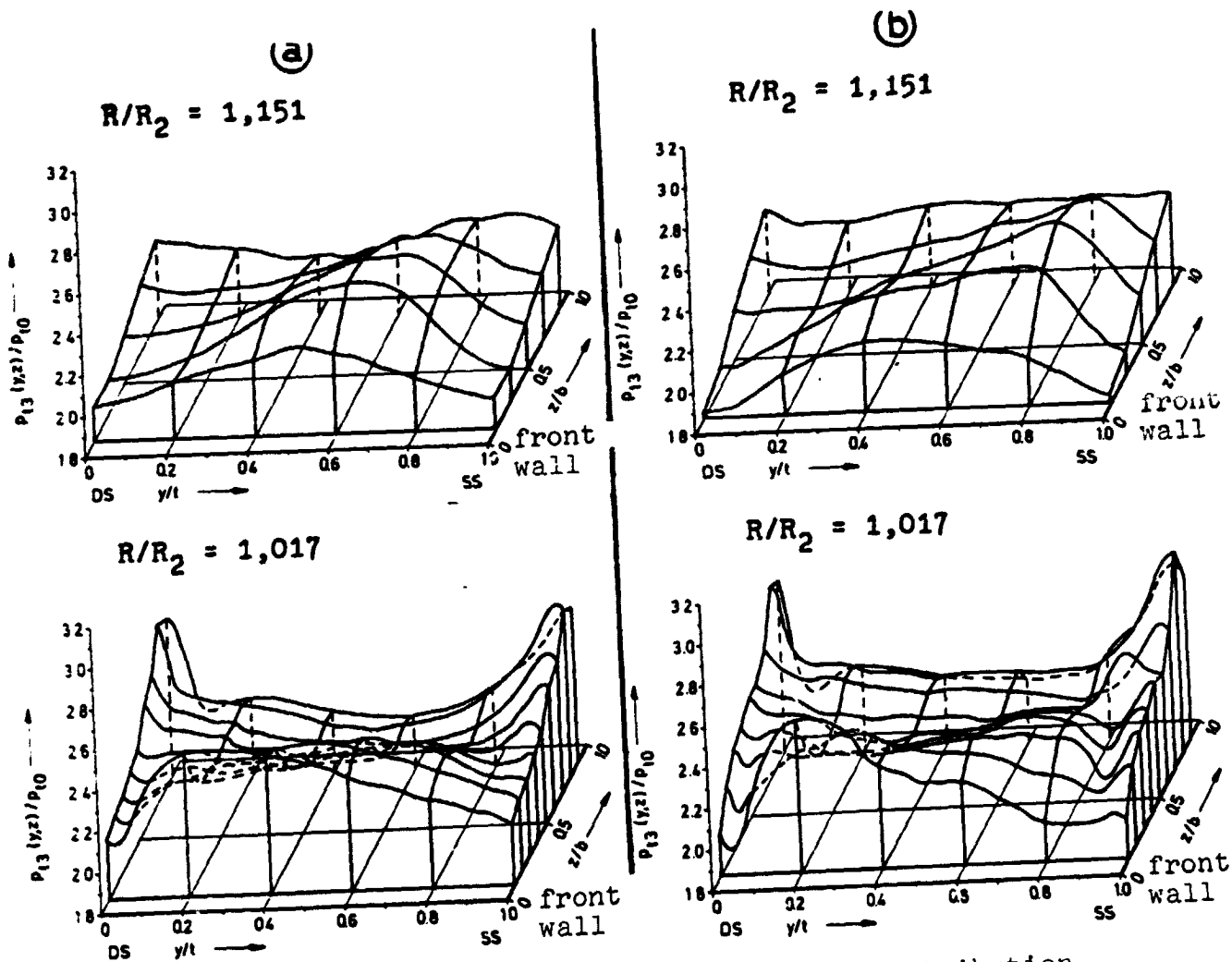


Fig. 8.4. Comparison of total pressure distribution  $P_{t3}(y,z)/P_{t0}$  in planes I and IV.

Operating points at  $n/\sqrt{\theta_0} = 14,000$  rpm  
 $m \sqrt{\theta_0}/\delta_0$  : (a) 4.53 kg/s, (b) 6.07 kg/s.

Thus, as an explanation for the observed development in total pressure there remains only the mechanism of reversible energy exchange discussed in Section 7.1.1. This is illustrated in Fig. 8.6 where the radial total pressure curve in the flow region of a blade channel is compared for two sections normal to the axis.

Close to the front wall of the diffuser ( $z/b = 0.1$ ) under the predominating influence of the wall friction, we observe throughout a drop in total pressure along the relative flow lines

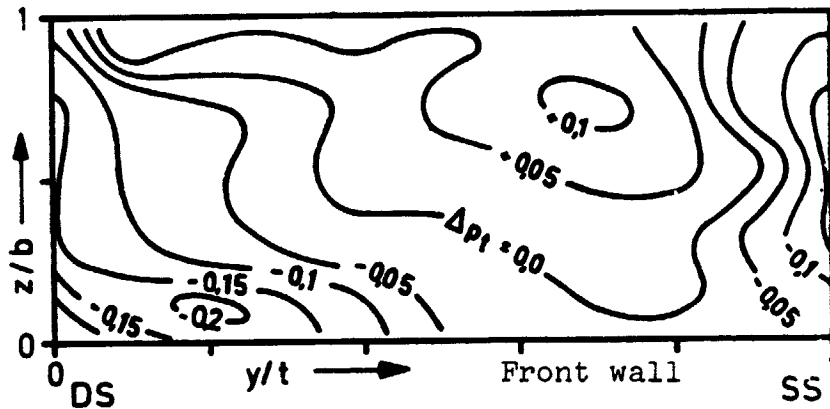


Fig. 8.5. Change in total pressure  $\Delta p_t$  between planes I and IV.

Operating point  $n/\sqrt{\theta_0} = 14,000$  rpm,  
 $\dot{m} \sqrt{\theta_0}/\delta_0 = 5.31$  kg/s

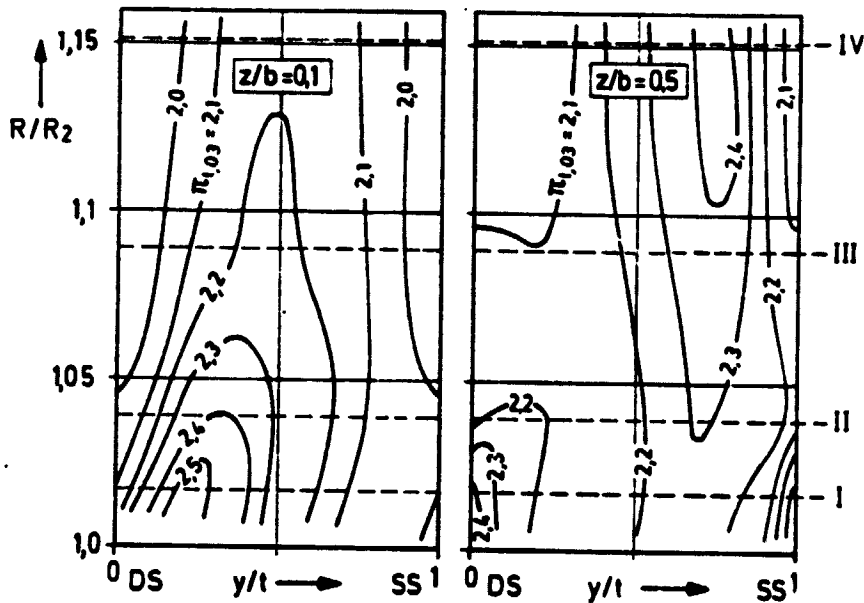


Fig. 8.6. Isobar graph of the total pressure ratio  $\Pi_{t,03}$  for the flow region of a blade channel in the diffuser inlet (vertical distance with respect to the spacing at  $R/R_2 = 1$ , increased by a factor of 3.2).

Operating point:  $n/\sqrt{\theta_0} = 14,000$  rpm,  
 $\dot{m} \sqrt{\theta_0}/\delta_0 = 5.31$  kg/s

( $y/t \approx \text{constant}$ ). By contrast, in the middle of the channel ( $z/b = 0.5$ ) the total pressure largely follows the total enthalpy development, for which applies the connection described in Eq. (6.1) with the change in static pressure over time. In actuality, what results here in the region of  $y/t \approx 0.4-0.8$  -- corresponding to the increase in static pressure per unit time shown in Fig. 8.2 -- is an increase in total pressure along the relative flow lines, whereas, for example, from  $R/R_2 = 1.089$ , a distinct drop in pressure follows a negative  $dp/dt$  close to the pressure side (also see the discussion on the  $q/p_{t0}$  curve in Fig. 8.20). /166

The above figures clearly illustrate an exchange of energy between areas with a different relative velocity level. Undoubtedly this mechanism also influences the mixing of the disturbed flow in the diffuser inlet region. Senoc and Ishida discuss comparable findings behind an impeller with backward bent blades in [7.5]. There the attempt was also made to quantitatively analyze the reversible exchange of energy based on Eq. (6.1). To be sure, this showed considerable dispersions in the numerical evaluation. Because of the pronounced wall friction effects in the diffuser which was only 14 mm wide, the increase in total pressure was at most only  $\Delta p_t \approx 0.01$  (cf. [7.5], Fig. 11) between  $R/R_2 = 1.014-1.1$ , as against  $\Delta p_{t,\text{max}} > 0.1$  in Fig. 8.5.

#### 8.1.2 Total Pressure Fluctuation and the Effect of Flow Line Bending on the Degree of Mixing

Further data on the development of the mixing process, especially on the degree of mixing in the disturbed jet-wake flow, can be derived from the distribution of the total pressure fluctuation coefficient  $f$ , defined according to Eq. (6.2), in the various measuring planes behind the impeller outlet.

First of all, the fluctuation distributions in planes I and IV are compared for two operating points in Fig. 8.7. In comparison to the conditions immediately behind the impeller outlet ( $R/R_2 = 1.017$ ), in plane IV ( $R/R_2 = 1.151$ ), we observe the following:

- only small changes in the fluctuation intensity in the jet region, i.e. the pressure side of the channel;
- a distinct increase in  $f$  in the core of the wake region;
- an increase in the region with a high fluctuation intensity in the direction of the rear wall of the diffuser and the suction side boundary of the flow channel. /167

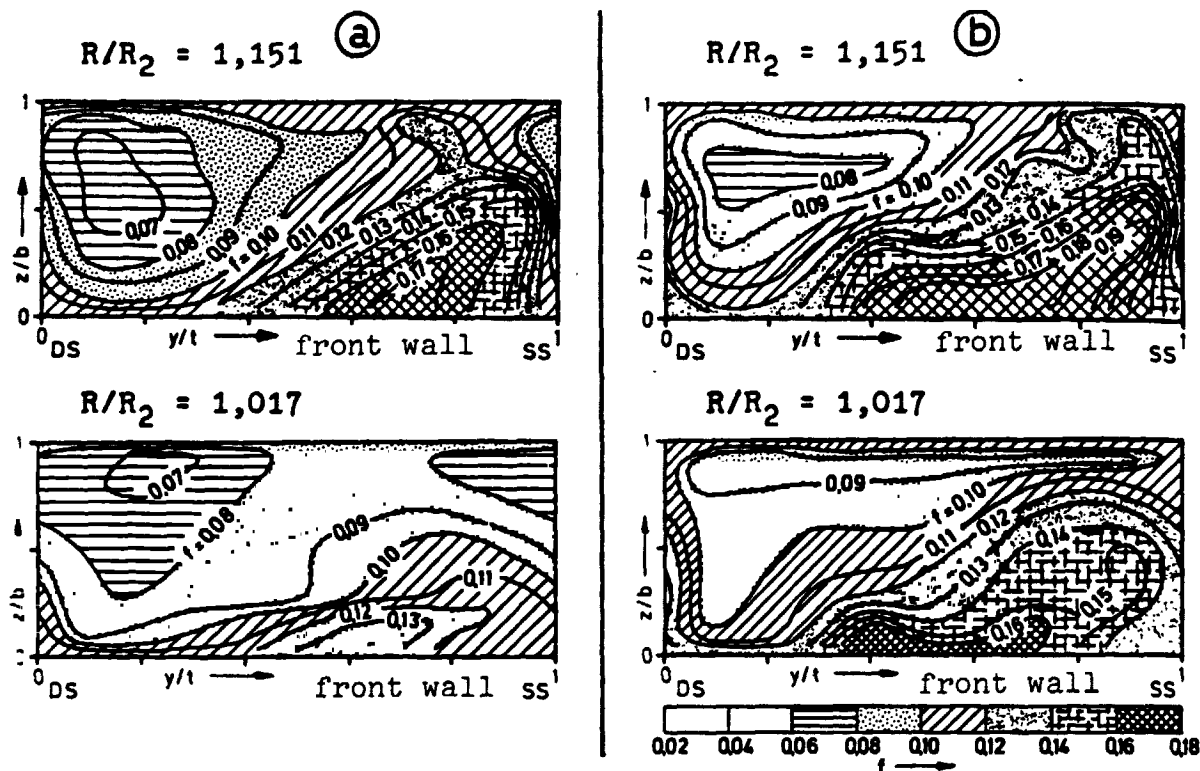


Fig. 8.7. Distribution of the total pressure fluctuation coefficient  $f$  in measuring planes I and IV.

Operating point at  $n/\sqrt{\theta_0} = 14,000$  rpm,  
 $m \sqrt{\theta_0}/\delta_0$  : (a) 4.53 kg/s, (b) 6.07 kg/s/

The same phenomena also show up in the detailed illustration /167 of the fluctuation development in planes I-IV, as presented in Fig. 8.8 for the operating point at 14,000 rpm, 5.31 kg/s. In addition, in the transition from plane I to II, we observe in the entire flow channel a distinct decrease in fluctuation intensity before up to plane IV a higher level of total pressure fluctuations reestablishes itself -- as already in Fig. 8.7.

In order to verify that this development does not result from the curve of the reference total pressure  $p_{t2}(y,z)$ , in Fig. 8.9 the area-averaged value of the absolute fluctuation intensity  $\bar{f}'$  (numerator in definition equation Eq. (6.2)) was related to the total intake pressure  $p_{t0}$ . The graph over the radii ratio  $R/R_2$  likewise shows a distinct minimum in the region of plane II ( $R/R_2 = 1.039$ ).

At the present time, an exact reason for this fluctuation curve based on fluid flow physics cannot be given. This is



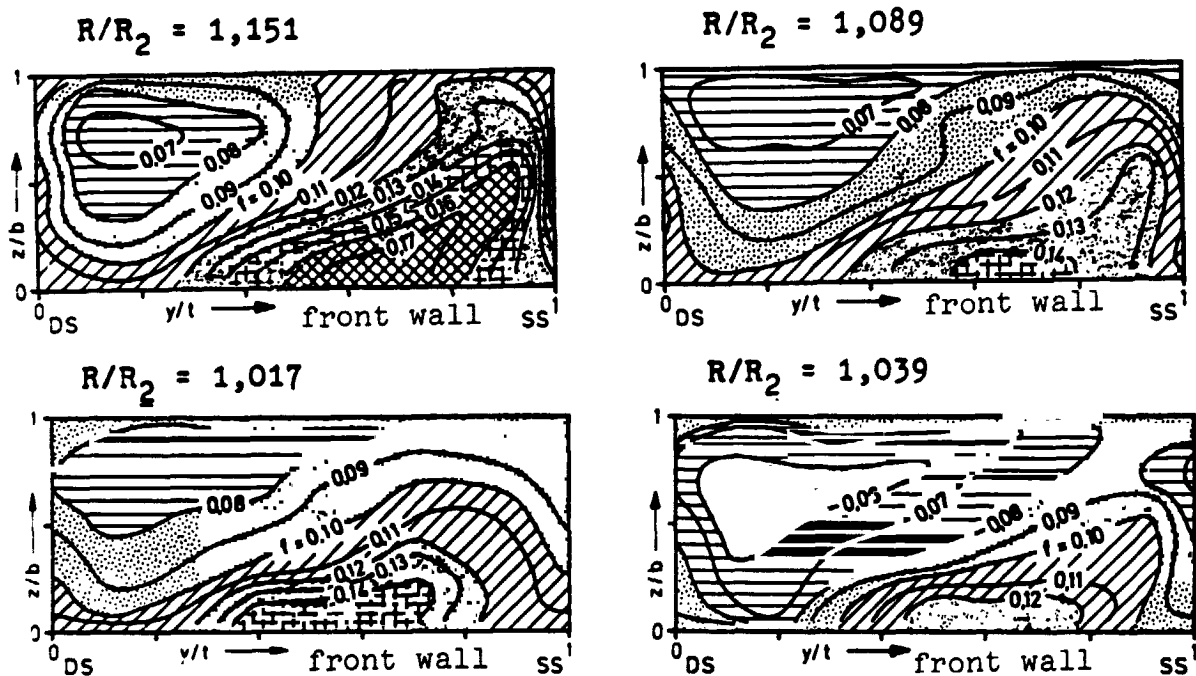


Fig. 8.8. Distribution of the total pressure fluctuation coefficient  $f$  in measuring planes I-IV (legend, see Fig. 8.7b).

Operating point:  $n/\sqrt{\theta_0} = 14,000$  rpm,  
 $\dot{m} \sqrt{\theta_0}/\delta_0 = 5,31$  kg/s.

primarily due to the possibly very different causes for the fluctuation in total pressure -- such as nonsteady relative flow or axially asymmetric diffuser flow. To be sure, certain estimates on the development of turbulence along the channel or jet-wake interfaces in the disturbed flow field can be made.

The influence of normal acceleration on the turbulence structure of planes of shear within the impeller flow was already discussed in Section 6.4.2. Obviously, the same mechanisms are also to be found in a consideration of the relative flow in the diffuser inlet region.

In a plane perpendicular to the rotor axis the following equation is regarded as a stability criterion for a plane of shear under the effect of Coriolis acceleration:

$$S_C = 2(r/R_2)^2 - (r/R_2) (r/u_2) (\partial w_3 / \partial r), \quad (8.2) \quad /169$$

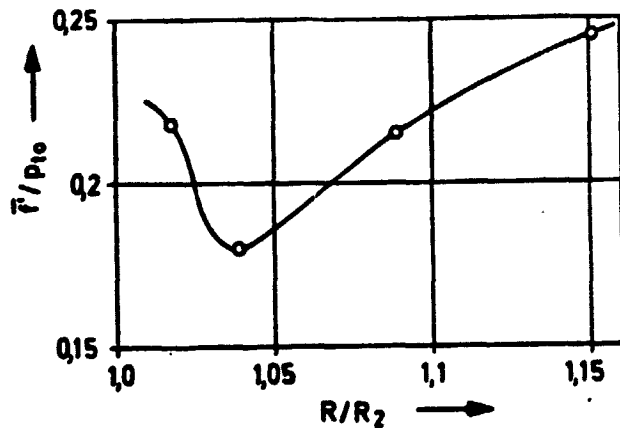


Fig. 8.9. Radial curve of the area-averaged, absolute fluctuation coefficient  $\bar{F}'/p_{t0}$ . Operating point  $n/\sqrt{\theta_0} = 14,000$  rpm,  $\dot{m} \sqrt{\theta_0}/\delta_0 = 5,31$  kg/s.

or the following equation under the effect of normal acceleration due to relative flow line bending:

$$S_N = \quad (8.3)$$

$$(w_3/u_2) (r/u_2) (\partial w_3/\partial r) + (w_3/u_2)^2$$

and for the overlapping of both effects:

$$S = S_C + S_N \quad (8.4)$$

with

$w_3$  = planes of shear - relative velocity

$r$  = bending radius of the plane of shear and the measuring plane in question

$u_2$  = circumferential velocity of the impeller in the outer radius  $R_2$ .

Positive values for  $S_C$ ,  $S_N$  and  $S$  in each case imply turbulent damping under the effect of Coriolis or normal acceleration or their overlapping. Conversely, negative values indicate turbulence excitation, i.e. increase mixing in the region of the plane of shear.

$S$  corresponds to the "Brunt-Vaisala frequency  $\omega_{BV}^2$ ," first given by Bradshaw in [6.22] for the two-dimensional case assumed here, i.e. the mean shearing stress, flow line bending and rotation lie in one plane. Equations (8.2)-(8.4) were also derived in detail by Hill, and by Senoo and Ishida in the discussion section of [7.5].

/170

In the following estimate of the effect of normal accelerations on the plane of shear stability behind the impeller in question here, the following, partially simplified, conditions are to be noted:

1. The flow field was evaluated for the test point at 14,000 rpm and a mass flow of 5.31 kg/s.
2. Plane of shear flow lines are considered at  $z/b = 0.3$ .

3. The results in a region close to the impeller -- based on measurements in planes I and II -- and in a region remote from the impeller (planes III and IV) are compared.
4. The conditions in the jet-wake interfaces on the front side of the jet SVS ( $y/t \approx 0.5$ ) (in the direction of rotation) and on the rear side of the jet SRS ( $y/t \approx 1.0$ ) are considered.
5. Both interfaces are based on the same bending curve which is taken from Fig. 8.1 b at  $z/b = 0.3$ .
6. The data on the relative velocity curve come from an exact digitalization with 101 values per spacing. Fig. 8.15 shows the relative velocity distribution only at selected points.

The results of this estimate listed in Table 8.1 show, first of all for the region close to the impeller ( $1.0 < R/R_2 < 1.05$ ) that the turbulent mixing of both interfaces is dampened under the dominating effect in the case in question of Coriolis acceleration (SVS) or normal acceleration (SRS). Whether the perceptible drop in total pressure fluctuation intensity at  $R/R_2 = 1.039$  (Figs. 8.8 and 8.9) is connected with this cannot, to be sure, be answered unambiguously with these results. Afterwards, in the impeller-remote region ( $1.05 < R/R_2 < 1.2$ ) with a simultaneous decrease in the flow line bending in each case, the effect of the Coriolis acceleration predominates. This causes severe damping on the front side of the jet, but on the rear side of the jet it causes an excitation of turbulent exchange.

/171

With respect to the disturbed jet-wake velocity distribution, from this it follows that the equalization due to the turbulent mixing of the two regions takes place primarily in the area of the rear of the jet starting at  $R/R_2 \approx 1.05$ . By contrast, the velocity gradient at the front of the jet -- starting at the impeller inlet -- becomes increasingly stabilized under the effect of Coriolis acceleration.

In the meridian plane within the impeller, the radial deflection primarily causes damping of the turbulent exchange movement, while behind the impeller outlet a renew increase is to be expected with insignificant flow line bending.

These expectations, derived from a simple estimation, are surprisingly well verified by the test results. In actuality, an increase in total pressure fluctuation in the direction towards the corner formed by the suction side of the channel and the

/172

TABLE 8.1 EVALUATION OF THE PROBLEM OF JET-WAKE INTERFACE STABILITY. OPERATING POINT:  $n/\sqrt{\theta_0} = 14,000$  RPM,  $m \sqrt{\theta_0}/\delta_0 = 5.31$  kg/s

z/b = 0.3		Computed data				Results		
measuring planes	circumferential position	$\frac{r}{R_2}$	$\frac{w_3}{u_2}$	$\frac{r}{u_2} \frac{\partial w_3}{\partial r}$	$S_C$	$S_N$	S	
I-II	SVS	0,30	0,37	-2,36	0,89	-0,74	+0,15	
	SRS	0,30	0,35	2,29	0,51	0,92	+0,41	
III-IV	SVS	0,75	0,39	-4,70	4,65	-1,68	+2,97	
	SRS	0,75	0,42	4,85	-2,51	2,21	-0,30	

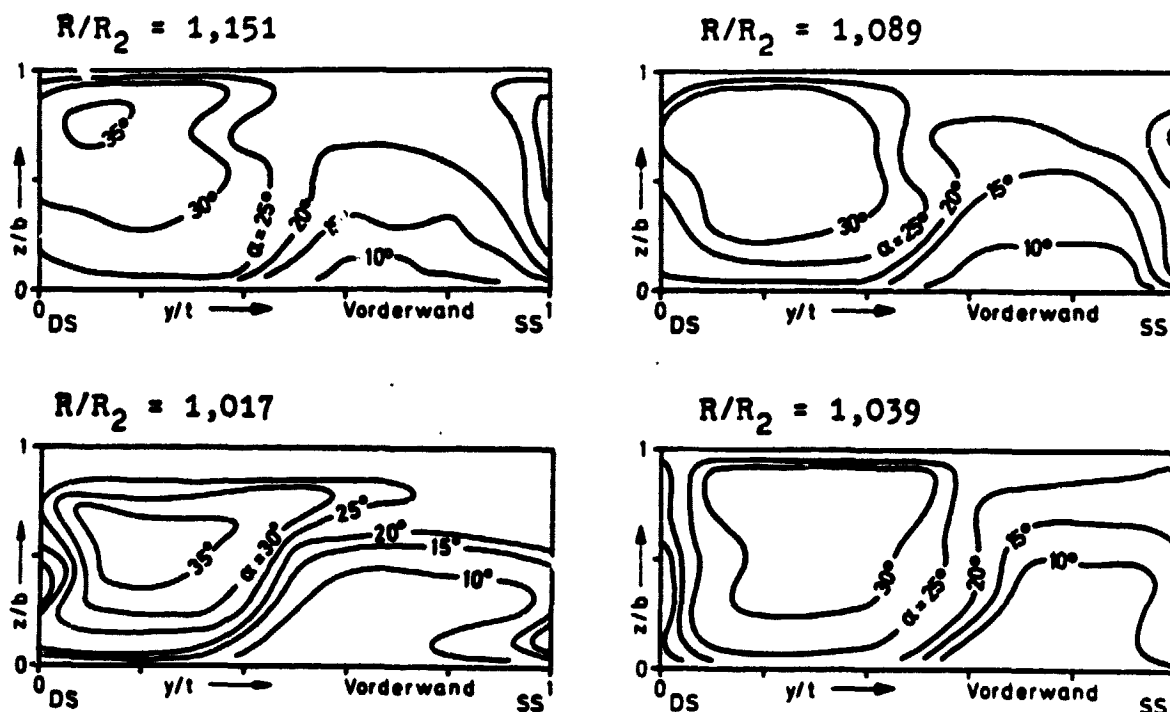
SVS = front of jet      SRS = rear of jet

rear wall of the diffuser can be seen in Figs. 8,7 and 8.8, and also the equalization of the disturbed velocity distributions shown in Figs. 8.12 and 8.13 illustrates the influence of the flow mechanisms in question.

### 8.1.3 The Velocity Field in the Absolute and Relative System

In order to simplify the representation of the complex mixing processes within the disturbed flow field the development of the absolute flow in the diffuser inlet region is shown separately for the flow direction  $\alpha$  and the radial velocity component  $c_{r3}$ . The direction distribution in planes I-IV can be seen in Fig. 8.10 for the operating point at 14,000 rpm and 5.31 kg/s. On the other hand, Fig. 8.11 compares the conditions in planes I and IV for the operating point near the pump limit and absorption limit. In an analogous manner, Figs. 8.12 and 8.13 show the development of the velocity distributions  $c_{r3}/u_2$ .

The radial development of the velocity field between planes I and IV (Figs. 8.10 and 8.12) clearly illustrates the jet-wake mixing process. Already we clearly see at the transition from plane I to II a decrease in the steep velocity and angle gradients over the diffuser width and at the rear of the jet ( $y/t = 0$  or 1), while the gradient at the front of the jet ( $y/t = 0.4-0.5$ ) even



Vorderwand = front wall

Fig. 8.10. Isocline graph of the absolute flow direction  $\alpha$  in planes I-IV.

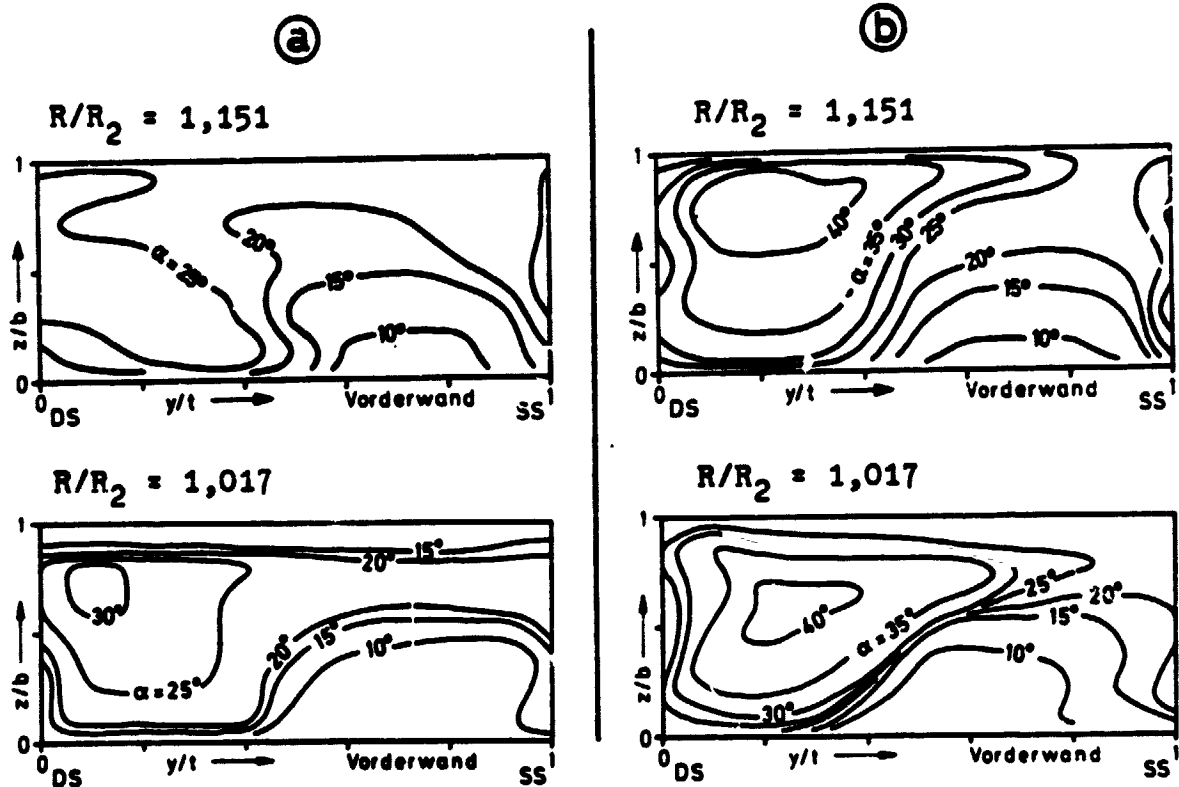
Operating point:  $n/\sqrt{\theta_0} = 14,000$  rpm,

$\dot{m} \sqrt{\theta_0}/\delta_0 = 5.31$  kg/s.

in plane IV is still conspicuously evident. This velocity curve underlines the effect of the mixing mechanisms discussed above in section 8.1.1 and 8.1.2 -- i.e. reversible energy exchange and turbulent mixing. These suggested that the wake region replenished itself from the region of the jet flow close to the rear wall of the diffuser and the suction side of the channel.

These observations are verified in Figs. 8.11 and 8.13 where the experimental results for the operating point close to the pump limit and absorption limit are compared. A comparison of the velocity distribution in plane IV ( $R/R_2 = 1.151$ ) shows that in the operating point with the greatest mass flow -- 6.07 kg/s -- the disturbance in the circumferential direction is also still clearly perceivable in the vicinity of the rear wall of the diffuser, while for the mass flow of 4.53 kg/s a largely evened out velocity curve has been established.

In addition, for all of the operating points shown we see



Vorderwand = front wall

Fig. 8.11. Isocline graphs of the absolute flow direction  $\alpha$  in planes I and IV.

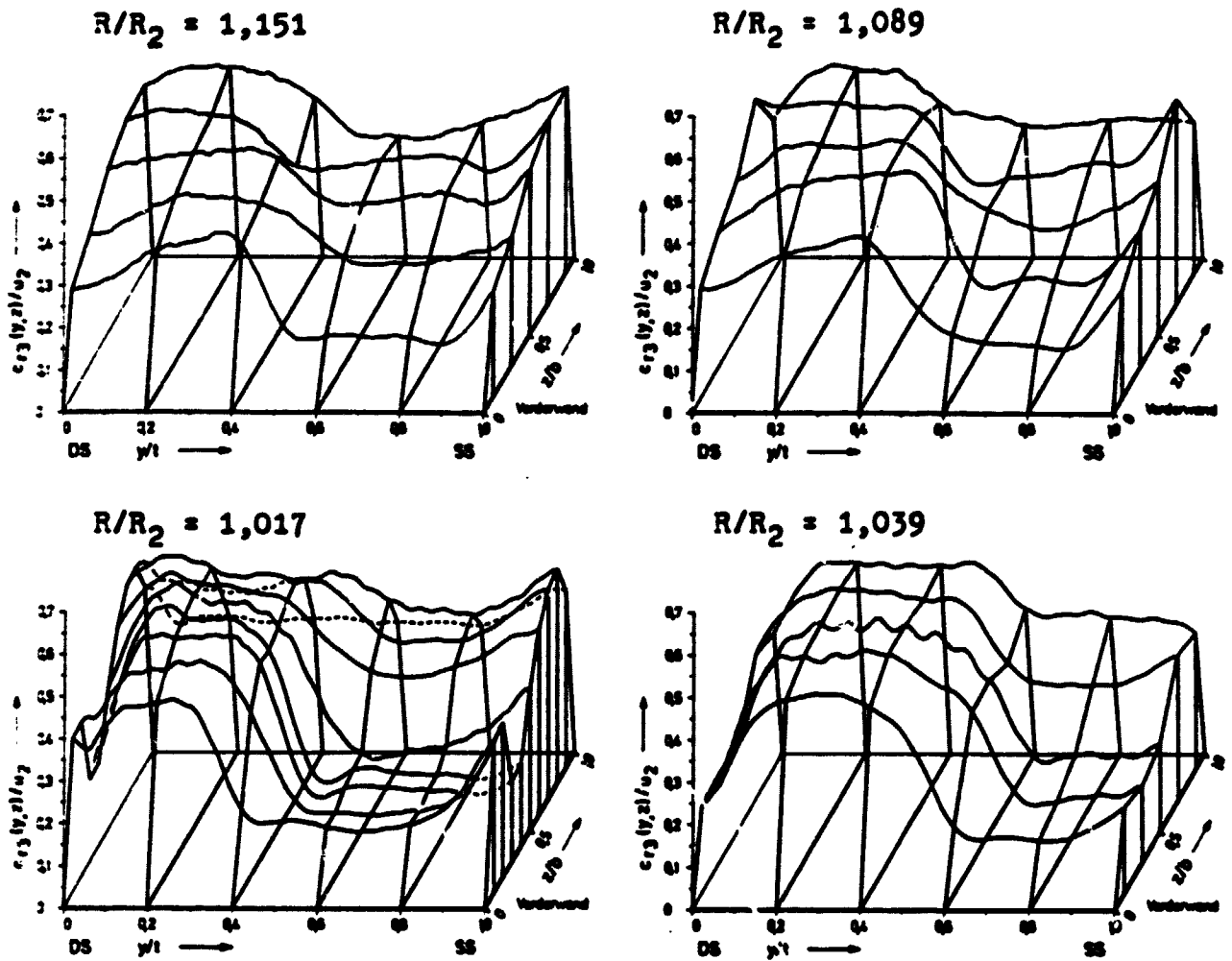
Operating point at  $n/\sqrt{\theta_0} = 14,000$  rpm,  
 $\dot{m} \sqrt{\theta_0}/\delta_0$  : a 4.53 kg/s, b 6.07 kg/s

that between planes I and IV there occurs a shift in the mass flow towards the rear wall of the diffuser. As a result of this, the boundary layer, generally visible at  $R/R_2 = 1.017$  close to the rear wall of the channel ( $z/b = 0.9$ ) is rapidly replenished.

/175

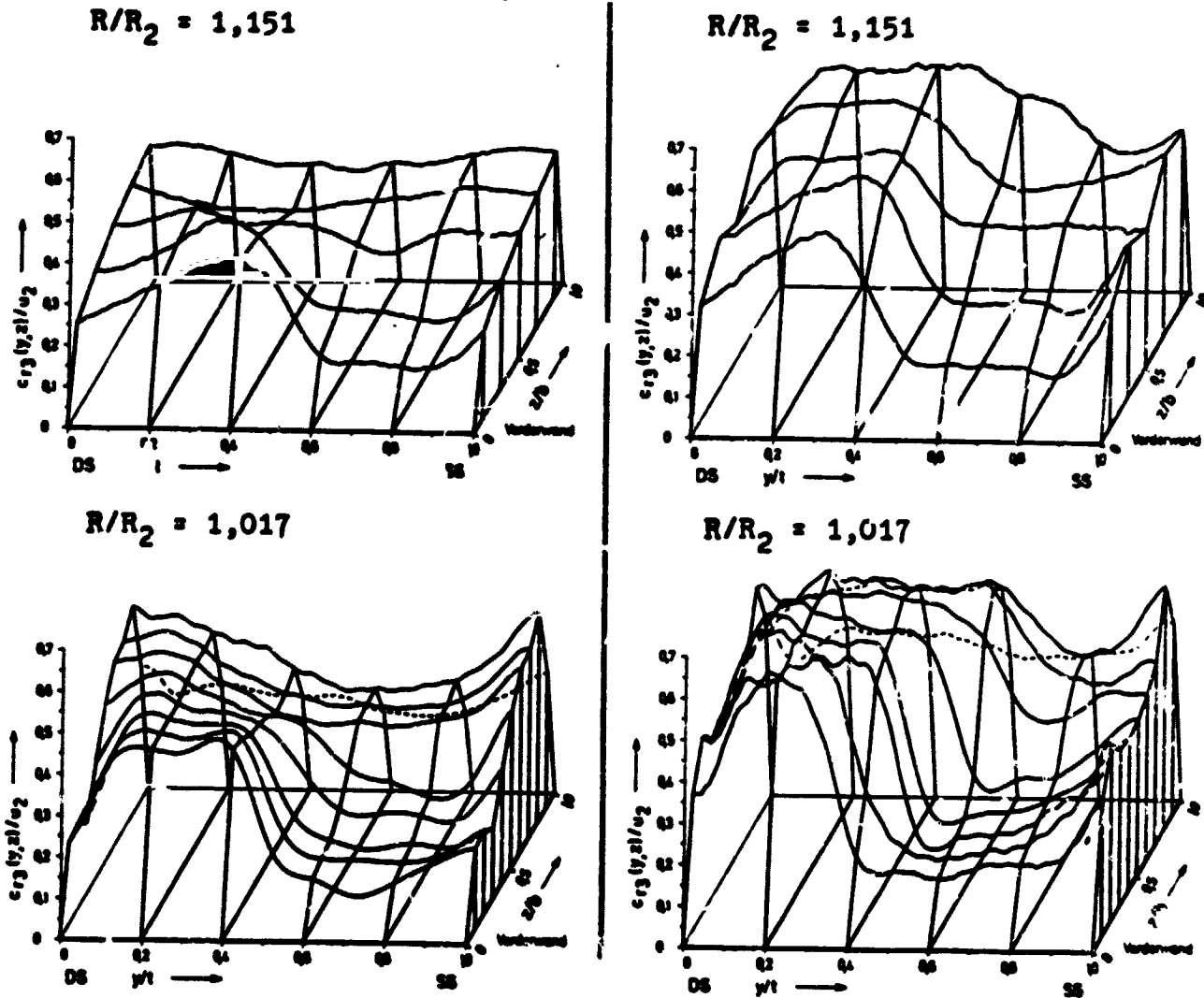
Fig. 8.14 also shows this in another form. Here for the three analyzed operating points at 14,000 rpm, the wake distributions in planes I and IV were compared. The shape of the wake regions was determined with the aid of definition equation (5.60) from the corresponding velocity curves  $c_{p3}/u_2$ . This also gave the "wake components" along the rear wall of the diffuser shown in plane I. Once again the graph refers to the flow region of an impeller blade channel. Of course, in the simplified rectangular form of the graph, the channel division and channel width here were adapted to the existing geometric conditions in planes I and IV. By this means, we obtain an impression which approximately represents the area and shape of

/176



Vorderwand = front wall

Fig. 8.12. Plotter diagrams of the velocity distribution  $c_{r3}/u_2$  in planes I-IV.  
Operating point:  $n/\sqrt{\theta_0} = 14,000$  rpm.  
 $\dot{m} \sqrt{\theta_0}/\delta_0 = 5.31$  kg/s.



Vorderwand = front wall

Fig. 8.13. Plotter diagrams of the velocity distribution  $c_{r3}/u_2$  in planes I and IV.

Operating point at  $n/\sqrt{\theta_0} = 14,000$  rpm,  
 $\sqrt{\theta_0}/\delta_0$  : (a) 4.53 kg/s, (b) 6.07 kg/s.



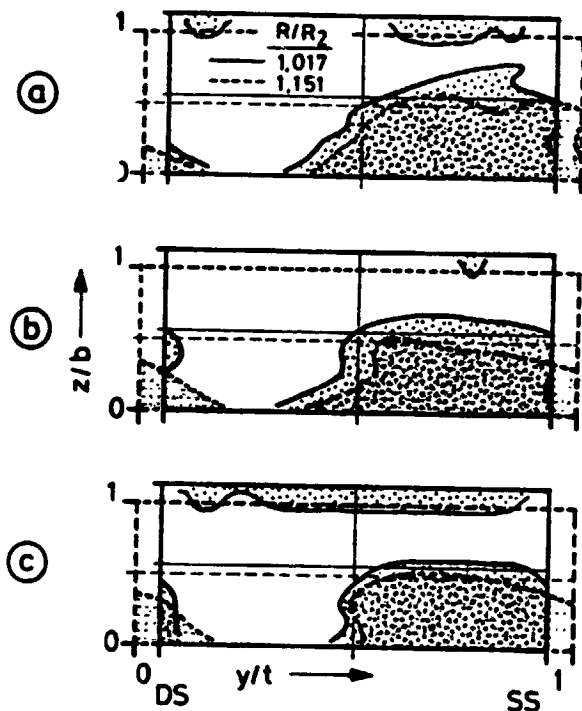


Fig. 8.14. Distribution of wake regions in planes I and IV. Operating points at  $n/\sqrt{\theta_0} = 14,000$  rpm,  $\dot{m} \sqrt{\theta_0}/\delta_0$ : (a) 6.07 kg/s, (b) 5.31 kg/s, (c) 4.53 kg/s.

the wake development in the diffuser inlet region.

Finally, a striking feature of the wake regions is the fact that the jet-wake separating line in the region of the front of the jet ( $y/t \approx 0.4-0.6$ ) lines up increasingly parallel to the rotor axis as the mass flow decreases, Fig. 8.14 a+c. This expresses the variable influence of the secondary flows on the flow field in the impeller (cf. Figs. 6.5 and 6.6).

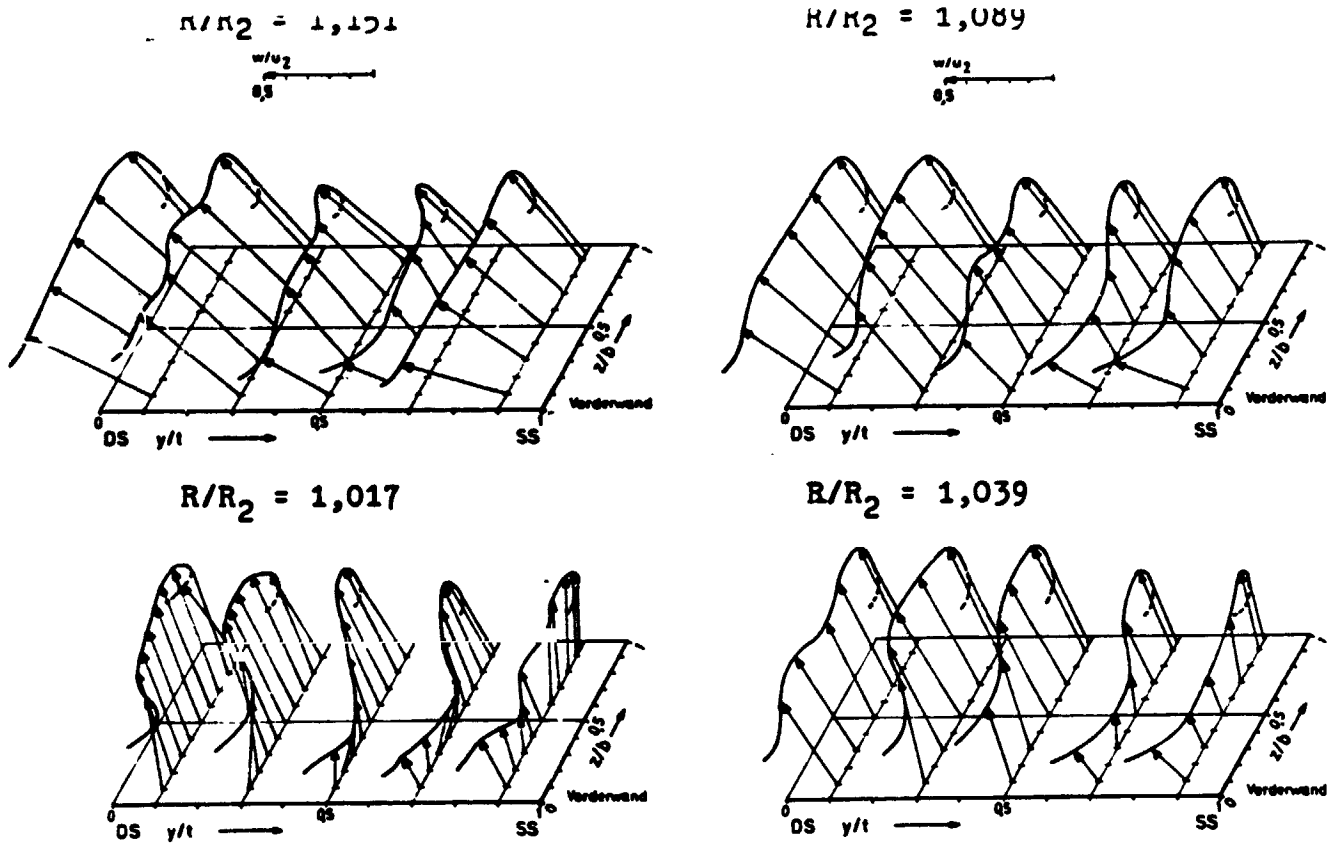
The intensity of the secondary flows is increasingly reduced by the kinematic conditions existing behind the impeller outlet and under the effect of shearing stresses on the diffuser walls. This can be seen in Figs. 8.13 and 8.14. The vector graphs in Fig. 8.15 illustrate the relative velocity development between planes I and IV for the operating point at 14,000 rpm, 5.31 kg/s, while Fig. 8.16 again shows the corresponding

/178

curves in planes I and IV for the operating point near the pump limit and absorption limit. We can clearly see how, on the way through the diffuser inlet region, both the differences in velocity magnitude and in direction for the relative velocity vectors largely cancel themselves out.

## 8.2 Comparison between Theoretical and Experimental Results Using as a Basis the Jet-Wake Flow Model

Experimental results on the increase in static pressure  $p/p_{t0}$  in the vaneless centrifugal diffuser are compared with theoretical pressure curves in Fig. 8.17. The theoretical curves here were calculated with expanded Dean-Senoo theory for compressible flows (Section 7.8). The symbols in the figure stand for mean values of nonsteady pressure transducer measurements which are defined by Eq. (5.38); and they indicate results which were determined with "conventional" wall pressure holes. For the most part, these are mean values



Vorderwand = front wall.

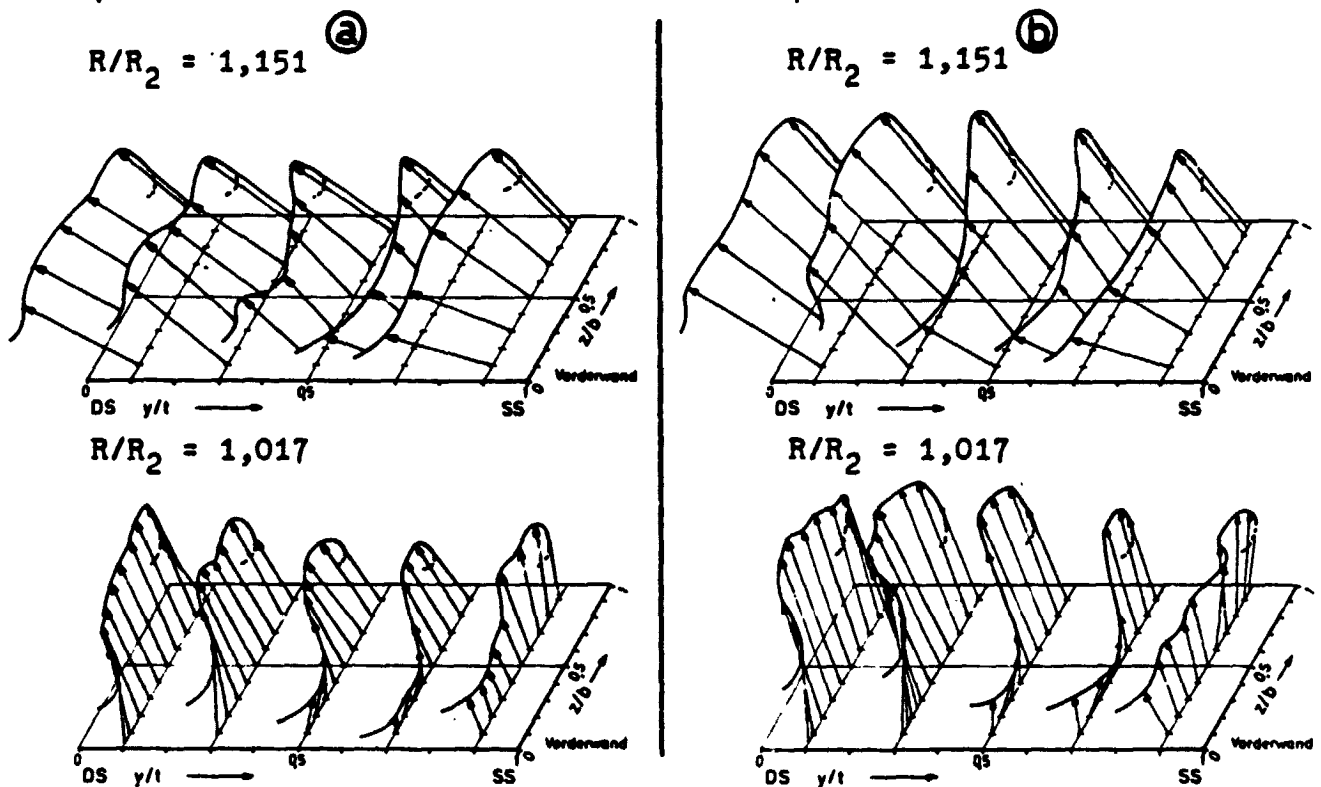
Fig. 8.15. Development of the relative velocity curve  $w_3/u_2$  in the diffuser inlet region, planes I-IV.

Operating point:  $n/\sqrt{\theta_0} = 14,000$  rpm,  
 $m \sqrt{\theta_0}/\delta_0 = 5.31$  kg/s.

based on several measurements on the same radius -- on the front and rear walls the diffuser, i.e. up to seven circumferential positions.

The figure legend -- lower left in Fig. 8.17 -- expresses in concise form the parameter variation in the calculated sample cases ① - ⑥. It also applies for the following figures up to and including Fig. 8.23. The meanings of these symbols are given below:

S/T + : Disturbed jet-wake flow; the input data for the theory were determined experimentally in measuring plane I ( $R_e/R_2 = 1.017$ );



Vorderwand = front wall

Fig. 8.16. Comparison of relative velocity curves  $w_3/u_2$  in planes I and IV, scale, see Fig. 8.15.

Operating point at  $n/\sqrt{\theta_0} = 14,000$  rpm,  
 $\dot{m} \sqrt{\theta_0}/\delta_0$  : (a) 4.53 kg/s, (b) 6.07 kg/s.

- : axially symmetrical substitute flow with the same mass flow and inlet torque as the momentum-averaged S/T flow. /179
- $c_f$  + : Wall friction coefficient  $c_f$  (R) corresponding to the broken-line curve in Fig. 7.3, taken into account; in addition, for the mass flow of 6.07 kg/s a sample case (1') with  $c_f = 0.0065 =$  constant was calculated;
- : without the effect of wall friction.
- $\zeta$  + : Interface friction coefficient  $\zeta = 0.25$ ;
- : without interface friction.

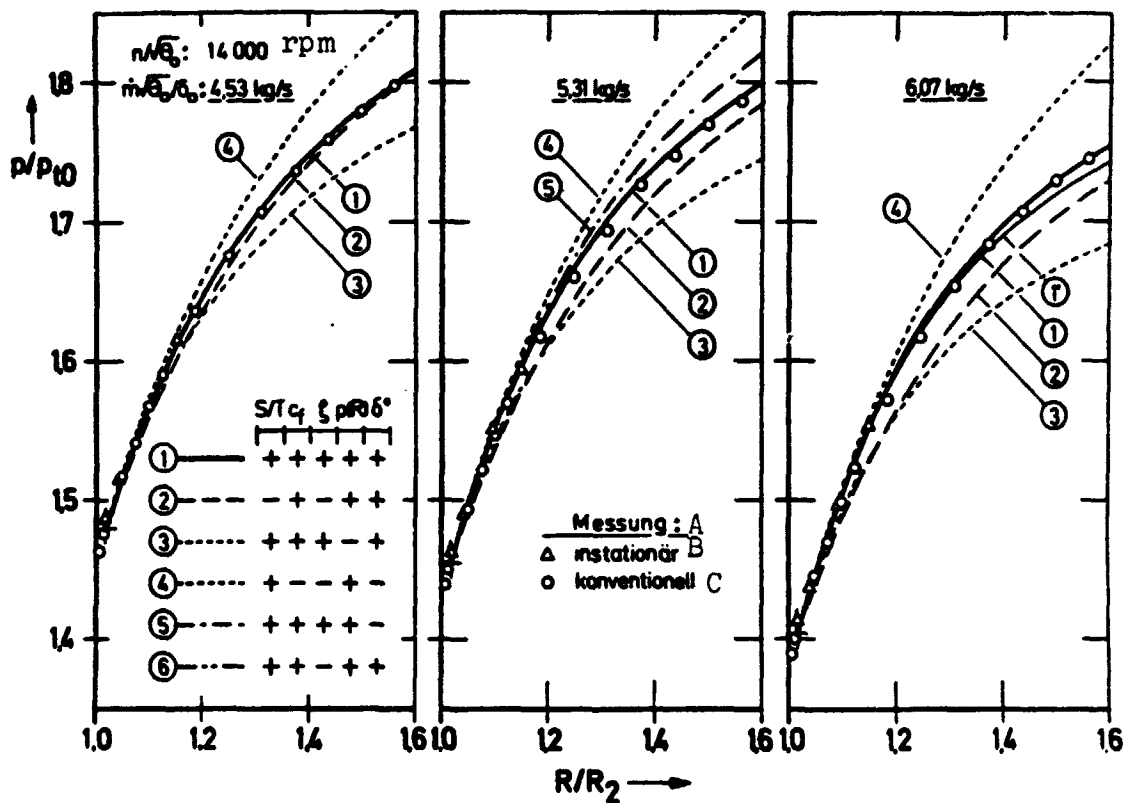


Fig. 8.17. Comparison of theoretical and measured values: curve of static pressure  $p/p_{t0}$  in the centrifugal diffuser. Remarks: curve ⑥ is not shown here, it coincides with ①; curve ① (6.07 kg/s) corresponds to ①, only the  $c_f$  curve differs.  
 Key: A) Measurement C) Conventional  
 B) Nonsteady

- $\rho(R)$  + : Compressible flow; /180  
 - : incompressible flow,  $\rho = \text{constant} = \rho_e$ .
- $\delta^*$  + : Boundary layer displacement thickness corresponding to the solid-line curve in Fig. 7.4, taken into account;  
 - : without boundary layer influence.

This yielded the following conditions for the theoretically calculated sample cases:

- ① - disturbed, friction-affected, compressible (like ①');
- ② - undisturbed, friction-affected, compressible (interface friction not applicable);
- ③ - disturbed, friction-affected, incompressible;
- ④ - disturbed, frictionless, compressible (boundary layer not applicable);
- ⑤ - like ①, but without boundary layer displacement;
- ⑥ - like ①, but without interface friction.

As Fig. 8.17 confirms, the measured static pressure curve is very well approximated by curve ① in all three operating points. It is striking that the measured values, in general, lie above the solution for the axially symmetrical substitute flow ②. This results from the larger inlet momentum of the disturbed flow. As the mass flow increases, the irregularity of the velocity distribution in the diffuser inlet increases (cf., for example, Fig. 6.8 and the  $\epsilon_{k3}(c)$  values in Table 6.1), and, accordingly, the differences between ① and ② increase.

The difference between curves ① and ③ reflects the effect of compressibility at quiescent mach numbers of the absolute velocity in the range  $M_{t,c3} = 0.73 - 0.78$ . Comparison of curve ④ with curve ① illustrates the effect of wall friction and interface friction<sup>1</sup>, as well as the effect of the boundary layer displacement thickness on the build up of static pressure in the diffuser. In addition, for the mass flow 5.31 kg/s, curve ⑤ gives the individual effect of the displacement thickness  $\delta^*$  in the case of friction-affected flow. Finally, curve ①' for 6.07 kg/s makes it possible to estimate the influence of modified wall friction coefficient --  $c_f = 0.0065$ .

/181

In summary, the following can be inferred from Fig. 8.17:

In order to make an exact determination of the static pressure in the vaneless diffuser of a highly loaded centrifugal compressor stage the following factors -- in order of importance -- must be taken into consideration:

- the compressibility,
- the disturbed jet-wake flow and

---

1. A graph of curve ⑥ -- effect of  $\zeta$  -- was dispensed with here; the deviations with respect to ① lie in the range of the accuracy of the graphs.

- the boundary layer displacement thickness.

The corresponding total pressure curve  $p_t/p_{t0} = f(R/R_2)$  is graphed in Fig. 8.18. In the Dean-Senoo Theory the total pressure

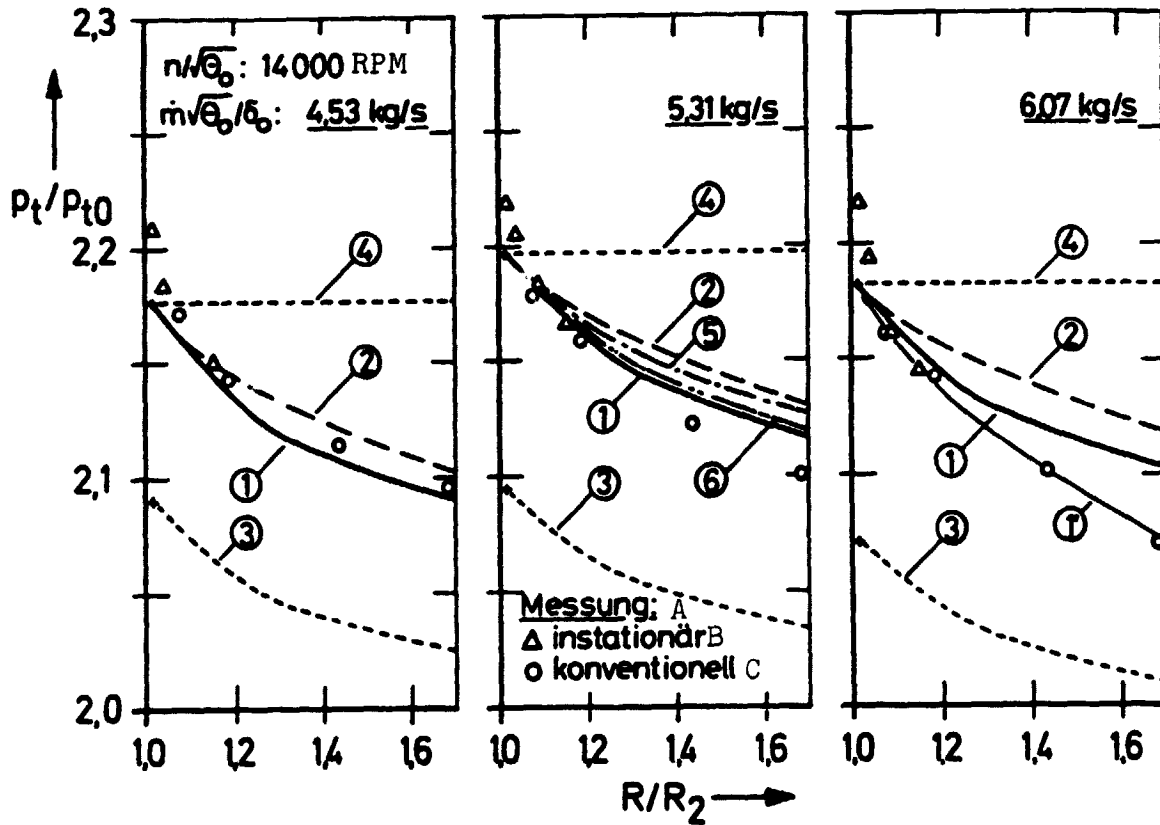


Fig. 8.18. Comparison between theoretical and measured values: radial curve of the total pressure ratio  $p_t/p_{t0}$ .

Key: A) Measurement      C) Conventional  
 B) Nonsteady

is calculated from the static pressure and the kinetic flow energy. With the two-dimensional jet-wake flow model -- especially given the assumption of a uniform relative flow direction  $\beta$  -- it is naturally not possible to fully approximate the real flow. This causes the difference between the measured and calculated total pressures at  $R_e/R_2 = 1.017$  (curve ③ shows the results for the incompressible flow). In order to make it easier to compare the theoretical pressure curves, in addition solution ② for the axially symmetrical substitute flow -- which indeed has a smaller

inlet momentum than the disturbed flow -- was referred to the theoretical initial total pressure of the disturbed, compressible flow (e.g. shift for ② in the case of 5.31 kg/s of  $p_t/p_{t0} = + 0.012$ ).

In curve ① for the disturbed, friction-affected flow the sharper drop in total pressure  $dp_t/dR$  with respect to ② in the range of the disturbed flow up to the mixing radii ratio  $R/R_2 = 1.25 - 1.3$  (cf. Fig. 8.20) is clearly evident. This is caused by the higher wall friction losses in the wake area (absolute velocity  $C_T > C_S$ , see Fig. 8.23) and by the interface friction. Theoretically the total efficiency between measuring points "0" (compressor inlet) and "4" ( $R/R_2 = 1.687$ ) is thereby reduced with respect to the undisturbed substitute flow ② only by an amount of  $\Delta\eta_{t,s} = -0.008, -0.008$  and  $0.01$  for the mass flows 4.53, 5.31 and 6.07 kg/s (cf. Fig. 8.25). The influence of the interface friction alone, as expressed in Fig. 8.18 by the difference between ① and ⑥ (5.31 kg/s), amounts to  $\Delta\eta_{t,s} = -0.002$ , hence an insignificant order of magnitude. These small loss components are not surprising in view of the relatively small relative kinetic energy which comes to bear in the mixing of the disturbed flow in the sample cases presented. In addition, however, mention must also be made here of the short comings of the simple theoretical model which will be discussed in summary at the end of this section. /182

Basically, curves ①, ② and ⑥ reveal the dominating effect of wall friction on the diffuser losses. In the theoretical calculations presented here,  $c_f(R)$  takes into account the actual wall friction. Usually, in a one-dimensional analysis of diffuser flow one introduces a dissipation coefficient  $c_d$ , which then in the form of an apparent wall friction also approximately allows for the dissipation of energy due to turbulent mixing and irregular velocity distributions. With the  $c_f$  curve used here, the Dean-Senoo Theory ignores the turbulent energy dissipation. If as a relative measure of the turbulence at the diffuser inlet one uses the total pressure fluctuation distributions from Fig. 6.4, then for the operating point at 14,000 rpm one sees a distinct increase in the average fluctuation intensity with increasing mass flow. Analogously to this, in Fig. 8.18 one observes increasing deviations between the measured total curves and the theoretical curve ①. Therefore it is obvious to suspect the turbulent energy dissipation, which is not taken into account, as the essential cause of these deviations. For a theoretical estimate of this effect, for the mass flow of 6.07 kg/s, the case of ① was calculated with an "apparent" wall friction coefficient  $c_d = c_f = 0.0065$  -- but with otherwise identical conditions with respect to ①. This curve closely approximates the measured drop in total pressure in the diffuser with the exception of the immediate inlet region. /183

Traupel [6.4] suggests  $c_d = 1.5-2 c_f$ . With this, the experimental value is well confirmed. It was not attempted, however, to further adapt the dissipation coefficient to the measured values. The theory used indeed offers precisely the possibility of analyzing a few individual effects more precisely, which otherwise are considered as a lump sum in the  $c_d$  values. So far we do not have a reliable correlation between the dissipation coefficient and the flow turbulence in the diffuser. The results shown in Figs. 6.4, 8.3, 8.4, 8.7-8.9 and 8.18 are indicative values for this.

In Fig. 8.19 the experimentally and theoretically determined angular momentum curves in the disturbed and mixed flow region of the centrifugal diffuser are compared for the three operating points selected. Curve ② again represents the solution for the axially symmetrical substitute flow -- with the same mass flow and inlet angular momentum as the disturbed flow. The other curves refer to jet-wake velocity distributions at the diffuser inlet. In the cases shown, the angular momentum of the wake region clearly exceeds the values for the jet region. It is striking that in the inlet radii ratio  $R_1/R_2 = 1.017$  the initial value of the theoretical curves for the disturbed flow do not exactly agree with the measured values of the jet region and wake region. Again, the reason for this is the assumption made in the model, for purposes of simplification, of a uniform relative flow direction  $\beta$ . In actuality, differences in direction of up to  $10^\circ$  between jet areas and wake areas occur in the real flow (cf. Fig. 8.22). /184

First of all, if we consider the frictionless solution ④ for the compressible, disturbed flow, it turns out that after a while the differences in angular momentum, even without the effect of friction, cancel themselves out and an undisturbed flow becomes established. This results from the rise in static pressure in the centrifugal diffuser and, coupled with this, the reversible exchange of energy between jet and wake regions (cf. Section 7.1.1). /185

First of all, we observe an increase in the angular momentum of the wake in the diffuser inlet region, i.e. the jet region transfers energy to the wake and thus also increases the differences in the jet-wake energy level. Then the direction of the energy transfer reverses -- the wake performs work on the jet region and thus contributes to the homogenization of the flow. Fig. 8.19 confirms that the radial distance of the zone of increasing angular momentum differences likewise increases with increasing mass flow.

Under the effect of wall friction and interface friction, the mixing of the disturbed flow is completed considerably more quickly than for the frictionless case ④. The basic mechanism



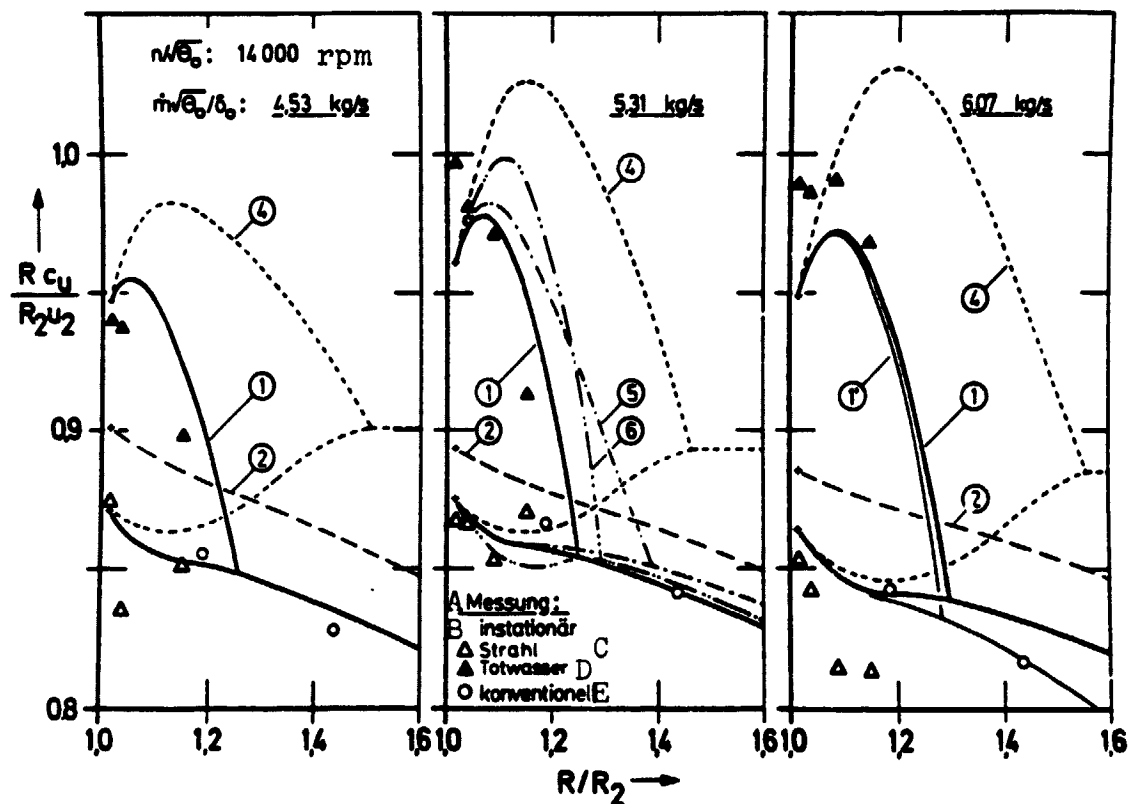


Fig. 8.19. Comparison between theoretical and measured values: radial angular momentum development for jet, wake and total flow.  
 Key: A) Measurement      D) Wake  
       B) Nonsteady        E) Conventional  
       C) Jet

of the energy exchange, however, can be perceived in all of the theoretical solutions for the disturbed flow. For the mass flow of 5.31 kg/s, the difference between curves ① and ⑥ illustrates the considerable effect which interface friction alone has on the homogenization of flow. At the same time, it turns out that the selection of an interface friction coefficient on the order of  $\zeta = 0.25$  is necessary in order to approximately predict the drop in the angular momentum of the wake which was found experimentally.

Curve ⑤ was calculated without boundary layer obstruction. It revealed that the decrease in the diffuser area ratio (outlet/inlet) causes an acceleration in the mixing process. The difference in wall friction coefficients between curves ①' ( $c_f = 0.0065$ ) and ① has, on the other hand no decisive perceivable effects in the jet-wake angular momentum curve -- as is obvious

for the mass flow of 6.07 kg/s. The effect of the higher  $c_f$  value first makes itself felt in the region of undisturbed flow in the form of a sharper drop in angular momentum. /186

We did not graph the incompressible curve ③. It nearly coincides with curve ①.

① The comparison of experimental values with theoretical curve ① shows that the theory indeed to a large degree accurately reproduces the tendency of the angular momentum curve for the disturbed flow. In places, however, there are sometimes larger deviations. In particular, it is striking that the theory -- because of the restrictive handicap of a uniform relative flow direction  $\beta$  -- obviously over estimates the increase in angular momentum of the wake in the diffuser inlet. Only for the mass flow of 6.07 kg/s do the measured values in the wake region produce a curve which suggests such a shape. It remains to be noted, of course, that these data, as mean values, represent the entire wake region. In Figs. 8.3-8.6, on the basis of the nonsteady total pressure measurements, the reversible exchange of energy in partial regions of the flow can also clearly be detected experimentally.

In Fig. 8.20 experimental results on the radial development of the most important parameter for characterising the jet-wake flow are compared with theoretical curve ①. The graphs show the curve of the surface component of the wake  $\epsilon = A_T/A$ , the relative velocity ratio  $\gamma = W_T/W_S$  and the interference parameter  $\delta = \epsilon(1-\gamma)$ . In general, the experimental values measured in the diffuser inlet region are in good agreement with the theoretical prediction. A striking feature is that the mixing of the disturbed flow is accomplished primarily due to the approximation of relative velocities, while the surface component of the wake of the total flow up to complete mixing is technically reduced only by 14-16%. As already mentioned in connection with the angular momentum distributions, a distinct relationship between the reduction in disturbance and mass flow can be seen in the  $\delta$  curve.

Also plotted in Fig. 8.20, as a result of the theoretical calculations was the radial curve of the fluctuation in pressure  $q$  related to the total pressure of the compressor inlet  $p_{t0}$ . By definition (cf. discussion in text for Fig. 7.1b),  $q$  is positive if the static pressure at the front of the jet (in the direction of rotation) is greater than at the rear of the jet, and thus at the same time the jet transfers energy to the wake. Thus, the pressure fluctuation  $q$  is a measure of the intensity and direction of the transfer of energy between the two flow regions. For example, in the radial  $q/p_{t0}$  curve for the mass flow of 5.31 kg/s we see a change in sign to negative values at  $R/R_2 = 1.12$ . If now, as a basis of comparison, we refer to the nonsteady /187

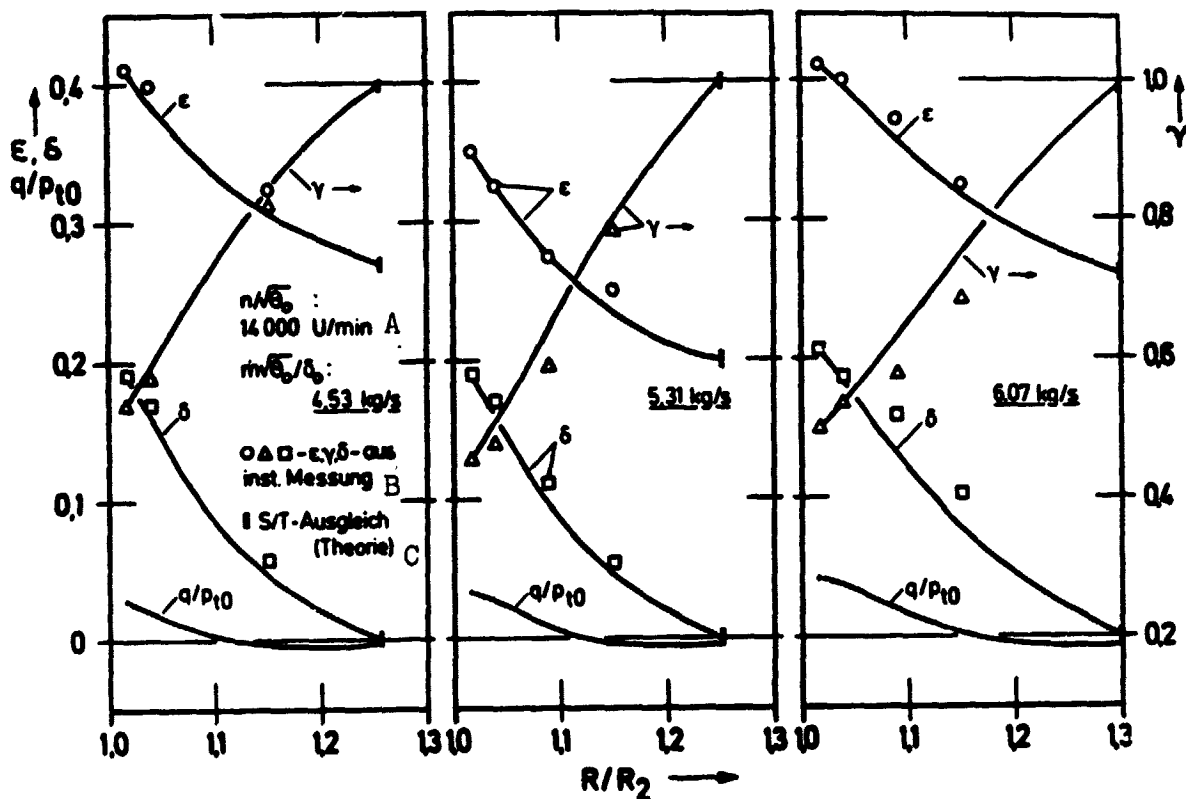


Fig. 8.20. Comparison between theoretical values (curve  $\textcircled{1}$ ) and measured values: curves of the surface component of the wake  $\epsilon$ , the relative velocity ratio  $\gamma$ , the interference parameter  $\delta$  and the pressure fluctuation  $q/p_{t0}$  in the diffuser inlet region  
 Key: A) rpm  
 B) From nonsteady measurement  
 C) Jet-wake mixing (theory)

measured static pressure curves -- Fig. 8.2 -- than in the two measuring planes immediately behind the impeller outlet ( $R/R_2 = 1.017$  and  $1.039$ ) we see pressure curves which basically resemble the curve of values measured in the impeller -- pressure maximum near the pressure side DS of the flow channel and minimum in the vicinity of the suction side. From this it follows that -- as a result of viscosity forces -- the transfer of energy in the impeller affects the static pressure curve behind the impeller up to about  $R/R_2 \approx 1.05$ . It is conceivable that these greater pressure variations here conceal those pressure pulsations which, theoretically, must occur as a result of interactions between jet and wake regions.



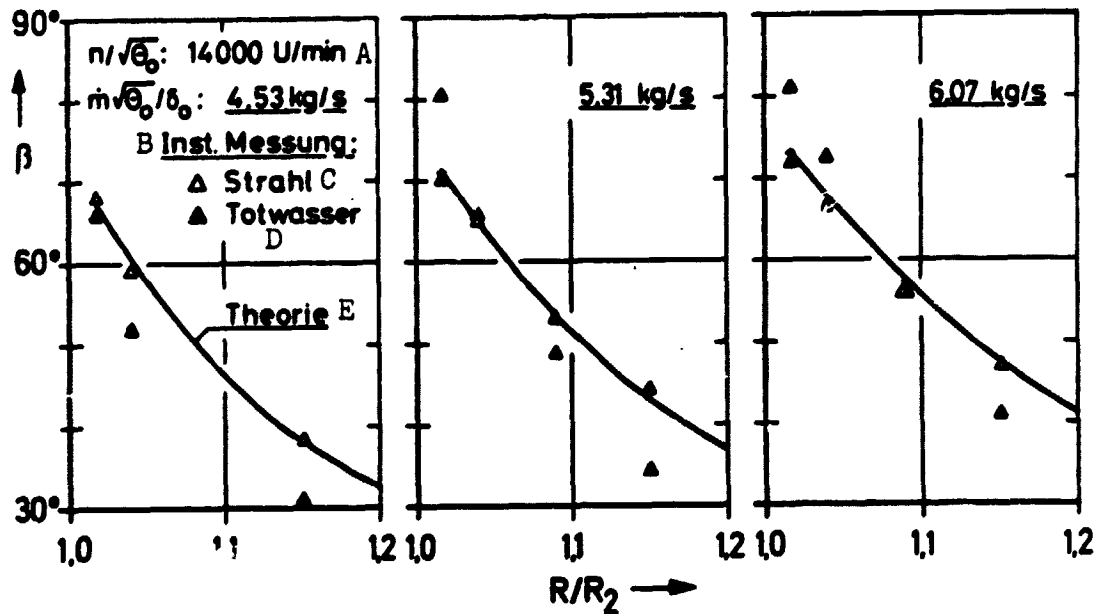


Fig. 8.22. Comparison between theory (1) and experiment: radial curve of the relative flow direction  $\beta$  for jet, wake and total flow.

Key: A) rpm                      C) Jet  
 B) Nonsteady measurement    D) Wake  
    E) Theory

Fig. 8.21 gives information about the mean values of the absolute flow direction measured in the diffuser inlet region or the for the jet and wake, and it also gives the corresponding theoretical curve with and without the effects of friction (1) and (4), as well the curve without the effect of interface friction  $\zeta$  (6). As a result of theoretical estimates based on the assumption of an insignificant wake mass flow, Dean and Senoo [7.1] and later Hess [8.1] reached the conclusion that the disturbed flow up to  $R/R_2 = 1.1$  have largely mixed. Fig. 8.21 confirms that this finding cannot be generalized, and at least given the existing, realistic facts in this case (blade angle  $\beta_{s2} = 90^\circ$ , finite wake mass flow) at  $R/R_2 = 1.1$  considerable fluctuations in direction still occur. Certainly these would also strongly affect the operational behavior of an incipient, bladed diffuser in this case.

As a final example of this series of comparisons between theory and experiment, in Fig. 8.22 the relative flow directions  $\beta$  measured in the jet and wake are compared with the curve of the momentum mean value  $\beta$  of theoretical curve (1). A striking

/188

/190

feature of the measured values for 5.31 and 6.07 kg/s is that  $\beta$  at the beginning of the wake at first exceeds by about  $10^\circ$  the angle of the jet region. But then the radial angle curve in the wake drops off more sharply and at  $R/R_2 = 1.151$  the wake values are clearly less than the jet values. The theory ignores this effect -- the possible consequences of this limitation have indeed already been referred to several times above -- however it quite closely approximates the prevailing jet curve for the mean momentum value. Fig. 8.25 shows the results of a parameter study (cf. Section 7.2) which allows us to estimate the upper limit of possible losses due to variable jet-wake relative flow directions.

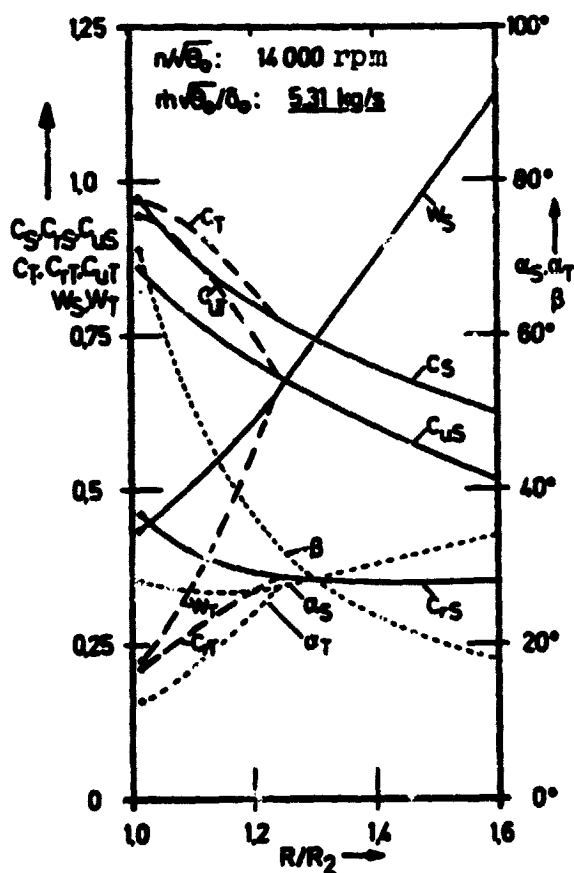


Fig. 8.23. Example for the theoretical calculation (1) of the disturbed jet-wake velocity curve in the centrifugal diffuser.

developed by Dean and Senoo also for highly loaded centrifugal compressor stages.

Finally, as a product of the friction-affected, compressible theory (1), Fig. 8.23 shows the radial curve of all velocity components and flow directions in the absolute and relative system for the jet, wake and the mixed flow (also designated with the subscript S = jet). This figure illustrates in the concise form of a typical example the development of the flow field during mixing of the jet-wake distribution in the vaneless diffuser of a highly-loaded centrifugal compressor stage.

If we take into account the measurement uncertainties (see Table 5.1) then in conclusion we can say that the comparison between experimental findings and the expanded theory for compressible flows carried out in Figs. 8.17-8.22 produced a good agreement. In particular, this is true for the prediction of the characteristic interference variable  $\epsilon$ ,  $\gamma$  and  $\delta$ , the rise in static pressure and the momentum curve in the disturbed diffuser flow. From this standpoint, the present investigations yield a confirmation of the simple two-dimensional jet-wake flow model

With certain qualifications, this is true for the prediction of diffuser losses. Essentially the theory accurately predicts the increased drop in total pressure in the region of the disturbed flow. Moreover, the possibility of an improved loss estimate was illustrated by introducing a turbulence-dependent dissipation coefficient. Larger deviations -- up to 1.5% with respect to the measured total pressure ratio -- are seen immediately behind the impeller outlet,  $1.0 < R/R_2 < 1.05$ . The theory ignores here, in particular, the momentum loss due to the rapid evening out of the absolute velocity distribution as is revealed, for example, in Fig. 8.3 in the development of total pressure between  $R/R_2 = 1.017$  and  $1.039$ . In addition, differences result from the simplified two-dimensional jet-wake model. Taking as a basis the actual form of the interface -- as it appears in Figs. 8.14 and 8.1 -- an increase in the jet-wake interface friction to two to three times the value of the simple theory can be predicted. An improved loss estimate could be obtained by a refinement of the model in which the total flow would be divided into several bands of constant, relative diffuser width  $\Delta z/b$  in order to better approximate the three-dimensional character of the jet-wake distribution in the diffuser inlet region.

/191

/192

### 8.3 Theoretical Parameter Study on the Jet-Wake Mixing Process

With the aid of the jet-wake theory, it is attempted in Fig. 8.24 to give indications of the variable mixing rates behind centrifugal impellers with backward bent and radially ending blades. Assuming that the diffuser inlet radius  $R_2$ , or diffuser inlet width  $b_2$  and impeller blade number  $z$  correspond to the dimensions of the stage being studied here, the realistic assumptions (specified in the upper right hand corner of Fig. 8.24) about a "normal disturbance" are made. Here the angular momentum parameter  $\lambda_2$  stands for the ratio of the circumferential component to the radial component of the absolute velocity:  $\lambda_2 = \bar{c}_{u2}/\bar{c}_{r2}$ . In addition, for the impeller with a blade angle of  $\beta_{s2} = 45^\circ$ , the mean jet-wake relative flow direction  $\beta_2$  was estimated at  $42.5^\circ$ , and correspondingly for the  $90^\circ$  impeller,  $\beta_2 = 75^\circ$ .

The legend in the upper left hand corner of the figure refers to the calculated cases. The solid-line curve is for the equal-area diffuser ( $R \cdot b = \text{constant}$ ). Moreover, the same assumptions are made for it as for the theoretical case 1 in Section 8.2 above. If we compare these results for both impellers, then it clearly follows from the curve of the disturbance parameter  $\delta = \epsilon(1-\gamma)$  and the curve of the relative velocity ratio  $\gamma = W_T/W_S$  that the disturbance behind the impeller with backward bent blades quickly subsides in the radial direction.

/193

Between the equal-area and parallel-walled diffuser ( $b = \text{constant}$ ) there are only insignificant differences in the  $\delta$  curve. To be sure, in the latter case the disturbance is completely eliminated only at infinity. The two remaining curves for  $c_f = f(R)$ ,  $\zeta = 0$  and  $c_f = 0$ ,  $\zeta = 0$  (calculation without boundary layer displacement) moreover clearly confirm the importance of the jet-wake interface friction  $\zeta$  for a rapid mixing of the flow.

To illustrate the efficiency losses through the jet-wake diffuser flow, Fig. 8.25 shows by what amount  $\Delta\eta_{t,s}$  the total efficiency of the stage decreases in the case of disturbed flow in comparison with an axially symmetric substitute flow. The total efficiency is defined as  $\eta_{i,04}$  Eq. (4.3). This theoretical estimate is based on the same conditions as the sample cases ① and ② at 14,000 rpm in Section 8.2. As a function of the surface component  $\epsilon_2$  of the wake, the following equivalencies were setup:  $\lambda_2 = c_{u2}/c_{r2} = 1, 3$  and  $5$ ; and  $\gamma_2 = W_T/W_S = 0.2$  and  $0.6$ . From this one can assume that the greatest portion of the jet-wake disturbances present, for all practical purposes, behind highly-loaded centrifugal impellers lie within these limits.

Thus, it turns out that the results for the 3 operating points at 14,000 rpm can well be incorporated into the picture of this parameter study. It appears realistic to assume a value of  $\Delta\eta_{t,s} \approx -0.02$  as the upper limit for the jet-wake mixing losses in the optimum operating range of a compressor stage. Of course, it should be noted that with pronounced jet-wake velocity differences,  $\gamma_2 \approx 0.02$ , and relatively large mass flows,  $\gamma_2 \approx 1$ , the losses can increase sharply. Values in this order of magnitude result when the absorption limit of the compressor performance graph is approached. The results shown here suggest, then, that 4 to 8 efficiency points of the sharp drop in efficiency frequently observed in this operational range be attributed to the mixing losses.

/194

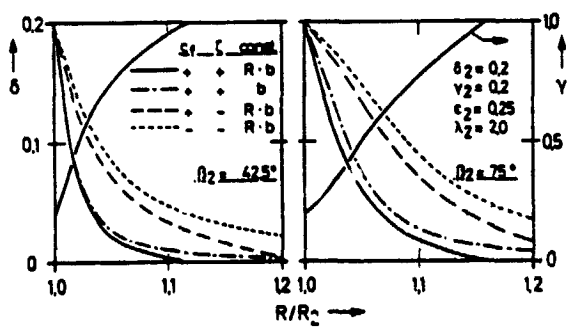


Fig. 8.24. Comparison of the radial development of a jet-wake disturbance behind a centrifugal impeller with backward bent and radially ending blades:  $\delta = \epsilon(1-\gamma)$ ,  $\gamma = W_T/W_S$ .



Within the scope of this loss analysis we will also discuss the results of the theoretical estimation treated in Section 7.2. By means of an expanded model it becomes possible to localize the hertofore ignored effect of variable jet-wake relative flow directions on the loss development. In Fig. 8.26 the measured disturbance data  $\beta_{eS}$ ,  $\epsilon_e$  and  $\gamma_e$  were given for the operating point at 14,000 rpm, 5.31 kg/s, in two radii ratios  $R_e/R_2 = 1.017$  and 1.151, and in addition the wake relative flow direction  $\beta_{eT}$  was systematically varied between  $0^\circ$  and  $90^\circ$ .

Fig. 8.25

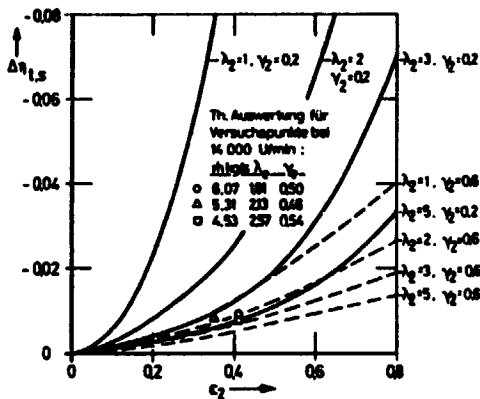


Fig. 8.26

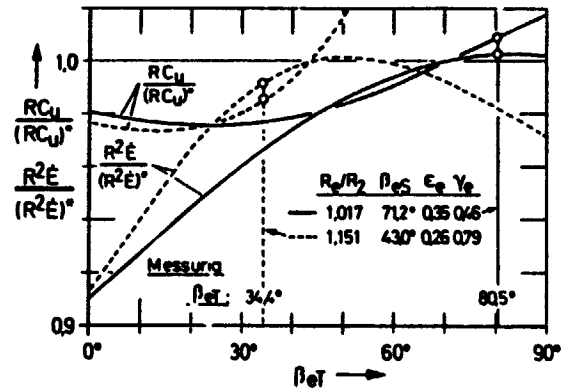


Fig. 8.25. Study on the effect of the jet-wake disturbance variables  $\epsilon_2$  and  $\gamma_2$ , as well as the angular momentum parameter  $\lambda_2$  on the total efficiency of the stage  $\eta_{t,s}$ .

Fig. 8.26. Effect of variable jet-wake relative flow directions  $\beta$  on the angular momentum  $R \cdot C_u$  and the kinetic energy flow  $\dot{E}$  in the mixing radius  $R$ , values in ( ) followed by an \* are for undisturbed flow  $\beta_{eT} = \beta_{eS}$ .

Fig. 8.22 had already shown that at  $R/R_2 = 1.017$  the wake angle  $\beta_{eT} = 80.5^\circ$  is greater than the corresponding value in the jet region, but at  $R/R_2 = 1.151$  with  $\beta_{eT} = 34.4^\circ$  it is clearly smaller than the corresponding value in the wake region. Under the conditions mentioned, it can be deduced from the curve of  $(R^2 \cdot \dot{E}) / (R^2 \cdot \dot{E})^*$  in Fig. 8.26, i.e. the ratio of the kinetic energy flow  $\dot{E}$  in the mixing radius  $R$  at  $(\beta_{eT} \neq \beta_{eS}) / (\beta_{eT} = \beta_{eS})$ , that for the sample case selected these additional losses amount to less than 1% of the kinetic flow energy. Altogether, /195

these results show that the consideration of the effect of variable jet-wake relative flow directions would have changed only slightly the loss predictions of the Dean-Senoo theory.

Finally, Fig. 8.27, for the geometry of the centrifugal compressor stage being studied here and for the theoretical assumptions corresponding to case ① (cf. Fig. 8.17) shows the effect which the angular momentum parameter  $\lambda_2$  and the disturbance variables  $\epsilon_2$  and  $\gamma_2$  have on the radial distance of the mixing radius  $R^*$  from the impeller outlet (related to blade division  $t_2$ ). From a practical standpoint, the flow for  $\gamma^* > 0.9$  is regarded as "equalized."

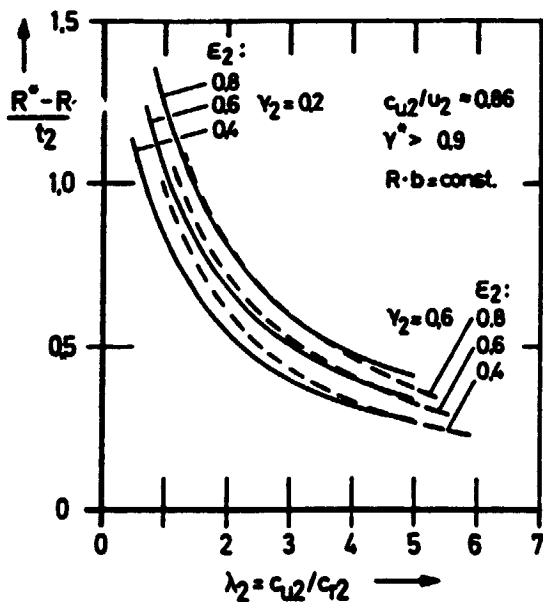


Fig. 8.27. Study on the effect of the angular momentum parameter  $\lambda_2$ , and of the jet-wake disturbance variables  $\epsilon_2$  and  $\gamma_2$  on the jet-wake mixing radius  $R^*$ .

## 9. Summary

With new measuring and evaluation techniques with high time resolution the development of disturbed, compressible flow behind a highly loaded centrifugal compressor impeller was exactly determined and theoretically analyzed in comparison with calculations based on a two-dimensional jet-wake flow model. The results enable basic conclusions to be drawn on the complex flow

A surprising feature of these findings is the small influence of the relative velocity ratio  $\gamma_2$ . With an approximately constant inlet angular momentum, the mixing radius ratio  $R^*/R_2$  primarily depends on the mass flow, the impeller blade number and the surface component  $\epsilon_2$  of the wake.

Additional findings of more extensive parameter studies on jet-wake mixing for impellers with backward bent blades are found in Dean and Senoo [7.1], and for  $90^\circ$ -impellers in Hess [8.1] and Johnston and Dean [7.2]. Of course, it should be noted that the assumption made in [7.2] and [8.1] of  $\epsilon_2 = 0$  is not very realistic in view of the experimental results presented here.

/196

pattern and the loss distribution in high-performance centrifugal compressors. Thus they yield important pre-conditions for the development of an improved stage design.

New measuring techniques had to be developed for the experimental analysis of the complex flow discharged from the impeller. In so doing, we succeeded in developing a measuring system which allows the disturbed flow pattern to be determined with quantitative exactness under very difficult measurement conditions.<sup>1</sup> The following points should be emphasized:

- the development of a measuring technique for determining the nonsteady direction field behind the impeller outlet which, for the flow analysis, makes possible the important transition into the relative system;
- the use of the synchronized sampling technique as an important prerequisite for the exact, digital processing of a large number of nonsteady test signal curves from a strongly fluctuating flow;
- the study on the operational behavior of miniature semiconductor transducers, as a precondition for the development of exact methods for nonsteady wall pressure and total pressure measurements. /198

With this measuring technique the disturbed flow behind a centrifugal compressor impeller with radially ending blades was studied in detail in several operating points at rotations speeds between 10,000 and 18,000 rpm and mass flows between 3.8 and 7.4 kg/s. Results of measurements made in four measurement planes staggered radially in the inlet region of the vaneless diffuser were presented. These include:

- the nonsteady wall pressure curves,
- the distributions of total pressure and total pressure fluctuation intensity,

---

1. As a by-product of these measuring technique investigations, a few findings resulted which did not find any direct expression in this study. They may, however, be of interest, for example for industrial development projects. These include, for example, estimates on the error reading of conventional pressure and temperature measuring methods in the nonsteady flow region or simple measuring systems which make possible a quick, qualitative analysis of the disturbed flow behind the impeller outlet. These results were included in Report [9.1].

- the distributions of the absolute flow direction, and derived from this
- the distributions of the radial component of the absolute velocity vector, and
- the distributions of the relative velocity vector.

Immediately behind the impeller output the relative flow possesses a clearly separate jet-wake distribution. This becomes more pronounced with increasing rotation speed and mass flow. The development of the disturbed flow in the impeller blade channel -- starting from a separation of flow in the region of the meridional bend in the channel -- is illustrated and discussed with the aid of sample measurements made with a laser technique for measuring velocity. The wake forms in the region of the front wall of the channel near the blade suction side. For the operating points studied and with respect to the total flow, it possesses a surface component of 35-41% at the impeller outlet and a mass flow component of 19-26%. The ratio of the jet-wake relative velocities ranges between 0.46-0.55. This small variation in disturbance parameters underlines the fact that the relative importance of individual flow mechanisms, which contribute to the creation and development of the region of separation in the impeller, is largely maintained in a large operational range. Characteristically, the distribution of the relative total pressure behind the impeller outlet show a high loss concentration in the wake region, while the jet region possesses an isentropic flow core. /199

The radial development of the measured velocity distributions clearly illustrates the equalization and mixing process within the disturbed flow. With the condition studied here, however, the disturbance -- above all in the region of the front wall of the diffuser -- is not yet completely eliminated up to the radii ratio  $R/R_2 = 1.15$ . By comparing the total pressure distribution in the various measurement radii behind the impeller outlet, the reversible exchange of energy between areas with high and low kinetic energy in the relative system was detected. Results of a theoretical study on the effect of Coriolis accelerations and normal accelerations on the turbulent mixing intensity at the jet-wake interfaces are in good agreement with the experimentally determined curves.

The development of the disturbed flow in the diffuser inlet region was exactly analyzed in a comparison of experimental results with calculations based on the two-dimensional jet-wake flow model of Dean and Senoo. In contrast to the original theory, the considerable effects with high-performance centrifugal compressors -- flow compressibility and boundary layer

displacement -- on the conversion of energy in the vaneless diffuser were also taken into consideration. With this expanded theory, calculated radial curves of the characteristic disturbance parameters and of the static pressure were in good agreement with measured values. By contrast, by the assumption of an axially symmetric flow the prediction for the rise in static pressure would be too low. The angular momentum distribution of the disturbed flow illustrates the effect of the reversible exchange of energy and of the jet-wake interface friction on the homogenization of the flow.

The radial total pressure development is clearly influenced by wall friction effects. Immediately behind the impeller outlet the disturbed flow leads to increased total pressure losses. In the operating points studied here, the total efficiency of the stage decreases by less than 2 points under the effect of the disturbed flow. A parameter study shows that these losses -- above all in the vicinity of the performance graph absorption limit -- may climb to 4-8 efficiency points. /200

Finally, it must be said that the results of the detailed measurements behind a highly-loaded centrifugal compressor impeller are closely approximated by the expanded jet-wake theory. At the present time, the application of this theory is still affected by the disadvantage that the starting conditions of the disturbed flow can be exactly determined only by constly measurements (in case one is not satisfied with estimates or results from simple measuring techniques [9.1]).

In the meantime, as a result of the introduction of the dual-focus laser method for measuring velocity, it has been possible also to exactly measure the flow pattern within cnetrifugal impellers. Theoretical flow models derived from such measurements should be capable of predetermining the condition of flow at the impeller outlet. Thus appears the possibility of simulating the complex flow in high-performance centrifugal compressors in a simplified model system based on the physics of fluid flow, and from this derive fairly optimal stage configurations.

Dietrich Eckardt, Certified Engineer  
5,000 Cologne 90, Linder Höhe

## REFERENCES

### Section 2

- 2.1 Smith, J.A., "Notes on some experimental researches on internal flow in centrifugal pumps and allied machines," Engineering 74, 763 (1902). /201
- 2.2 Carrard, A., "On the calculation of centrifugal impellers," La Technique Moderne 15, 65-71 and 100-104 (1923).

### Section 3

- 3.1 Traupel, W., Thermische Turbomaschinen [Thermal Turbomachines], Vol. 1 edition 2, Springer, Berlin, Göttingen, Heidelberg, 1966.
- 3.2 Schodl, R., "A new optical velocity-measuring method, 'dual-beam laser method'" DFVLR Report, No. 12, 506-508 (1973).
- 3.3 Kurtz, A.L. and J.C. Kicks, "Development and application of ultra-miniature pressure transducers for wind tunnel models," Proc. of the 15th National ISA-Aerospace Instrumentation Symp., 1969, Las Vegas.
- 3.4 Armentrout, E.C., "Development of a high-frequency-response-pressure-sensing-rake for Turbofan Engine tests, NASA TM X-1959 (1970).
- 3.5 Weyer, H., Bestimmung der zeitlichen Druck-mittelwerte in stark fluktuierender Strömung, insbesondere in Turbomaschinen [Determination of Mean Pressure Values over Time in a Strongly Fluctuating Flow, in Particular in Turbomachines], Dissertation Rheinisch-Westfälische Technische Hochschule, Aachen.
- 3.6 Lederer, P.S., "Performance-testing pressure transducers," Instr. & Control Systems, 93-99 (1967).
- 3.7 "Guide for specifications and tests for strain gage [sic] pressure transducers for aerospace testing," Inst. Soc. of America, Pittsburgh Pa., Report R.P. 37.3 (1964). /202
- 3.8 Bryer, D.W. and R.C. Pankhurst, Pressure Probe Methods for Determining Wind Speed and Flow Direction, NPL, Her Majesty's Stationery Office, London, 1971.

- 3.9 Hinze, J.O., Turbulence -- An Introduction to its Mechanism and Theory, McGraw-Hill, New York, Toronto, London, 1959.
- 3.10 Eckardt, D. "Applications of dynamic measurement techniques for unsteady flow investigations in centrifugal compressors," von Karman Institute for Fluid Dynamics, Brussels, Lecture Series 66 "Advanced Radial Compressors" March, 1974.
- 3.11 Nielsen, P.E. and C.G. Rasmussen, "Measurement of the frequency curve of amplitude and phase," DISA Information No. 4, 18-24 (1967).
- 3.12 Giese, K., and C. Schreck, "Hot-wire measurements on rotating impellers of turbomachines, Part II," Technica 18, 103-108 (1969).
- 3.13 Spangenberg, W.G., "Heat-loss characteristics of hot-wire anemometers at various densities in transonic and supersonic flow," NACA TN-3381 (1955).

#### Section 4

- 4.1 "Aerodynamic-thermodynamic design of the centrifugal compressor impeller for the research project entitled 'Centrifugal Compressor' of the Forschungsvereinigung Verbrennungskraftmaschinen e.V. [Internal Combustion Engine Research Association]," Cost Study Report 314/69, Daimler-Benz A.-G., Stuttgart, 1969.
- 4.2 Eckardt, D., "Study of impeller flow in highly-loaded centrifugal compressor stages, Part I: Experimental setup, measurement technique, flow analysis; Part II: Experimental data," Research Report of the Forschungsvereinigung Verbrennungskraftmaschinen e.V. [as for reference 4.1] No. 154 (1974). /203
- 4.3 Hungenberg, H.G. and H. Weyer, "A noncontact method for monitoring and measuring the effective gap between impeller blades and the housing of turbomachines during operation," DLR Research Report 72-40 (1972).
- 4.4 Traupel, W. "Theory of strongly disturbed flows in tunnels and turbomachines," Research Report of the Forschungsvereinigung Verbrennungskraftmaschinen e.V. [as above] No. 153 (1970).
- 4.5 Kaily, J.W., and R.E. Nece, "Chamber-dimension effects on induced flow and frictional resistance of enclosed rotating discs,": Trans. ASME, Seried D, 82, 217 f (1960).

## Section 5

- 5.1 Ludwig, R., Methoden der Fehler- und Ausgleichrechnung [Methods of Error Calculation and Balancing Calculation], Vieweg, Braunschweig, 1969.

## Section 6

- 6.1 Eckardt, D., "Instantaneous measurements in the jet-wake discharge flow of a centrifugal compressor impeller," Trans. ASME, Series A, J. of Engg. for Power 97, 337-346 (1975).
- 6.2 Neuhäuser, H., "Calculation of the flow in the vaneless annular space of the centrifugal compressor," Progress reports of the VDI [Society of German Engineers] Journals, Series 7, No. 37. (1975).
- 6.3 Voorde, V.D., C.B. Bos, J. [sic], "Measured and calculated turbulent boundary layer flow in a vaneless radial diffuser," TNO-IWECO Report No. 80922/1 (1972). /204
- 6.4 Traupel, W., Die Theorie der Strömung durch Radialmaschinen [The Theory of Flow through Centrifugal Jets], Braun, Karlsruhe, 1962.
- 6.5 Dean, R.C., Jr., D.D. Wright, and P.W. Runstadler, Jr., Fluid mechanics analysis of high pressure ratio centrifugal compressor data, USAAVLABS Technical Report 69-76, AD 872161 (1970).
- 6.6 Fischer, K. and D. Thoma, "Investigation of the flow conditions in a centrifugal pump," Trans. ASME 54, 141-155 (1932).
- 6.7 Hamrick, J.T., J. Miszisin, and D.J. Michel, "Study of three-dimensional flow distribution based on measurements in a 48-ince radial inlet centrifugal impeller," NACA TN-3101 (1954).
- 6.8 Fujie, K., "Three-dimensional investigation of flow in centrifugal impeller with straight-radial blades," Bulletin of JSME 1, 42-49 (1958).
- 6.9 Senoo, Y., M. Yamaguchi and M. Nishi, "A photographic study of the three-dimensional flow in a radial compressor," Trans. ASME, J. of Engrg. for Power 90, 237-244 (1968).
- 6.10 Fowler, H.S., "Research on the Internal Aerodynamics of the Centrifugal Compressor," 11th Anglo-American Aeronautical Conference, 8-12 Sept., 1969, London, Paper No. 19.



- 6.11 Schodl, R., "A dual-focus velocimeter for turbomachine applications," von Karman Institute for Fluid Dynamics, Brussels, Lecture Series 78 "Advanced Testing Techniques in Turbomachines", April 1975.
- 6.12 Eckardt, D., "Study of impeller flow in highly-loaded centrifugal compressor stages," Research Report of the Forschungsvereinigung Verbrennungskraftmaschinen e.V. [as above], Frankfurt/M., No. 183 (1975) and supplement I, DFVLR Internal Report 352-75/9 (1975). /205
- 6.13 Eckardt, D. and R. Schodl, Three-Dimensional Flow Studies in a High-Speed Centrifugal Compressor Impeller Using a Laser Velocimeter. Improvements in Fluid Machines and Systems for Energy Conversion, Hoepfli, Mailand, 1976, pp. 1-35.
- 6.14 Eckardt, D., "Detailed flow investigations within a high-speed centrifugal compressor impeller," Trans. ASME, J. of Fluids Engrg. 98, 390-402 (1976).
- 6.15 Stanitz, J.D., "Two-dimensional compressible flow in turbomachines with conic flow surface," NACA Pr. 935 (1949).
- 6.16 Stanitz, J.D. and V.D. Prian, "A rapid approximate method for determining velocity distribution on impeller blades of centrifugal compressors," NACA TN-2421 (1951).
- 6.17 Prian, V.D. and D.J. Michel, "An analysis of flow in rotating passage of large radial-inlet centrifugal compressor at tip speed of 700 feet per second," NACA TN-2584 (1951).
- 6.18 Domm, U. and P. Hergt, "The energy distribution in three centrifugal impellers of different widths," AVA Research Report 63-01, 138-154 (1963).
- 6.19 Dean, R.C. Jr. "The fluid dynamic design of advanced centrifugal compressors," von Karman Institute for Fluid Dynamics, Brussels, Lecture Series 66 "Advanced Radial Compressors," March 1974.
- 6.20 Traupel, W., "Vortex systems in blade rows and turbomachines," ZAMP 4, 298-311 (1953).
- 6.21 Howard, J.H.G., "Analytical theory of secondary flow in a centrifugal impeller," Trans. of the Engrg. Inst. of Canada 9, No. B-1, pp. 1-9 (1966). /206

- 6.22 Bradshaw, P., "Effects of streamline curvature on turbulent flow," AGARDograph No. 196 (1973).
- 6.23 Johnston, J.P. " The effects of rotation on boundary layers in turbomachine rotors," NASA SP-304, Part I, 207-249 (1974).
- 6.24 Moore, J., "A wake and an eddy in a rotating radial flow passage," Trans. ASME, J. of Engrg. for Power 95, 215-219 (1973).
- 6.25 Eide, S.A. and J.P. Johnston, "Prediction of the effects of longitudinal wall curvature and system rotation on turbulent boundary layers," Stanford Univ., Thermosciences Div., Mech. Eng. Dept. Report PD-19 (1974).
- 6.26 Taylor, E.S., "The skewed boundary layer," Trans. ASME J. of Basic Engrg. 81, 297-304 (1959)
- 6.27 Traupel, W., "Report on the state of the theory of the centrifugal compressor impeller, October, 1976," Research Report of the Forschungsvereinigung Verbrennungskraftmaschinen e.V. [as above], Frankfurt/M., No. 224, 1977.
- 6.28 Eckardt, D., "Study of the impeller flow in highly-loaded centrifugal compressor stages. Supplemental report to FVV No. 183.1975 with a systematic compilation of results," Research report of the Forschungsvereinigung Verbrennungskraftmaschinen, e.V. [as above], Frankfurt/M., No. 207, 1976.
- 6.29 Traupel, W., "Fundamental features of a theory of the centrifugal compressor impeller," Research Report of the Forschungsvereinigung Verbrennungskraftmaschinen e.V. [as above] Frankfurt/M., No. 207 (1976).

## Section 7

/207

- 7.1 Dean, R.C. Jr. and Senoo, Y., "Rotating wakes in vaneless diffusers," Trans. ASME, J. of Basic Engrg. 82, 563-574 (1960).
- 7.2 Johnston, J.P. and Dean, R.C., Jr., "Losses in vaneless diffusers of centrifugal compressors and pumps," Trans. ASME, J. of Engrg for Power 88, 49-62 (1966).
- 7.3 Watson, N. and D.R. Ingham, "Compressible flow in a radial vaneless diffuser," Symposium on Internal Flows, University of Salford, April 1971, Paper 8, pp. A 56 to A 65.

- 7.4 Foa, J.V., "A new method of energy exchange between flows and some of its applications," Rensselaer Polytechnic Institute, Techn. Report TR A2 5009 (1955).
- 7.5 Senoo, Y. and M. Ishida, "Behavior of a severely Asymmetric flow in a vaneless diffuser," Trans. ASME, J. of Engrg. for Power 97, 375-387 (1975).
- 7.6 Zurmühl, R., Praktische Mathematik für Ingenieure und Physiker [Practical Mathematics for Engineers and Physicists], Springer, Berlin, 1963.
- 7.7 Van Le, N., Discussion contribution to [7.1], Trans. ASME, J. of Basic Engrg. 82, 571-572 (1960)
- 7.8 Senoo, Y, and M. Ishida, Private correspondence, 1972.
- 7.9 Rotta, J.C., Turbulente Strömungen [Turbulent Flows], Teubner, Stuttgart, 1972.
- 7.10 Dean, R.C., Jr., Private correspondence, 1972.
- 7.11 Scholz, N., "Theoretical resistance coefficients and optimum radii ratios of centrifugal diffusers with a turbulent boundary layer," BMW Triebwerksbau [BMW Propulsion Systems Construction], Internal Report G-020-02, (1958).

## Section 8

/208

- 8.1 Hess, K., "Rotating wake regions in the vaneless diffuser of a centrifugal compressor," AVA Research Report 63-01, pp. 40-54 (1963).

## Section 9

- 9.1 Eckardt, D., "Advanced experimental techniques for centrifugal compressor development," ASME Fluid Dynamics Institute, Radial Flow Turbomachinery Course, Hanover, N.H. USA, Proc. SC 3 (1976), also in DFVLR Internal Report 352-76/9 (1976).

## Appendix

- III.1 Pfau, H., "Temperature measurements for flow investigation, in particular on centrifugal compressors," Konstruktion 19/12, 478-484 (1967).
- III.2 Moffat, R.J. and R.C. Dean, Jr., "Wake interaction effects and performance characteristics of stagnation-type

thermocouple," in Welliver, A.D. and J. Acurjo,  
"Element Design and Development of Small Centrifugal  
Compressors," USAAVLABS TR 67-30, Vol. II, AD 384 924,  
pp. 267-298 (1967).

I. Investigation of Temperature Effects on Miniature  
Semiconductor Pressure Transducers

Experimental Setup and Measurement Program

For these investigations and for calibrating the total temperature probe a thermostat was designed and built which meets particularly high demands for measurement accuracy and control accuracy of the experimental temperature. Fig. I.1 shows the main construction of the apparatus. B; separating the

/210

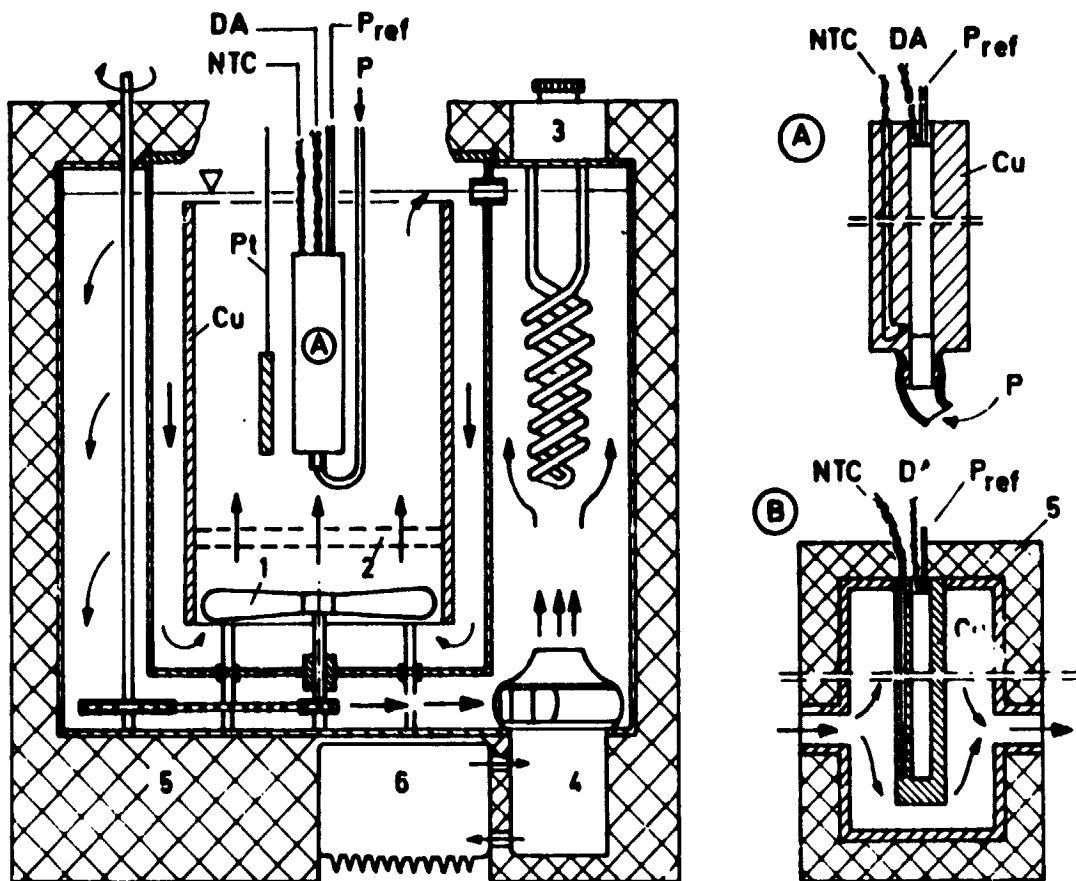


Fig. I.1. Experimental setup for investigating temperature effects on miniature semiconductor pressure transducers. A - Thermostat adapter for pressure calibration at variable ambient temperature; B - adapter for investigating the temperature gradient effect; 1 - propeller; 2 - straightener; 3 - hot/cold control; 4 - circulating pump; 5 - insulation; 6 - condenser; DA - pressure transducer; NTC - thermistor, Pt - resistance thermometer; p - test pressure;  $p_{ref}$  - atmospheric pressure.

measuring bath and the heating bath and building in a stirring propeller (1) and straightener (2) in the measuring bath, and building in a circulating pump (4) in the heating bath, very uniform temperature fields are produced within the test region (A). A special bath fluid<sup>1</sup> makes it possible to operate the thermostat at calibration temperatures between  $-20^{\circ}\text{C}$  and  $+250^{\circ}\text{C}$ . The sensitivity of response of the hot/cold control (3) is around 0.5K and the measurement accuracy of the calibrated Pt resistance thermometer with a 5-place digital ohmmeter is  $\pm 0.1\text{K}$ . To study the effect of changing ambient temperatures on the zero point drift and the sensitivity of the semiconductor pressure transducers the adapter (A) shown in Fig. I.1 (upper right) was inserted into the thermostat (modified for  $p_t$  probes). Thus the transducer can be acted upon with the pressure (p) at various ambient temperatures, while at the same time the temperature in the immediate vicinity of the pressure transducer membrane is measured by means of a NTC thermistor.

Prior to the actual pressure calibration, the uncooled total pressure transducers were carefully exposed to alternating temperatures several times (including approximately 2 hours at  $+150^{\circ}\text{C}$ ) and thus the effect of artificial aging was achieved.

After complete cooling of the bath, pressure calibration curves were then plotted at each of 4 ambient temperatures ( $20^{\circ}\text{C}$ ,  $60^{\circ}\text{C}$ ,  $100^{\circ}\text{C}$ ,  $140^{\circ}\text{C}$ ) for all the total pressure probes, Kulite XBL-9-093-25 G (maximum operating temperature,  $175^{\circ}\text{C}$ ). In addition, four Kulite XQL-093-25 wall pressure transducers (maximum operating temperature  $120^{\circ}\text{C}$ ), which were installed in the centrifugal compressor in water-cooled adapters, were calibrated for a general check of the operating behavior of semiconductor pressure transducer --  $20^{\circ}\text{C}$ ,  $60^{\circ}\text{C}$  and  $100^{\circ}\text{C}$ . /211

Deviating from the U.S. test conditions (cf. [3.6, 3.7]), which when making temperature changes suggest gradients of approximately 10K per hour, a difference of forty K between the test temperatures was bridged in about thirty minutes.<sup>2</sup> But then the test temperature, as specified, is held constant for 45 minutes before the pressure calibration is made. During the calibration, the readings of the Pt resistance thermometer and the NTC thermistor differ by less than 0.2 K.

For investigating temperature gradient effects on the zero point reading of semiconductor pressure transducers adaptor (B) shown in Fig. I.1 (lower right) was used. It could alter-

- 
1. Marlotherm L, Chemische Werke Huls.
  2. Based on empirical values associated with the change in operating point of the centrifugal compressor where the steady state is reached in less than 30 minutes.

nately be connected to the water circuit of two thermostats. After the pressure transducer (DA) inserted in the Cu cylinder had been held constant at 295 K for 45 minutes, the switch was made to the second thermostat with a higher water temperature. During this process, the curve of the pressure transducer output voltage and the temperature on the measuring membrane were continuously recorded (cf. Fig. 3.7).

## II. The Synchronized Sampling Technique

/212

### Principles and Basic Equipment Design

In the signal processing of rapidly changing, periodically recurrent and very noisy test signals by means of the synchronized sampling technique (SST), two aspects of the technique are of prime importance:

1. The test signal is expanded over time (expansion factor up to  $10^{10}$ ) and the Fourier spectrum of the signal is transformed downward to frequencies which lie in the operating range of a normal x-y recorder.
2. The average, periodically recurrent signal component is separated from stochastically distributed signal fluctuations. This considerably improves the signal-to-noise ratio.

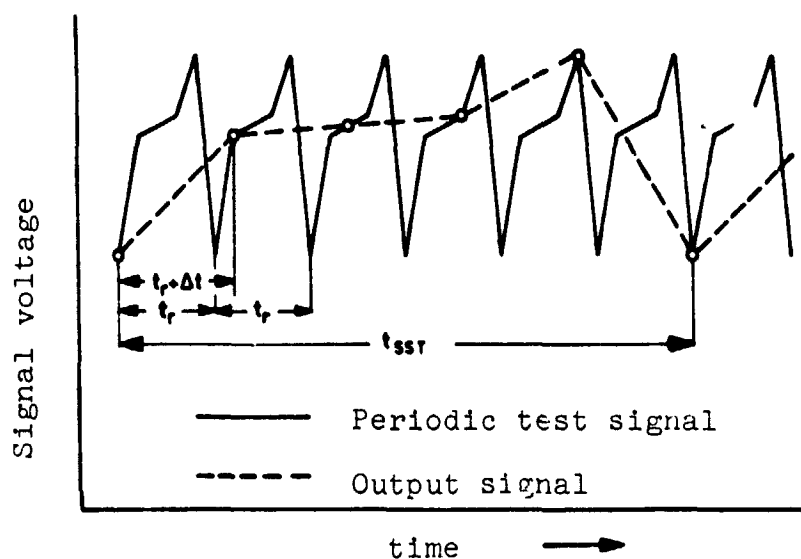


Fig. II.1. Principle of the expansion over time of a periodic test signal with the aid of the simplified sampling technique, expansion factor  $\alpha = 6$ .

This process is explained by referring to Fig. II.1. If one scans the instantaneous voltage of the test signal in the time intervals  $t = t_p + \Delta t$ , whereby  $\Delta t$  is steadily increased, this produces the output signal represented by the circles. If the scanning points are sufficiently dense, then the SST output signal gives an image of the test signal expanded over time. The expansion factor is  $\alpha = t_p/\Delta t$  and can be made any size with  $\Delta t \rightarrow 0$ .

Thus the synchronous sampling technique is an electronic "Analogon" to the familiar optical stroboscope technique in which a periodically recurrent pattern is "apparently" thereby slowed down so that it is not observed continuously but only momentarily in certain time intervals, whose reference is fixed to the repetition rate of the original process.

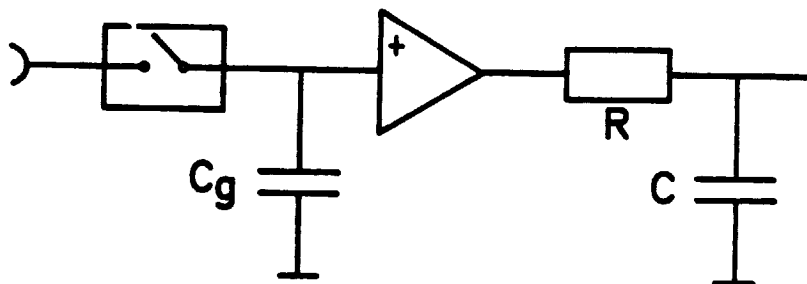


Fig. II.2. Block diagram of the "sample/hold/integration" unit of the SST apparatus.

To accomplish the pointwise scanning requires a selection logic and a rapid switch (cf. Fig. II.2). In order to achieve high resolution the opening time of the switch  $t_g$  must be small with respect to the period duration of the test signal  $T$ . So that the scanned voltage between the measurement periods holds good, it is stored on a condenser  $C_g$ . The following low-pass filter evens the jumps between the individual scanning points and is used for averaging.

#### Taking the Mean

Fig. II.3 will help explain the SST averaging principle. At position a it shows a nonsteady signal voltage curve with a period of  $T = t_p$ .



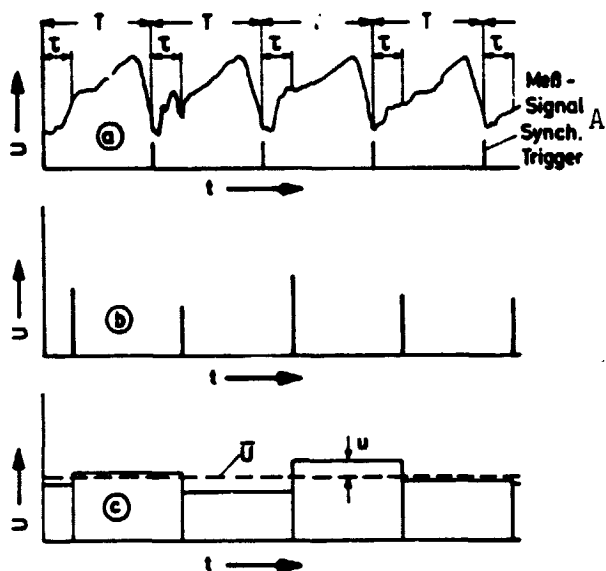


Fig. II.3. Diagram of the sampling process:  
 (a) - periodic input signal ( $\tau$ : phase relationship of the samples); (b) - sampler output (pulse height corresponds to the instantaneous signal value at  $\tau$ ); (c) - output signal of the voltage stabilizer.

Key: A) Test signal synchronization trigger.

corresponding to the mean value stands out more sharply.

The effective value of the fluctuation intensity of the test signal  $\sqrt{u^2}$  is formed at the a.c. voltage output of the voltage stabilizer.

In the language of statistics, the sampling scanning process produces a sequence of scattering individual measurements  $U_i$ .

In a first approximation the RC term averages over the measured values  $U_i$  which were recorded within the time constants RC (integration time  $t_i$ ). The number of measurements is  $n = t_i/\tau_r$ .

For stochastically distributed signal deviations the signal-to-noise ratio is improved by a factor of  $\sqrt{n}$ . Therefore, the signal-to-noise ratio can be improved at will if the time con-

The beginning of the period is marked by trigger impulses which are picked up by a trigger disc with the aid of a ferromagnetic magnetoresistor transducer. This turns around with the compressor shaft. The scanning takes place in each case at point  $\tau$  after the trigger pulse, i.e. in this example the measurement is made without any scanning shift ( $\Delta t = 0$ ). This restriction simplifies the description and produces practically the same result as a treatment with  $0 \neq \Delta t \ll \tau_r$ .

At each signal scanning the condenser  $C_g$  is charged with the instantaneous signal voltage, position (b). It holds this voltage until the next scanning and what arises is the so-called box car train signal, position (c). This signal train consists of the d.c. component  $\bar{U}$ , which gives the mean value, and an a.c. component  $u$ , which originates from stochastically distributed disturbances. The interfering a.c. voltage is suppressed in the low-pass filter after  $C_g$ , so that the d.c. component

stant of the RC term is made sufficiently large a large  $t_1$ , however, the total measuring time  $t_m$  must also be correspondingly increased in order to prevent a reduction of the upper limit frequencies of the measuring system. Thus the upper limit for signal-to-noise improvements is set by practicable measuring times and the long term stability of the compressor operating condition.

Further information on the SST measuring principle can be obtained from the quantitative appraisal in Table II.1.

Fig.II.4 shows the principle arrangement of the sampling apparatus used in the form of a block diagram. In addition, a

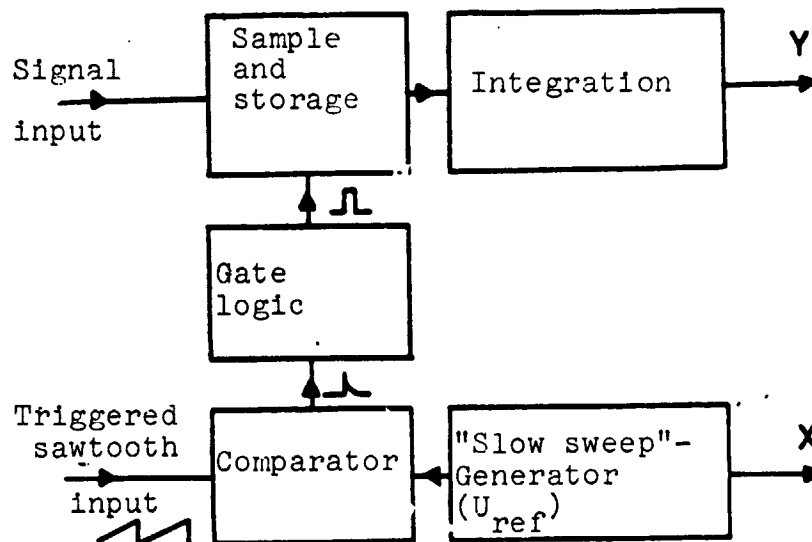


Fig. II.4. Block diagram of the Sampling Apparatus for averaging periodic test signals.

cathode ray oscillograph is required, on whose screen the signal train to be transferred is adjusted by means of the synchronous trigger. The SST scanning measuring time for the entire screen width (10 cm) is generally  $t_m = 2$  minutes. The position in time of the sample is set by a voltage  $U_{ref}$  while  $t_m$  steadily increased. A comparator compares this voltage with the internal sawtooth voltage of the oscillograph which is triggered anew each time the beam passes, and when there is coincidence on the rising side of the saw tooth it gives off an impulse which controls a momentarily closing switch (gate time  $t_g$ ) through which the instantaneous signal value is connected to the averaging condensor. Since a quasi d.c. voltage

/217

TABLE II. 1. QUANTATIVE APPRAISAL ON THE USE OF THE SYNCHRONIZED SAMPLING TECHNIQUE

Problem:

The nonsteady wall pressure curve for the region of a blade spacing is to be transferred to a x-y recorder and digitalized in parallel with this.

Example:

Rotation speed  $n = 18,000$  rpm, Blade number  $z = 20$   
 Signal frequency  $6$  kHz ( $167 \mu\text{s}/t$ )  
 (Blade spacing  $t$ )

Option: Horizontal time sweep on the cathode ray  
 oscillograph  $20 \mu\text{s}/\text{cm}$   
 Screen width  $10$  cm

→ 1,2 signal divisions per screen width

→ Beam transit time  $t_s = 200 \mu\text{s}$

→ Sweep frequency  $3$  kHz ( $t_r = 0.333$  ms)

Option: SST - Integration time  $t_i = 0.5$  s

SST - Gate time  $t_g = 2 \mu\text{s}$

→ Number of samples per mean value  $n = t_i/t_r = 1,500$

→ Improvement of the signal-to-noise ratio by a factor of  $\sqrt{n} = 38.7$  (31,8 dB)

Instrument constant: SST measuring time for screen width  
 $t_m = 120$  s

→ Digital signal resolution ( $t_m/t_i$ )  $< 240$  values

→ Time expansion  $t_m/t_s = 6 \cdot 10^5$

is measured at the condenser, the measurement uncertainty, under normal conditions even for signals up into the MHz range, is less than  $\pm 0.5\%$ . The accuracy with respect to time -- with appropriate constancy of rotation speed -- is limited only by the sawtooth of the oscillograph. By calibration, an accuracy of better than 1% can easily be obtained here.

### III. Total Temperature Measurement in the Disturbed Flow behind the Impeller Outlet /218

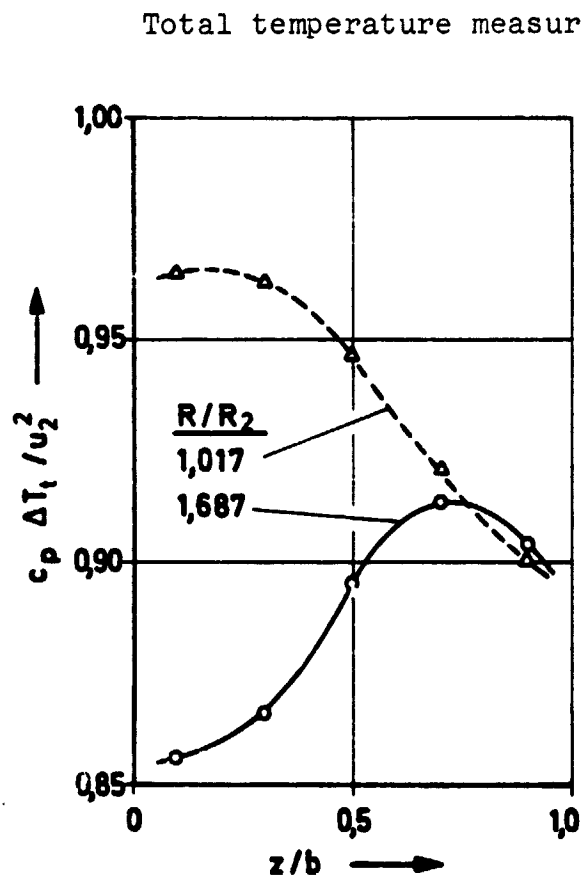


Fig. III.1. Curve of the total temperature increase, plotted over diffuser width, measured in two radii ratios behind the impeller outlet. Operating point:  $n/\sqrt{\theta_0} = 16,000$  rpm,  $\dot{m}\sqrt{\theta_0}/\delta_0 = 6.88$  kg/s.

of a total temperature probe with nonsteady oncoming flow. The following, simplified estimate, taking as a basis the "block" velocity distribution shown in Fig. III.2 above, will indicate

Total temperature measurements with slow stagnation temperature probes immediately behind the centrifugal compressor impeller showed larger temperature increases -- up to about 10% -- than were measured downstream in the vicinity of the diffuser outlet. As an example, Fig. Fig. III.1 shows total temperature profiles (with correction of an average recovery factor  $R_f$ ) measured in two radii ratios over the diffuser width. The difference in these two curves is especially strong in the region of the front wall of the channel.

The reason for the higher temperature reading given by the probe installed immediately behind the impeller outlet is basically the particularly pronounced irregularity of the relative flow over the channel spacing in this reason. /219

Pfau [III.1] studied the effect of various velocity distribution on the temperature readings of impellers with backward bent blades.

For impellers with radially ending blades, Moffat and Dean [III.2] carried out detailed theoretical analyses on the heat transfer condition at the sensor

the order of magnitude of the error in the temperature reading as a function of the disturbance parameters generally used in this study, i.e. the wake component  $\epsilon$  and the relative velocity ratio of the wake and  $w_T/w_S$ .<sup>1</sup>

For the mass averaged total temperature increase, i.e. the real temperature increase after the termination of the mixing process, the following equations are valid:

$$\Delta \bar{T}_t = [c_{m,T} \epsilon \Delta T_{t,T} + c_{m,S} (1-\epsilon) \Delta T_{t,S}] / \bar{c}_m \quad , \quad (\text{III.1a})$$

(Assumption: density  $\rho = \text{constant}$ ) and

$$\Delta \bar{T}_t = \nu u^2 / c_p \quad . \quad (\text{III.1b})$$

The latter equation ignores components of the temperature increase due to internal disc friction and turbulent exchange movements at the impeller outlet. In the following equations it is also only valid for the jet region and wake region:

$$\Delta T_{t,S} = u (u - c_{m,S} / \text{tg } \bar{\beta}) / c_p \quad , \quad (\text{III.2a}) \quad /220$$

$$\Delta T_{t,T} = u (u - c_{m,T} / \text{tg } \bar{\beta}) / c_p \quad , \quad (\text{III.2b})$$

whereby in keeping with Fig. III.2 it is assumed:

$$\bar{\beta} = \beta_S = \beta_T \quad .$$

The symbols are defined as follows:

$\Delta \bar{T}_t$  total temperature increase  $\bar{T}_{t3} - \bar{T}_{t0}$ .

$c_p$  specific heat at constant pressure,

$\bar{c}_m$  mean meridian velocity,

$\epsilon$  relative wake component of a spacing,

---

1. The derived system of equations largely correspond to an unpublished system worked out by Conrad-Daimler-Benz A.G. 1971.

- $\mu$  reduced output factor,
- $u$  circumferential velocity,
- $\beta$  direction of the relative flow with respect to the negative circumferential tangent.

On the sensor of the total temperature probe the temperature increase indicated is  $\Delta T_{t,a}$ . Under the simplifying assumption of identical heat transfer coefficients in the jet region and wake region, the following equation applies:

$$\Delta T_{t,a} = \epsilon \cdot \Delta T_{t,T} + (1 - \epsilon) \cdot \Delta T_{t,S} \quad (III.3)$$

If we substitute Eqs. (III.2a,b) in Eq. (III.3), then the following equation follows with the flow coefficient  $\bar{\phi} = \bar{c}_m / u$ :

$$\Delta T_{t,a} = u^2 (1 - \bar{\phi} / \operatorname{tg} \bar{\beta}) / c_p \quad (III.4)$$

By using Eq. (III.1b) we obtain the relationship between the indicated and mass averaged total temperature increase:

$$\Delta T_{t,a} / \Delta \bar{T}_t = (1 - \bar{\phi} / \operatorname{tg} \bar{\beta}) / \mu \quad (III.5)$$

whereby the following relationship is used:

$$\bar{c}_m = \epsilon \cdot c_{m,T} + (1 - \epsilon) \cdot c_{m,S} \quad (III.6) \quad /221$$

In order to produce a reference for the disturbed velocity distribution Eqs. (III.1a,b) are set equal and Eqs. (III.2a,b) are used. If we solve for  $\operatorname{tg} \bar{\beta}$  we obtain the following:

$$\operatorname{tg} \bar{\beta} = \frac{\bar{\phi}}{1 - \mu} \left[ \frac{\epsilon \cdot c_{m,T}^2 + (1 - \epsilon) \cdot c_{m,S}^2}{\bar{c}_m^2} \right]$$

If we substitute for  $c_{m,S}$  using Eq. (III.6), then the following equation follows:

$$\operatorname{tg} \bar{\beta} = \frac{\bar{\phi}}{1 - \mu} \left[ 1 + \frac{\epsilon}{1 - \epsilon} \left( \frac{\bar{c}_m - c_{m,T}}{\bar{c}_m} \right)^2 \right]$$

or with the following notation

$$\lambda = \frac{\epsilon}{1 - \epsilon} \left( \frac{\bar{c}_m - c_{m,T}}{\bar{c}_m} \right)^2 \quad (\text{III.7})$$

we finally obtain

$$\text{tg } \bar{\beta} = \bar{\omega} \frac{1 + \lambda}{1 - \mu} \quad (\text{III.8})$$

This substituted into Eq. (III.5) then gives:

$$\frac{\Delta T_{t,a}}{\Delta \bar{T}_t} = \frac{1 + \lambda / \mu}{1 + \lambda} \quad (\text{III.9})$$

To introduce the disturbance parameter  $\gamma = w_T/w_S$ , Eq. (III.7) is rearranged with Eq. (III.6) and the meridian velocity ratio  $c_{m,T}/c_{m,S}$  is replaced by  $\gamma$  since  $\beta_S = \beta_T$ . With Eq. (III.9) we finally obtain an equation for the error in the total temperature reading which, for a specific reduced output factor  $\mu$ , depends only on the disturbance parameters  $\epsilon$  and  $\gamma$ :

$$\lambda = \frac{\epsilon(1 - \epsilon)(1 - \gamma)^2}{[1 - \epsilon(1 - \gamma)]^2} \quad (\text{III.10}) \quad /222$$

As an example of such a parameter study, Fig. III.2 shows the curve of  $\Delta T_{t,a}/\Delta \bar{T}_t$  as a function of the disturbance variable  $l=w_T/w_S$  for three wake components  $\epsilon$ . An evaluation was made in each case for a value of the reduced output factor  $\mu$  which is typical for impellers with a given blade angle of  $\beta_{S2}$ . It turns out that the error in the temperature reading increase with increasing  $\epsilon$  and  $l=w_T/w_S$ : or with decreasing  $\mu$ .

The order of magnitude of the error in the reading reveals that exact measurements of total temperatures in the flow discharged from the impeller are only possible in areas in which the disturbances have largely subsided.

Conversely, it is possible, from the comparison of temperature measurements at different distances behind the impeller, /223

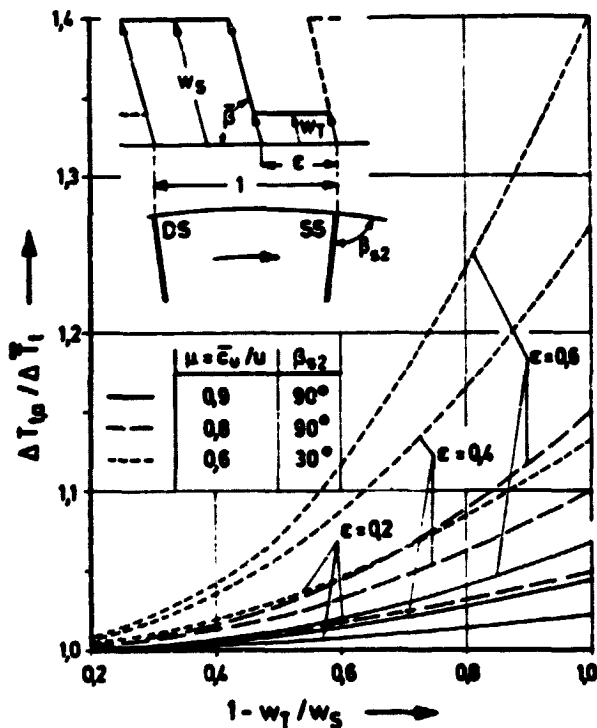


Fig. III.2. Parameter study for estimating the error in the reading of total temperature probes with irregular incoming flow.

to infer the degree of non-uniformity, even if this can only be qualitative because of the large number of simplifying assumptions.

For example, analysis of the findings shown in Fig. III.1 permits us to state that the flow behind the impeller outlet in the backward section of the channel ( $z/b > 0.6$ ) is largely equalized in the circumferential direction, i.e. the circumferential disturbance of the flow field (wake region) lies in the region of the front wall of the channel and -- assuming  $w_T/w_s = 0$  -- there it assumes a wake component of at most about 50% of the spacing.

In view of the simple measuring method, these statements coincide remarkably well with the results of the detailed flow studies using measuring techniques with high time resolution.

IV. Definition of the Relative Total Pressure  $P_{t,rel}$  /224

Starting with the energy equation in the relative system, the following equation holds for the relative total enthalpy  $h_{t,rel}$

$$h_{t,rel} = h + w^2/2 - u^2/2 \quad (IV.1)$$

with  $h$  = static enthalpy;  $w$  = relative velocity;  $u$  = circumferential velocity.

For a relative flow without energy transfer (as a result of "internal" disc friction on the housing wall) the following equation is valid along a flow line:

$$h_{t,rel} = c_p \cdot T_{t,rel} = \text{const.} \quad (IV.2)$$



with  $T_{t,rel}$  = relative total temperature.

In particular, it follows from Eqs. (IV.1) and (IV.2), with nontwisting oncoming flow to the impeller ( $w^2/2 - u^2/2 = c^2/2$ ) that:

$$T_{t,rel} = T_{t0,N} \quad (IV.3)$$

with  $T_{t0,N}$  = (standard) intake total temperature.

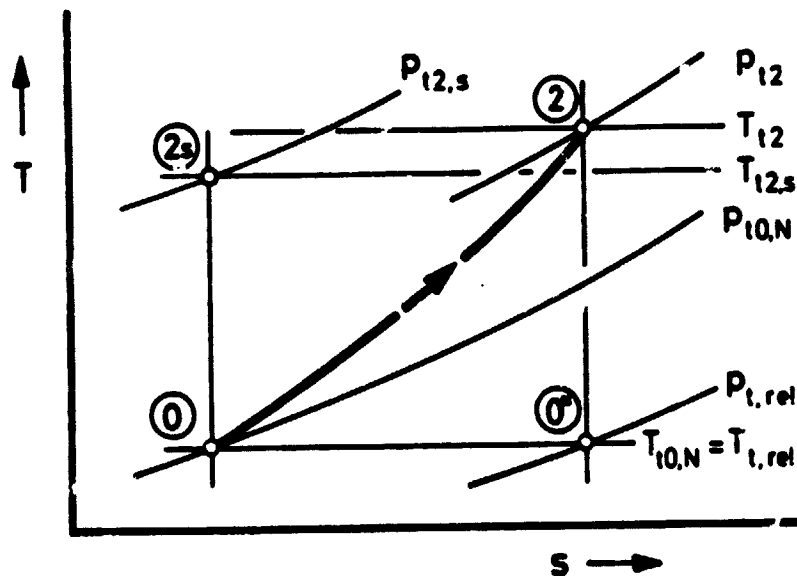


Fig. IV.1.  $T,s$  diagram for any pressure change between the total states ① and ②.

In the  $T,s$  diagram, Fig. IV.1, the relative total pressure  $P_{t,rel}$  is defined by the state ①\*:

- it lies on the isotherm valid in the relative system according to Eq. (IV.3) and
- it has the same entropy as the actual final compression pressure  $p_{t2}$ .

1. The same definition was used by Dean and co-workers in ([6.5], appendix VII). The derivation of the relative total pressure  $P_{t,rel}$  from the "relative total enthalpy relationship  $h_{t,rel} =$ " (cont. on p. 181)

With the isentropic relationship, the following equation is valid:

$$P_{t2}/P_{t,rel} = (T_{t2}/T_{t,rel})^{\kappa/(\kappa-1)} \quad (IV.4)$$

Along the isotherms  $T_{t,rel} = \text{constant}$ , the Gibbs equation reads as follows:

$$T ds = c_p dT - dp/\rho, \quad \text{and} \quad (IV.5)$$

$$ds/R = - dp/(\rho RT) = - dp/p \quad (IV.6)$$

with  $s$  = entropy;  $R$  = gas constant;  $\rho$  = density;  $c_p$  = specific heat at constant pressure;  $\kappa$  = isentropic exponent.

In the inlet standard condition --  $P_{t0,N}$ ,  $T_{t0,N}$  -- the entropy  $s_0$  is set equal to zero analogous to Eq. (5.18). If we integrate Eq. (IV.6) from state 0 to state 0\*, then we obtain the following:

$$(s_{0^*} - s_0)/R = s/R = - \ln(P_{t,rel}/P_{t0,N}), \quad (IV.7)$$

or the following equation for the relative total pressure ratio in the impeller:

/226

$$P_{t,rel}/P_{t0,N} = e^{-s/R}. \quad (IV.8)$$

---

constant is sensible from the energy standpoint, since for an observer rotating with the system the impeller shaft is at rest, hence no work of any kind is transmitted. In the case of a conceivable definition of the "total pressure of the relative flow"  $p'_{t,rel}$  -- based on the "total enthalpy of the relative flow"  $h'_{t,rel} = h + w^2/2 = h_{t,rel} + u^2/2$  -- this condition is not met. The U.S. literature distinguishes -- more clearly in words -- between  $p_{t,rel}$  (relative total pressure) and  $p'_{t,rel}$  (relative stagnation pressure).

Curriculum Vitae

Name: Dietrich Eckardt

Date of birth: [REDACTED]

Place of birth: [REDACTED]

Parents: Hans Eckardt and Irmgard Eckardt  
[REDACTED]

Marriage: March 13, 1970 to Gabriele Eckardt, née Feldmeier

Education: 1950-1954 Volksschule Hof/  
Bayern

1954-1963 Oberrealschule Hof/  
Bayern

July 17, 1963 School leaving  
certificate

1963-1978 Research at the  
Berlin technical University in  
the field of "Theoretical  
Mechanical Engineering" (process  
technology) and 1 year of  
practical experience in industry.

Nov. 14, 1968 Certificate  
document

Occupation: Since Nov. 1, 1968 scientific  
colleague at the Institut für  
Luftstrahlantriebe der Deutschen  
Forschungs-und Versuchsanstalt  
für Luft- und Raumfahrt e.V.  
[Institute for Jet Propulsion  
units of the German Aeronautics  
and Space Research and Test  
Center] in Cologne-Porz.